Production and efficiency improvement of perovskite solar cells using the new 3-step method

Yuji Okamoto

February 2019

Production and efficiency improvement of perovskite solar cells using the new 3-step method

Yuji Okamoto
Doctoral Program in Materials Science

Submitted to the Graduate School of Pure and Applied Sciences in Partial Fulfillment of the Requirements for the Degree of Doctor of Philosophy in Engineering

at the
University of Tsukuba

Preface

The studies presented in this thesis were carried out under the guidance of Associate Professor Yoshikazu Suzuki in the Development of Materials Science at the Graduate School of Pure and Applied Sciences, University of Tsukuba. In this thesis, a new 3-step fabrication method of perovskite solar cell was developed to form bandgap gradients at the both top and bottom sides of perovskite layer.

Perovskite solar cells have attracted much attention, since they can be fabricated by a simple spin-coating method and demonstrate a relatively high power conversion efficiency (PCE). The maximum PCE of perovskite solar cells has recently reached to 23.7%.

For further improvement of PCE, a formation of bandgap gradient at the surface of perovskite light absorbing layer is a promising way. It is effective to improve the PCE by enhancing a carrier transport efficiency. For example, a formation of bandgap gradients at the top and bottom sides has been widely studied for CIGS solar cells, which was carried out by making compositional difference using dry processes. On the other hand, the formation of bandgap gradient at the bottom side is difficult for the perovskite solar cells prepared by a wet-process, e.g., spin-coating, since the compositional difference is usually produced by post-treatments and it can form the bandgap gradient only at the top surface side. Therefore, in this thesis, the new 3-step fabrication method was developed to form the bandgap gradients at the both top and bottom sides of the perovskite layer.

$CH_3NH_3PbI_3$ ($MAPbI_3$) is generally used as a material for the light absorbing layer of perovskite solar cells. When the $MAPbI_3$ layer is prepared by a standard 2-step method, i.e. pre-coating of PbI_2 layer and post-conversion to $MAPbI_3$ by reacting with CH_3NH_3I (MAI), unreacted PbI_2 remains at the bottom side. To produce compositional differences in the perovskite layer, $CH(NH_2)_2I$ (FAI) solution was additionally spin-coated as the 3rd step. By the additional spin-coating, the FA concentration difference was produced in the perovskite layer, and a multiple bandgap structure was successfully obtained by forming the bandgap gradient at the bottom side. Furthermore, the simultaneous formation of bandgap gradients at the both top and bottom sides was also realized by adding trace NaI into the FAI solution. The PCE of perovskite solar cells was effectively improved by the additional spin-coating. The effects of additional spin-coating on crystal structure, composition, film morphology and optical property of perovskite layer were also studied in detail.

Yuji Okamoto

February, 2019

Table of contents

Chapter 1

Introduction

Chapter 1: Introduction

1.1 Introduction of solar cells

Recently, an introduction amount of photovoltaic power system has increased due to an issue of global warming mainly caused by CO_2 emission [1,2]. Therefore, a further improvement of the conversion efficiency of solar cells is necessary. Besides the most popular silicon (Si) based solar cells, there are a variety of solar cells. The classification of solar cells is shown in **Fig. 1.1**, and the maximum power conversion efficiency (PCE) of these solar cells is shown in **Fig. 1.2**. Solar cells can be classified into Si based type, compound type, organic type, quantum dot type, and organic/inorganic hybrid type.

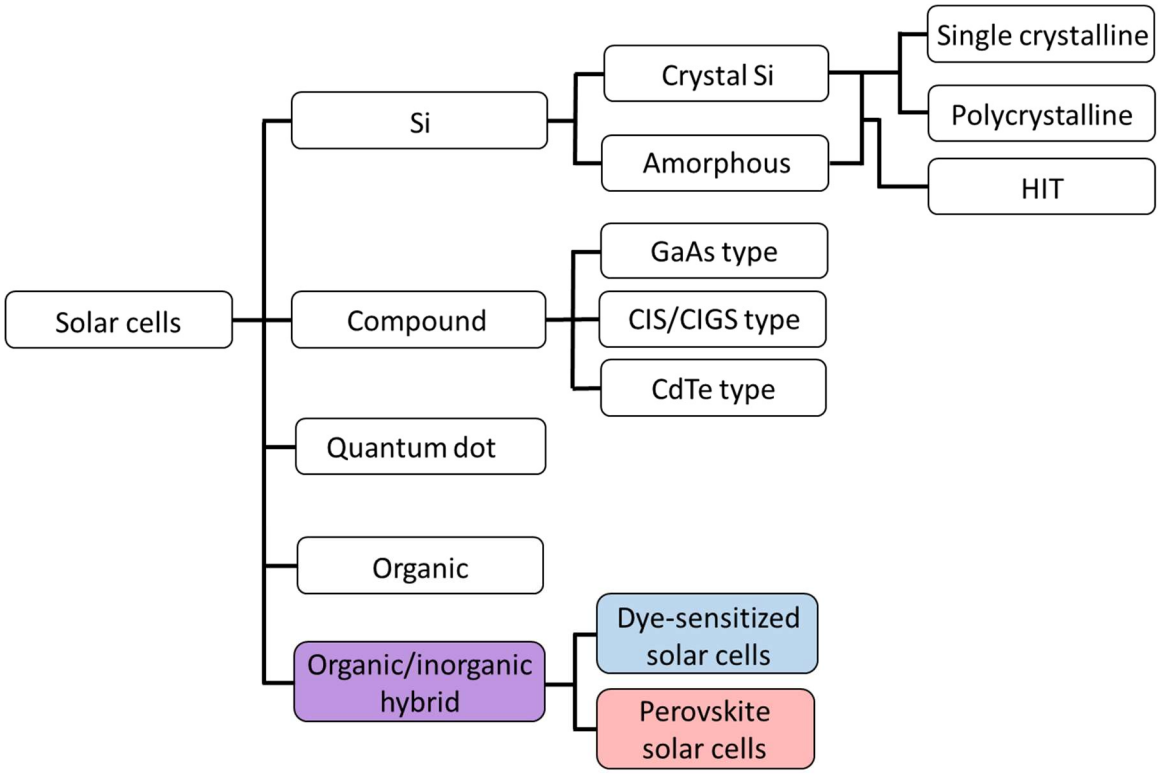

Fig. 1.1 Classification of solar cells [3].

Single crystalline Si based solar cells

This solar cell uses a monocrystalline Si as the raw material, and the maximum power conversion efficiency (PCE) at the laboratory level is currently 26.1% [4]. A relatively high PCE of ~16-20% can be obtained even for the commercial modules [5]. However, the production cost is relatively high compared with the other solar cells since a large single crystal Si substrate is required to produce a module. Recently, the production cost has been reduced thanks to progresses of the production technology, and its market share among the various solar cells is increasing.

Polycrystalline Si based solar cells

This solar cell uses a polycrystalline Si as the row material. The maximum PCE is 22.3% [4]. The

production cost is lower than that of single crystalline Si solar cell, but the PCE is lower. However, the share of the polycrystalline Si based solar cell is the highest in the solar cell market.

Amorphous Si based solar cells

This solar cell uses an amorphous Si as the row material. The maximum PCE is 14.0% [4]. Since the optical absorption coefficient of amorphous silicon is larger than that of single crystal silicon, a thin film type solar cell can be produced, which is effective to reduce the consumption of Si. The PCE is lower than those of crystalline Si solar cells.

Hetero-junction type (HIT) Si solar cells

This solar cell is composed of a heterojunction of crystalline Si and amorphous Si. It is called HIT (Hetero-junction with Intrinsic Thin Layer) type Si solar cells. The single crystalline Si is sandwiched by the amorphous Si. The maximum PCE is 26.6% [4]. It has a higher voltage, PCE and thermal stability than single crystal silicon solar cell. However, the production cost is higher due to the multijunction structure.

Compound type solar cells

This solar cell uses the compound of more than two elements as the raw material, such as groups II-IV and groups III-V in a periodic table. Since the bandgap is controlled by the combination of materials, a relatively high PCE can be obtained. In addition, they have large light absorption coefficients, so thin film type solar cells can be produced. There are several types of the compound type solar cells, such as CdTe (maximum PCE: 22.1% [4]), CIS ($CuInSe_2$), CIGS ($Cu(In, Ga)Se_2$), maximum PCE: 22.9% [4]), and GaAs types.

Quantum dot type solar cells

This solar cell uses a quantum dot as the row material. The size of particles used for the light absorbing layer is reduced to nanometer size. Since the absorbing light-wavelength can be tuned by changing the size of the quantum dot, a theoretical PCE is expected to be over ~ 63%. The maximum PCE is currently 16.6% [4].

Organic type solar cells

This solar cell is composed of organic electron donor layer and organic hole acceptor layer. This structure is similar to a p-n junction of an inorganic type solar cell. The PCE was ~1% in 2000, but the maximum PCE is currently 15.6% [4]. Although the PCE is still smaller than those of the other inorganic type solar cells, the production cost can be lower.

Organic/inorganic hybrid solar cells

This solar cell consists of a combination of organic and inorganic materials, and fabrication techniques of both organic and inorganic solar cells are used. There are basically two organic/inorganic hybrid solar cells, i.e. dye-sensitized solar cells and perovskite solar cells. This thesis focuses on the perovskite solar cells. The details will be described in the next section.

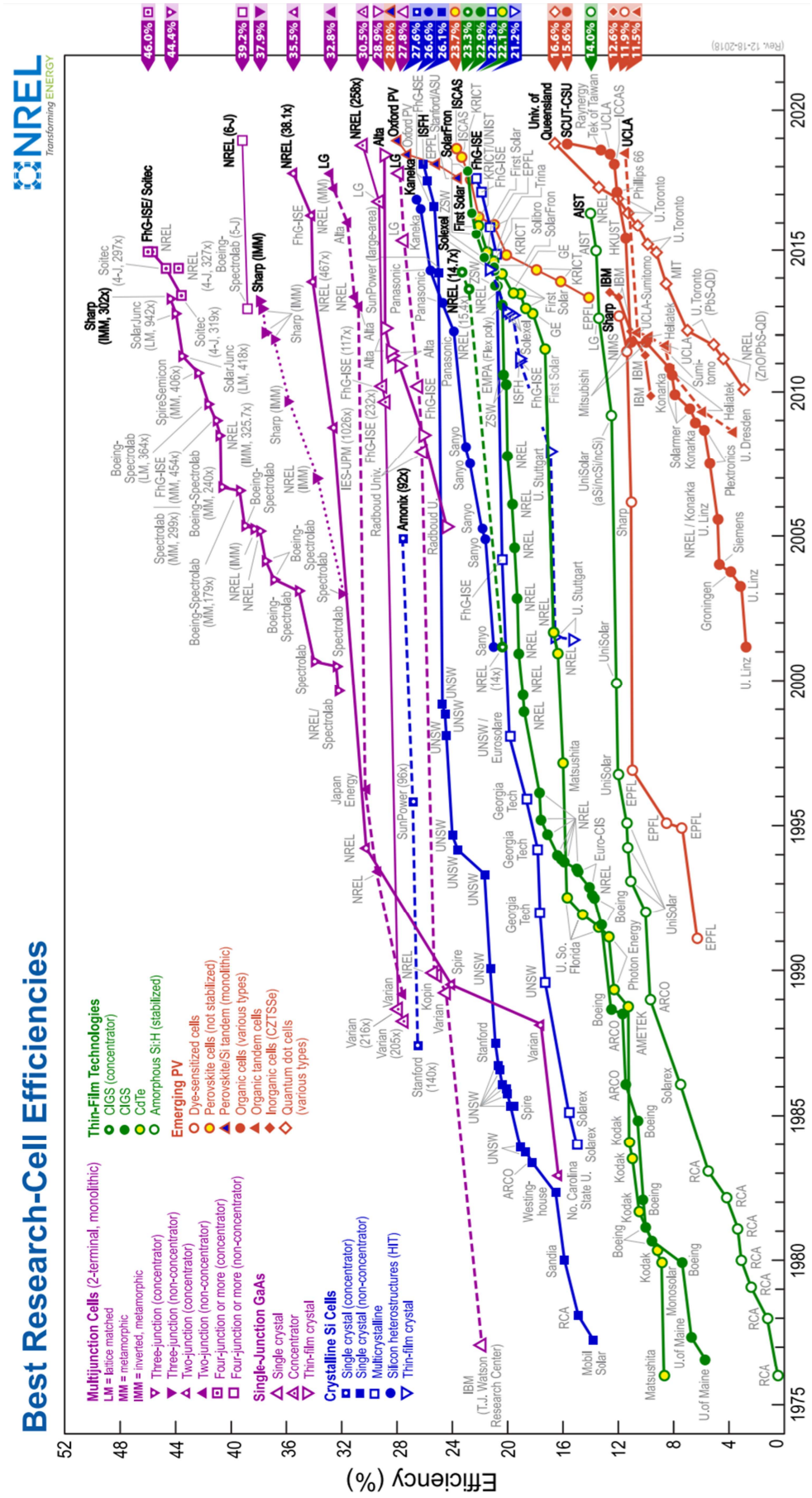

Fig. 1.2 Maximum power conversion efficiency of solar cells [4].

1.2 Introduction of perovskite solar cell

1.2.1 History of perovskite solar cell

The perovskite solar cell was developed based on the dye-sensitized solar cells, so it is better to describe about the dye-sensitized solar cells firstly. In the dye-sensitized solar cells, organic dyes are fixed on an oxide mesoporous layer. The dyes absorb the light which cannot be absorbed by the oxide semiconductor (dye-sensitization) and generate electrons [6]. In 1991, Prof. Grätzel's group firstly reported the dye-sensitized solar cells [7]. The cell had a transparent conductive oxide (TCO) glass, TiO_2 mesoporous layer prepared on the TCO glass, and organic dyes fixed on the TiO_2 mesoporous layer. They were sandwiched by the other TCO glass, and an electrolyte was injected into the gap of TCO glasses (**Fig. 1.3**). Under the sun light irradiation, the organic dyes are excited and emit electrons. The electrons are transported to outside through the conduction band of TiO_2, and electricity is generated. The PCE was ~7% in the first report [7], but the PCE of ~10 % was reported in 1993 [8]. After that, the dye-sensitized solar cells attracted much attention as a new generation low-cost solar cell, since it had a relatively high PCE of over 10% in spite of its easy fabrication process. The PCE was gradually increased and the maximum PCE is currently 11.9% [4].

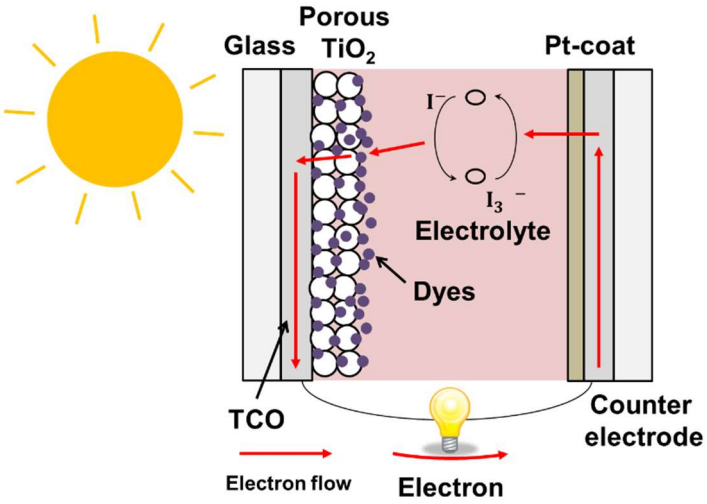

Fig. 1.3 Structure and working principle of dye-sensitized solar cells.

In the meantime, Prof. Miyasaka's group reported a unique dye-sensitized solar cell which used organometal trihalide perovskite: $CH_3NH_3PbX_3$ (X= I or Br) as the sensitizer in 2009 [9]. They prepared the light absorbing layer using $CH_3NH_3PbX_3$ in the TiO_2 mesoporous layer, and PCE of 3.8% was achieved. However, there was a problem on the stability due to a dissolution of $CH_3NH_3PbX_3$ in the electrolyte, which resulted in the degradation of the PCE. In 2012, Prof. Park's group used a solid-state hole transport layer (HTL, spiro-MeOTAD) instead of the electrolyte to solve the problem, and they obtained the PCE of 9.7% [10]. Furthermore, Lee et al. [11] reported the PCE of 10.9% by using a mesoporous Al_2O_3 layer and the spiro-MeOTAD based HTL in the same year. These reports gave a big impact on the researchers, since the maximum PCE comparable to that of dye-sensitized solar cells was achieved just in 3 years from the first report. After that, many researchers started to work on the perovskite solar cell, and the cell structure, preparation method, and composition of materials have been widely studied.

At the initial stage of the research, this solar cell was regarded as one of the dye-sensitized solar cells. However, it generated the PCE of 10.9% even with the Al_2O_3 mesoporous layer which does not transport the electrons [11]. This is significantly different characteristics from the dye-sensitized solar cells. Therefore, this solar cell is recently regarded as a new category of the solar cell, and it is called as a "perovskite solar cell". The maximum PCE of the perovskite solar cell already reached to 23.7% [4], which is close to that of the single crystalline Si solar cells, recorded in just 9 years from the first report. This rapid increase of PCE is a feature of perovskite solar cells. Since the research on upsizing of the perovskite solar cells has already started, a productization of this solar cell can be expected [12].

1.2.2 Material for perovskite light absorbing layer ($CH_3NH_3PbI_3$)

Methyl-ammonium lead iodide: $CH_3NH_3PbI_3$

Methyl-ammonium lead iodide ($CH_3NH_3PbI_3$, $MAPbI_3$) has been widely used as a material for the light absorbing layer of the perovskite solar cells. It is an organic/inorganic hybrid perovskite ionic crystal. Perovskite is a mineral name of calcium titanate ($CaTiO_3$), which was named after Russian scientist "Perovsky" who discovered the mineral $CaTiO_3$. Currently, the crystal structure of $CaTiO_3$ represented by ABX_3 is called as a perovskite structure, and there are many functional materials which have the perovskite structure, such as ferroelectric $BaTiO_3$ and $Pb(Zr,Ti)O_3$ [13].

Figure 1.4 shows a crystal structure of a cubic perovskite-type structure. The ideal perovskite-type structure has a cubic unit cell (e.g. $SrTiO_3$), but there are also many compounds with lower symmetry unit cells (ex. tetragonal and orthorhombic). The tolerance factor is a factor which shows stability and distortion of the perovskite structure. The tolerance factor t is given by the **eq. 1.1**, where r_A, r_B, and r_X are the ionic radii of the ions located in A, B and X sites, respectively.

$$\text{tolerance factor } (t) = (r_A + r_X) \,/\, \sqrt{2}\,(r_B + r_X) \qquad \textbf{(eq. 1.1)}$$

The tolerance factor must be within ~0.8-1.1 to form the perovskite structure. When $t = 1$, the crystal structure has a cubic unit cell, and when $t < 1$ or $t > 1$, the crystal structure is distorted into tetragonal, orthorhombic, or rhombohedral unit cell.

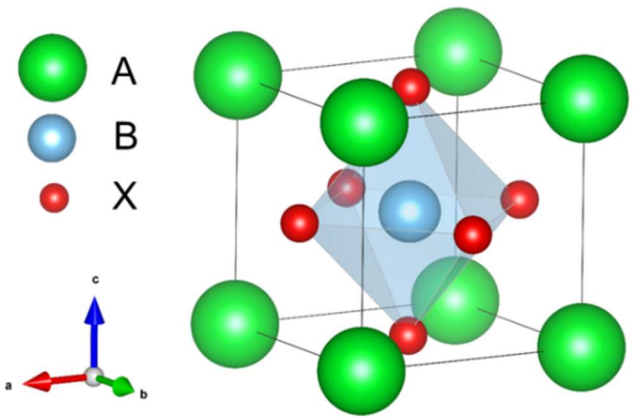

Fig. 1.4 Crystal structure of cubic perovskite structure **(**drown by VESTA ver. 3.4.4 [14]).

$CH_3NH_3PbI_3$ has the perovskite structure, and the A, B, and X sites are occupied by $CH_3NH_3^+$, Pb^{2+}, and I^- ions, respectively. The crystal phase changes by the temperature. In 1987, Politsch et al. [15] reported that $CH_3NH_3PbI_3$ has an orthorhombic phase at $T < 162$ K (P na2$_1$, low temperature phase), tetragonal phase at 162 K $< T <$ 327 K (I 4/mcm, room temperature phase), and cubic phase at 327 K $< T$ (Pm3m, high temperature phase). On the other hand, Stoumpos et al. [16] recently reported that $CH_3NH_3PbI_3$ has tetragonal phase of (P 4mm) and (I 4cm) for the high temperature phase and room temperature phase, and orthorhombic phase (Pnma) for the low temperature phase. **Figure 1.5** shows crystal structures of $CH_3NH_3PbI_3$ for the cubic, tetragonal, and orthorhombic phases. According to the study by Oku et al. [17], the lattice parameters of orthorhombic phase are a = 8.8362 Å, b = 12.5804 Å, c = 8.5551 Å, those for tetragonal phase are a = 8.800 Å, c = 12.685 Å, and that for cubic phase is a = 6.391 Å.

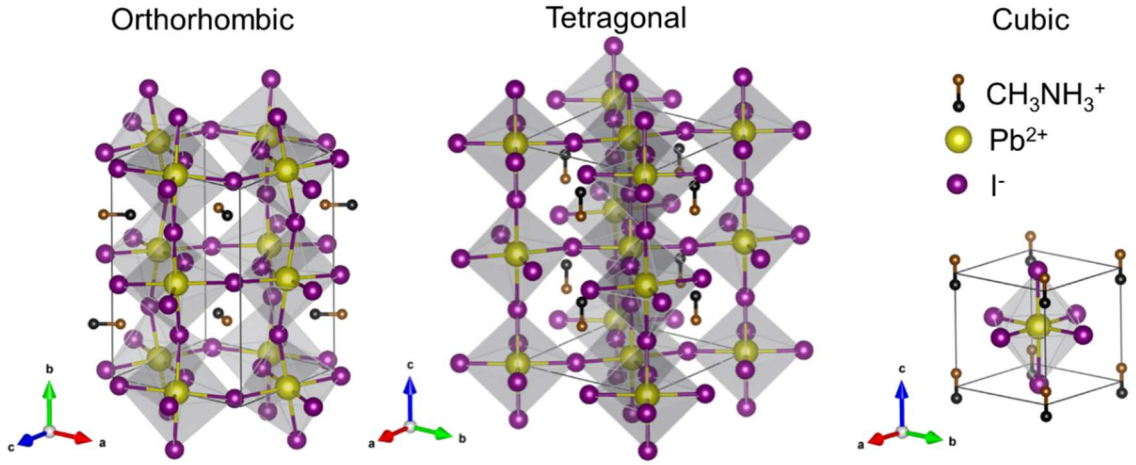

Fig. 1.5 Crystal structures of $CH_3NH_3PbI_3$ for cubic, tetragonal, and orthorhombic phases (drown by VESTA ver. 3.4.4 [14]).

Characteristics of $CH_3NH_3PbI_3$

$CH_3NH_3PbI_3$ has desirable characteristics as a light-absorbing layer of solar cell. Firstly, the preparation process of $CH_3NH_3PbI_3$ layer is very simple. The $CH_3NH_3PbI_3$ layer can be formed just by spin-coating a precursor solution and annealing at a temperature of ~100°C. Since the annealing temperature is relatively low, it is possible to form the $CH_3NH_3PbI_3$ layer on a plastic film substrate and to produce a flexible perovskite solar cell (**Fig. 1.6(a)** [18]). Also, a large-scale vacuum equipment is not necessary unlike the inorganic type solar cells, so the $CH_3NH_3PbI_3$ film can be fabricated with low cost. Secondary, the bandgap value is suitable to absorb the entire visible light in the sun light. The bandgap of $CH_3NH_3PbI_3$ is reported to be ~1.5-1.6 eV [10,19] which can absorb the most of the visible light: $\lambda <$ ~800 nm. Since the sun light has the largest light intensity at the visible light region, $CH_3NH_3PbI_3$ can absorb the sun light and generate electrons efficiently. Thirdly, a light absorption coefficient is high: ~10^5 cm^{-1} (**Fig. 1.6 (b)** [20]), which is equivalent to those of inorganic semiconductors such as Si and CIGS. This high absorption coefficient enables to absorb the most of visible light with a film thickness of several hundred nanometers. Fourthly, the $CH_3NH_3PbI_3$ has a very long carrier diffusion length. The carrier diffusion length of $CH_3NH_3PbI_3$ was reported to be ~100 nm, and it can be further prolonged to ~1 μm by mixing Cl^- into the X site ($CH_3NH_3PbI_{3-x}Cl_x$) [21]. Since the thickness of the perovskite layer is usually several hundred nanometers, the generated carriers can be transported efficiently.

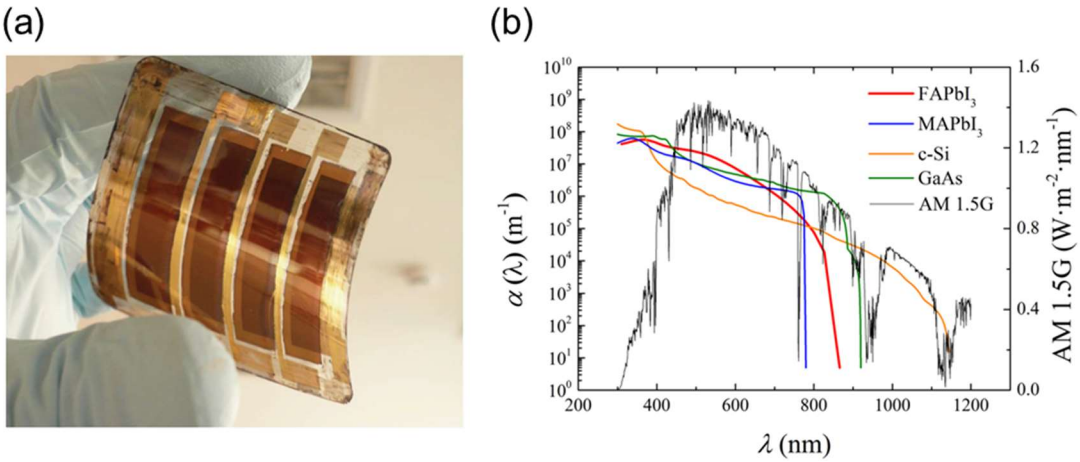

Figs. 1.6 (a) Appearance of flexible perovskite solar cell reported by Giacomo et al. [18], and (b) comparison of absorbance coefficients reported by Xie et al. [20].

1.2.3 Structure, working principle, and fabrication method of perovskite solar cell

Structure of perovskite solar cells

The perovskite solar cell has three layers to generate and transport carriers (electrons and holes), a perovskite light absorbing layer, an electron transport layer (ETL), and a hole transport layer (HTL). The perovskite light absorbing layer is sandwiched by the ETL and HTL. The structures can be categorized into three types by the usage of the ETL and HTL. The three structure types are shown in **Fig. 1.7**.

(1) Mesoporous structure

This structure is composed of a TCO glass, ETL, perovskite layer, HTL, and metal electrodes. Oxide semiconductors, such as TiO_2, SnO_2, and ZnO, are usually used for the ETL. The spiro-MeOTAD ([2,2',7,7'-Tetrakis(N,N-di-p-methoxyphenylamino)-9,9'-spirobifluorene] is widely used for the HTL, and gold (Au) or silver (Ag) are used for the metal electrodes. In the mesoporous structure, the ETL is composed of compact and mesoporous layers. A part of perovskite film is infiltrated into the mesoporous layer, and the other part forms a perovskite capping layer. In this thesis, this mesoporous structure was used.

As described in section 1.2.1, the perovskite solar cell was developed based on the dye-sensitized solar cell. Since the dye-sensitized solar cells used a TiO_2 mesoporous layer for the electron transport, the mesoporous structure was used at the beginning of research on perovskite solar cells. At that time, it was believed that the generated electrons must be injected into the mesoporous TiO_2 layer in the same way as the dye-sensitized solar cells. However, in 2012, a PCE > 10% was reported with the Al_2O_3 mesoporous layer [11]. This result indicated that $CH_3NH_3PbI_3$ can separate and transport the carriers (electrons and holes) by itself, since Al_2O_3 cannot transport the electrons due to its too high conduction band level. The perovskite solar cells do not always need the mesoporous layer for the electron transport. Because of these reasons, the planar structure was developed.

(2)&(3) Planar and inverted planar structure

The planar structure has the only compact layer for the ETL [22,23]. Since this structure is simpler than

the mesoporous structure, it is beneficial to reduce the production cost and to investigate the mechanisms of this solar cell. The thickness of the perovskite layer is usually less than ~500 nm due to the high optical absorption coefficient of $CH_3NH_3PbI_3$, and $CH_3NH_3PbI_3$ has the long carrier diffusion length of ~100 nm-1 μm. Therefore, the generated carriers in the perovskite layer can reach to the compact layer (ETL) by itself without the mesoporous layer, which realizes the planar structure. Recently, the structure without HTL was also reported [24,25]. The other type is an inverted planar structure. This structure has the ETL and HTL in opposite positions to those of the normal planar type structure [26,27]. [6,6]-phenyl C61-butyric acid methyl ester (PCBM) and fullerene (C60) are widely used for the ETL, and poly(3,4-ethylenedioxythiophene) poly(styrene-sulfonate) (PEDOT: PSS) and NiO are used for the HTL.

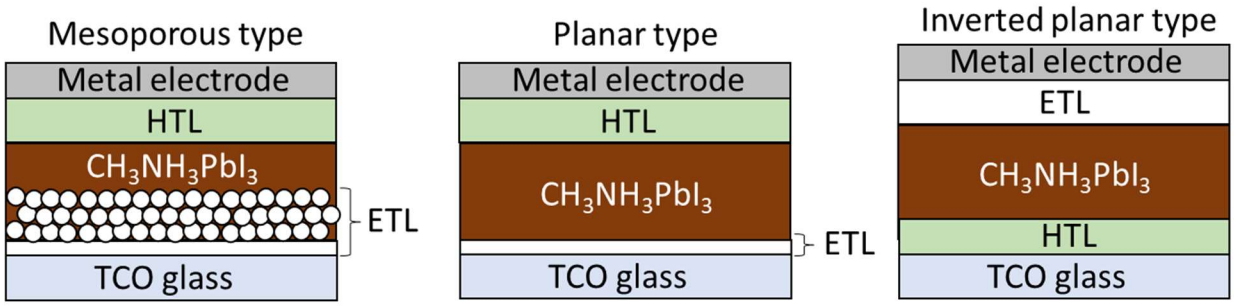

Fig. 1.7 Three types structure of perovskite solar cells.

Working principle of the perovskite solar cells

Figure 1.8 shows the working principle of the perovskite solar cells. The model is based on the mesoporous-type perovskite solar cells. Under the sun light irradiation from the TCO glass side, the perovskite layer is exited and emits the electrons and holes. The electrons and holes are transported to outside through the conduction band (CB) of ETL (TiO_2) and the highest occupied molecular orbital (HOMO) level of the HTL (spiro-MeOTAD), respectively. Therefore, the position of the conduction band of ETL and the HOMO level of HTL are important for the electron and hole transports. The CB level of ETL and HOMO level of HTL should be lower and higher than the CB and valence band (VB) levels of $CH_3NH_3PbI_3$, respectively.

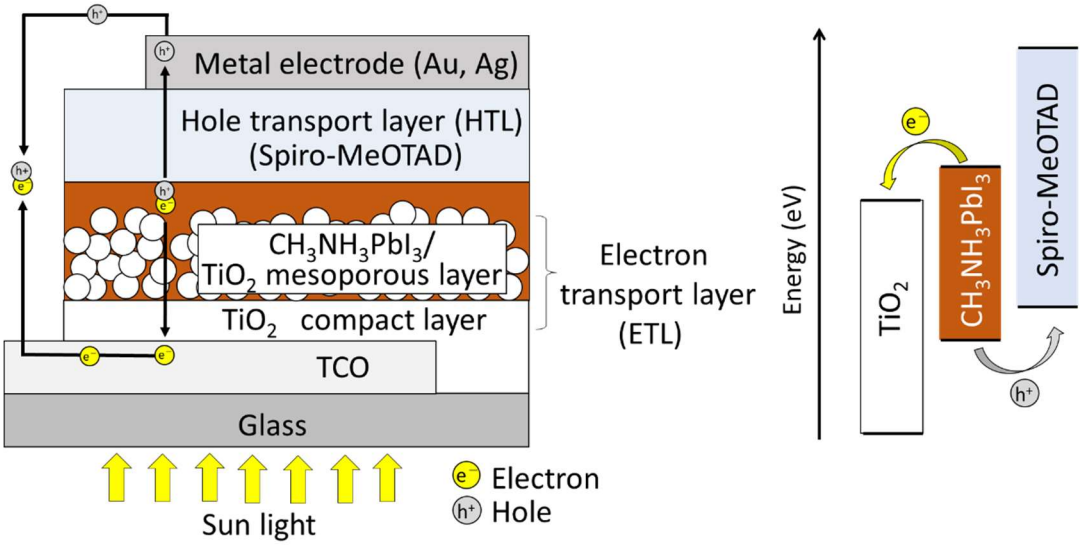

Fig. 1.8 Schematic illustration of a structure of perovskite solar cell and its energy diagram.

Fabrication method of perovskite layer

The perovskite light absorbing layer ($CH_3NH_3PbI_3$) is generally fabricated by reacting PbI_2 and CH_3NH_3I (MAI). In general, the preparation methods are categorized into two methods: 1-step method and 2-step method (**Fig. 1.9**). In the 1-step method, the $CH_3NH_3PbI_3$ layer is prepared by one-step spin-coating of a precursor solution composed of PbI_2 and CH_3NH_3I. Since this method is simpler than the 2-step method, it is suitable for the low-cost production. However, if the spin-coating conditions or the compositions of precursor solution are not optimized, it is difficult to obtain a well-covered perovskite layer on the ETL [22,28]. To solve this problem, an anti-solvent dripping method was developed [29,30]. By spin-coating a poor solvent, such as toluene and chlorobenzene, just after the spin-coating of perovskite precursor solution, the nucleation of $CH_3NH_3PbI_3$ is significantly accelerated, and a smooth and compact perovskite layer can be obtained. However, this method is very sensitive to the process conditions, such as the amount of poor solvent and timing of the spin-coating, so the handling is difficult.

On the other hand, in the 2-step method, the PbI_2 film is firstly prepared, and CH_3NH_3I post-treatment using solution or vapor is secondary carried out to synthesize the $CH_3NH_3PbI_3$. The 2-step method requires another step compared with the 1-step method, but it is relatively easy to obtain well-covered perovskite layer. However, the 2-step method still has a problem as described below. Thus, in this thesis, the 2-step method was mainly focused.

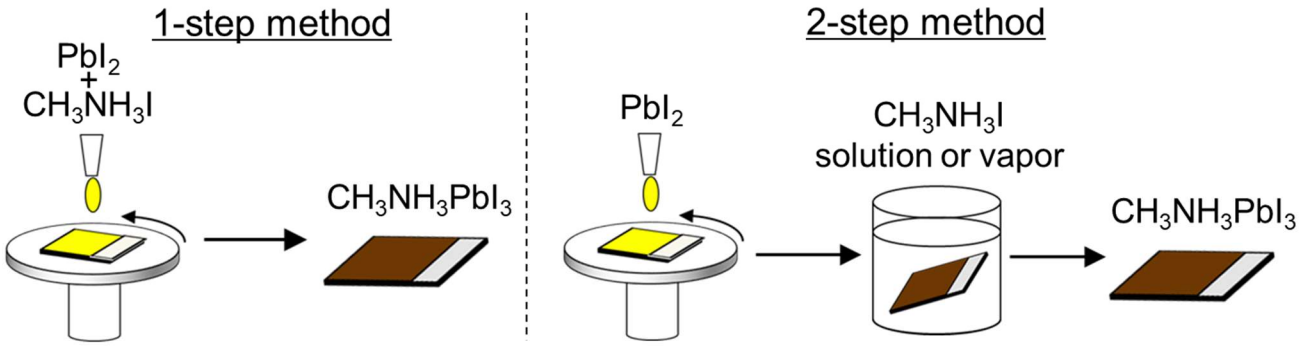

Fig. 1.9 Schematic illustration of 1-step and 2-step methods for the preparation of perovskite layer.

Problem of the 2-step method

In the 2-step method, the PbI_2 layer is firstly prepared and then it reacts with CH_3NH_3I to obtain $CH_3NH_3Pb1_3$. Since $CH_3NH_3PbI_3$ is formed from the surface of PbI_2 layer, the diffusion of CH_3NH_3I into the deep part of the PbI_2 layer is gradually hindered, and this causes a residual unreacted PbI_2 at the bottom of the perovskite layer (**Fig. 1.10**) [31,32].

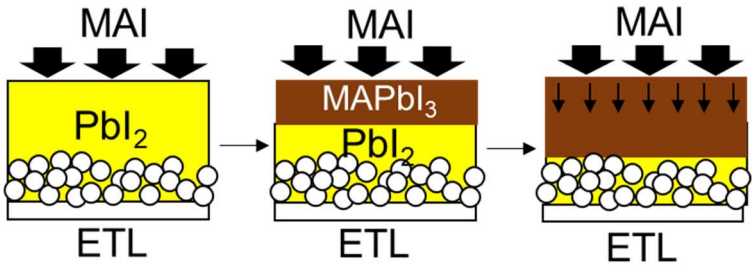

Fig. 1.10 Schematic illustration of a forming process of unreacted PbI_2 in a typical 2-step method.

Some improved processes were proposed to solve this problem, e.g., solvent selection and morphological control of PbI_2 layer. At the begging of the research, N,N-dimethylformamide (DMF) was usually used as a solvent of PbI_2 solution. When DMF is used as the solvent, the formed PbI_2 layer is well-crystalized during the annealing, and it makes difficult for CH_3NH_3I to diffuse into the deep part of PbI_2 layer. To suppress the crystallization of PbI_2 layer, dimethyl sulfoxide (DMSO) was used as the solvent. Since DMSO forms a complex with PbI_2, the crystallization of PbI_2 layer was suppressed and the reaction with CH_3NH_3I was prompted. As a result, the unreacted PbI_2 was suppressed and photovoltaic performance was improved [33,34]. The second approach was to form a mesoporous PbI_2 layer. The conventional PbI_2 layer using DMF as the solvent was a relatively dense film. Cao et al. [35] prepared a mesoporous PbI_2 layer by using a molecular level pore-forming agent. The mesoporous structure facilitated the penetration of CH_3NH_3I into the deep part of the PbI_2 layer, and the $CH_3NH_3PbI_3$ layer without unreacted PbI_2 was achieved with the enhanced photovoltaic performance.

On the other hand, it was also reported that the unreacted PbI_2 was beneficial to achieve the better photovoltaic performance. Since the conduction band of PbI_2 is located at higher position than that of $CH_3NH_3PbI_3$, the unreacted PbI_2 is effective to suppress the back-flow of the electrons and to suppress a carrier recombination [31]. Therefore, it is still unclear that the complete elimination of unreacted PbI_2 has positive or negative effect on the photovoltaic performance. Still, the author of this thesis thinks that the reduction of unreacted PbI_2 amount is a key to obtain a high PCE.

1.2.4 Compositional engineering and bandgap gradient structure for perovskite layer

Compositional engineering of perovskite layer

Since $CH_3NH_3PbI_3$ has a perovskite structure (ABX_3), when Pb^{2+} in the B site is fixed, it is possible to change the monovalent cation in the A site and the halogen ion in the X site. The replacement of the ions changes the lattice constant and bandgap of the material, which is effective to improve the photovoltaic performance and stability. Formaminidium ion ($CH(NH_2)_2^+$, FA^+) and Cs^+ ions have been widely used for the substitution of A site. Cl^- and Br^- are used for the substitution of halogen ion in the X site. **Table 1.1** summarizes the tolerance factors and bandgaps of the perovskite materials when the ion in the A site ($CH_3NH_3^+$) is replaced with Cs^+ or FA^+ ion and the ion in X site (I^-) is replaced with Cl^- or Br^- ion. The ionic radius of Pb^{2+} is 1.19 Å [36].

The tolerance factor approaches to 1 and the band gap becomes smaller by using larger cations for the A site. For example, $FAPbI_3$ has a tolerance factor of 0.987 and a bandgap of 1.47 eV [37], which is closer to the optimal bandgap value of 1.4 eV for the solar cell application. As for the anion substitution, the tolerance factor approaches to 1 by using smaller anion for the X site, and the smaller anions give the larger bandgaps. In this way, the bandgap can be tuned by the compositional engineering.

Table 1.1 Ionic radius, tolerance factor and bandgap of perovskite materials when Pb^{2+} in the B site is fixed and ions for the A site and X site are varied.

A site cation	Cs^+	MA^+ ($CH_3NH_3^+$)	FA^+ ($CH(NH_2)_2^+$)
Ionic radius (Å)	1.88[36]	2.17[38]	2.53[38]
Tolerance factor ($APbI_3$)	0.851 ($CsPbI_3$)	0.912 ($MAPbI_3$)	0.987 ($FAPbI_3$)
Bandgap (eV) ($APbI_3$)	1.73 ($CsPbI_3$) [39]	1.5-1.6 ($MAPbI_3$)[10.19]	1.47 ($FAPbI_3$)[37]

X site anion	Cl^-	Br^-	I^-
Ionic radius (Å)	1.81[36]	1.96[36]	2.20[36]
Tolerance factor ($MAPbX_3$)	0.938 ($MAPbCl_3$)	0.927 ($MAPbBr_3$)	0.912 ($MAPbCl_3$)
Bandgap (eV) ($MAPbX_3$)	3.11 ($MAPbCl_3$)[40]	2.29 ($MAPbBr_3$)[41]	1.5-1.6 ($MAPbI_3$)

Cesium lead iodide ($CsPbI_3$)

$CsPbI_3$ has better thermal and air stability than $CH_3NH_3PbI_3$. The α-phase $CsPbI_3$ has the perovskite structure and bandgap of 1.73 eV which is also suitable for a top cell of the tandem solar cell with Si. However, δ-$CsPbI_3$ (non-perovskite structure, yellow color, bandgap: 2.82 eV [39], not suitable for solar cell application) is also synthesized, since it is more stable than α-phase $CsPbI_3$ at room temperature ($T < 315°C$), which decreases the PCE [42].

Formamidinium lead iodide ($FAPbI_3$)

$FAPbI_3$ has better thermal stability than $CH_3NH_3PbI_3$. The α-phase $FAPbI_3$ has a bandgap of 1.47 eV which is closer to the optimal bandgap value of 1.4 eV as the solar cell application. However, δ-$FAPbI_3$ (non-perovskite structure, yellow, bandgap: 2.43 eV [43]) is also synthesized, since it is more stable than α-phase $FAPbI_3$ at room temperature, which decreases the PCE.

Both δ-$CsPbI_3$ and δ-$FAPbI_3$ are stable at room temperature, and hence, the stabilization of α-phase at room temperature is a challenging research topic. The incorporation of other cation and anion is a way to achieve the stable α-phase. For example, the tolerance factor approached to 1 by incorporating the smaller Br^- ion to $CsPbI_3$, and the formation of δ-$CsPbI_3$ can be suppressed. It is also reported that the formation of δ-$FAPbI_3$ is suppressed by incorporating MA^+ and Br^- ions due to the change of lattice constant and relaxation of the lattice strain [44,45].

Methyl-ammonium lead chloride ($CH_3NH_3PbCl_3$)

$CH_3NH_3PbCl_3$ has a too large bandgap for the solar cell application, so pure $CH_3NH_3PbCl_3$ is usually not used for the light absorbing layer.

Methyl-ammonium lead bromine ($CH_3NH_3PbBr_3$)

$CH_3NH_3PbBr_3$ also has a too large bandgap for the solar cell application, so pure $CH_3NH_3PbBr_3$ is usually not used for the light absorbing layer. However, the incorporation of Br^- into the I^- based perovskite layer is widely studied. By incorporating the Br^-, the bandgap becomes larger, which results in an increase of open circuit voltage (V_{OC}) and decrease of short circuit current density (J_{SC}). Furthermore, since the structure changes from the tetragonal to the cubic structure and tolerance factor also approaches to 1 by the Br^- incorporation, the air stability can be improved [41].

As described above, when each material is used for the perovskite light absorbing layer as a pure phase, there are some problems. However, by combining the materials, the advantage of each material can be achieved without crucial negative effects. Therefore, the mixed composition of these ions has recently studied to achieve the both high PCE and stability. For example, (MAFA)Pb(IBr) or (CsMAFA)Pb(IBr) system-based perovskite solar cells achieved a PCE of ~20% with higher stability than those pure composition-based perovskite solar cells [46,47].

Bandgap gradient structure

The generated electrons and holes in the perovskite light absorbing layer are transported through conduction band and valence band (HOMO level for HTL) of each layer as shown in **Fig. 1.8**, and hence, the band alignment is important factor to achieve high photovoltaic performance. The importance of band alignment is applied not only for the perovskite solar cells but also for all kinds of solar cells, since they have a similar mechanism of the carrier transport.

As for the light absorbing layer, a formation of bandgap gradient is a promising way to enhance the photovoltaic performance. For example, the formation of bandgap gradient structure at the front and back side of CIGS (Cu, In, Ga, Se) light absorbing layer has been widely studied by changing the Ga ratio or by substituting Se with S [48,49]. Since the bandgap gradient is a driving forth of the carrier transport, the carrier transport efficiency is improved and the photovoltaic performance is also enhanced.

In the case of perovskite solar cells, some researchers reported the formation of bandgap gradient at the top surface side of the perovskite layer, which resulted in the enhanced photovoltaic performance. Cho et al. [50] and Kim et al. [51] formed the I-Br anionic gradient structures by making Br rich area at the top surface side (**Fig. 1.11**). Since $CH_3NH_3PbBr_3$ has the larger bandgap and the valence band position is located at the lower position than those of $CH_3NH_3PbI_3$, the bandgap gradient can be obtained. It effectively suppressed the carrier recombination by improving a hole extraction at the top surface side, which resulted in the improved photovoltaic performance. Thus, the formation of bandgap gradient is a promising way to enhance the maximum conversion efficiency of the perovskite solar cells.

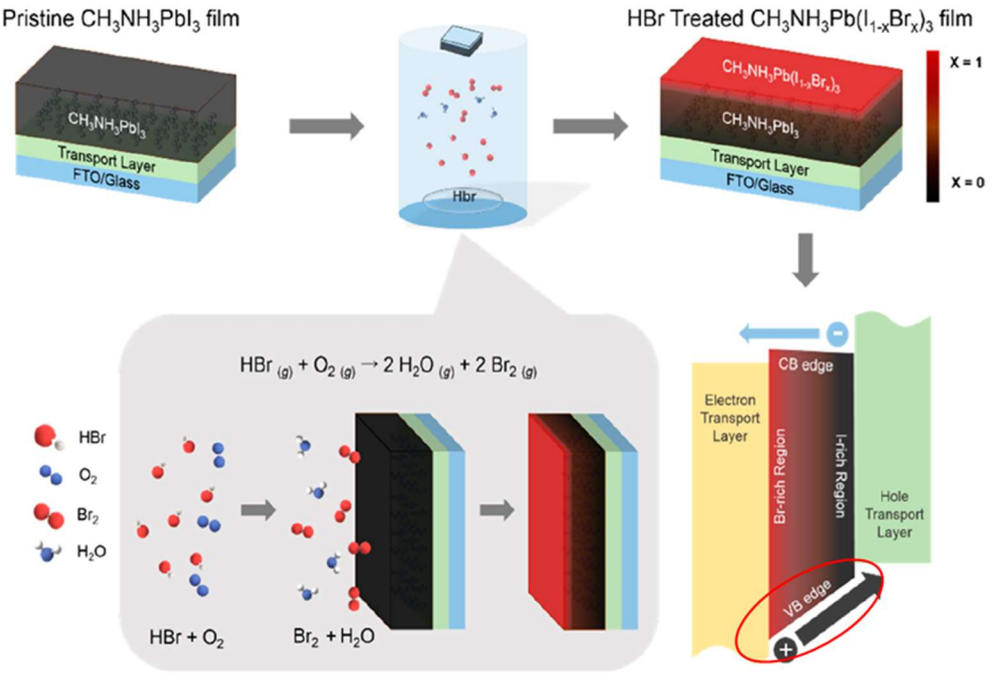

Fig. 1.11 Schematic illustration of a formation of bandgap gradient by making I-Br concentration gradient reported by Kim et al. [51].

For further advancement on the bandgap gradient structure of perovskite solar cells, it is necessary to form the bandgap gradient at the bottom side of perovskite layer. The formation of bandgap gradient at the bottom side is relatively easy when the perovskite layer is formed layer by layer using dry processes, such as chemical vapor deposition (CVD) and sputtering, but the dry process will increase the production cost. On the other hand, the formation of bandgap gradient at the bottom side by wet processes, such as spin-coating and dipping method, is difficult, since the compositional difference is produced by post-treatments and it can form the bandgap gradient only at the top surface side. Therefore, the new preparation method of perovskite layer which can control the band structure of both top and bottom sides is necessary for further enhancement of the photovoltaic performance.

1.3 Objective of this thesis

From these backgrounds, in this thesis, the author attempted to form the bandgap gradients at the both top and bottom sides of the perovskite layer (multiple bandgap structure) by making compositional differences. To achieve the structure, the author proposes a new 3-step method using additional MAI or FAI spin-coating. In this method, the unreacted PbI_2 was used as a material to produce the compositional difference at the bottom side. The additional FAI spin-coating will convert $MAPbI_3$ into $FA_xMA_{1-x}PbI_3$ and it will also convert the unreacted PbI_2 into FA rich layer ($FAPbI_3$ or $FA_yMA_{1-y}PbI_3$ ($y > x$)). Since $FAPbI_3$ has the smaller bandgap than $MAPbI_3$, the FA concentration difference will make the bandgap gradient at the bottom side.

The objectives of this thesis are to develop a new 3-step method which enables to form the bandgap gradients at the both top and bottom sides of the perovskite layer and enhance the photovoltaic performance of perovskite solar cells. This thesis consists of following chapters.

In Chapter 2, the conversion of unreacted PbI_2 in the 2-step prepared perovskite layer was carried out by the 3-step method using MAI additional spin-coating (**Fig. 1.12**). Also, a compositional change was also attempted by the additional spin-coating of a MABr solution. The conversion of the unreacted PbI_2 and compositional change were analyzed by X-ray diffraction (XRD), and the effects of additional spin-coating on the optical property and film morphology were evaluated by ultraviolet-visible absorption spectroscopy (UV-Vis) and scanning electron microscopy (SEM), respectively. The solar cell performances were evaluated by measuring current density-voltage (*J-V)* characteristics of the prepared cells.

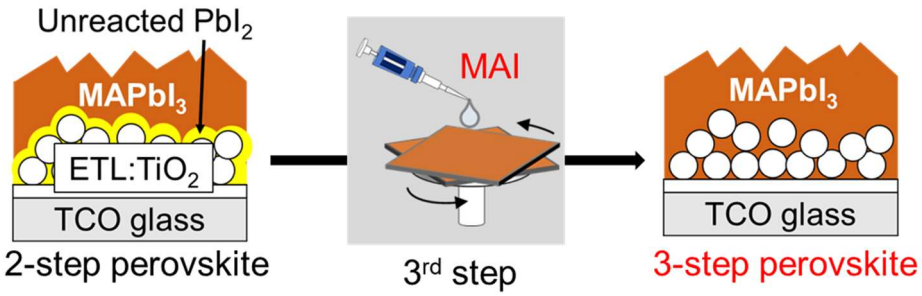

Fig. 1.12 Schematic illustration of the 3-step method using additional MAI spin-coating for conversion of unreacted PbI_2 into perovskite.

In Chapter 3, the multiple bandgap structure was formed by making the bandgap gradient at the bottom side (near the ETL). The compositional difference was produced by the 3-step method using additional FAI spin-coating on the 2-step prepared perovskite layer (**Fig. 1.13**). Since the expected FA rich area was too thin to be detected by XRD or UV-Vis, steady-state photoluminescence (PL) measurement was carried out from the top and back sides of the perovskite layer. The effect of additional FAI spin-coating on the photovoltaic performance was also investigated.

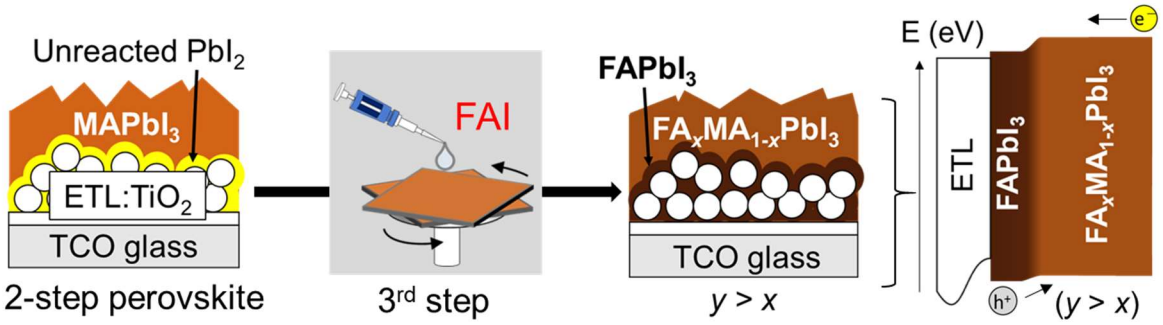

Fig. 1.13 Schematic illustration of the 3-step method using additional FAI spin-coating for formation of multiple bandgap structure at the bottom side of perovskite layer.

In Chapter 4, the small amount of NaI was added into the 3rd step FAI spin-coating solution to form the bandgap gradients at the both top and bottom sides of the perovskite layer simultaneously (**Fig. 1.14**). The small amount of Na^+ in the 3rd step solution will be doped only at the top side of the perovskite layer, and it will enlarge the bandgap at the top surface with keeping the bandgap gradient at the bottom side. The effects of NaI addition on the bandgap, film morphology, and photovoltaic performance were also investigated.

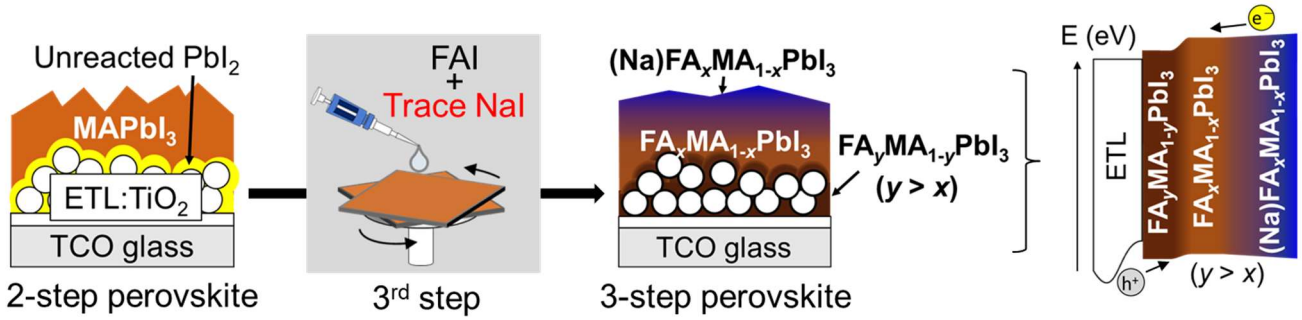

Fig. 1.14 Schematic illustration of the 3-step method with NaI addition for simultaneous formation of bandgap gradients at the top and bottom sides of perovskite layer.

In Chapter 5, the important results and discussion of this thesis were summarized.

References

[1] Ministry of Economy, Trade and Industry, Agency for Natural Resources and Energy, FY2017 Annual Report on Energy (Energy White Paper 2018) PDF version, Part 2 Energy Trends, Chapter 1 Domestic Energy Trends (in Jpn.).

[2] Ministry of Economy, Trade and Industry, Agency for Natural Resources and Energy, FY2017 Annual Report on Energy (Energy White Paper 2018) PDF version, Part 2 Energy Trends, Chapter 2 International Energy Trends (in Jpn.).

[3] K. Sato, Ichiban yasashi rikokei Basic of solar cell, Softbank Creative, (in Jpn., 2011/4/23).

[4] Research Cell Record Efficiency Chart by The National Renewable Energy Laboratory, https://www.nrel.gov/pv/assets/pdfs/pv-efficiencies-07-17-2018.pdf, (2018/12/24).

[5] M. Yamaguchi, M. A. Green, Y. Ohshita, N. Kojima, Fundamentals and applications of solar cells from silicon to organic and quantum nano, Maruzen Publishing Co.,Ltd., (2010/07/30, in Jpn.).

[6] H. Arakawa, Dye-sensitized solar cells, CMC Publishing Co.,Ltd., (2001/5/25, in Jpn.).

[7] B. O'Regan, M. Grätzel, A low-cost, high-efficiency solar cell based on dye-sensitized colloidal TiO_2 films, *Nature*, **353**, 737-740 (1991).

[8] M. K. Nazeeruddin, A. Kay, I. Rodicio, R. Humphry-Baker, E. Mueller, P. Liska, N. Vlachopoulos, M. Graetzel, Conversion of light to electricity by cis-X_2bis(2,2'-bipyridyl-4,4'-dicarboxylate)ruthenium(II) charge-transfer sensitizers (X = Cl-, Br-, I-, CN-, and SCN-) on nanocrystalline TiO_2 electrodes, *J. Am. Chem. Soc*., **115**, 6382-6390 (1993).

[9] A. Kojima, K. Teshima, Y. Shirai, T. Miyasaka, Organometal halide perovskites as visible-light sensitizers for photovoltaic cells, *J. Am.Chem. Soc*., **131**, 6050-6051 (2009).

[10] H. S. Kim, C. R. Lee, J. H. Im, K.B. Lee, T. Moehl, A. Marchioro, S. J. Moon, R. Humphry-Baker, J. H. Yum, J. E. Moser, M. Grätzel, N.G. Park, Lead iodide perovskite sensitized all-solid-state submicron thin film mesoscopic solar cell with efficiency exceeding 9%, *Sci Rep*. **2**, 591 (2012).

[11] M. M. Lee, J. Teuscher, T. Miyasaka, T. N. Murakami, H. J. Snaith, Efficient hybrid solar cells based on meso-superstructured organometal halide perovskites, *Science*, **42**, 643-647, (2012).

[12] Y. Chen, L. Zhang, Y. Zhang, H. Gaoa, H. Yan, Large-area perovskite solar cells – a review of recent progress and issues, *RSC Adv*., **8**, 10489–10508.

[13] T. R. Shrout, S. J. Zhang, Lead-free piezoelectric ceramics: Alternatives for PZT?, J. *Electroceram*. **19**, 113–126 (2007).

[14] K. Momma, F. Izumi, "VESTA 3 for three-dimensional visualization of crystal, volumetric and morphology data, *J. Appl. Crystallogr*., **44**, 1272-1276 (2011).

[15] A. Poglitsch, D. Weber, Dynamic disorder in methylammoniumtrihalogenoplumbates (II) observed by millimeter-wave spectroscopy, *J. Chem. Phys*., **87**, 6373-6378 (1987).

[16] C. C. Stoumpos, C. D. Malliakas, and M. G. Kanatzidis, "Semiconducting tin and lead iodide perovskites with organic cations: Phase transitions, high mobilities, and near-infrared photoluminescent properties, *Inorg. Chem.*, **52**, 9019- (2013).

[17] T. Oku, Crystal structures of $CH_3NH_3PbI_3$ and related perovskite compounds used for solar cells, *Solar Cells - New Approaches and Reviews ed L A Kosyachenko (InTech)*, **77**, chapter 3 (2015).

[18] F. D. Giacomo, V. Zardetto, A. D'Epifanio, S. Pescetelli, F. Matteocci, S. Razza, A. D. Carlo, S. Licoccia, W. M. M. Kessels, M. Creatore, T. M. Brown, Flexible perovskite photovoltaic modules and solar cells based on atomic layer deposited compact layers and UV-irradiated TiO_2 scaffolds on plastic substrates, *Adv. Energy Mater*. 1401808 (2015).

[19] H. S. Jung, N. G. Park, Perovskite solar cells: from materials to devices, *small*, **11**, 1 (2015).

[20] Z. Xie, S. Sun, Y. Yan, L. Zhang, R. Hou, F. Tian, G. G. Qin, Refractive index and extinction coefficient of $NH_2CH = NH_2PbI_3$ perovskite photovoltaic material, *J. Phys.: Condens. Matter*., **29**, 245702 (2017).

[21] S. D. Stranks, G. E. Eperon, G. Grancini, C. Menelaou, M. J. P. Alcocer, T. Leijtens, L. M. Herz, A. Petrozza, H. J. Snaith, Electron-hole diffusion lengths exceeding 1 micrometer in an organometal trihalide

perovskite absorber, *Science*, **342**, 341–344 (2013).

[22] G. E. Eperon, V. M. Burlakov, P. Docampo, A. Goriely, H. J. Snaith, Morphological control for high performance, solution-processed planar heterojunction perovskite solar cells, *Adv. Funct. Mater.*, **24**, 151–157 (2014).

[23] M. Liu, M. B. Johnston, H. J. Snaith, Efficient planar heterojunction perovskite solar cells by vapour deposition, *Nature*, **501**, 395–398 (2013).

[24] A. Mei, X. Li, L. Liu, Z. Ku, T. Liu, Y. Rong, M. Xu, M. Hu, J. Chen, Y. Yang, M. Grätzel, H. Han, A hole-conductor–free, fully printable mesoscopic perovskite solar cell with high stability, *Science* **345**, 295-298 (2014).

[25] S. Aharon, S. Gamliel, B. E. Cohen, L. Etgar, Depletion region effect of highly efficient hole conductor free $CH_3NH_3PbI_3$ perovskite solar cells. *Phys. Chem. Chem. Phys*. **16**, 10512-10518 (2014).

[26] J. Y. Jeng, Y. F. Chiang, M. H. Lee, S. R. Peng, T. F. Guo, P. Chen, T. C. Wen, $CH_3NH_3PbI_3$ perovskite/fullerene planar-heterojunction hybrid solar cells, *Adv. Mater*., **25**, 3727–3732 (2013).

[27] J. Y. Jeng, K. C. Chen, T. Y. Chiang, P. Y. Lin, T. D. Tsai, Y. C. Chang, T. F. Guo, P. Chen, T. C. Wen, Y. J. Hsu, Nickel oxide electrode interlayer in $CH_3NH_3PbI_3$ perovskite/PCBM planar-heterojunction hybrid solar cells, *Adv. Mater.*, **26**, 4107–4113 (2014).

[28] T. Salim, S. Sun, Y. Abe, A. Krishna, A. C. Grimsdale, Y. M. Lam, Perovskite-based solar cells: impact of morphology and device architecture on device performance, *J. Mater. Chem. A*, **3**, 8943-8969 (2015).

[29] N. J. Jeon, J. H. Noh, Y. C. Kim, W. S. Yang, S. Ryu, S. I. Seok, Solvent engineering for high-performance inorganic–organic hybrid perovskite solar cells, *Nat. Mater*., **13**, 897–903 (2014).

[30] M. Xiao, F. Huang, W. Huang, Y. Dkhissi, Y. Zhu, J. Etheridge, A. Gray-Weale, U. Bach, Y.-B. Cheng, L. Spiccia, A fast deposition-crystallization procedure for highly efficient lead iodide perovskite thin-film solar cells, *Angew. Chem*.,**126**, 10056–10061 (2014).

[31] D. H. Cao, C. C. Stoumpos, C. D. Malliakas, M. J. Katz, O. K. Farha, J. T. Hupp, M. G. Kanatzidis, Remnant PbI_2, an unforeseen necessity in high-efficiency hybrid perovskite-based solar cells?, *APL Mater.*, **2**, 091101 (2014).

[32] T. J. Jacobsson, J. P. Correa-Baena, E. H. Anaraki, B. Philippe, S. D. Stranks, M. E. F. Bouduban, W. Tress, K. Schenk, J. Teuscher, J. E. Moser, H. Rensmo, A. Hagfeldt, Unreacted PbI_2 as a double-edged sword for enhancing the performance of perovskite solar cells, *J. Am. Chem. Soc*. **138**, 10331−10343 (2016).

[33] W. Li, J. Fan, J. Li, Y. Mai, L. Wang, Controllable grain morphology of perovskite absorber film by n molecular self-assembly toward efficient solar cell exceeding 17%, *J. Am. Chem. Soc*., **137**, 10399−10405 (2015).

[34] Y. Wu, A. Islam, X. Yang, C. Qin, J. Liu, K. Zhang, W. Penga, L. Han, Retarding the crystallization of PbI_2 for highly reproducible planar-structured perovskite solar cells via sequential deposition. *Energy Environ. Sci*., **7**, 2934–2938 (2014).

[35] J. Cao, F. Wang, H. Yu, Y. Zhou, H. Lu, N. Zhao, C. P. Wong, Porous PbI_2 films for the fabrication of efficient, stable perovskite solar cells via sequential deposition, *J. Mater. Chem. A*, **4**, 10223–10230 (2016).

[36] R. D. Shannon, Revised effective ionic radii and systematic studies of interatomic distances in halides and chalcogenides. *Acta. Cryst*., **A 32**, 751–767 (1976).

[37] T. M. Koh, K. Fu, Y. Fang, S. Chen, T. C. Sum, N. Mathews, S. G. Mhaisalkar, P. P. Boix, T. Baikie, Formamidinium-containing metal-halide: an alternative material for near-IR absorption perovskite solar cells, *J. Phys. Chem. C*, **118**, 16458−16462 (2014).

[38] M. Saliba, T. Matsui, K. Domanski, J. Y. Seo, A. Ummadisingu, S. M. Zakeeruddin, J. P. Correa-Baena, W. R. Tress, A. Abate, A. Hagfeldt, M. Grätzel, Incorporation of rubidium cations into perovskite solar cells improves photovoltaic performance. *Science,* **354**, 206−209 (2016).

[39] W. Ahmad, J. Khan, G. Niu, J. Tang, Inorganic $CsPbI_3$ perovskite-based solar cells: a choice for a tandem device, *Sol. RRL*, **00**, 1700048 (2017)

[40] N. Kitazawa, Y. Watanabe, Y. Nakamura, Optical properties of $CH_3NH_3PbX_3$ (X = halogen) and their

mixed-halide crystals, *J. Mater. Sci.,* **37**, 3585−3587 (2002).

[41] J. H. Noh, S. H. Im, J. H. Heo, T. N. Mandal, S. I. Seok, Chemical management for colorful, efficient, and stable inorganic–organic hybrid nanostructured solar cells, *Nano Lett*., **13**, 1764–1769 (2013).

[42] Q. Wang, X. Zheng, Y. Deng, J. Zhao, Z. Chen, J. Huang, Stabilizing the a-phase of $CsPbI_3$ perovskite by sulfobetaine zwitterions in one-step spin-coating films, *Joule*, **1**, 371–382, (2017).

[43] D. Yao, C. Zhang, N. D. Pham, Y. Zhang, V, T, Tiong, A. Du, Q. Shen, G. J. Wilson, H. Wang, Hindered formation of photoinactive δ-$FAPbI_3$ phase and hysteresis-free mixed-cation planar heterojunction perovskite solar cells with enhanced efficiency via potassium incorporation, *J. Phys. Chem. Lett*., **9**, 2113−2120 (2018).

[44] L. Q. Xie, L. Chen, Z. A. Nan, H. X. Lin, T. Wang, D. P. Zhan, J. W. Yan, B. W. Mao, Z. Q. Tian, Understanding the cubic phase stabilization and crystallization kinetics in mixed cations and halides perovskite single crystals, *J. Am. Chem. Soc*., **139**, 3320−3323 (2017).

[45] X. Zheng, C. Wu, S. K. Jha, Z. Li, K. Zhu, S. Priya, Improved phase stability of formamidinium lead triiodide perovskite by strain relaxation, *ACS Energy Lett*. **1**, 1014−1020 (2016).

[46] N. J. Jeon, J. H. Noh, W. S. Yang, Y. C. Kim, S. Ryu, J. Seo, S. I. Seok, Compositional engineering of perovskite materials for high-performance solar cells, *Nature*, **517**, 476-479 (2015).

[47] M. Saliba, T. Matsui, J. Y. Seo, K. Domanski, J. P. Correa-Baena, M. K. Nazeeruddin, S. M. Zakeeruddin, W. Tress, A. Abate, A. Hagfeldt, M. Grätzel, Cesium-containing triple cation perovskite solar cells: Improved stability, reproducibility and high efficiency, *Energy Environ. Sci*., **9**, 1989–1997 (2016).

[48] Y. C. Wang, H. P. D. Shieh, Double-graded bandgap in $Cu(In,Ga)Se_2$ thin film solar cells by low toxicity selenization process, *Appl. Phys. Lett*., **105,** 073901 (2014).

[49] T. Kato, $Cu(In,Ga)(Se,S)_2$ solar cell research in Solar Frontier: Progress and current status, *Jpn. J. Appl. Phys*., **56**, 04CA02 (2017).

[50] K. T. Cho, S. Paek, G. Grancini, C. Roldán-Carmona, P. Gao, Y. Lee, M. K. Nazeeruddin, Highly efficient perovskite solar cells with a compositionally engineered perovskite/hole transporting material interface, *Energy Environ. Sci*. **10**, 621–627 (2017).

[51] M. C. Kim, B. J. Kim, D.Y. Son, N. G. Park, H. S. Jung, M. Choi, Observation of enhanced hole extraction in Br concentration gradient perovskite materials, *Nano Lett*. **16**, 5756-5763 (2016).

Chapter 2

Conversion of unreacted PbI_2 into perovskite by an additional MA(I/Br) spin-coating

Chapter 2: Conversion of unreacted PbI_2 into perovskite by an additional MA(I/Br) spin-coating

2.1 Introduction

As described in Chapter 1, the 2-step method has a problem of unreacted PbI_2. To suppress the unreacted PbI_2, some improved methods were developed, such as a use of DMSO for the solvent of PbI_2 solution to hinder the crystallization [1,2] and as a formation of mesoporous PbI_2 film for better CH_3NH_3I (MAI) diffusion [3]. On the other hand, in this chapter, the author attempted to convert the unreacted PbI_2 into perovskite phase and to control the composition of perovskite layer by spin-coating MA(I/Br) solutions as the 3rd step. Furthermore, the 2-step prepared $CH_3NH_3PbI_3$ ($MAPbI_3$) layer usually has cuboidal perovskite particles, which produces a relatively rough surface [4]. Recently, Yang et al. [5] reported that a pin-hole-less and smooth perovskite layer was obtained by spin-coating MABr solution on the 1-step prepared $MAPbI_3$ layer due to the grain growth thorough Ostwald ripening growth. Therefore, the additional spin-coating of MA(I/Br) solutions will possibly improve the morphology of the 2-step prepared perovskite layer.

The purposes of this chapter are (1) to convert the unreacted PbI_2 into perovskite (**Fig. 2.1**), (2) to control the composition of perovskite layer, and (3) to improve the film morphology by spin-coating MA(I/Br) solutions on the 2-step prepared perovskite layer. These improvements will enhance the photovoltaic performance of the perovskite solar cells.

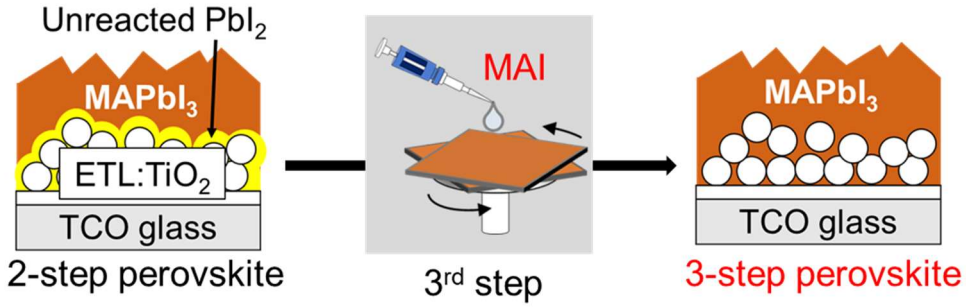

Fig. 2.1 Schematic illustration of the 3-step method using additional MAI spin-coating for conversion of unreacted PbI_2 into perovskite.

2.2 Experimental

A schematic illustration of prepared cell structure is shown in **Fig. 2.2(a)**. The cell size was 12.5×12.5 mm^2. It has an electron transport layer (ETL) / a perovskite layer / a hole transport layer (HTL) with the area of ~9×12.5 mm^2 and three Ag electrodes (one on TCO glass for cathode and two on [ETL/Perovskite layer/ HTL] for anodes). The probes for the measurement of photovoltaic performance were contacted at the points drown as the black dots in **Fig. 2.2(a)**. The black mask shown in **Fig. 2.2 (b)** was used to limit the light irradiation area on the cell.

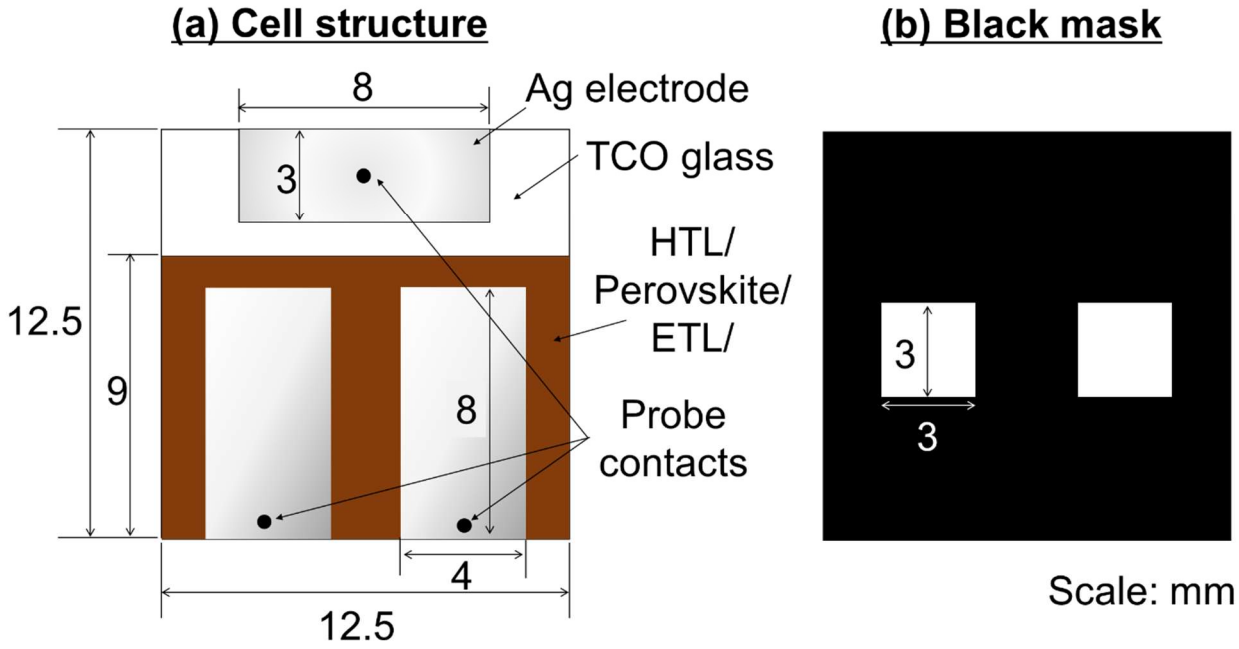

Figs. 2.2 Schematic illustrations of (a) cell structure and (b) black mask used for photovoltaic performance measurement.

2.2.1 Preparation method of perovskite solar cell

Preparation of electron transport layer (ETL) on TCO glass

Transparent conductive oxide (TCO, Type-0052, 10 Ω/sq., Geomatec) glasses were used as the substrates. The TCO substrates were patterned by etching with Zn powder (>96.0%, Tokyo Chemical Industry) and 1 M HCl (Wako Pure Chemical Industry) as shown in **Fig. 2.3**. The TCO in the area of 2.5 mm from the bottom was etched to avoid short circuit by the contact with probes.

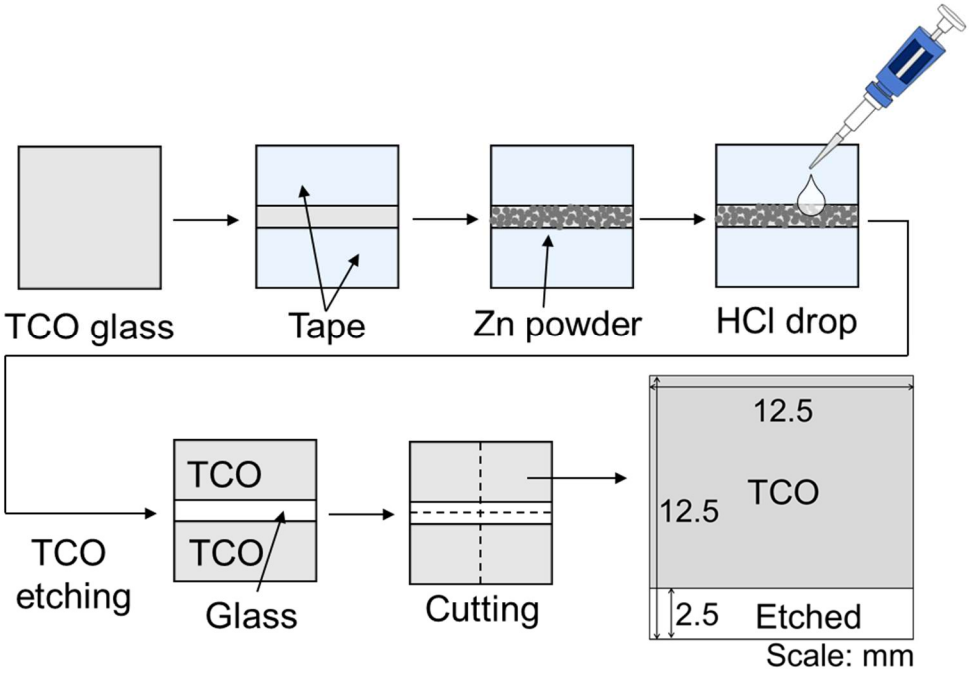

Fig. 2.3 Schematic illustration of TCO etching processes.

Then, the ETLs were prepared on the TCO substrates as shown in **Fig. 2.4**. The substrates were cleaned by ultrasonication in ethanol for 5 min and dried in air. The TiO_2 compact layers were prepared by spray-pyrolysis method; a solution of titanium diisopropoxide bis(acetylacetonate) (TAA, 75 wt% in isopropanol, Sigma-Aldrich) mixed with ethanol at the volume ratio of TAA:ethanol=2:25 was sprayed on the patterned substrates at 500°C. TiO_2 mesoporous layers were then prepared by spin-coating a TiO_2 paste (18NR-T, Dyesol), which was diluted in ethanol at the weight ratio of 1:5, on the substrates at 4000 rpm for 25 s and annealed at 500°C for 30 min. The coated substrates were immerged in a 40 mM $TiCl_4$ (99.0 %, Wako Pure Chemical Industry) solution diluted in distilled water at 70°C for 30 min, followed by rinsing with ethanol and annealing at 500°C for 30 min.

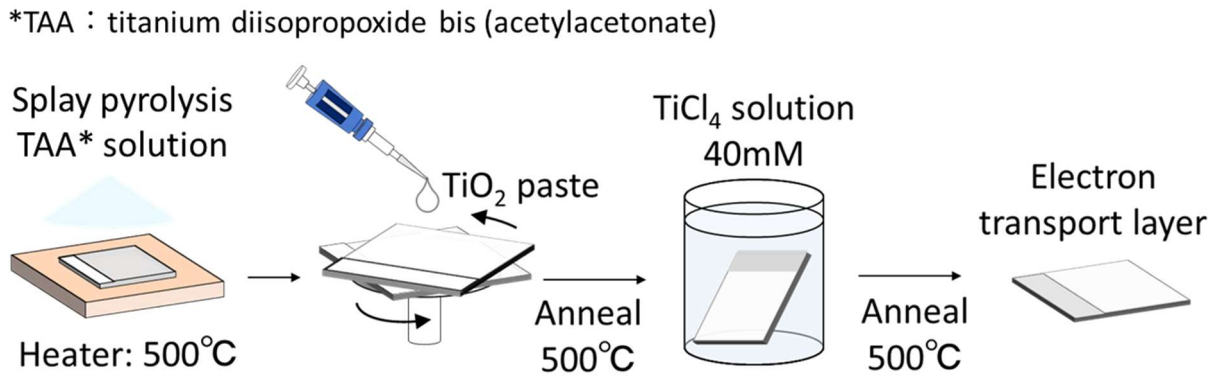

Fig. 2.4 Schematic illustration of preparation processes of electron transport layer (ETL).

Preparation of perovskite layer, hole transport layer (HTL) and metal electrodes

The perovskite layer and HTL were prepared in air with humidity of ~30%. The preparation processes are depicted in **Fig. 2.5**. The TiO_2 coated substrates and 1 M PbI_2 (>98.0 %, Tokyo Chemical Industry) solution in N,Ndimethylformamide (DMF, 99.5 %, Nacalai tesque) were pre-heated at 60°C. Then, the PbI_2 solution was spin-coated on the substrates at 3000 rpm for 20 s (i.e. the 1st step). After annealing at 60°C for 10 min, the substrates were dipped in a 10 mg/mL of CH_3NH_3I (MAI, 98 %, Wako Pure Chemical Industry) solution dissolved in isopropanol for 20 s, followed by rinsing with isopropanol and annealing at 60°C for 10 min (i.e. the 2nd step). Then, 20 μL of MAI solution (20 mg/mL), CH_3NH_3Br (MABr, 98 %, Wako Pure Chemical Industry) solution (14 mg/mL) or mixed solution of MAI and MABr ((10 mg+7 mg)/mL) were dropped on the prepared $MAPbI_3$ layers during the spinning at 4000 rpm for 35 s (i.e. the 3rd step).

The 3-step treated substrates were annealed at 60°C for 10 min, and then, the HTLs with the thickness of ~200 nm were prepared by spin-coating a spiro-MeOTAD solution. The spiro-MeOTAD solution in 1 mL chlorobenzene (99%, Nacalai tesque) was composed of 73 mg spiro-MeOTAD (99%, Sigma-Aldrich), 28.8 μL 4-*tert*-butylpyridine (TBP, 96.0%, Sigma-Aldrich) and 17 μL solution of [520 mg/mL lithium bis(trifluoromethylsulphonyl)imide salt (>98.0%, Tokyo Chemical Industry) in acetonitrile (99.5%, Wako Pure Chemical Industry)]. Finally, Ag electrodes with the thickness of ~50 nm were deposited on the HTLs with a thermal evaporator under 3×10^{-5} Torr. The completed solar cell is shown in **Fig. 2.6**.

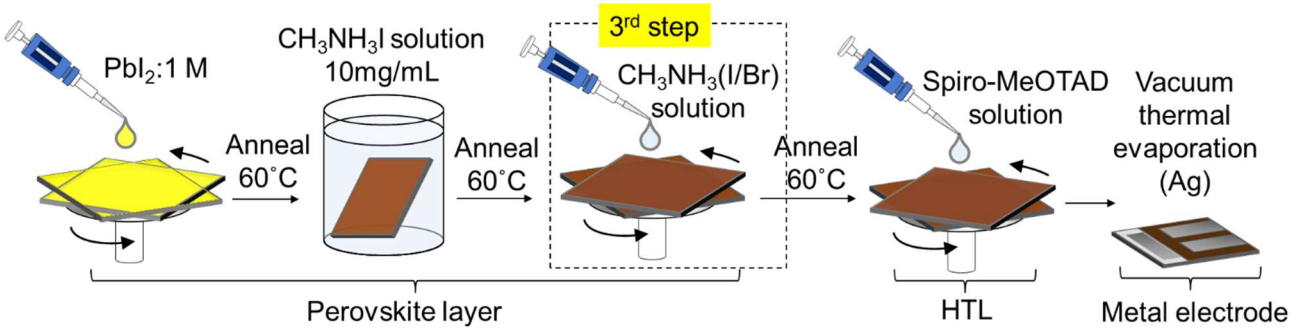

Fig. 2.5 Schematic illustration of preparation processes for perovskite layer, hole transport layer (HTL), and metal electrodes.

Fig. 2.6 Appearance of the perovskite solar cell. The cell size is 12.5×12.5 mm^2.

Herein after, $CH_3NH_3Pb(I/Br)_3$ and $CH_3NH_3(I/Br)$ will be denoted as $MAPb(I/Br)_3$ and MA(I/Br), respectively. As for the prepared samples, the relationship between the sample names and preparation conditions are summarized in **Table 2.1**.

Table 2.1 Relationship between sample names and preparation conditions in Chapter 2.

Additional spin-coating	Without	MAI solution	MA(I/Br) mixed solution	MABr solution
Sample names	2-step only	Additional MAI	Additional MA(I,Br)	Additional MABr

2.2.2 Characterizations

X-ray diffraction (XRD)

Crystal structure and phases analysis of the prepared perovskite layers or completed cells were carried out by XRD (Multiflex, Cu-K_α, 40 kV and 40 mA, Rigaku). The sample was set so that the height of surface matches that of sample holder (**Fig. 2.7**).

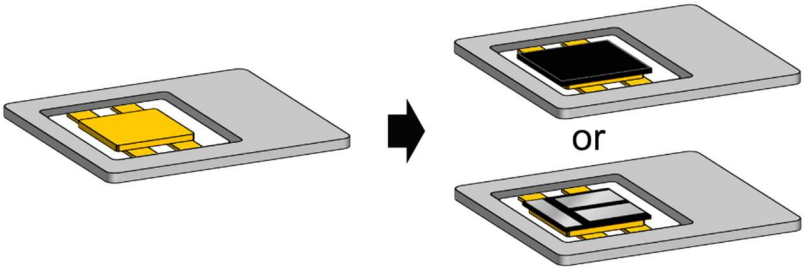

Fig. 2.7 Schematic illustration of sample set for XRD analysis. The perovskite layer on ETL or completed cell were used for the measurement.

Ultraviolet-visible absorption spectroscopy (UV-Vis)

Optical absorbance and transmittance spectra of the prepared perovskite layers on ETLs were measured by UV-Vis (UV-1280, Shimadzu). The light was irradiated from back TCO glass side (**Fig. 2.8**).

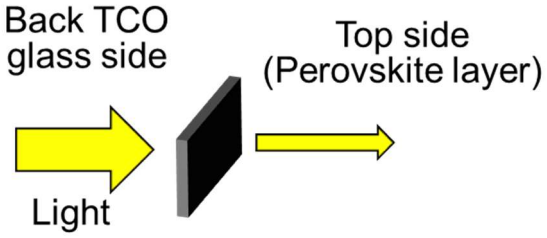

Fig. 2.8 Schematic illustration of UV-Vis. The light was irradiated from back TCO glass side.

Bandgap estimation

To estimate bandgaps of the prepared perovskite layers, the absorbance spectra were converted to Tauc plots. The Tauc equation is expressed as following (**eq. 2.1**) [6],

$$(\alpha h\nu)^{1/n} = A(h\nu - E_g) \qquad \textbf{(eq. 2.1)}$$

where α is an absorption coefficient, $h\nu$ is the photon energy (h is Planck constant, ν is frequency), A is a constant, and E_g is a bandgap gap. n takes "1/2" for a direct bandgap material and "2" for an in direct bandgap material. Since $MAPbI_3$ has the direct bandgap, $n = 1/2$ is used for $MAPbI_3$. The α is expressed by the following equation (**eq. 2.2**),

$$I = I_0 \exp(-\alpha \times t)$$

$$\ln \frac{I_0}{I} = \alpha \times t \qquad \textbf{(eq. 2.2)}$$

where I is transmitted light intensity, I_0 is incident light intensity, and t is thickness of the sample. Since the absorbance (A_λ) is expressed by following equation (**eq. 2.3**),

$$A_\lambda = -log_{10}\left(\frac{I}{I_0}\right) \qquad \textbf{(eq. 2.3)}$$

the α is calculated by following equation (**eq. 2.4**).

$$\alpha = \frac{2.303 \times A_\lambda}{t} \qquad \textbf{(eq. 2.4)}$$

Tauc plots for $MAPbI_3$ is obtained by plotting $(\alpha h\nu)^2$ for vertical axis and photon energy ($h\nu$) for horizontal axis. Then, a straight line is fitted to the liner part of the Tauc plots, and the bandgap is obtained from the photon energy at the intersection of the fitted straight line and background of the Tauc plots.

Scanning electron microscopy (SEM)

Surface and cross-section of the perovskite layers on ETLs were observed by SEM (JSM-5600LV, JEOL and SU-8020, Hitach High-technologies). For the cross-sectional observation, samples were broken into two pieces by making a notch with a diamond cutter, and the fracture surface was observed (**Fig. 2.9**).

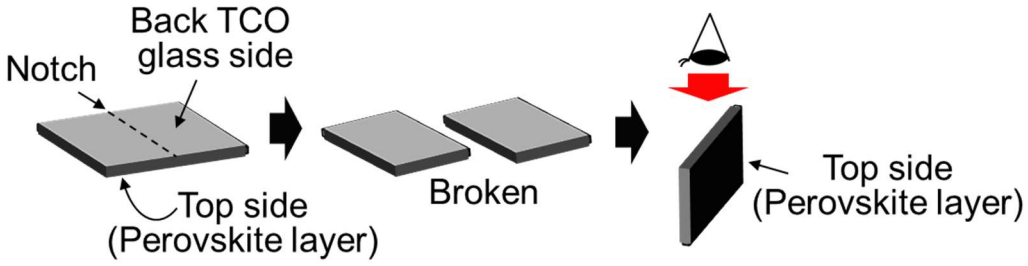

Fig. 2.9 Schematic illustration of sample preparation for cross-sectional SEM observation.

Current density-voltage (*J-V*) characterization

J-V characteristics were measured to evaluate photovoltaic performance with a DC voltage and current source/monitor (6241A, ADC Co.) and with a solar simulator (XES-40S1, SAN-EI Electric) which was calibrated to AM 1.5, 100 mW/cm^2 with a standard silicon photodiode (BS-520BK, Bunkokeiki). The voltage step and delay time were 20 mV and 50 ms, respectively. The voltage scan range was 0-1.1 V. The perovskite solar cells usually have a problem of hysteresis [7]; i.e. the different *J-V* characteristics are obtained depending on the voltage scan direction. Hence, the *J-V* characteristics were measured with both forward and back scans (forward scan: 0.0 → 1.1 V, back scan: 1.1 → 0.0 V). The active area was limited to 0.087 cm^2 by using a black mask.

There are two contact ways to the electrodes of perovskite solar cells as shown in **Fig. 2.10**. For the first method, the solar cell is turned over and it is placed on the metal pins for the contact. In this case, the light is irradiated from upper side. On the other hand, for the second method, the probes are touched from upper side and the light is irradiated from the bottom side. The first method was used in this thesis. **Fig. 2.11** shows a laboratory-made sample stage for *J-V* measurement.

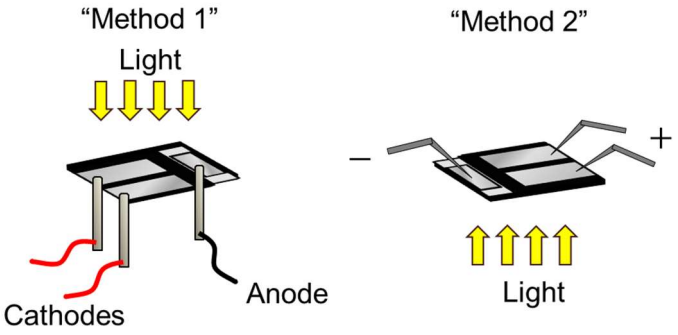

Fig. 2.10 Contact methods of probes and electrodes for the *J-V* measurement.

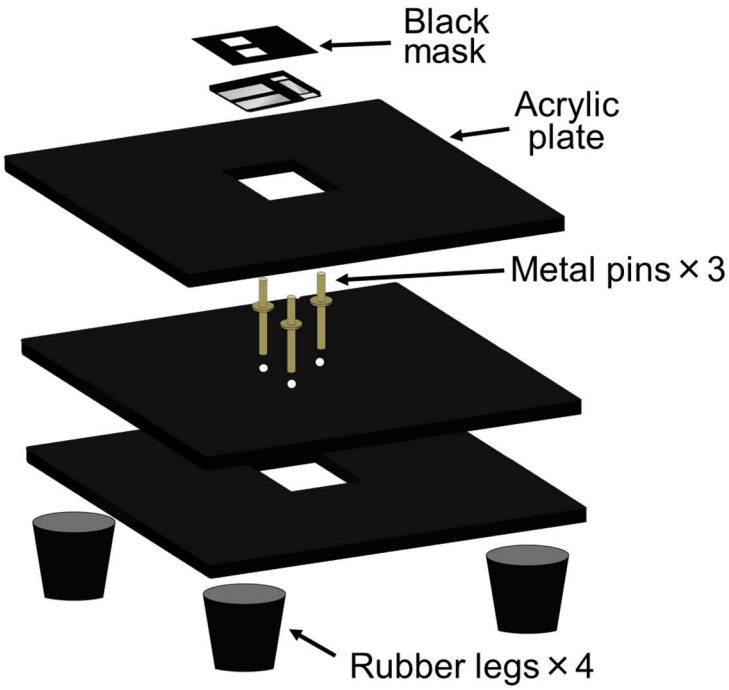

Fig. 2.11 Schematic illustration of the laboratory-made *J-V* measurement stage.

Parameters obtained from the *J-V* measurement

By measuring the current with applied voltage, the *J-V* curve as shown in **Fig. 2.12** is obtained. From the *J-V* curve, the *J-V* characteristics can be obtained, and those parameters are used for the evaluation of photovoltaic performance.

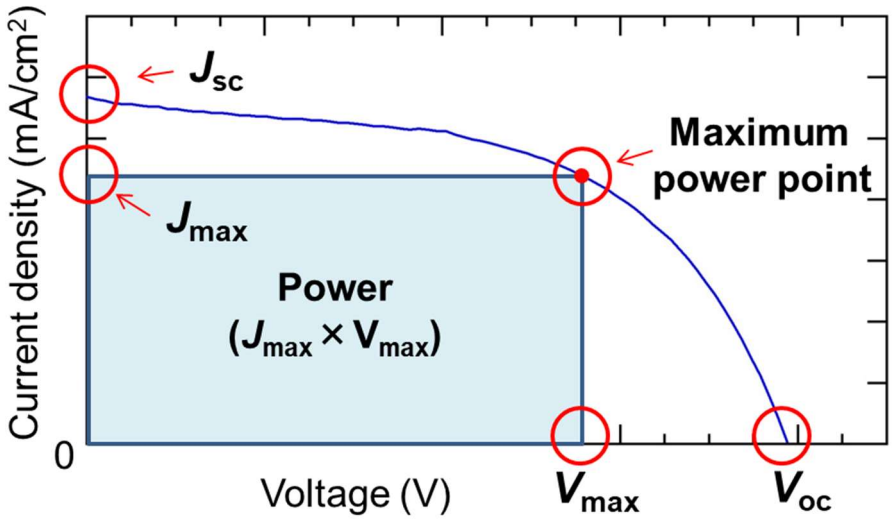

Fig. 2.12 *J-V* curve obtained from *J-V* measurement of solar cells.

Short circuit current density: J_{SC} (mA/cm^2)

J_{SC} is a current density obtained under the short circuit condition (applied voltage = 0), and it is the maximum current obtained from the solar cell. A short circuit current (I_{SC}) is generally measured in the actual *J-V* measurement. The J_{SC} is obtained by dividing the I_{SC} by the light irradiated area.

Open circuit voltage: V_{OC} (V)

V_{OC} is a voltage obtained under the open circuit condition (current = 0), and it is the maximum voltage obtained from the solar cell.

Fill factor: *FF*

FF is calculated by following equation, where the J_{max} and V_{max} are the current density and voltage at the maximum power point, respectively.

$$FF = (J_{max} \times V_{max}) / (J_{SC} \times V_{OC}) \quad \textbf{(eq. 2.5)}$$

Since the ideal maximum power obtained from the solar cell is calculated by $J_{SC} \times V_{OC}$, the *J-V* curve should be a square shape for the ideal solar cells. However, some resistance or leak current exists in the actual cell, and they decrease the generated power. Therefore, the actual power ($J_{max} \times V_{max}$) is lower than the ideal power. *FF* expresses a ratio of the actual power and the ideal power. When *FF* is closer to 1, the solar cell has smaller resistance and leak current, and the higher photovoltaic performance can be obtained.

Power conversion efficiency: PCE (%)

PCE is calculated by following equation (**eq. 2.6**). It expresses what percentage of the incident light energy is converted to electricity by the solar cell.

$$\begin{aligned} \text{PCE (\%)} &= \text{Generated power (mW)} / \text{Incident light intensity (mW)} \times 100 \\ &= (J_{max}\ (\text{mA/cm}^2) \times V_{max}\ (\text{V})) / 100\ (\text{mW/cm}^2) \times 100 \\ &= V_{OC} \times J_{SC} \times FF \end{aligned} \quad \textbf{(eq. 2.6)}$$

The incident light intensity is generally calibrated to AM 1.5, 100 mW/cm^2 to measure the photovoltaic performance under the fixed condition. Air mass (AM) represents an optical path length of the sun light through atmosphere of the Earth. The spectrum of sun light is different before and after traveling through the atmosphere, since the atmosphere partially absorbs or scatters the sun light. The spectrum of the sun light which enters vertically against the sea level is AM 1, and the AM 1.5 corresponds to the spectrum of solar zenith angle of ~48.2° (**Fig. 2.13**). The AM 1.5, light intensity of 100 mW/cm^2, and measurement temperature of 25°C are used as Standard Test Cell conditions.

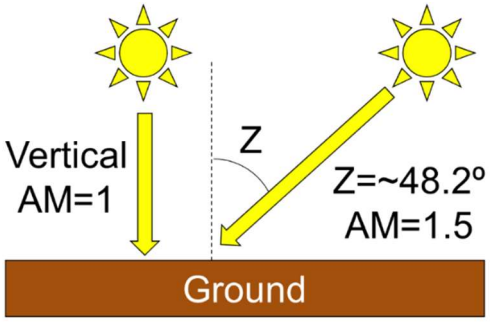

Fig. 2.13 Relationship between air mass (AM) and incident angle of sun light.

2.3 Results and Discussion

2.3.1 Phase and crystal structure analysis of perovskite layer

Figure 2.14 shows XRD patterns of the prepared perovskite solar cells in the range of 2θ = 10-70° and enlarged ones at 2θ = 27.5-29.0°. For the 2-step only sample, relatively strong peaks at ~12.6°, ~14.5°, ~28.3°, and ~35.2° were confirmed. The peaks at ~14.5°, ~28.3°, and ~35.2° correspond to 110, 220, and 312 peaks of tetragonal $MAPbI_3$ [8], indicating that $MAPbI_3$ was synthesized from the reaction of PbI_2 and MAI. However, since the peak at ~12.6° corresponding to 001 peak of PbI_2 [9] was also conformed, the unreacted PbI_2 remained in the 2-step prepared perovskite layer. After the additional spin-coating (the 3rd step), the intensity of PbI_2 peak significantly decreased and those for perovskite increased. This result indicates that the unreacted PbI_2 was converted into perovskite phase by the additional spin-coating. Although the 3-step prepared perovskite layers still had small amount of unreacted PbI_2, it may be converted into perovskite phase by controlling the concentration or contact time of the additional spin-coating solution.

As for the zoomed range at 27.5-29.0°, the peaks at ~28.0° and ~28.3° corresponding to the 004 and 220 peaks of tetragonal $MAPbI_3$ [8] were confirmed for the additionally MAI spin-coated perovskite layer. The 004 peak was not clearly confirmed in the 2-step only sample possibly due to the smaller peak intensity than that for additionally MAI spin-coated sample. With the additional spin-coating of the MA(I,Br) and MABr solution, the 220 peaks were shifted to larger angle and intensities of 004 peaks became smaller. The peak shift to large angle and the disappearance of the peak split indicate the shrinkage of lattice constants and the phase change from tetragonal phase to cubic phase. Since the ionic radius of Br^- is smaller than that of I^- and the $MAPbBr_3$ has cubic phase at the room temperature as mentioned in Chapter 1, these results suggest that the formation of $MAPbI_{3-x}Br_x$ by the substitution of I^- with Br^- [10,11].

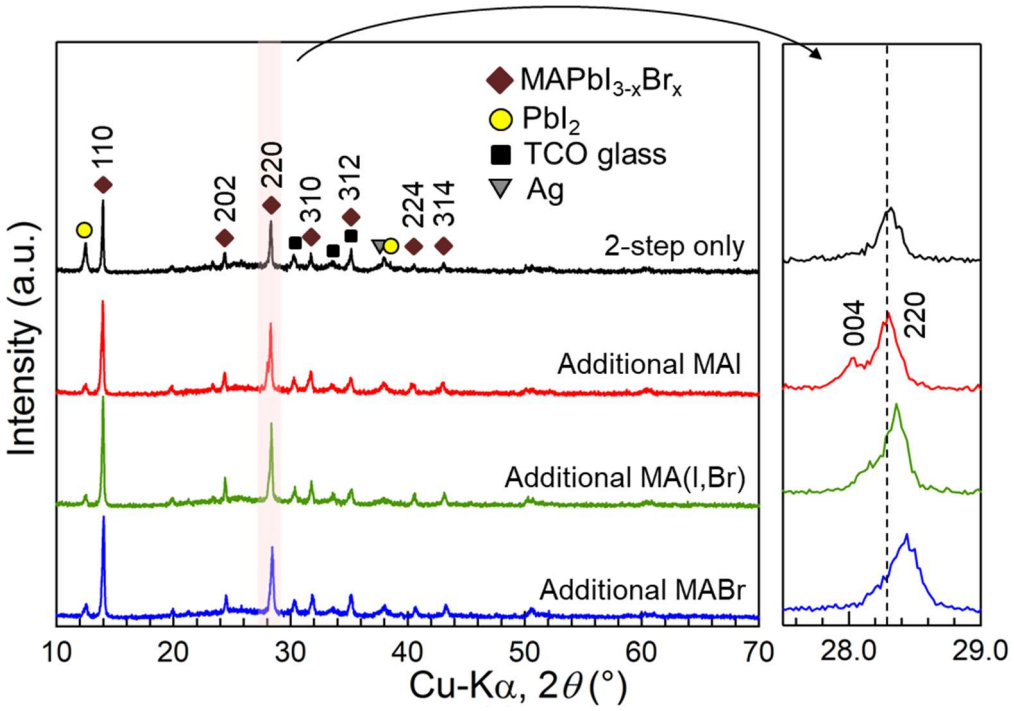

Fig. 2.14 XRD patters of the prepared perovskite layers on ETLs with and without additional MA(I/Br) spin-coating.

Then, the amount of unreacted PbI_2 converted into perovskite by the additional spin-coating was estimated from the integrated intensity of the PbI_2 peak at ~12.6° (001 reflection). **Figure 2.15** shows XRD patterns of a PbI_2 layer (1st step, before dipping in MAI), 2-step prepared $MAPbI_3$, and additionally MAI spin-coated perovskite layers at 11-15°. The integrated intensities of the PbI_2 peaks (001 reflection) and $MAPbI_3$ peaks (110 reflection) estimated from the XRD data are summarized in **Table 2.2**. The integrated intensity of the PbI_2 peak decreased to ~20% of the original value after the dipping in MAI solution (2nd step). This suggests that ~80% of PbI_2 was converted into $MAPbI_3$ and ~20% of PbI_2 still remains as the unreacted PbI_2 in the 2-step prepared perovskite layer. After the additional MAI spin-coating (3rd step), the integrated intensity of PbI_2 further decreased to ~5% of the original value, which indicates that the additional spin-coating further converted ~15% of unreacted PbI_2 into perovskite.

The increase of integrated intensity for $MAPbI_3$ peak by the conversion of 1% PbI_2 is calculated to be ~96.8 cps·deg (7779/80.4). From this estimation, the conversion of 15% of PbI_2 by the additional spin-coating will increase the integrated intensity of $MAPbI_3$ peak by ~1440 cps·deg (96.8 × 14.9). Therefore, the expected integral intensity of $MAPbI_3$ peak after the additional MAI spin-coating is ~9220 cps·deg (7779+1440). Actually, the integrated intensity of the $MAPbI_3$ peak obtained from the XRD data was ~9300 cps·deg, which is in good agreement with the expected value. This result suggests a proportional relationship between the decrease of integrated intensity for PbI_2: 001 peak and increase of $MAPbI_3$: 110 peak. It supports an accuracy of the estimation for decreased amount of PbI_2.

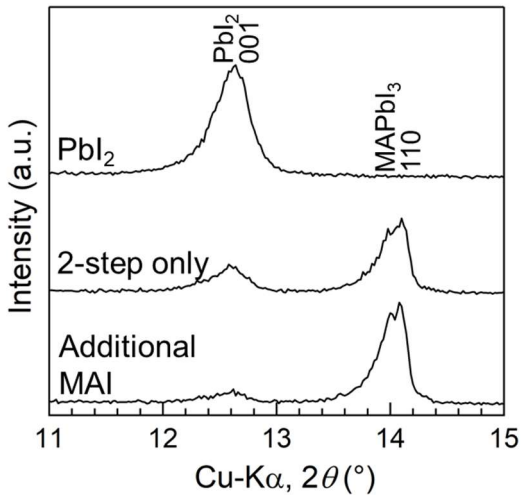

Fig. 2.15 XRD patterns of a PbI_2 layer (1st step, before dipping in MAI), 2-step prepared $MAPbI_3$ (2nd step), and additionally MAI spin-coated perovskite layers (3rd step) at 11-15°.

Table 2.2 Integrated intensities of the PbI_2 peaks (001 reflection) and $MAPbI_3$ peaks (110 reflection) in XRD.

		PbI_2 (1st step)		2-step only (2nd step)		Additional MAI (3rd step)
Integrated intensity	PbI_2 001 reflection	12769 (100%)	−80.4% →	2498 (19.6%)	−14.9% →	599 (4.7%)
	$MAPbI_3$ 110 reflection	0		7779		9301

2.3.2 Optical property analysis and bandgap estimation of perovskite layer

Figure 2.16 shows absorbance spectra of the prepared perovskite layers on ETLs in the range of 600-800 nm. The Tauc plots converted from the absorbance spectra are shown in **Fig. 2.17**, and the estimated bandgaps are summarized in **Table 2.3**. The 2-step prepared sample showed an absorption edge at ~780 nm, and the bandgap was estimated to be ~1.59 eV. This is comparable value with some reported bandgaps of $MAPbI_3$ [12,13]. The absorption edge of the additionally MAI spin-coated sample also existed at ~780 nm and the bandgap value was ~1.60 eV, which was similar to that of 2-step prepared sample. Since the bandgaps were comparable between 2-step prepared sample and additionally MAI spin-coated sample, the additional MAI spin-coating converted the unreacted PbI_2 into $MAPbI_3$ without obvious effects on the composition. On the other hand, blue-shifts of absorption edges and increases of bandgaps were confirmed for the additionally MA(I,Br) and MABr spin-coated samples. The bandgaps of additional MA(I,Br) and MABr were estimated to be 1.63 eV and 1.66 eV, respectively. Since the bandgap of $MAPbBr_3$ is larger than that of $MAPbI_3$ [14,15], these results also indicate the conversion of $MAPbI_3$ into $MAPbI_{3-x}Br_x$ by the substitution of I^- with Br^-.

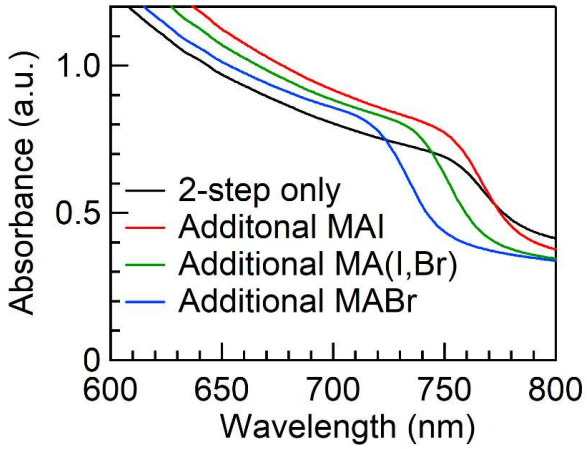

Fig. 2.16 Absorbance spectra of the prepared perovskite layers.

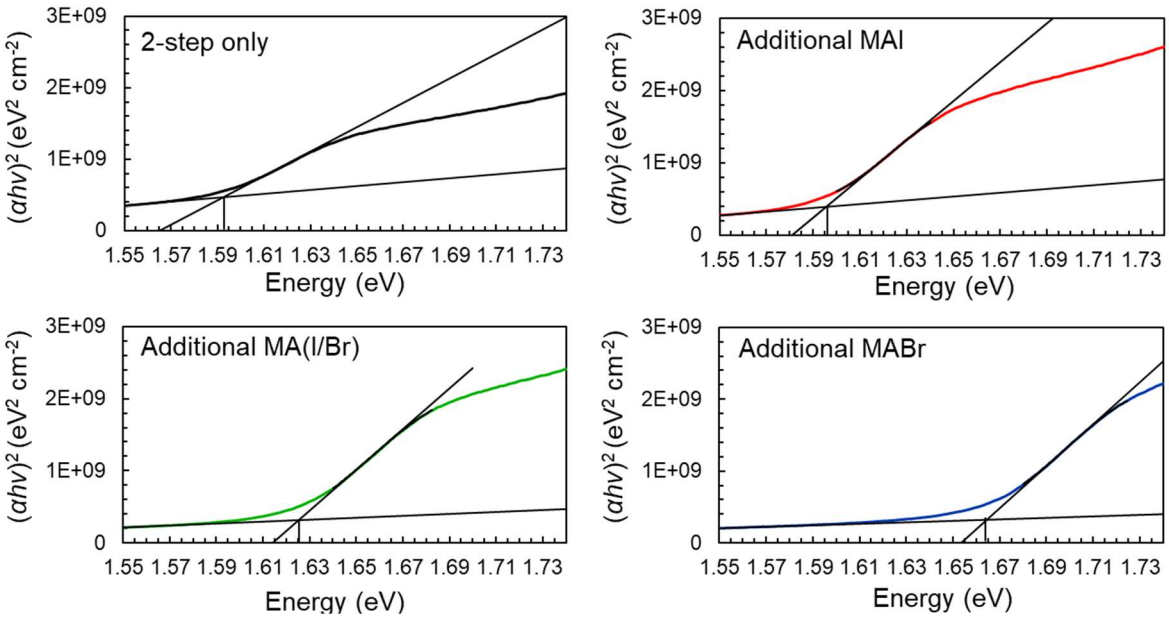

Fig. 2.17 Tauc plots of the prepared perovskite layers converted from the absorbance spectra.

Table 2.3 Estimated bandgaps from the Tauc plots of the prepared perovskite layers.

Samples	E_g (eV)
2-step only	1.59
Additional MAI	1.60
Additional MA(I,Br)	1.63
Additional MABr	1.66

It is reported that the correlation between Br^- ratio (x) and bandgap is nonlinear, and the bandgap can be estimated from following quadratic equation (**eq. 2.7**) [10,15], where the b is a bowing constant.

$$E_g(x) = E_g(CH_3NH_3PbBr_3)\frac{x}{3} + E_g(CH_3NH_3PbI_3)\left(1 - \frac{x}{3}\right) - \frac{x}{3}\left(1 - \frac{x}{3}\right)b \qquad \textbf{(eq. 2.7)}$$

Sutter-Fella et al. [15] fabricated eight $MAPbI_{3-x}Br_x$ based perovskite cells with changing the x values and measured the bandgaps. In their case, the bandgaps of $MAPbI_3$ ($x = 0$) was ~1.6 eV, and the following quadratic equation (**eq. 2.8**) with $b = 0.34$ was obtained by fitting the correlation between the x value and bandgaps.

$$E_g(x) = 1.598 + 0.36\left(\frac{x}{3}\right) + 0.34\left(\frac{x}{3}\right)^2 \qquad \textbf{(eq. 2.8)}$$

Since the bandgap value of their $MAPbI_3$ layer is comparable to that of this study, the x values of $MAPbI_{3-x}Br_x$ were estimated for additional MA(I,Br) and MABr spin-coated samples using the **eq. 2.8**. The x value of additionally MA(I,Br) spin-coated sample was estimated to be ~0.2 (i.e., $CH_3NH_3PbI_{2.8}Br_{0.2}$) and that for additionally MABr spin-coated cell was estimated to be ~0.5 (i.e., $CH_3NH_3PbI_{2.5}Br_{0.5}$).

Figure 2.18 shows transmittance spectra of the prepared perovskite layers on ETLs. The additionally spin-coated samples showed smaller transmittance than that of 2-step prepared sample at the wavelength < ~780 nm, which indicates the better light absorption. The improved light absorption is ascribed to the additionally synthesized perovskite from the conversion of unreacted PbI_2.

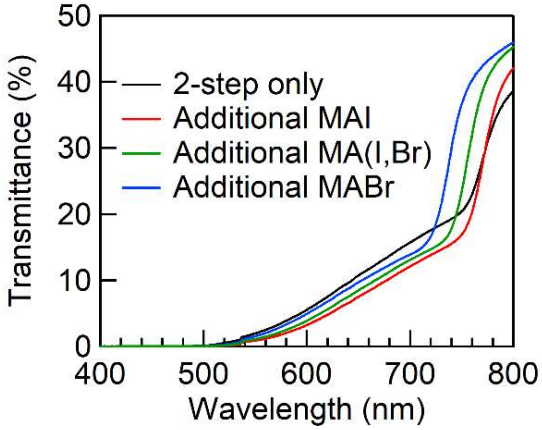

Fig. 2.18 Transmittance spectra of the prepared perovskite layers on ETLs.

2.3.3 Microstructure observation of perovskite layer

Figures 2.19(a)-(c) show surface SEM images of the prepared perovskite layers on ETLs: (a) 2-step prepared, (b) additionally MAI spin-coated and (c) additionally MABr spin-coated samples. The 2-step prepared sample had cuboid-shaped particles with a diameter of ~500 nm-1 μm, which is in good agreement with the reported morphology of the 2-step prepared perovskite layer [4]. After the additional spin-coating, the diameter of the particles was comparable to that of 2-step prepared sample, but the edges of particles became somewhat roundish. Furthermore, the particles partially connected to each other, which formed a network among the perovskite particles (see red arrows).

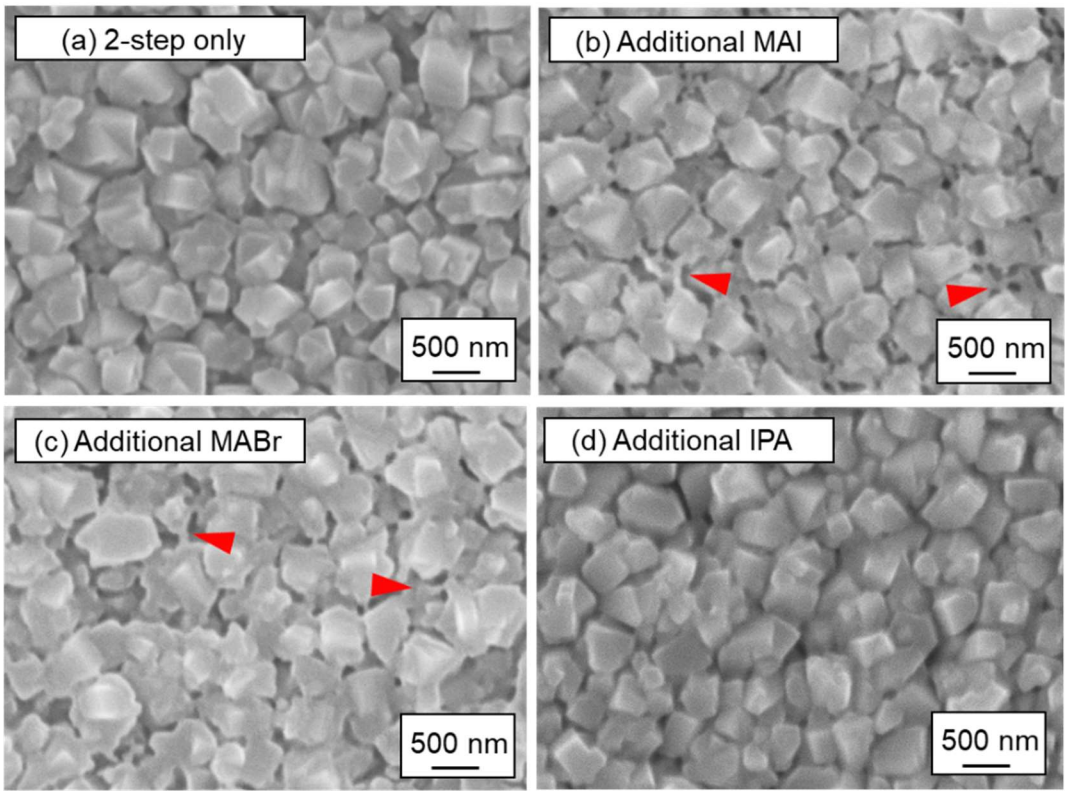

Figs. 2.19 Surface SEM images of the (a) 2-step prepared, (b) additionally MAI spin-coated, (c) additionally MABr spin-coated, and (d) additionally isopropanol (IPA) spin-coated perovskite layers.

This microstructure development is attributable to the surface dissolution of perovskite particles by the additionally spin-coated MA(I/Br) solutions. The grain growth mechanism of 2-step prepared perovskite layer is explained by Ostwald ripening growth; i.e. small $MAPbI_3$ particles dissolved in the CH_3NH_3(I/Br) solutions and it redeposits on the other larger particles as following equation (**eq. 2.9**) [16].

$$CH_3NH_3PbI_3 + I^- \rightleftarrows CH_3NH_3^+ + PbI_4^{2-} \qquad \textbf{(eq. 2.9)}$$

This suggests that the surface of perovskite particles can be slightly dissolved in the additionally spin-coated MA(I/Br) solutions. Therefore, the morphological change can be caused by the surface dissolution of the perovskite particles into the additionally spin-coated samples and the dispersion of the solutions during the spin-coating, which formed the networks among the perovskite particles (i.e., liquid-phase assisted grain

growth). **Figure 2.19 (d)** shows surface SEM images of the perovskite layer with additional spin-coating of only isopropanol (IPA). The perovskite particles still kept the sharp edges even after the IPA spin-coating and the morphological change were not confirmed. This result indicates that MAI or MABr in the isopropanol are necessary to change the morphology, and it supports the expected mechanism of the morphological change (liquid-phase assisted grain growth).

Figures 2.20(a)-(c) show cross-sectional SEM images of the prepared perovskite layers on ETLs: (a) 2-step prepared, (b) additionally MAI spin-coated, and (c) MABr spin-coated samples. From the SEM images, all the samples were composed of perovskite/mesoporous TiO_2 layer: ~200 nm and perovskite capping layer: ~400 nm. No obvious difference was confirmed on the thickness. As for the surface morphology, the surface of the perovskite capping layer for 2-step prepared sample was relatively rough due to the cuboid-shaped $MAPbI_3$ particles with the sharp edge. After the additional spin-coating of MAI or MABr solution, the surface became slightly smoother and the grain boundary became ambiguous due to the dissolution of particle surface.

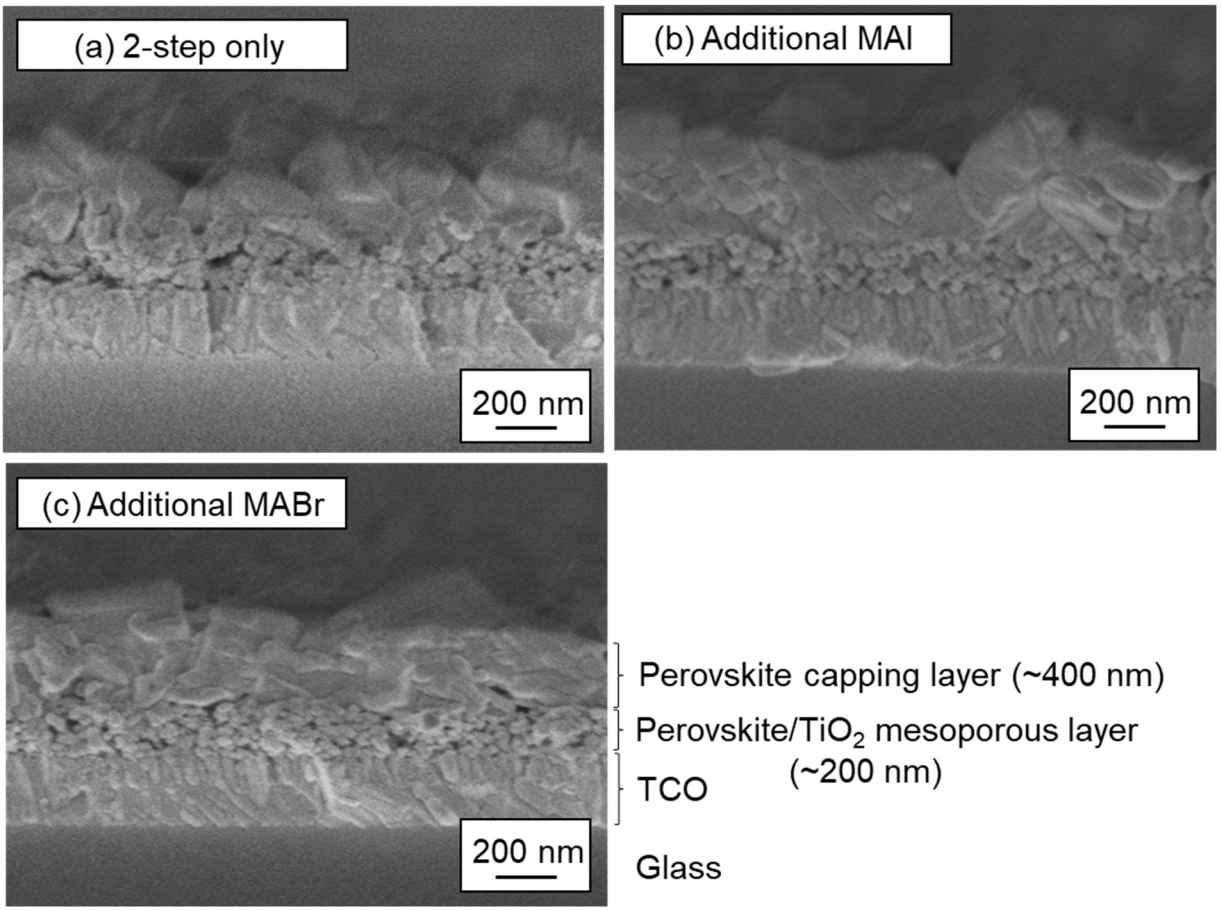

Figs. 2.20 Cross-sectional SEM images of the prepared perovskite layers on ETLs: (a) 2-step prepared, (b) additionally MAI spin-coated, and (c) additionally MABr spin-coated samples.

Figure 2.21 shows cross-sectional SEM image of the additionally MABr spin-coated sample with HTL and Ag electrode. The thickness of the HTL depended on the position due to the non-flat surface of perovskite layer, but the thickness was within ~100-200 nm. Meanwhile, the thickness of the Ag electrode was ~50 nm. Those thickness should be similar in all the samples, since the deposition conditions of HTL and Ag electrodes were same in all the samples.

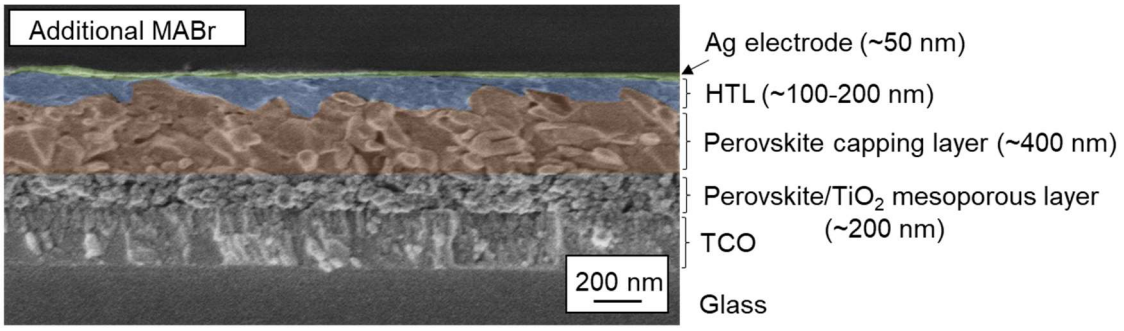

Fig. 2.21 Cross-sectional SEM image of the additionally MABr spin-coated sample with HTL and Ag electrode.

The perovskite/mesoporous TiO_2 layer and perovskite capping layer were observed from the cross-sectional SEM observation, but the observation of TiO_2 compact layer was difficult due to its too thin thickness. Hence, the thicker TiO_2 compact layers were prepared to estimate the thickness of TiO_2 compact layer in the actual cell. The TiO_2 compact layer for the actual cell was prepared by spraying the TiO_2 precursor solution 9 times on the TCO glass with heating at 500°C. For the estimation of the thickness, thicker TiO_2 compact layers were prepared by spraying 18, 27, and 36 times. **Figure 2.22** show the cross-sectional SEM images of the TiO_2 compact layers with spraying 18, 27, and 36 times. The thickness of the TiO_2 compact layers prepared by spraying 18, 27, and 36 times were ~60, 90, and 120 nm, respectively. Since the thickness increased ~30 nm with increasing the spraying number by 9 times, the thickness of the TiO_2 compact layer for the actual cell (9 times spraying) was estimated to be ~30 nm.

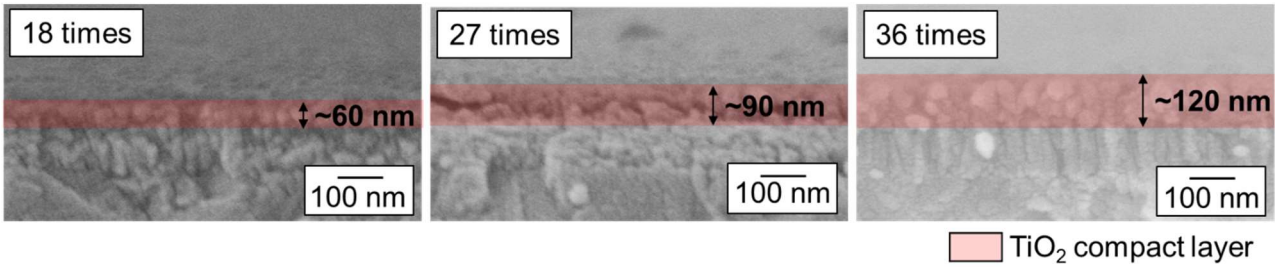

Fig. 2.22 Cross-sectional SEM images of TiO_2 compact layers prepared on TCO glasses by spraying a TiO_2 precursor solution 18, 27, and 36 times.

2.3.4 Evaluations of photovoltaic performance and stability in air

Evaluation of photovoltaic performance

Figure 2.23(a) shows typical *J-V* curves of the prepared solar cells measured just after the preparation with back scan. The *J-V* characteristics (average of 8 cells) are summarized in **Table 2.4**. The 2-step prepared cell displayed J_{SC} of 21.2 mA/cm^2, V_{OC} of 0.91 V, *FF* of 0.66 and PCE of 12.9%. With the additional MAI spin-coating, J_{SC} and V_{OC} increased to 22.1 mA/cm^2 and 0.94 V, respectively. As a result, the larger PCE of 14.4% was achieved. The increase of J_{SC} is ascribed to the enhanced light absorption by the additionally synthesized $MAPbI_3$ from the unreacted PbI_2 as seen in **Fig. 2.18**. The V_{OC} improvement is also attributable to the conversion of unreacted PbI_2 as is reported by Jacobsson et al. [17]. Additionally, the smoother surface and decrease of grain boundary as observed in **Figs. 2.19 and 2.20** are also contributable to the V_{OC} improvement, since the grain boundary forms carrier trap sites and it results in the carrier recombination [18].

As for the effects of I^- substitution with Br^-, J_{SC} decreased and V_{OC} increased with increasing the Br ratio in the additional spin-coating solution. J_{SC} of 20.8 mA/cm^2, V_{OC} of 0.95 V, *FF* of 0.71 and PCE of 14.2% for the additionally MA(I,Br) spin-coated cell and J_{SC} of 19.5 mA/cm^2, V_{OC} of 0.99 V, *FF* of 0.70 and PCE of 13.5% for the additionally MABr spin-coated cell were obtained. The decrease of J_{SC} is due to the balance of a positive effect by the enhanced light absorption and a negative effect of enlarged band gap which shortens the wavelength range of light absorption. The larger V_{OC} than that of additionally MAI spin-coated cell is due to the increase of bandgap. The V_{OC} and bandgap generally have a positive correlation. For example, an increase of bandgap by incorporating Br^- into $MAPbI_3$ perovskite layer ($MAPbI_3 \rightarrow MAPbI_{3-x}Br_x$) generates larger V_{OC} [10,19].

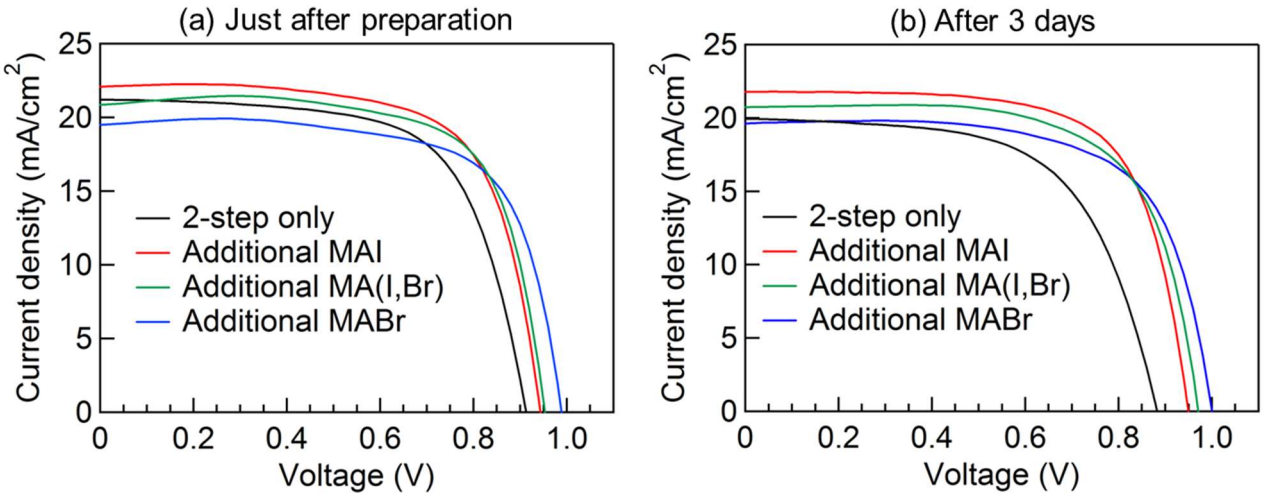

Figs. 2.23 *J-V* curves of the prepared solar cells (back scan) measured (a) just after the preparation and (b) after 3 days.

Table 2.4 *J-V* characteristics (back scan) of prepared solar cells measured just after the preparation (left) and after 3 days (right). The values are average of 8 cells.

Samples	Just after preparation				After 3 days			
	J_{SC} (mA/cm^2)	V_{OC} (V)	*FF*	PCE (%)	J_{SC} (mA/cm^2)	V_{OC} (V)	*FF*	PCE (%)
2-step only	21.2	0.91	0.66	12.9	20.9	0.90	0.63	11.9
Additional MAI	22.1	0.94	0.69	14.4	22.2	0.93	0.69	14.4
Additional MA(I,Br)	20.8	0.95	0.71	14.2	20.7	0.96	0.67	13.4
Additional MABr	19.5	0.99	0.70	13.5	20.0	0.98	0.67	13.1

As a result, all the 3-step prepared cells showed the enhanced PCEs compared with that of the 2-step prepared cell, indicating the 3-step method using the additional MA(I/Br) is effective to improve the photovoltaic performance of the 2-step prepared perovskite solar cells. Although an abnormal behavior of slight current drop at around 0 V were observed for the 3-step cells as shown in **Fig. 2.23(a)**, it almost disappeared after 3 days as shown in **Fig. 2.23(b)**. Since the current drop was not observed in the 2-step

prepared cell, it was possibly caused by the morphological change of perovskite particles or an excess MAI or MABr on the surface of perovskite layer by the additional spin-coating.

As mentioned in the section 1.2.3, the perovskite solar cells usually have the problem of hysteresis between the forward and back scans in the *J-V* measurement. Therefore, the hysteresis of the prepared cells was investigated. The typical *J-V* curves and characteristics (average of 8 cells) measured on 3 days after the preparation with forward scan are shown in **Fig. 2.24** and **Table 2.5**. The hysteresis factor was calculated by following equation (**eq. 2.10**) and is included in the **Table 2.5**.

$$\text{Hysteresis factor} = \text{PCE (forward scan)} / \text{PCE (back scan)} \qquad \textbf{(eq. 2.10)}$$

The hysteresis was confirmed in all the cells, and the hysteresis factors were comparable among them except for additionally MABr spin-coated cell. As for the mesoporous-type perovskite solar cells, some researchers reported that the hysteresis became larger by decreasing the thickness of mesoporous layer, and relatively large hysteresis was confirmed for the thickness < ~200 nm [20,21]. Since the prepared cells in this study had the TiO_2 mesoporous layers with the thickness of ~150 nm as shown in **Figs. 2.20(a)-(c)**, the observed hysteresis can be suppressed by increasing the thickness of mesoporous layer.

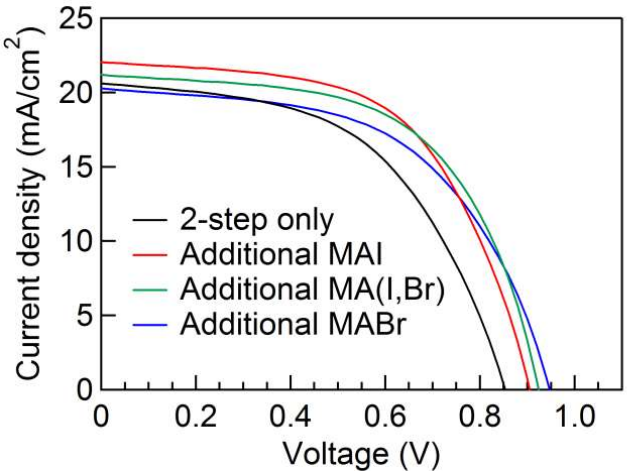

Fig. 2.24 *J-V* curves of the prepared perovskite solar cells measured with forward scan.

Table 2.5 *J-V* characteristics of prepared solar cells measured with a forward scan after 3 days from the preparation. The values are average of 8 cells.

Samples	J_{SC} (mA/cm^2)	V_{OC} (V)	*FF*	PCE (%)	Hysteresis value
2-step only	21.0	0.85	0.51	9.2	0.77
Additional MAI	22.5	0.89	0.56	11.3	0.78
Additional MA(I,Br)	21.2	0.91	0.53	10.4	0.78
Additional MABr	20.2	0.91	0.48	8.9	0.68

Evaluation of stability in air

Since the perovskite solar cells usually have a problem of poor stability in air due to the decomposition of $MAPbI_3$, the stability test was carried out. The solar cells were stored in air and in dark with the humidity of ~30%, and the *J-V* measurements were repeated as shown in **Fig. 2.25(a)**. **Figure 2.25(b)** shows the normalized PCEs of 2-step prepared, additionally MAI spin-coated, and additionally MABr spin-coated cells as a function of time. The 2-step prepared cell started to decrease the PCE from the next day of fabrication, and the PCE became less than 60 % of the original value after 700 h. On the other hand, the additionally spin-coated cells retained the original PCE values up to ~150 h, and they still showed more than 80% even after 700 h. These results suggest that the 3-step prepared samples had better air stability than 2-step prepared sample. The improved stability is attributable to the decrease of contact surface area with moisture due to the decrease of grain boundary, which suppresses the decomposition of perovskite into PbI_2 (**Fig. 2.26**).

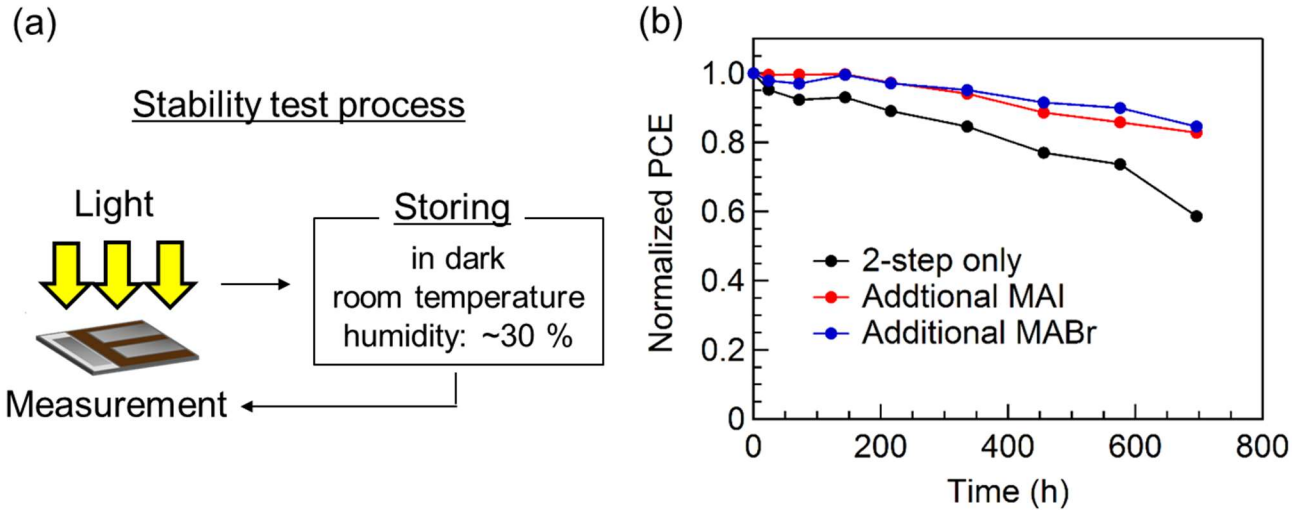

Figs. 2.25 (a) Schematic illustration of a stability test in air with humidity of ~30%, and (b) normalized PCEs of 2-step prepared, additionally MAI spin-coated, and additionally MABr spin-coated cells as a function of time.

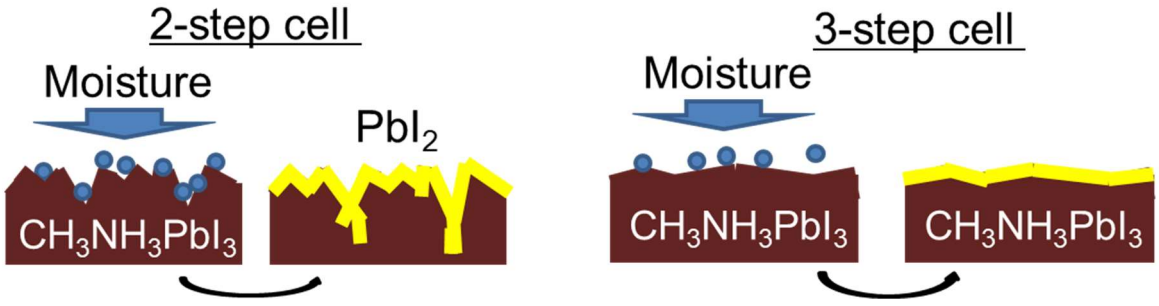

Fig. 2.26 Possible mechanism of the improved air stability for the 3-step prepared cells.

2.4 Conclusions

In this chapter, the 3-step method, i.e. additional spin-coating of MA(I/Br) solution, was demonstrated to convert the unreacted PbI_2 in the 2-step prepared perovskite layer. The additional spin-coating successfully converted the unreacted PbI_2 into perovskite phase, and the light absorption of the perovskite layer was enhanced. Meanwhile, the additional spin-coating of MA(I,Br) and MABr solutions transformed $MAPbI_3$ into $MAPbI_{3-x}Br_x$ and shrank the light absorption wavelength range by enlarging the bandgap. The formation of networks among the perovskite particles and the decrease of grain boundary were also observed by the dissolution of the $MAPbI_3$ particle surface. The additional MAI spin-coating increased both J_{SC} and V_{OC}, and the PCE was highly improved from 12.9 to 14.4%. Although the additional MA(I,Br) and MABr spin-coating slightly decreased J_{SC}, larger V_{OC} than that of additionally MAI spin-coated cell was obtained, which produced PCEs of 14.2% for the additionally MA(I,Br) spin-coated cell and 13.5% for the additionally MABr spin-coated cell. Furthermore, the stability in air was also improved by the additional spin-coating. These results suggest that the 3-step method is effective to (1) convert the unreacted PbI_2 into perovskite, (2) to control the composition of the perovskite layer, and (3) to improve the surface morphology, which enhances the photovoltaic performance.

Most part of this chapter has been published in *Mater. Sci. Semicond. Process*., **71**, 1-6 (2017). http://dx.doi.org/10.1016/j.mssp.2017.06.049. [22]

References

[1] W. Li, J. Fan, J. Li, Y. Mai, L. Wang, Controllable grain morphology of perovskite absorber film by molecular self-assembly toward efficient solar cell exceeding 17%, *J. Am. Chem. Soc*., **137**, 10399−10405 (2015).

[2] Y. Wu, A. Islam, X. Yang, C. Qin, J. Liu, K. Zhang, W. Penga, L. Han, Retarding the crystallization of PbI_2 for highly reproducible planar-structured perovskite solar cells via sequential deposition. *Energy Environ. Sci*., **7**, 2934–2938 (2014).

[3] J. Cao, F. Wang, H. Yu, Y. Zhou, H. Lu, N. Zhao, C. P. Wong, Porous PbI_2 films for the fabrication of efficient, stable perovskite solar cells via sequential deposition, *J. Mater. Chem. A,* **4**, 10223–10230 (2016).

[4] J. H. Im, I. H. Jang, N. Pellet, M. Grätzel, N. G. Park, Growth of CH3NH3PbI3 cuboids with controlled size for high-efficiency perovskite solar cells, *Nat. Nanotechnol.*, **9**, 927–932 (2014).

[5] M. Yang, T. Zhang, P. Schulz, Z. Li, G. Li, D. H. Kim, N. Guo, J. J. Berry, K. Zhu, Y. Zhao, Facile fabrication of large-grain $CH_3NH_3PbI_{3-x}Br_x$ films for high-efficiency solar cells via CH_3NH_3Br selective ostwald ripening, *Nat. Commun*., **7**, 12305 (2016).

[6] T. Wang, B. Daiber, J. M. Frost, S. A. Mann, E. C. Garnett, A. Walsh, B. Ehrler, Indirect to direct bandgap transition in methylammonium lead halide perovskite, *Energy Environ. Sci*., **10**, 509-515 (2017).

[7] B. Chen, M. Yang, S. Priya, K. Zhu, Origin of *J*−*V* hysteresis in perovskite solar cells, *J. Phys. Chem. Lett*., **7**, 905−917 (2016).

[8] T. Oku, Crystal structures of $CH_3NH_3PbI_3$ and related perovskite compounds used for solar cells, *Solar Cells - New Approaches and Reviews ed L A Kosyachenko (InTech)*, **77**, chapter 3 (2015).

[9] A. Bahtiar, S. Rahmanita, Y. D. Inayatie, Pin-hole free perovskite film for solar cells application prepared by controlled two-step spin-coating method, *IOP Conf. Ser.: Mater. Sci. Eng*., **196**, 012037 (2017).

[10] J. H. Noh, S. H. Im, J. H. Heo, T. N. Mandal, S. I. Seok, Chemical management for colorful, efficient, and stable inorganic−organic hybrid nanostructured solar cells. *Nano Lett*., **13**, 1764−1769 (2013).

[11] D. M. Jang, K. Park, D. H. Kim, J. Park, F. Shojaei, H. S. Kang, J. P. Ahn, J. W. Lee, J. K. Song, Reversible halide exchange reaction of organometal trihalide perovskite colloidal nanocrystals for full-range band gap tuning, *Nano Lett.*, **15**, 5191−5199 (2015).

[12] H. S. Kim, C. R. Lee, J. H. Im, K.B. Lee, T. Moehl, A. Marchioro, S. J. Moon, R. Humphry-Baker, J. H. Yum, J. E. Moser, M. Grätzel, N.G. Park, Lead iodide perovskite sensitized all-solid-state submicron thin film mesoscopic solar cell with efficiency exceeding 9%, *Sci Rep*., **2**, 591 (2012).

[13] H. S. Jung, N. G. Park, Perovskite solar cells: from materials to devices, *small*, **11**, 1 (2015).

[14] S. A. Kulkarni, T. Baikie, P. P. Boix, N. Yantara, N. Mathews, S. Mhaisalkara, Band-gap tuning of lead halide perovskites using a sequential deposition process, *J. Mater. Chem. A*, **2**, 9221–9225 (2014).

[15] C. M. Sutter-Fella, Y. Li, M. Amani, J. W. Ager, F. M. Toma, E. Yablonovitch, I. D. Sharp, A. Javey, High photoluminescence quantum yield in band gap tunable bromide containing mixed halide perovskites, *Nano Lett*., **16**, 800−806 (2016).

[16] S. Y. Kim, H. J. Jo, S.J. Sung, D. H. Kim, Perspective: understanding of ripening growth model for minimum residual PbI_2 and its limitation in the planar perovskite solar cells. *APL Mater*., **4**, 100901 (2016).

[17] T. J. Jacobsson, J. P. Correa-Baena, E. H. Anaraki, B. Philippe, S. D. Stranks, M. E. F. Bouduban, W. Tress, K. Schenk, J. Teuscher, J. E. Moser, H. Rensmo, A. Hagfeldt, Unreacted PbI_2 as a double-edged sword for enhancing the performance of perovskite solar cells, *J. Am. Chem. Soc*. **138**, 10331−10343 (2016).

[18] X. Ren, Z. Yang, D. Yang, X. Zhang, D. Cui, Y. Liu, Q. Wei, H. Fan, S. F. Liu, Modulating crystal grain size and optoelectronic properties of perovskite films for solar cells by reaction temperature. *Nanoscale*, **8**, 3816−3822 (2016).

[19] W. Zhu, C. Bao, F. Li, T. Yu, H. Gao, Y. Yi, J. Yang, G. Fu, X. Zhou, Z. Zou, A halide exchange engineering for $CH_3NH_3PbI_{3-x}Br_x$ perovskite solar cells with high performance and stability, *Nano Energy*, **19**, 17–26

(2016).

[20] C. Liu, J. Fan, X. Zhang, Y. Shen, L. Yang, Y. Mai, Hysteretic behavior upon light soaking in perovskite solar cells prepared via modified vapor-assisted solution process, *ACS Appl. Mater. Interfaces*, **7**, 9066–9071 (2015).

[21] H. J. Snaith, A. Abate, J. M. Ball, G. E. Eperon, T. Leijtens, N. K. Noel, S. D. Stranks, J. T. W. Wang, K. Wojciechowski, W. Zhang, Anomalous hysteresis in perovskite solar cells, *J. Phys. Chem. Lett*., **5**,1511−1515 (2014).

[22] Y. Okamoto, Y. Suzuki, Perovskite solar cells prepared by a new 3-step method including a PbI_2 scavenging step, *Mater. Sci. Semicond. Process*., **71**, 1-6 (2017).

Chapter 3

Formation of multiple bandgap structure at the bottom side of perovskite layer by an additional FAI spin-coating

Chapter 3: Formation of multiple bandgap structure at the bottom side of perovskite layer by an additional FAI spin-coating

3.1. Introduction

As described in Chapter 1, the band alignment is important for the perovskite solar cells. The author previously controlled the band alignments of electron transport layers in dye-sensitized solar cells [1,2] and perovskite solar cells [3,4] by using $SrTiO_3$, $CaTiO_3$, and $BaTiO_3$ instead of TiO_2. On the other hand, in this chapter, the control of band alignment in the perovskite light absorbing layer was focused. When the perovskite layer is prepared by wet processes, such as spin-coating or dipping process, the bandgap gradient is generally formed at the top surface side by post-treatments [5,6]. However, for further enhancement of the conversion efficiency, the bandgap gradient should be formed at the both top and bottom sides. Therefore, the author attempted to form the bandgap gradient at the bottom side of the perovskite layer (multiple bandgap structure) by using the 3-step method.

In Chapter 2, the $CH_3NH_3(I/Br)$ (MA(I/Br)) solution was spin-coated on the 2-step prepared perovskite layer to convert the unreacted PbI_2 and to control the composition [7], while, instead of the MA(I/Br) solution, a formaminidium iodide ($CH(NH_2)_2I$, FAI) solution was additionally spin-coated in this chapter. **Figure 3.1** shows the strategy for the preparation of the multiple bandgap structure. The unreacted PbI_2 has been considered to exist at the bottom of the perovskite layer (near the ETL) in the 2-step method, since it is produced by an insufficient MAI diffusion into the deep part of PbI_2 layer. Actually, Kim et al. [8] and Ummadisingu et al. [9] confirmed the existence of unreacted PbI_2 in the area of several tens of nanometers from TiO_2 compact layer for the planar type structure and in the TiO_2 mesoporous layer for the mesoporous structure, respectively.

In this study, the unreacted PbI_2 was used to form the multiple bandgap structure. By the additional spin-coating of the FAI solution, $MAPbI_3$ will be changed into $FA_xMA_{1-x}PbI_3$ by the substitution of MA^+ with FA^+. In addition, the FAI spin-coating will convert the unreacted PbI_2 into FA rich perovskite layer ($FAPbI_3$) at the bottom side. Since $FAPbI_3$ has a smaller bandgap than $MAPbI_3$ and has the conduction band and valence band at lower positions, the multiple bandgap structure can be obtained by producing the bandgap gradient at the bottom side (**Fig.3.1**), which should be effective to improve the photovoltaic performance.

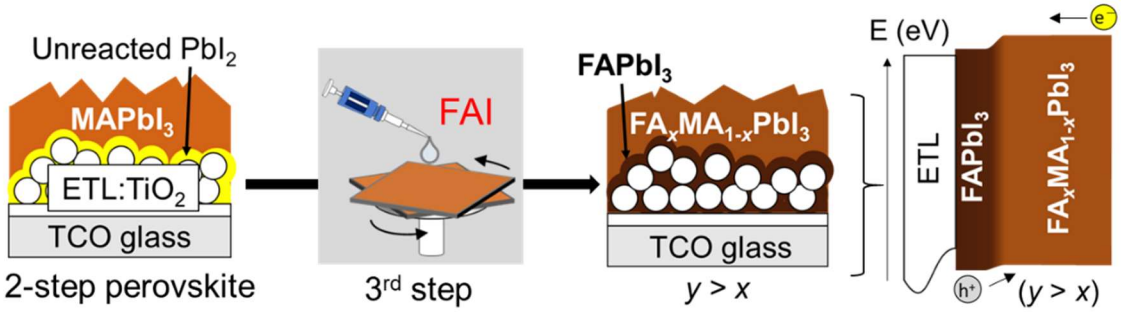

Fig. 3.1 Design concept of the formation of multiple bandgap structure at the bottom side of perovskite layer by 3-step method using additional FAI spin-coating.

3.2 Experimental

3.2.1 Preparation method of perovskite solar cell

Preparation of electron transport layer (ETL) on TCO glass

Transparent conductive oxide (TCO, Type-0052, 10 Ω/sq., Geomatec) substrates were patterned by etching with Zn powder (>96.0%, Tokyo Chemical Industry) and 1 M HCl (Wako Pure Chemical Industry). Then, the substrates were cleaned by the ultrasonication in ethanol for 5 min and dried in air. The TiO_2 compact layers were prepared by spray-pyrolysis method; a solution of titanium diisopropoxide bis(acetylacetonate) (TAA, 75 wt% in isopropanol, Sigma-Aldrich) mixed with ethanol at the volume ratio of TAA:ethanol=2:25 was sprayed on the patterned substrates at 500°C. TiO_2 mesoporous layers were then prepared by spin-coating a TiO_2 paste (18NR-T, Dyesol), diluted in ethanol at the weight ratio of TiO_2-paste:ethanol=1:5, on the substrates at 4000 rpm for 25 s and by annealing at 500°C for 30 min. In this chapter, the immersion of the substrates in $TiCl_4$ solution was skipped, since the photovoltaic performance was comparable with and without $TiCl_4$ treatment. Then, the substrates were exposed to ultraviolet light for 1 night in order to improve the contact between ETL and a PbI_2 solution in the next section (**Fig. 3.2**).

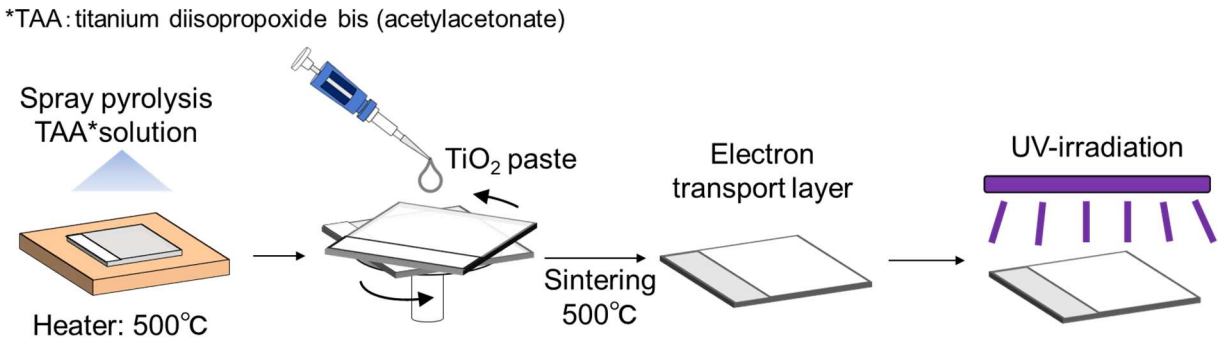

Fig. 3.2 Schematic illustration of preparation processes of electron transport layer (ETL).

Preparation of perovskite layer, hole transport layer (HTL) and metal electrodes

The perovskite layers and the hole transport layers (HTLs) were prepared in air with humidity of ~30% (**Fig. 3.3**). The TiO_2 coated substrates were pre-heated at 60°C. A 1 M PbI_2 solution (>98.0%, Tokyo Chemical Industry) in DMF (99.5%, Nacalai tesque) was also pre-heated at 60°C. The PbI_2 solution was then spin-coated on the substrates at 3000 rpm for 20 s. After annealing at 60°C for 10 min, the substrates were dipped in a 10 mg/mL solution of MAI (98%, Wako Pure Chemical Industry) dissolved in isopropanol (99.5%, Nacalai tesque) for 20 s, followed by rinsing with isopropanol and by annealing at 60°C for 10 min. Then, 20 μL of the MAI solution (0.13 M: 20 mg/mL) or FAI (≥98%, Sigma-Aldrich) solutions of three concentrations (0.06 M: 10.8 mg/mL, 0.13 M: 21.6 mg/mL and 0.19 M: 32.4 mg/mL) was dropped on the prepared $MAPbI_3$ films during the spinning at 4000 rpm.

After annealing at 60°C for 10 min, the HTLs with the thickness of ~200 nm were prepared by spin-coating a spiro-MeOTAD solution at 4000 rpm for 35 s. The spiro-MeOTAD solution in 1 mL chlorobenzene (99%, Nacalai tesque) was composed of 73 mg spiro-MeOTAD (99%, Sigma-Aldrich), 28.8 μL 4-*tert*-butylpyridine (TBP, 96.0%, Sigma-Aldrich) and 17 μL solution of [520 mg/mL lithium

bis(trifluoromethylsulphonyl)imide salt (>98.0%, Tokyo Chemical Industry) in acetonitrile (99.5%, Wako Pure Chemical Industry)]. Finally, Ag electrodes with the thickness of ~50 nm were deposited on the HTLs with a thermal evaporator under the pressure of 3×10^{-5} Torr.

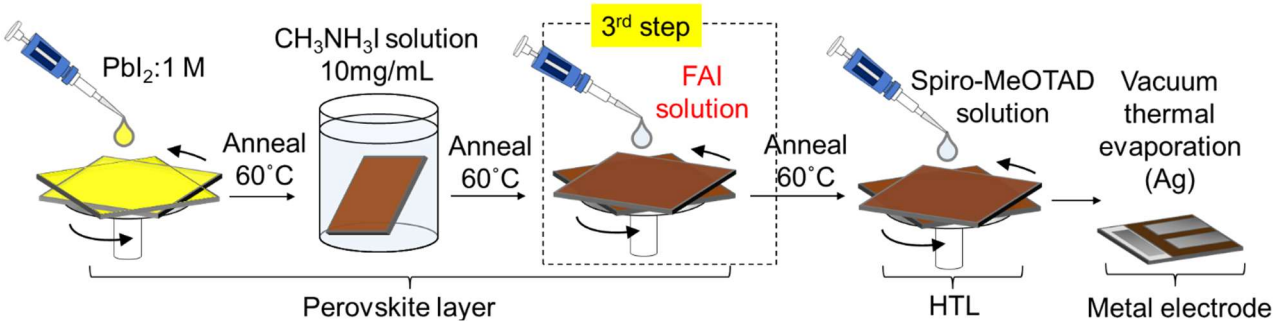

Fig. 3.3 Schematic illustration of preparation processes of perovskite layer, hole transport layer (HTL), and metal electrodes.

Hereinafter, the solar cells with 0.13 M additional MAI spin-coating will be denoted as MAI: 0.13 M and those with additional 0.06 M, 0.13 M and 0.19 M FAI spin-coating will be denoted as FAI: 0.06 M, FAI: 0.13 M and FAI: 0.19 M, respectively (**Table 3.1**).

Table 3.1 Relationship between sample names and preparation conditions in Chapter 3.

Additional spin-coating	MAI solution 0.13 M	FAI solution 0.06 M	FAI solution 0.13 M	FAI solution 0.19 M
Sample names	MAI: 0.13 M	FAI: 0.06 M	FAI: 0.13 M	FAI: 0.19 M

3.2.2 Characterizations

X-ray diffraction (XRD)

Crystal structure and phases analyses of the prepared perovskite layers was carried out by XRD (Multiflex, Cu-K_α, 40 kV and 40 mA, Rigaku). The sample was set so that the height of surface matches that of sample holder (**Fig. 2.7**).

Ultraviolet-visible absorption spectroscopy (UV-Vis)

Optical absorbance and transmittance of the prepared perovskite layers on ETLs were measured by UV-Vis (UV-1280, Shimadzu). The light was irradiated from back TCO glass side (**Fig. 2.8**). The bandgap was estimated from Tauc plots converted from the absorbance spectra.

Scanning electron microscopy (SEM)

The surface morphology and cross-section of the perovskite layers on ETLs were observed using SEM (SU-8020, Hitach High-technologies). For the cross-sectional observation, the samples were broken into two pieces by making a notch with a diamond cutter, and the fracture surface was observed (**Fig. 2.9**).

Steady-state photoluminescence (PL)

PL spectra of the prepared perovskite layers on ETLs were measured using Ramascope System1000 (Renishaw) with an excitation laser of wavelength 325 nm (IK5651R-G, Kimmon).

Current density-voltage (*J-V*) characterization

J-V characteristics were measured for the evaluation of photovoltaic performance with a DC voltage and current source/monitor (6241A, ADC Co.) and with a solar simulator (XES-40S1, SAN-EI Electric) which was calibrated to AM 1.5, 100 mW/cm^2 with a standard silicon photodiode (BS-520BK, Bunkokeiki). The voltage step and delay time were 20 mV and 50 ms, respectively. The voltage scan range was 0-1.1 V. The active area was limited to 0.084 cm^2 by using black mask. The *J-V* curves were measured by reverse (1.1 V → 0 V) and forward (0 V → 1.1 V) scans.

Incident photon-to-current conversion efficiency (IPCE)

IPCE spectra were measured in a direct current mode (SM-250, Bunkoukeiki). The IPCE is defined by the following equation (**eq. 3.1**), and it shows how efficiently the device converts the incident light into electricity at each wavelength.

$$\text{IPCE} = \frac{\text{Number of collected electrons}}{\text{Number of incident photons}} \qquad \textbf{(eq. 3.1)}$$

3.3 Results and Discussion

3.3.1. Phase and crystal structure analysis of perovskite layer

Figure 3.4 shows XRD patterns of perovskite layers on ETLs prepared by the 2-step and the 3-step methods using additional MAI or FAI spin-coating. The 2-step prepared sample had a relatively large peak of unreacted PbI_2 at 2θ = ~12.8°. For the 3-step prepared samples, the peak intensity of unreacted PbI_2 significantly decreased due to a conversion of the unreacted PbI_2 into the perovskite phase. Although the small peak of unreacted PbI_2 at ~12.8° still remained in the 3-step prepared samples, the peak intensity decreased with increasing the FAI concentration. Furthermore, the peaks for the perovskite shifted to smaller angles by the additional FAI spin-coating as seen in the enlarged XRD patterns at 13-15°, and the peak shift became larger with increasing the FAI concentration. The peak shit to the smaller angle indicates the increase of lattice constants. Since the FA^+ has larger ionic radius than MA^+ as described in Chapter 1, these results suggest that the additional FAI spin-coating yielded $FA_xMA_{1-x}PbI_3$ by partially substituting MA^+ with FA^+, and the x value in $FA_xMA_{1-x}PbI_3$ became larger with increasing the FAI concentration.

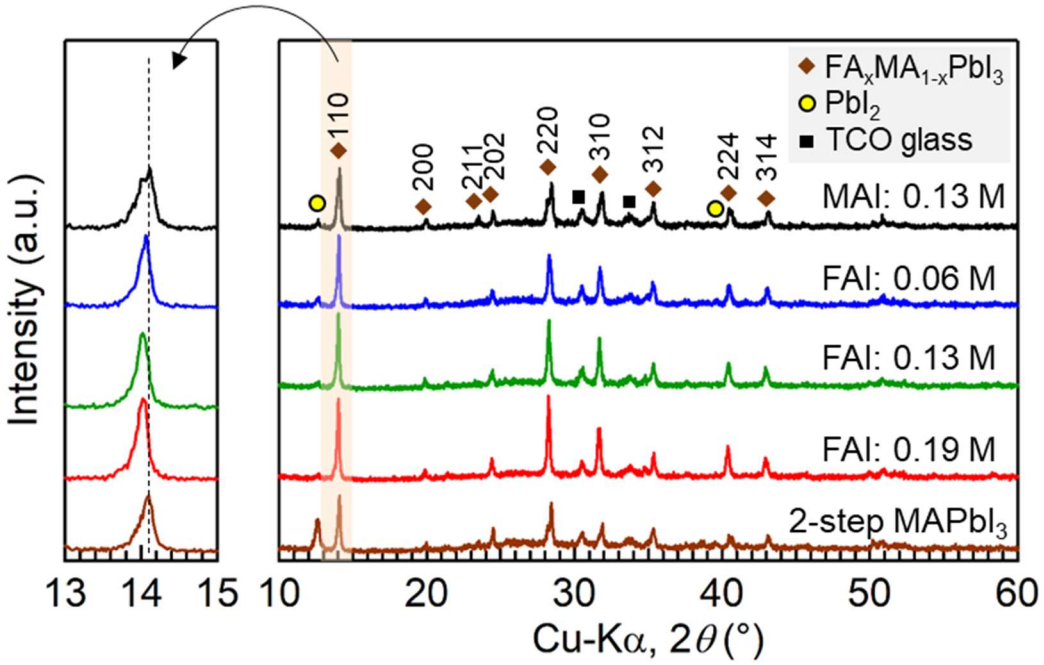

Fig. 3.4 XRD patterns of perovskite layers on ETLs prepared by the 2-step method or 3-step method using additional MAI or FAI spin-coating.

3.3.2 Optical property analysis and bandgap estimation of perovskite layer

Figure 3.5 shows the absorbance spectra of the 3-step prepared perovskite layers on ETLs. The absorption edge of MAI: 0.13 M was located at ~780 nm, and the absorption edge shifted to longer wavelength by spin-coating the FAI solutions. The bandgaps of prepared perovskite layers were estimated using Tauc plots converted from the absorption spectra as shown in **Fig. 3.6**. The estimated bandgap values are summarized in **Table 3.2**. The bandgap of MAI: 0.13 M was ~1.58 eV, which was comparable to the reported bandgap of $MAPbI_3$ (~1.55-1.6 eV) [10,11]. As for the FAI spin-coated samples, the bandgaps of FAI: 0.06 M, 0.13 M and 0.19 M were ~1.56 eV, 1.55 eV and 1.54 eV, respectively. The decrease of bandgap with increasing the FAI concentration was confirmed. These results also indicate the increase of x value in the $FA_xMA_{1-x}PbI_3$ with increasing the FAI concentration, since the bandgap of α-$FAPbI_3$ (~1.47 eV [12]) is smaller than that of $MAPbI_3$.

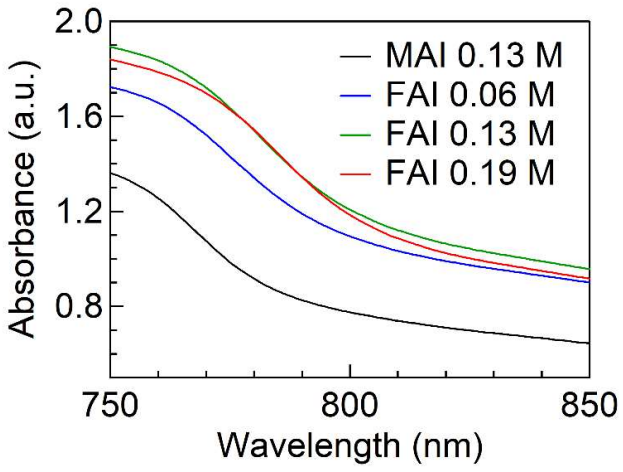

Fig. 3.5 Absorbance spectra of the 3-step prepared perovskite layers.

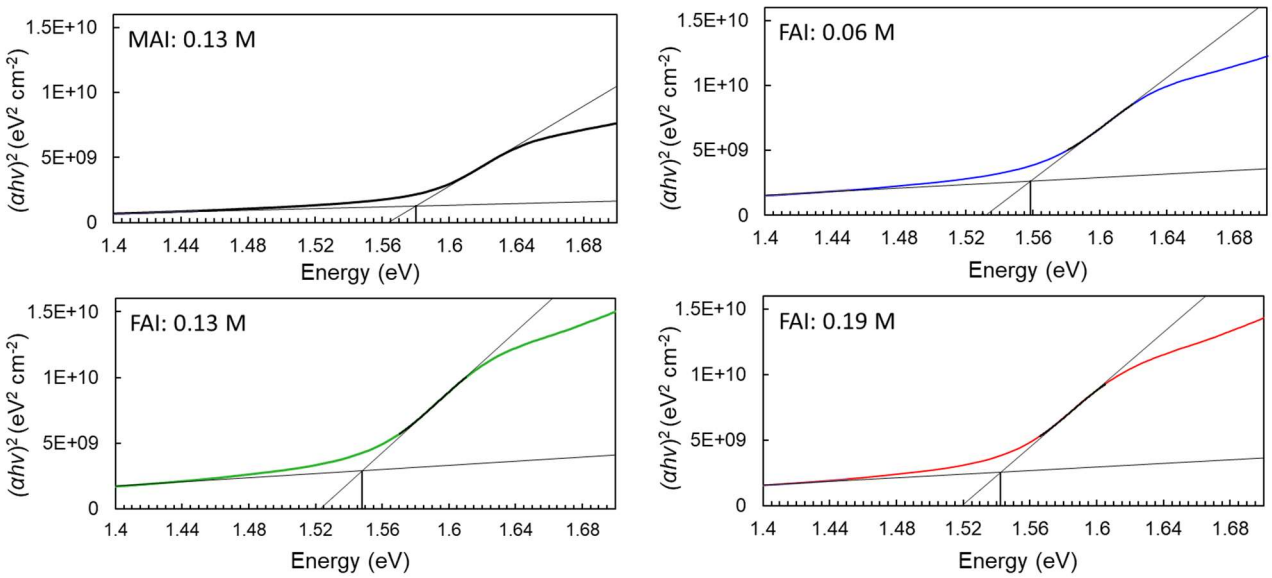

Fig. 3.6 Tauc plots converted from the absorbance spectra of the prepared perovskite layers on ETLs.

Table 3.2 Estimated bandgap values from the Tauc plots of prepared perovskite layers on ETLs.

Samples	E_g (eV)
MAI: 0.13 M	1.58
FAI: 0.06 M	1.56
FAI: 0.13 M	1.55
FAI: 0.19 M	1.54

Figure 3.7 shows the transmittance spectra of the 3-step prepared perovskite layers on ETLs. The transmittance of the additionally FAI spin-coated perovskite layers were smaller than that of MAI: 0.13 M at the wavelength > 650 nm, which indicates the better light absorption.

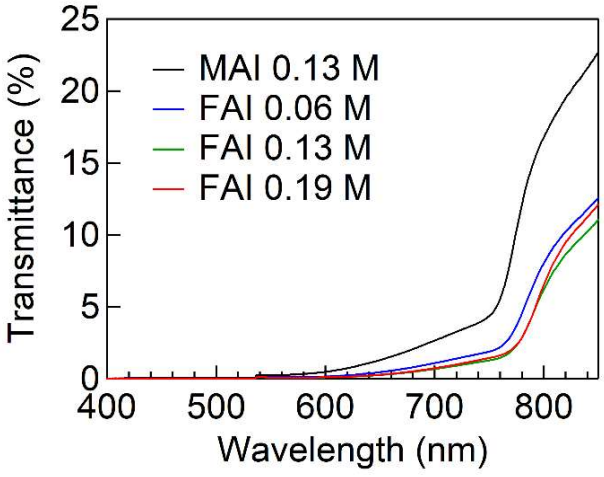

Fig. 3.7 Transmittance spectra of the 3-step prepared perovskite layers.

3.3.3 Microstructure observation of perovskite layer

Figures 3.8(a)-(d) show surface SEM images of the 3-step prepared layers on ETLs. The size of perovskite particle was comparable in all the samples with the diameter of ~0.5-1 μm. As observed in Chapter 2, some bridge-like networks between perovskite particles were observed in MAI: 0.13 M, which can be formed by the surface dissolution of perovskite particles during the additional spin-coating, i.e., liquid-phase assisted grain growth (see also **Fig. 3.9** as enlargement). On the other hand, the bridge-like networks were not frequently observed in the additionally FAI spin-coated samples. Instead, the grain boundaries became unclear (i.e. intergranular voids were filled) and small pores at the surface of perovskite particles were observed, especially in FAI: 0.19 M. These morphological changes for the FAI samples are also attributable to the surface dissolution of perovskite particle although the morphology was slightly different from additionally MAI spin-coated case.

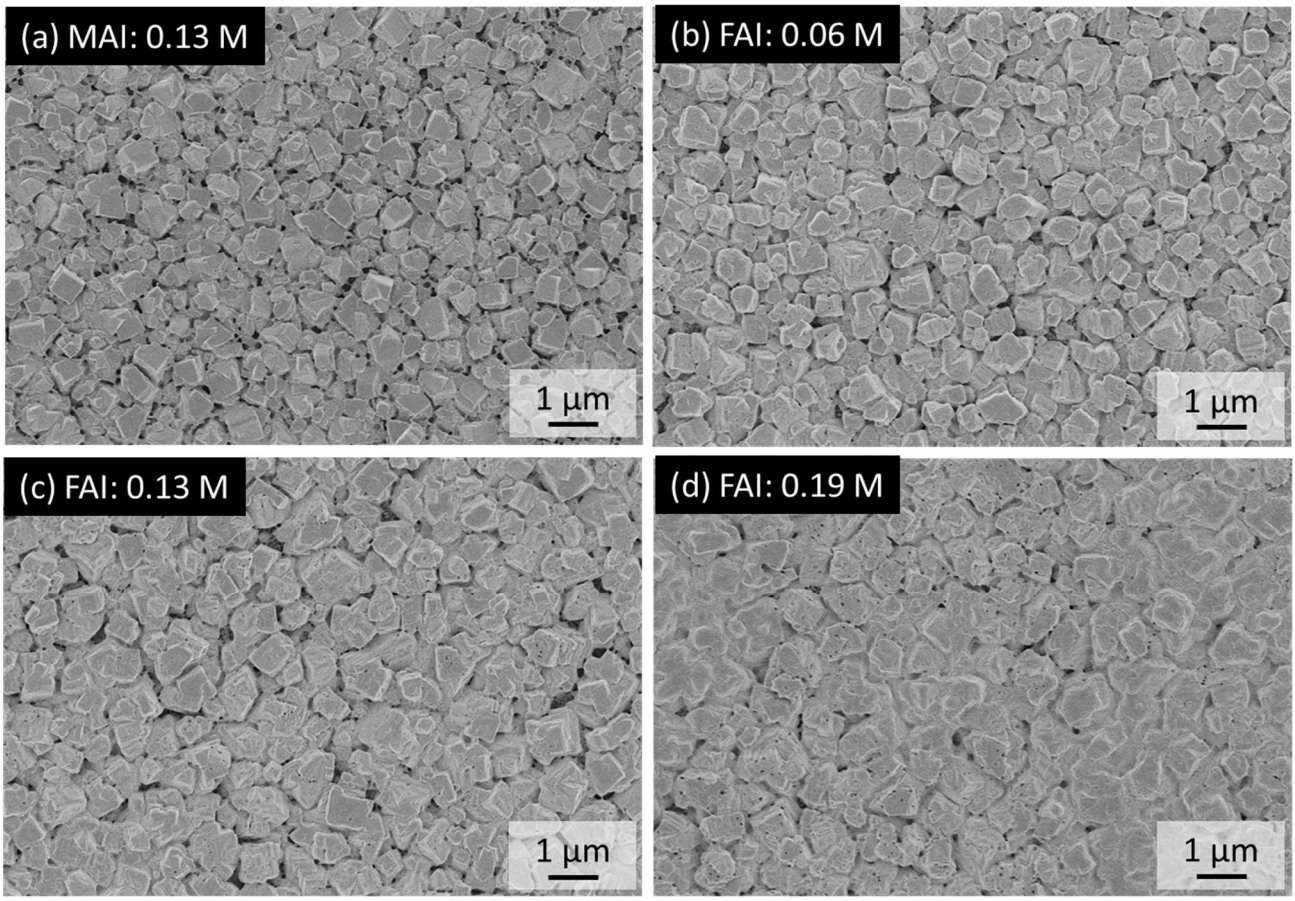

Figs. 3.8 Surface SEM images of the prepared perovskite layers for (a) MAI: 0.13 M, (b) FAI: 0.06 M, (c) FAI: 0.13 M and (d) FAI: 0.19 M.

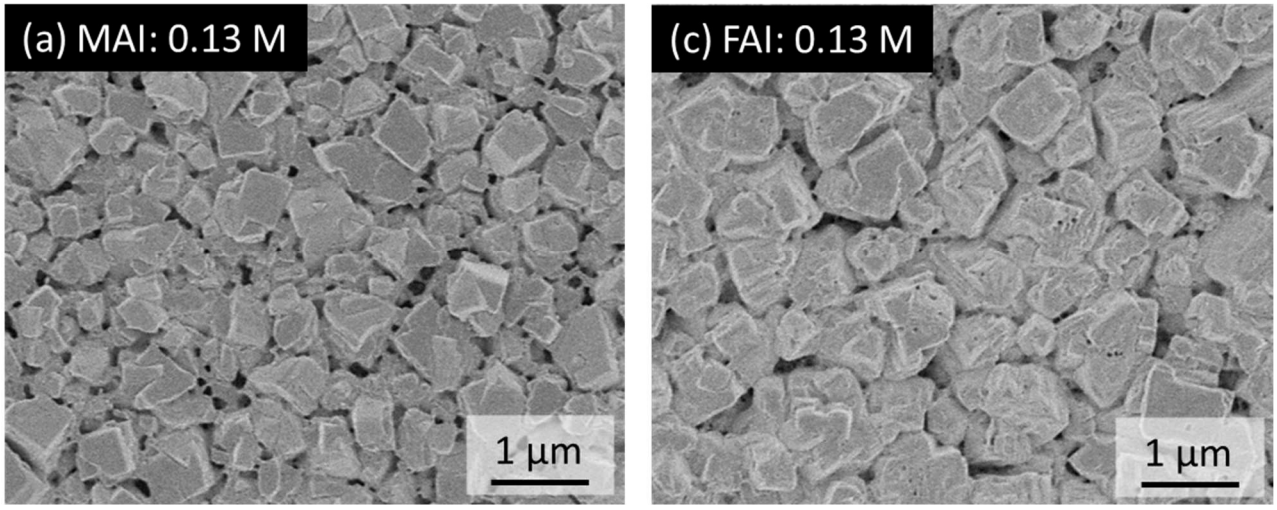

Figs. 3.9 Enlarged surface SEM images of the (a) MAI: 0.13 M and (c) FAI: 0.13 M.

Figures 3.10(a)-(d) show cross-sectional SEM images of the 3-step prepared perovskite layers on ETLs. All the samples had comparable thickness consisted of the TiO_2 compact layer (~30 nm), TiO_2 mesoporous/perovskite layer (total: ~150 nm) and the perovskite capping layer (~400 nm). The grain boundary became unclear with increasing the FAI concentration (**Figs. 3.10(b)-(d)**), which is in good agreement with the surface SEM images.

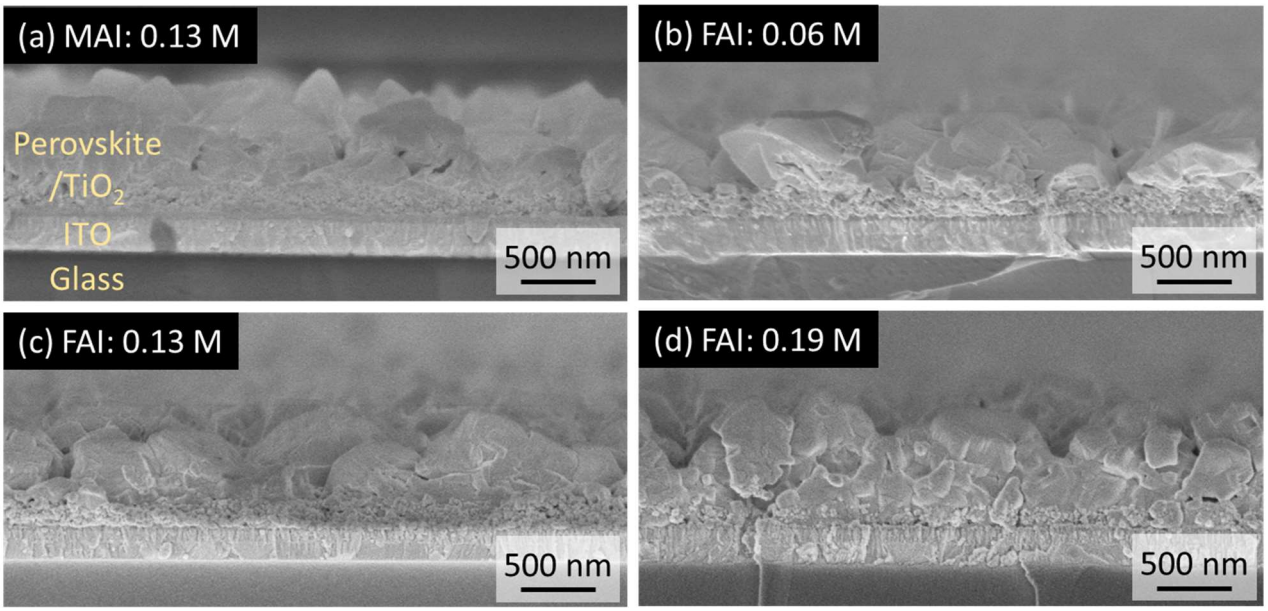

Figs. 3.10 Cross-sectional SEM images of the prepared perovskite layers for (a) MAI: 0.13 M, (b) FAI: 0.06 M, (c) FAI: 0.13 M and (d) FAI: 0.19 M.

3.3.4 Detection of multiple bandgap structure

Then, the detection of multiple bandgap structure was carried out. The unreacted PbI_2 was reported to exist mainly near the ETL [8,9]. Since the conversion of unreacted PbI_2 into the perovskite phase was confirmed by XRD analysis (**Fig. 3.4**), there must be the FA rich perovskite layer near the ETL. This layer should produce the bandgap gradient as illustrated in **Fig. 3.1,** which may result in the multiple bandgap structure. If the multiple layers were formed in the perovskite layer, the double peaks or double band edges may be confirmed in XRD pattern or absorbance spectrum. However, those differences were not confirmed from **Figs. 3.4 and 3.5** possibly due to the too thin thickness and small volume of the FA rich layer.

To detect the "XRD and UV-Vis-invisible" multiple layered structure, the PL measurements from the top and back substrate sides were carried out. He-Cd laser with the wavelength of 325 nm was used to excite the perovskite layer. A commercial slide glass plate (No. 10005000, Marienfeld) was used as the substrate for the sample to avoid the absorption of the laser by the TCO layer (**Fig. 3.11**). The penetration depth of the laser in the (FA,MA)PbI_3 layer was estimated to be ~25-50 nm from inverses of absorption coefficients of $MAPbI_3$ and $FAPbI_3$ at the wavelength of 325 nm (α = ~2-4×10^7 m^{-1}) [13,14], which is sufficiently thin to evaluate the expected FA rich layer.

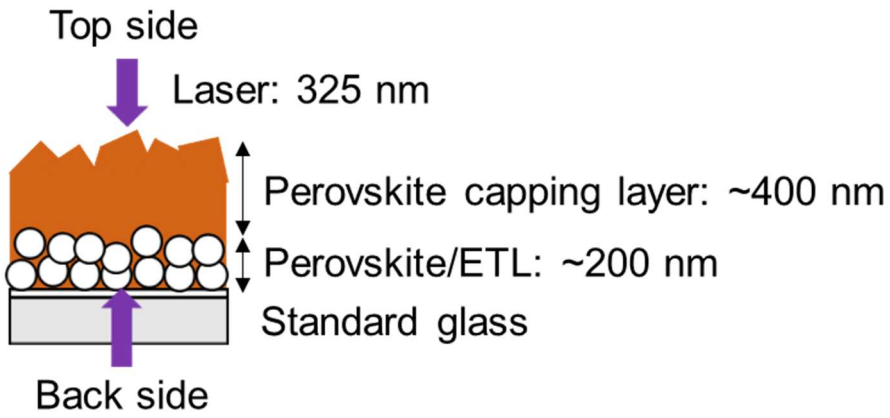

Fig. 3.11 Schematic illustration of the PL measurement for the prepared perovskite layers on ETLs.

Figure 3.12 shows the normalized PL spectra of perovskite layers on ETLs for MAI: 0.13 M and FAI: 0.06, 0.13, 0.19 M. When the laser was irradiated from the top side, MAI: 0.13 M showed the band to band transition PL peak at ~774 nm, and the peak position shifted to longer wavelength with increasing the FAI concentration in the spin-coated solution. FAI: 0.19 M showed the peak at ~792 nm. The peak shift to longer wavelength indicates the decrease of bandgap by the additional FAI spin-coating, and the tendency is in good agreement with the results of absorbance (**Fig. 3.5**). When the laser was irradiated from the back-substrate side, MAI: 0.13 M showed the peak at the comparable position to that measured from top side. On the other hand, the additionally FAI spin-coated samples showed peak shifts to longer wavelength compared with the peaks measured from top side, i.e. smaller bandgap. In addition, the peak shift became larger with increasing the FAI concentration of the spin-coated solution.

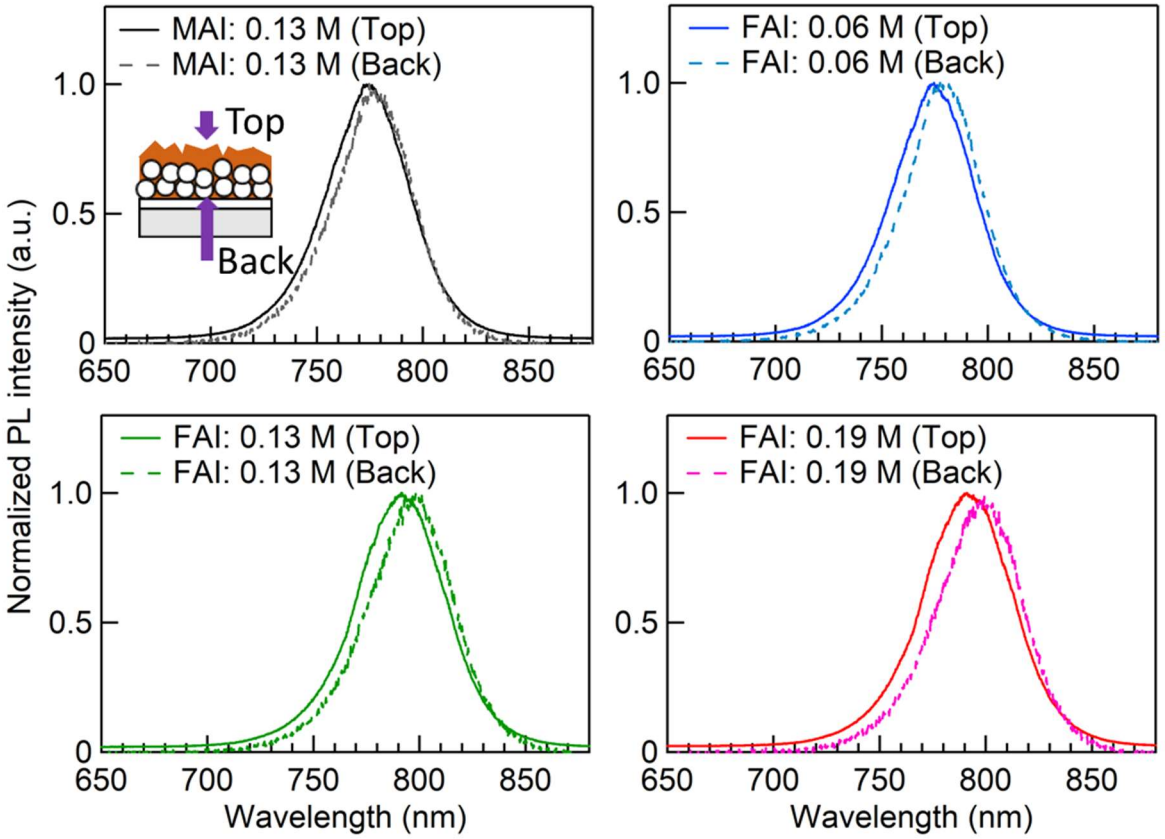

Fig. 3.12 PL spectra measured from perovskite top side and back substrate side for the 3-step prepared perovskite layers on ETLs.

These results strongly suggest that the additionally FAI spin-coated samples are composed of a FA-poor $FA_xMA_{1-x}PbI_3$ layer with the larger bandgap and a FA-rich $FA_yMA_{1-y}PbI_3$ ($y > x$) layer with the smaller bandgap at the bottom side (near the ETL) as shown in **Fig. 3.13**. Also, the bandgap difference became larger with increasing the FAI concentration in the spin-coating solution. It was expected that the pure $FAPbI_3$ would be formed near the ETL from the reaction of unreacted PbI_2 and FAI. However, considering the bandgap value, the obtained FA rich layer must contain MA^+ in the composition ($FA_yMA_{1-y}PbI_3$) possibly due to the diffusion of MA^+ during the reaction between FAI and unreacted PbI_2. This multiple bandgap structure at the bottom side must be effective to suppress the carrier recombination and to improve the solar cell performance, similarly to the bandgap gradient structures reported in the literatures [5,6].

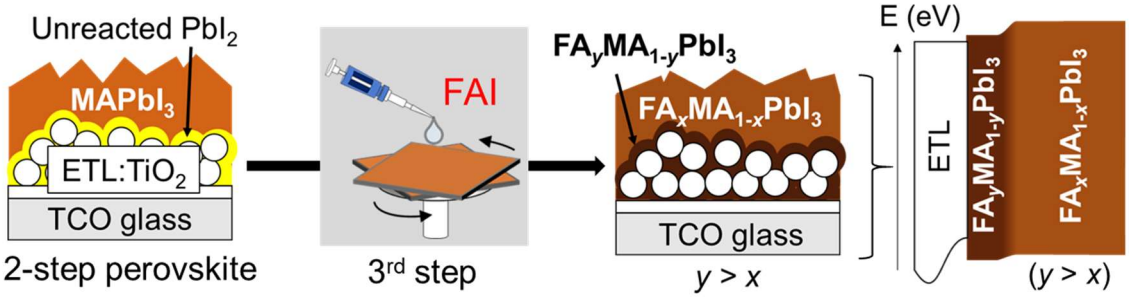

Fig. 3.13 Schematic illustration of the estimated structure of the perovskite layer for FAI: 0.19 M.

3.3.5 Evaluation of photovoltaic performance

Figure 3.14 and **Table 3.3** show *J-V* curves and characteristics of the 3-step prepared perovskite solar cells (reverse scan), respectively. The values in the table are average of 10 cells for FAI: 0.19 M and of 15 cells for others. Firstly, the differences between MAI: 0.13 M and FAI: 0.13 M are discussed to investigate the effect of FAI spin-coating. MAI: 0.13 M showed *J*sc of 23.5 mA/cm^2, *V*oc of 0.97 V, *FF* of 0.71 and PCE of 16.3%, whereas FAI: 0.13 M had *J*sc of 24.1 mA/cm^2, V_{OC} of 0.96 V, *FF* of 0.73 and PCE of 16.8%. Therefore, FAI: 0.13 M showed 0.5 point (3.1%) higher efficiency than MAI: 0.13 M.

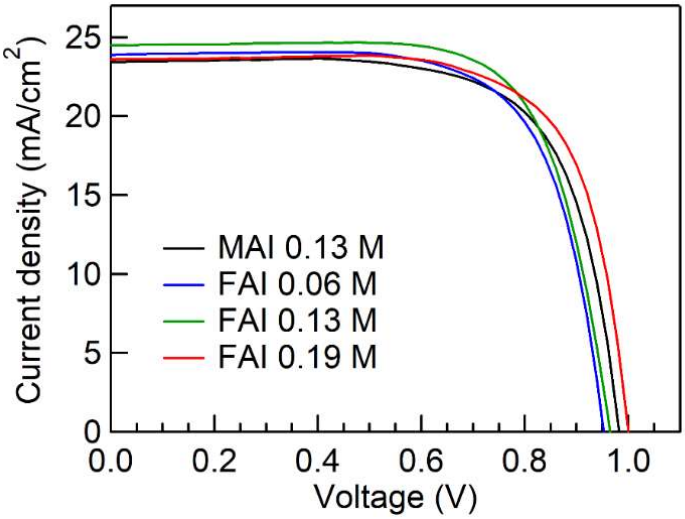

Fig. 3.14 *J-V* curves of the 3-step prepared perovskite solar cells (back scan).

Table 3.3 *J-V* characteristics of the 3-step prepared perovskite solar cells (reverse scan). The values are average of 10 cells for FAI: 0.19 M and 15 cells for others.

Samples	J_{SC} (mA/cm^2)	V_{OC} (V)	*FF*	PCE (%)
MAI: 0.13 M	23.5	0.97	0.71	16.3
FAI: 0.06 M	23.4	0.95	0.70	15.5
FAI: 0.13 M	24.1	0.96	0.73	16.8
FAI: 0.19 M	23.5	0.99	0.73	17.0

To clarify the reason of J_{SC} improvement for FAI: 0.13 M, IPCE spectra were measured as shown in **Fig. 3.15**. The IPCE spectrum of FAI: 0.13 M was shifted to longer wavelength than that of MAI: 0.13 M due to the red shift of absorption edge. Since the IPCE values at the wavelength $\lambda <$ ~750 nm were comparable between MAI: 0.13 M and FAI: 0.13 M, the enlarged light absorbing wavelength by the smaller bandgap is reason for the enhanced *J*sc. The slight decrease of V_{OC} in FAI: 0.13 M is also ascribed to its smaller bandgap, since the V_{OC} and bandgap generally have a positive correlation as mentioned in Chapter 2. However, the decrease of V_{OC} by the decreased bandgap may be suppressed by the multiple bandgap structure.

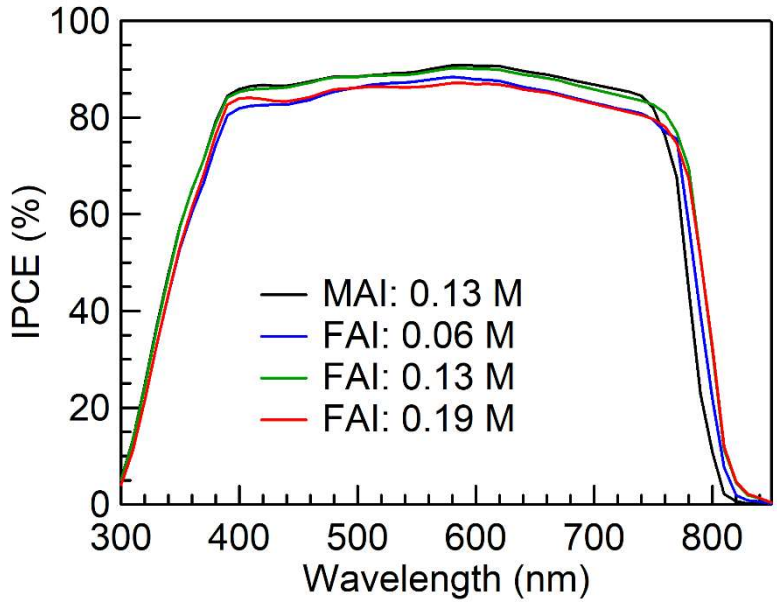

Fig. 3.15 IPCE spectra of the 3-step prepared perovskite solar cells.

In this study, the bandgap difference of the perovskite layer for MAI: 0.13 M and FAI: 0.13 M was ~0.03 eV, and the V_{OC} difference was 0.01 V. This decreasing amount of V_{OC} is smaller than some reported values. For example, Zhao et al. [15] prepared the $FA_xMA_{1-x}PbI_3$ based perovskite solar cells by 1-step method without the multiple bandgap structure. In their case, $FA_xMA_{1-x}PbI_3$ based samples with the ~0.03 eV smaller bandgap showed ~0.03 V smaller V_{OC} than that of $MAPbI_3$ based sample. In addition, Salado et al. [16] also reported the larger decrease of V_{OC} than that of this study. This suppression of the V_{OC} decrease is attributable to the multiple bandgap structure, since the multiple bandgap structure generally has an effect of V_{OC} enhancement by suppressing the carrier recombination.

Then, the effects of FAI concentration on the photovoltaic performance are discussed. As for the *J*sc, it increased from 23.4 mA/cm^2 to 24.1 mA/cm^2, and then decreased to 23.5 mA/cm^2 by increasing the FAI concentration from 0.06 M to 0.13 M and 0.19 M (**Table 3.3**). The increase in J_{SC} from FAI: 0.06 M to 0.13 M is attributable to the better conversion of the unreacted PbI_2 into perovskite, which enhanced the light absorption. While, the decrease in J_{SC} from FAI: 0.13 M to 0.19 M may be attributable to the excess FAI which remained at the grain boundaries and surfaces of the perovskite layer. Indeed, the IPCE spectrum of FAI: 0.19 M was smaller than that of FAI: 0.13 M in spite of their comparable transmittance spectra. As for the effect of FAI concentration on V_{OC}, it increased from 0.95 V to 0.96 V, and again increased to 0.99 V by increasing the FAI concentration from 0.06 M to 0.13 M and 0.19 M (**Table 3.3**), despite the decreased bandgaps (~1.56 eV, 1.55 eV and 1.54 eV). This V_{OC} enhancement can be attributed to (1) the decrease of unreacted PbI_2, (2) the decrease of grain boundary, and (3) the suppression of carrier recombination by the multiple bandgap structure.

Some of the prepared solar cells showed an abnormal behavior, i.e., current drop around J_{SC}, especially for FAI: 0.19 M, as shown in **Fig. 3.16**. The *J*-*V* characteristics of these samples were not included in the averaged photovoltaic performance in **Table 3.3** because their *FF* values must be incorrect. Since the behavior

was observed more frequently in the samples with the spin-coating of higher concentrated FAI solution (FAI: 0.19 M), it may be ascribed to the excess FAI on the perovskite layer.

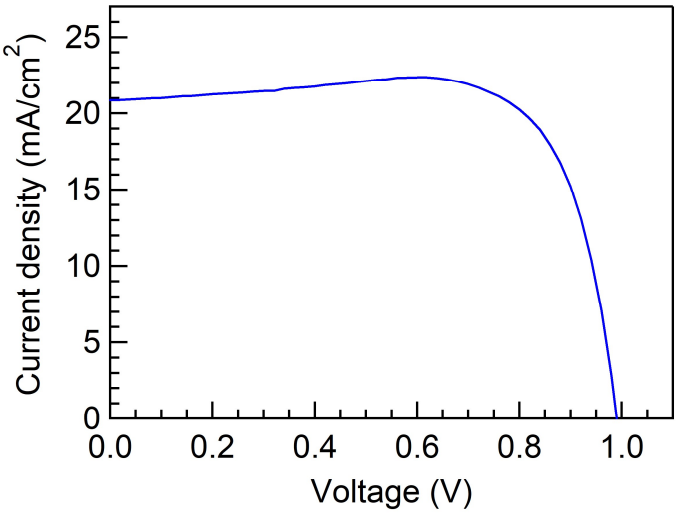

Fig. 3.16 *J-V* curve of the perovskite solar cell with an abnormal current drop near the J_{SC}.

To verify the assumption, the atomic ratio of iodide (I) and lead (Pb) at the surface of perovskite layer ($FA_xMA_{1-x}PbI_3$) was measured by energy dispersive X-ray spectrometry (EDS). If the excess FAI ($HC(NH_2)_2I$) exists on the surface of $FA_xMA_{1-x}PbI_3$, the atomic ratio of iodide will increase and that of lead will decrease. **Figure 3.17** shows atomic ratios of iodide and lead at the surface of the additionally FAI spin-coated perovskite layers. Actually, the atomic ratio of iodide increased and that of lead decreased with increasing the FAI concentration. This result supports the assumption of the excess FAI on the perovskite layer. To remove the excess FAI, the FAI: 0.19 M sample was rinsed with isopropanol (IPA) and annealed for 10 min after the additional spin-coating process (**Fig. 3.18**). With the IPA rinsing, the atomic ratio of iodide became smaller, which suggests the removal of the excess FAI.

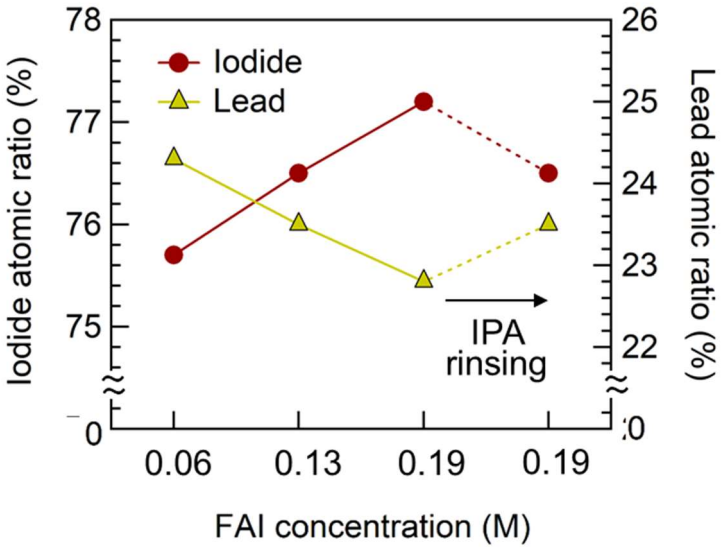

Fig. 3.17 Atomic ratios of iodide and lead at the surface of the perovskite layers for the additionally FAI spin-coated samples.

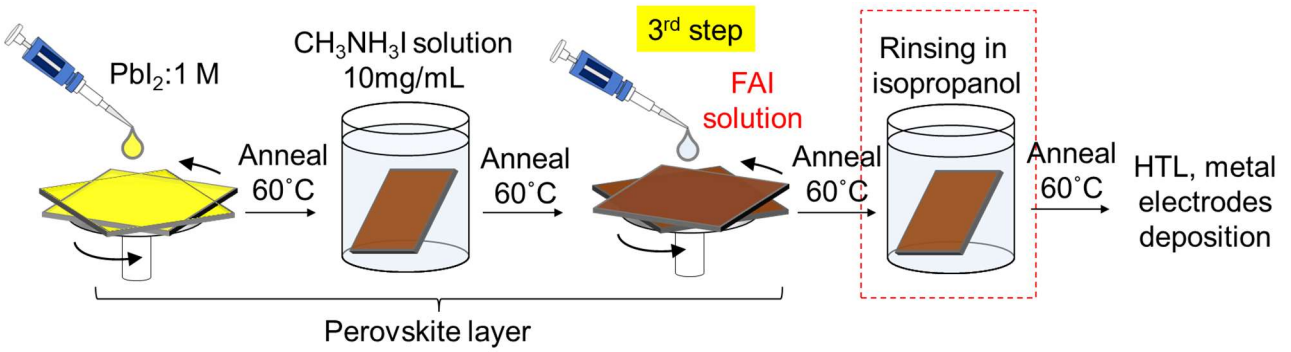

Fig. 3.18 Isopropanol rinsing process for the removal of excess FAI on the perovskite layer.

The *J-V* characteristics (reverse scan, average of 15 devices) of the FAI: 0.19 M with IPA rinsing are summarized in **Table 3.4**. Although the V_{OC} slightly decreased compared to that without IPA rinsing, the J_{SC} increased up to 24.4 mA/cm^2, and the largest PCE (average) of 17.2% was obtained. In addition, the current drop behavior around J_{SC} was hardly observed for the IPA-rinsed samples. From these results, the decrease of J_{SC} from FAI: 0.13 M to 0.19 M samples (**Table 3.3)** and the abnormal current drop are due to the excess FAI on the perovskite layer. **Figure 3.19** shows the *J-V* curve and characteristics of the best performance cell (reverse scan, non-average) with the maximum PCE of 18.1%.

Table 3.4 *J-V* characteristics (reverse scan) of FAI: 0.19 M with isopropanol rinsing and 10 min annealing after the additional spin-coating process. The values are average of 15 cells.

Sample	J_{SC} (mA/cm^2)	V_{OC} (V)	*FF*	PCE (%)
FAI: 0.19 M with IPA rinsing	24.4	0.97	0.73	17.2

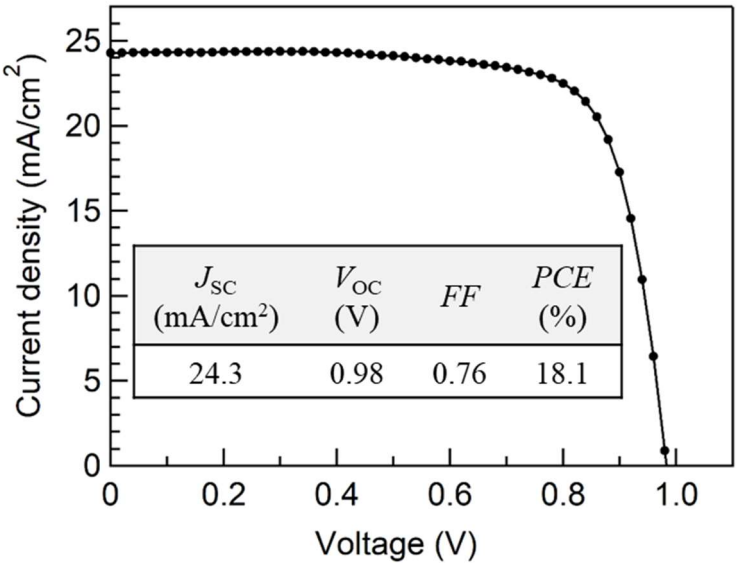

Fig. 3.19 *J-V* curve and characteristics (reverse scan) of the best performance cell: FAI: 0.19 M with isopropanol rinsing and 10 min annealing after the additional spin-coating.

3.3.6 Effects of annealing temperature and contact time of FAI solution

Effects of annealing temperature after the additional spin-coating

The annealing temperature of ~150-170°C is generally used to prepared a pure $FAPbI_3$ perovskite layer, because δ-$FAPbI_3$ (non-perovskite phase, yellow) turns to α-$FAPbI_3$ (perovskite phase, black) at the temperature range [17,18]. Hence, effects of annealing temperature after the additional spin-coating was investigated (**Fig. 3.20**).

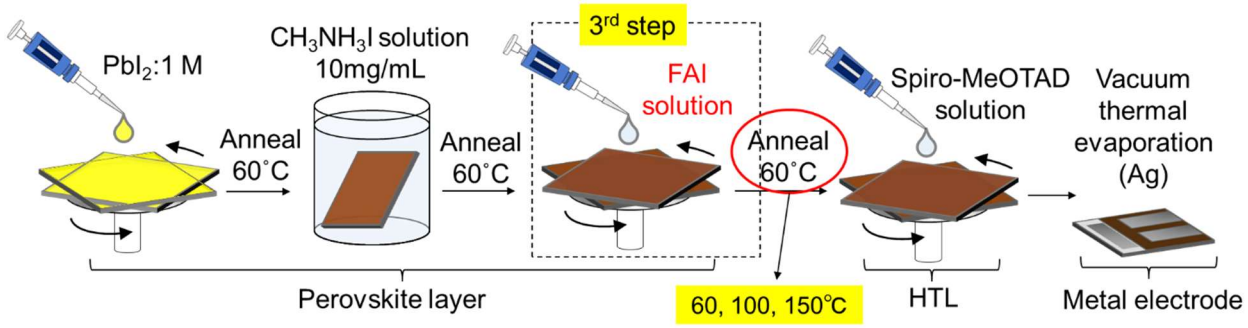

Fig. 3.20 Investigation of effects of annealing temperature after the additional spin-coating.

Figure 3.21 shows the box plots of *J-V* characteristics (reverse scan) for FAI: 0.13 M annealed at 60, 100 and 150°C. The 14-15 cells were prepared to make the plots. The cells annealed at 100°C showed comparable J_{SC} and V_{OC} to the cells annealed at 60°C. However, the PCE was slightly smaller due to the decrease of *FF*. When the annealing temperature increased up to 150°C, all the parameters significantly decreased and the scatterings became large. These results indicate that the 60°C is the best annealing temperature in this study, which is a different tendency from pure $FAPbI_3$ based perovskite solar cells.

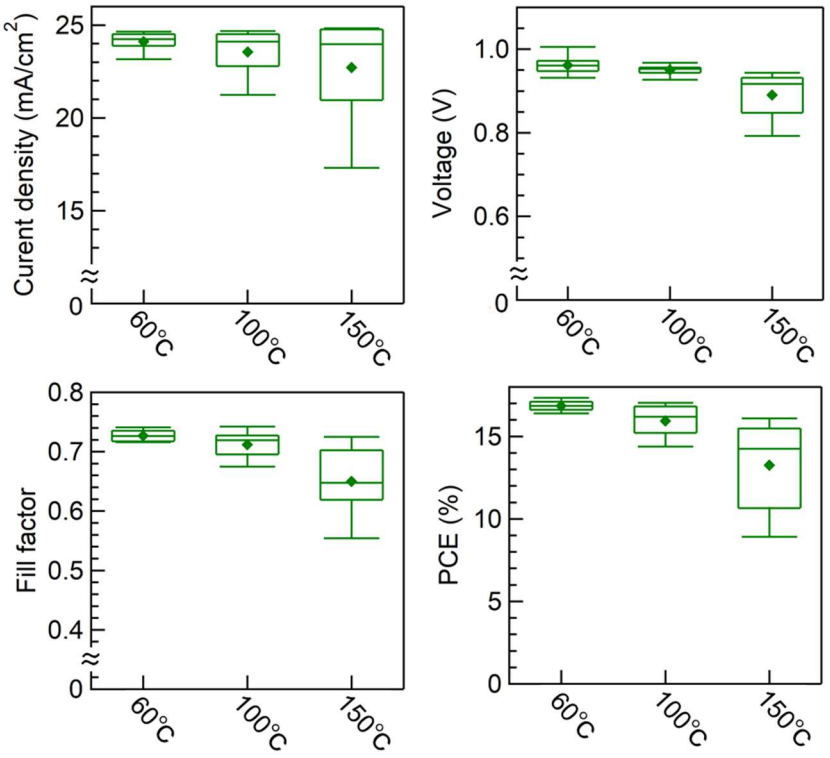

Fig. 3.21 Box plots of *J-V* characteristics for FAI: 0.13 M annealed at 60, 100 and 150°C. The 14-15 cells were prepared. In the box plot, center dots and horizontal lines represent average and median values.

As described in sections 3.3.1 and 3.3.2, the additionally FAI spin-coated perovskite layers were composed of $FA_xMA_{1-x}PbI_3$. The x value must be smaller than 0.5 considering their bandgaps, which means that the characteristics of the FAI spin-coated perovskite layers were closer not to $FAPbI_3$ but to $MAPbI_3$. $MAPbI_3$ is reported to be decomposed by annealing at ~120-160°C [19,20]. In addition, significant decrease of the *J-V* characteristics and an increase of PbI_2 peak intensity in XRD were confirmed for MAI: 0.13 M by annealing at 150°C as shown in **Figs. 3.22** and **3.23(a)**. Since the increase of PbI_2 peak intensity by the annealing is also confirmed in FAI: 0.13 M as shown in **Fig. 3.23(b)**, the different characteristics of the FAI spin-coated cells from the pure $FAPbI_3$ based perovskite solar cell is attributable to the composition difference.

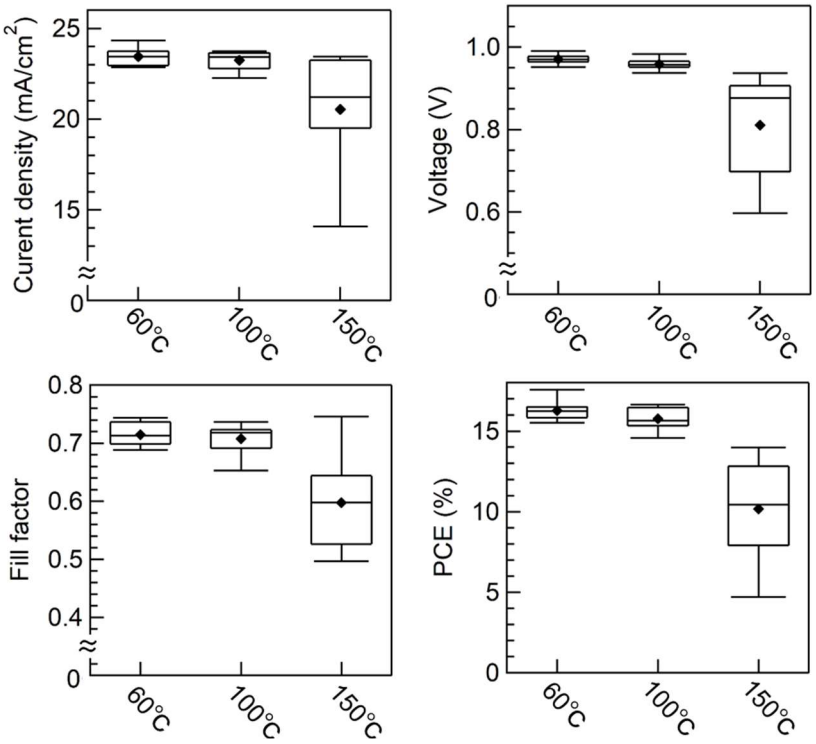

Fig. 3.22 Box plots of *J-V* characteristics of MAI: 0.13 M annealed at 60, 100 and 150°C. The 12-15 cells were prepared. In the box plot, center dots and horizontal lines represent average and median values.

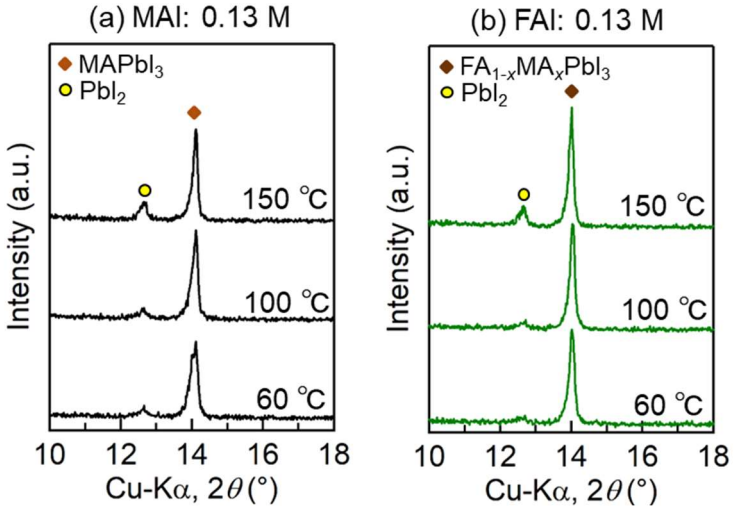

Figs. 3.23 XRD patterns of perovskite layers for (a) MAI: 0.13 M and (b) FAI: 0.13 M annealed at 60, 100 and 150°C.

Effect of contact time between perovskite layer and FAI solution

Then, the effect of contact time of perovskite layer and FAI solution was investigated. The FAI or MAI solution was dropped during the spinning of sample (waiting time 0 s). However, in this section, the solution was firstly dropped on the 2-step prepared sample, and the sample was spun after the waiting time of 5, 10, or 20 s. For the former case (waiting time 0 s), the solution was dropped without cooling of the sample to room temperature after the annealing at 60°C, but for the latter case, the solution was dropped after cooling of sample temperature to room temperature. **Table 3.5** shows the *J-V* characteristics (back scan) of the prepared cells with and without the waiting time. The values are average of 2 cells.

J_{SC}, V_{OC}, and *FF* increased with the waiting time of 5 and 10 s compared with those without the waiting time, which resulted in enhanced PCE of 18.6% and 19.0%. However, those parameters decreased by increasing the waiting time up to 20 s. These results indicate that the appropriate waiting time is effective to improve the photovoltaic performance. Since the waiting time of 10 s was easier to handle and demonstrated the highest PCE, this preparation condition will be used in the next chapter.

Table 3.5 *J-V* characteristics (reverse scan) of FAI: 0.19 M with and without waiting time after dropping the FAI: 0.19 M solution on the 2-step prepared perovskite layers. The values are average of 2 cells.

Waiting time (s)	J_{SC} (mA/cm^2)	V_{OC} (V)	*FF*	PCE (%)
0	24.4	1.00	0.73	17.7
5	25.0	1.01	0.74	18.6
10	24.9	1.02	0.75	19.0
20	24.3	1.00	0.71	17.2

Fig. 3.24 shows the surface SEM images of the perovskite layer with the waiting time of 0 and 10 s. The size of perovskite particle became larger with the waiting time of 10 s possibly due to the grain growth during the waiting time. This increase of particle size can result in the enhanced photovoltaic performance.

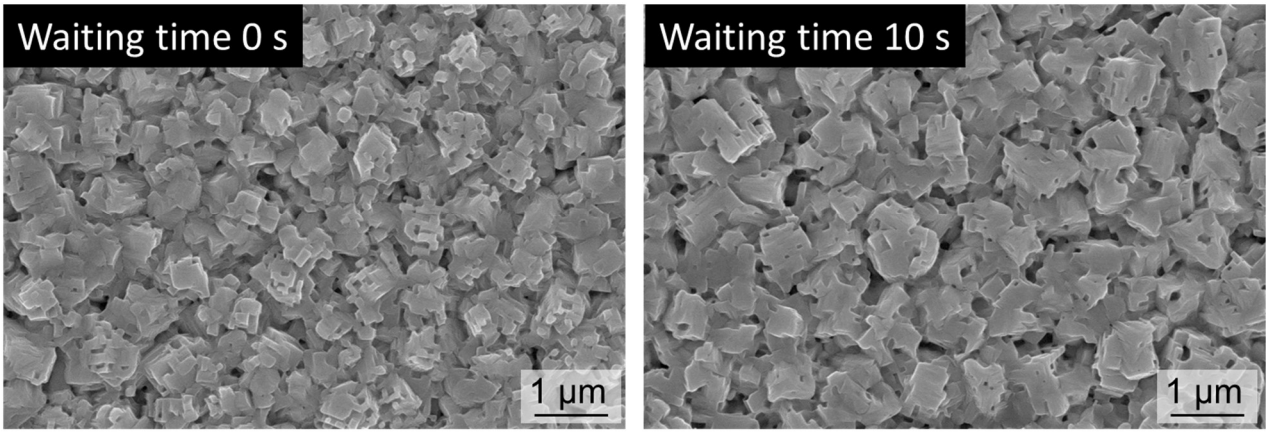

Fig. 3.24 Surface SEM images of the prepared perovskite layers on ETLs with waiting time of 0 or 10 s after dropping the FAI: 0.19 M solution on the 2-step prepared perovskite layers.

3.4 Conclusions

In this chapter, the bandgap gradient was formed at the bottom side of the perovskite layer (multiple bandgap structure) by the 3-step method using additional FAI spin-coating. In conclusions:

(1) The additional FAI spin-coating shrank the bandgap of perovskite layer due to the formation of $FA_xMA_{1-x}PbI_3$ by substituting MA^+ with FA^+. Moreover, the layered structure with different FA concentrations was formed by converting the unreacted PbI_2 into FA rich $FA_yMA_{1-y}PbI_3$ ($y > x$) (bandgap gradient), which resulted in the multiple bandgap structure at the bottom side (near the ETL).

(2) The 3-step prepared cells with the FAI spin-coating (FAI: 0.13 M) had larger J_{SC} (24.1 mA/cm^2) and slightly smaller V_{OC} (962 mV) compared to the additionally MAI spin-coated cell (MAI: 0.13 M), due to the smaller bandgap of FAI spin-coated cells. However, the decrease of V_{OC} was suppressed possibly by the multiple bandgap structure. As a result, the larger PCEs (average) of 16.8% was obtained for FAI: 0.13 M (16.3% for MAI: 0.13 M).

(3) The increase of FAI concentration in the spin-coated solution was effective to increase J_{SC} due to the effective PbI_2 conversion and decrease of bandgap. In addition, it also improved V_{OC} possibly due to the decrease of unreacted PbI_2, decrease of grain boundary, and suppression of carrier recombination by the multiple bandgap structure. The best PCE (average) of 17.2% was achieved for FAI: 0.19 M.

The additional FAI spin-coating on the 2-step prepared perovskite layer can produce the multiple bandgap structure at the bottom side, and it is effective to enhance the photovoltaic performance.

Most part of this chapter has been published in *ACS Appl. Energy Mater.*, **1**, 1389−1394 (2018). https://doi.org/10.1021/acsaem.8b00178 [21]

References

[1] Y. Okamoto, Y. Suzuki, Perovskite-type $SrTiO_3$, $CaTiO_3$ and $BaTiO_3$ porous film electrodes for dye-sensitized solar cells, *J. Ceram. Soc. Jpn*., **122**, 728–731 (2014).

[2] Y. Okamoto, Y. Suzuki, Double-layer dye-sensitized solar cells using $SrTiO_3$ and $BaTiO_3$ second layer with enhanced photovoltaic performance, *J. Ceram. Soc. Jpn*., **123**, 967-971 (2015).

[3] Y. Okamoto, Y. Suzuki, Mesoporous $BaTiO_3/TiO_2$ double layer for electron transport in perovskite solar cells, *J. Phys. Chem. C,* **120**, 13995−14000 (2016).

[4] Y. Okamoto, R. Fukui, M. Fukuzawa, Y. Suzuki, $SrTiO_3/TiO_2$ composite electron transport layer for perovskite solar cells *Mater. Lett.*, **187**, 111-113 (2017).

[5] M. C. Kim, B. J. Kim, D.Y. Son, N. G. Park, H. S. Jung, M. Choi, Observation of enhanced hole extraction in Br concentration gradient perovskite materials, *Nano Lett*. **16**, 5756-5763 (2016).

[6] K. T. Cho, S. Paek, G. Grancini, C. Roldán-Carmona, P. Gao, Y. Lee, M. K. Nazeeruddin, Highly efficient perovskite solar cells with a compositionally engineered perovskite/hole transporting material interface, *Energy Environ. Sci*. **10**, 621–627 (2017).

[7] Y. Okamoto, Y. Suzuki, Perovskite solar cells prepared by a new 3-step method including a PbI_2 scavenging step, *Mater. Sci. Semicond. Process*., **71**, 1-6 (2017).

[8] S. Y. Kim, H. J. Jo, S. J. Sung, D. H. Kim, Perspective: Understanding of ripening growth model for minimum residual PbI_2 and its limitation in the planar perovskite solar cells, *APL Mater.,* **4**, 100901 (2016).

[9] A. Ummadisingu, M. Grätzel, Revealing the detailed path of sequential deposition for metal halide perovskite formation, *Sci. Adv.* **4**, e1701402 (2018).

[10] H. S. Kim, C. R. Lee, J. H. Im, K.B. Lee, T. Moehl, A. Marchioro, S. J. Moon, R. Humphry-Baker, J. H. Yum, J. E. Moser, M. Grätzel, N.G. Park, Lead iodide perovskite sensitized all-solid-state submicron thin film mesoscopic solar cell with efficiency exceeding 9%, *Sci Rep*., **2**, 591 (2012).

[11] H. S. Jung, N. G. Park, Perovskite solar cells: from materials to devices, *small*, **11**, 1 (2015).

[12] T. M. Koh, K. Fu, Y. Fang, S. Chen, T. C. Sum, N. Mathews, S. G. Mhaisalkar, P. P. Boix, T. Baikie, Formamidinium-containing metal-halide: an alternative material for near-IR absorption perovskite solar cells, *J. Phys. Chem. C*, **118**, 16458−16462 (2014).

[13] M. A. Green, A. Ho-Baillie, H. J. Snaith, The emergence of perovskite solar cells, *Nature Photon.*, 8, 506-514 (2014)

[14] Z. Xie, S. Sun, Y. Yan, L. Zhang, R. Hou, F. Tian, G. G. Qin, Refractive index and extinction coefficient of $NH_2CH = NH_2PbI_3$ perovskite photovoltaic material, *J. Phys.: Condens. Matter*., **29**, 245702 (2017).

[15] Y. L. Zhao, J. F. Wang, B. G. Zhao, C. C. Jia, J. P. Mou, L. Zhu, J. Song, X. Q. Gu, Y. H. Qiang, Fabrication of mixed perovskite organic cation thin films via controllable cation exchange, *Chin. Phys. B*., **27**, 024208 (2012).

[16] M. Salado, L. Calio, R. Berger, S. Kazim, S. Ahmad, Influence of the mixed organic cation ratio in lead iodide based perovskite on the performance of solar cells, *Phys.Chem.Chem.Phys*., **18**, 27148-27157 (2016).

[17] J. W. Lee, D. J. Seol, A. N. Cho, N. G. Park, High-efficiency perovskite solar cells based on the black polymorph of $HC(NH_2)_2PbI_3$. *Adv. Mater*., **26**, 4991–4998 (2014).

[18] S. Wozny, M. Yang, A. M. Nardes, C. C. Mercado, S. Ferrere, M. O. Reese, W. Zhou, K. Zhu, Controlled humidity study on the formation of higher efficiency formamidinium lead triiodide-based solar cells, *Chem. Mater*., **27**, 4814−4820 (2015).

[19] L. C. Chen, C. C. Chen, J. C. Chen, C. G. Wub, Annealing effects on high-performance $CH_3NH_3PbI_3$ perovskite solar cells prepared by solution-process, *Sol. Energy*, **122**, 1047–1051 (2015).

[20] M. R. Ahmadian-Yazdi, F. Zabihi, M. Habibi, M. Eslamian, Effects of process parameters on the characteristics of mixed-halide perovskite solar cells fabricated by one-step and two-step sequential coating, *Nanoscale Res. Lett*., **11**:408 (2016).

[21] Y. Okamoto, T. Yasuda, M. Sumiya, Y. Suzuki, Perovskite solar cells prepared by advanced three-step

method using additional $HC(NH_2)_2I$ spin-coating: efficiency improvement with multiple bandgap structure, *ACS Appl. Energy Mater*., **1**, 1389−1394 (2018).

Chapter 4

Simultaneous formation of bandgap gradients at the both top and bottom sides of perovskite layer by an additional spin-coating of FAI-NAI solution

Chapter 4: Simultaneous formation of bandgap gradients at the top and bottom sides of perovskite layer by an additional spin-coating of FAI-NAI solution

4.1 Introduction

In Chapter 2, the conversion of unreacted PbI_2 in the 2-step prepared perovskite layer into perovskite was demonstrated by the 3-step method [1]. In Chapter 3, the formation of bandgap gradient (multiple bandgap structure) at the bottom side of perovskite layer was demonstrated by additionally spin-coating the FAI solution [2]. In this chapter, the author attempted to control the bandgap gradients at the both top and bottom sides of perovskite layer simultaneously by adding NaI into the 3rd step FAI solution.

In order to keep the perovskite structure, Goldschmidt tolerance factor [$t = (r_A + r_I)/\sqrt{2}(r_{Pb} + r_I)$] must be within ~0.8-1.1 [3]. Considering the Goldschmidt tolerance factor, monovalent cations of Rb^+, K^+, Na^+, and Li^+ are too small (for A site) to keep the perovskite structure of $APbI_3$ [4]. However, Saliba et al. [4] recently reported that a doping of appropriate amount of Rb^+ into a CsMAFA-system perovskite crystal is effective to achieve a high PCE of > 21% with high stability. After their report, K^+ or Na^+ doping has been studied, since they are much cheaper than Rb [5,6].

An ionic radius of Na^+ is particularly small (1.39 Å for A site with 12 coordination [7]) compared to those of Cs^+ (1.88 Å), Rb^+ (1.72 Å) and K^+ (1.64 Å), and hence, it is still not clear whether Na^+ is incorporated into the A site or into the interstitial sites. Still, the appropriate amount of Na^+ or K^+ doping is reported to be effective to increase the grain size of perovskite layer, to improve the crystallinity, and to decrease the trap density, which resulted in an enhancement of PCE [8,9]. Furthermore, suppose that Na^+ ion can be incorporated into the A-site, it is expected to increase a band gap of perovskite layer, since a bandgap of "$NaPbI_3$" is reported to be larger than those of $FAPbI_3$ and $MAPbI_3$ as shown in **Fig. 4.1** [10,11].

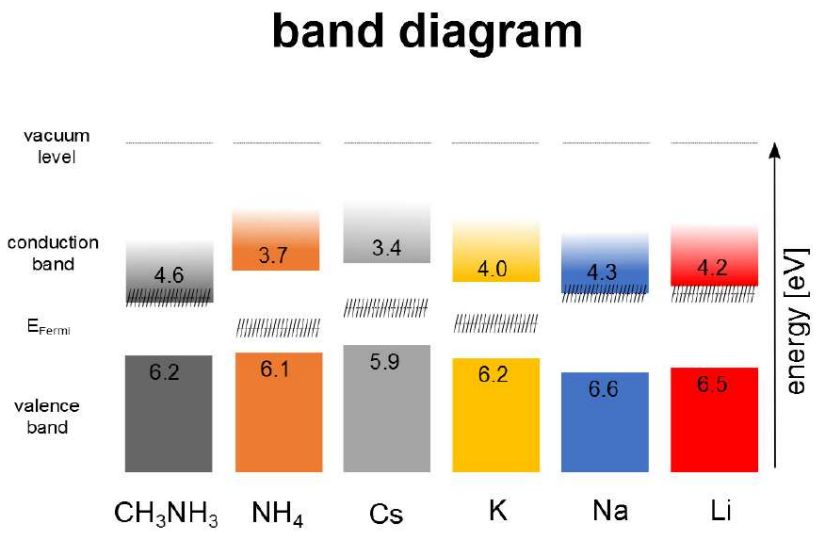

Fig. 4.1 Band diagram of various $APbI_3$ compounds reported by Dimesso et al. [11].

The hypothesis brought me an idea that an addition of trace-NaI into the 3rd step FAI solution may form the bandgap gradients at the top and bottom sides simultaneously. The NaI addition will form a larger bandgap area at the vicinity of the top surface with keeping a smaller bandgap (FA rich area) at the bottom side as shown in **Fig. 4.2**. The top surface with larger bandgap will be effective to further improve the carrier transport as reported by Kim et al. [12] and Cho et al. [13]. Besides, in the previous studies, Na^+ was doped by adding NaI into a perovskite precursor solution [8,9]. On the other hand, in this study, Na^+ will be doped by a post-treatment. Therefore, new insights about the Na^+ post-treatment can be obtained.

The purposes of this chapter are to produce the bandgap gradients at the both top and bottom sides of the perovskite layer simultaneously by adding NaI into the FAI solution and to enhance the photovoltaic performance.

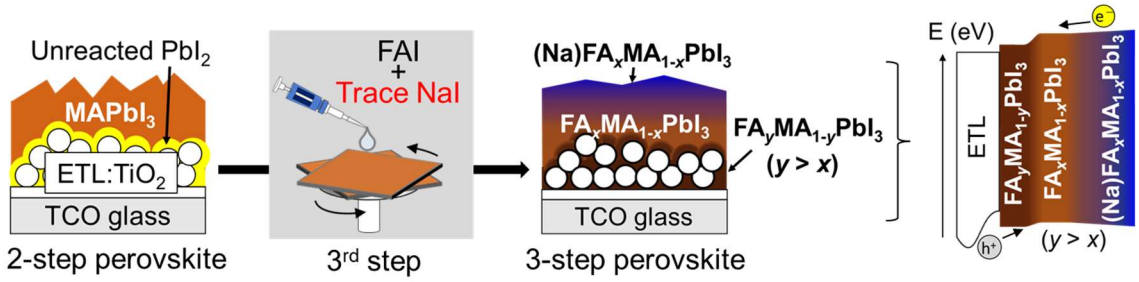

Fig. 4.2 Design concept for simultaneous formation of bandgap gradients at the top and bottom sides of perovskite layer by the additional spin-coating of FAI solution with trace NaI.

4.2 Experimental

4.2.1 Preparation method of perovskite solar cell

Preparation of electron transport layer (ETL) on TCO glass

Transparent conductive oxide (TCO, Type-0052, 10 Ω/sq., Geomatec) substrates were patterned by etching with Zn powder (>96.0%, Tokyo Chemical Industry) and 1 M HCl (Wako Pure Chemical Industry). Then, the substrates were cleaned by an ultrasonication in ethanol for 5 min and dried in air. The TiO_2 compact layers were prepared by spray-pyrolysis method; a solution of titanium diisopropoxide bis(acetylacetonate) (TAA, 75wt% in isopropanol, Sigma-Aldrich) mixed with ethanol at the volume ratio of TAA:ethanol=2:25 was sprayed on the patterned substrates with heating at 500°C. TiO_2 mesoporous layers were then prepared by spin-coating a TiO_2 paste (18NR-T, Dyesol), diluted in ethanol at the weight ratio of TiO_2 paste:ethanol=1:5, on the substrates at 4000 rpm for 25 s and by annealing at 500°C for 1 h. Then, the substrates were exposed to ultraviolet light for 1 night in order to improve the contact with the PbI_2 solution in the next section (**Fig. 3.2**).

Preparation of perovskite layer, hole transport layer (HTL) and metal electrodes

The perovskite layers and the HTLs were prepared in air with humidity of ~34%. The TiO_2 coated substrates were pre-heated at 60°C. A 1 M solution of PbI_2 (>98.0%, Tokyo Chemical Industry) in DMF (99.5%, Nacalai tesque) was also pre-heated at 60°C. The PbI_2 solution was spin-coated on the substrates at 3000 rpm for 20 s (1st step). After annealing at 60°C for 10 min, the substrates were dipped in a 10 mg/mL solution of MAI (98%, Wako Pure Chemical Industry) dissolved in isopropanol (99.5%, Nacalai tesque) for 20 s, followed

by rinsing with isopropanol (IPA) and by annealing at 60°C for 10 min (2nd step). Then, 20 µL of 0.19 M FAI (32.4 mg/mL, ≥98%, Sigma-Aldrich) solution in isopropanol was dropped on the prepared $MAPbI_3$ layers. After the waiting time of 10 s, the substrates were spun at 4000 rpm for 25 s (3rd step). As for the NaI addition, the NaI was added in the FAI solution to be four different concentrations (1.5, 3, 6, 12 mM), and the solutions were used for the 3rd step spin-coating. After the annealing at 60°C for 10 min, the substrates were rinsed with IPA to eliminate excess FAI or NaI on the surface, and then annealed at 60°C for 10 min.

The HTLs with the thickness of ~200 nm were prepared by spin-coating a spiro-MeOTAD solution at 4000 rpm for 35 s. The spiro-MeOTAD solution in 1 mL chlorobenzene (99%, Nacalai tesque) was composed of 73 mg spiro-MeOTAD (99%, Sigma-Aldrich), 28.8 µL 4-*tert*-butylpyridine (TBP, 96.0%, Sigma-Aldrich) and 17 µL solution of [520 mg/mL lithium bis(trifluoromethylsulphonyl)imide salt (>98.0%, Tokyo Chemical Industry) in acetonitrile (99.5%, Wako Pure Chemical Industry)]. Finally, Ag electrodes with the thickness of ~50 nm were deposited on the HTLs with a thermal evaporator under the pressure of 3×10^{-5} Torr (**Fig. 4.3**).

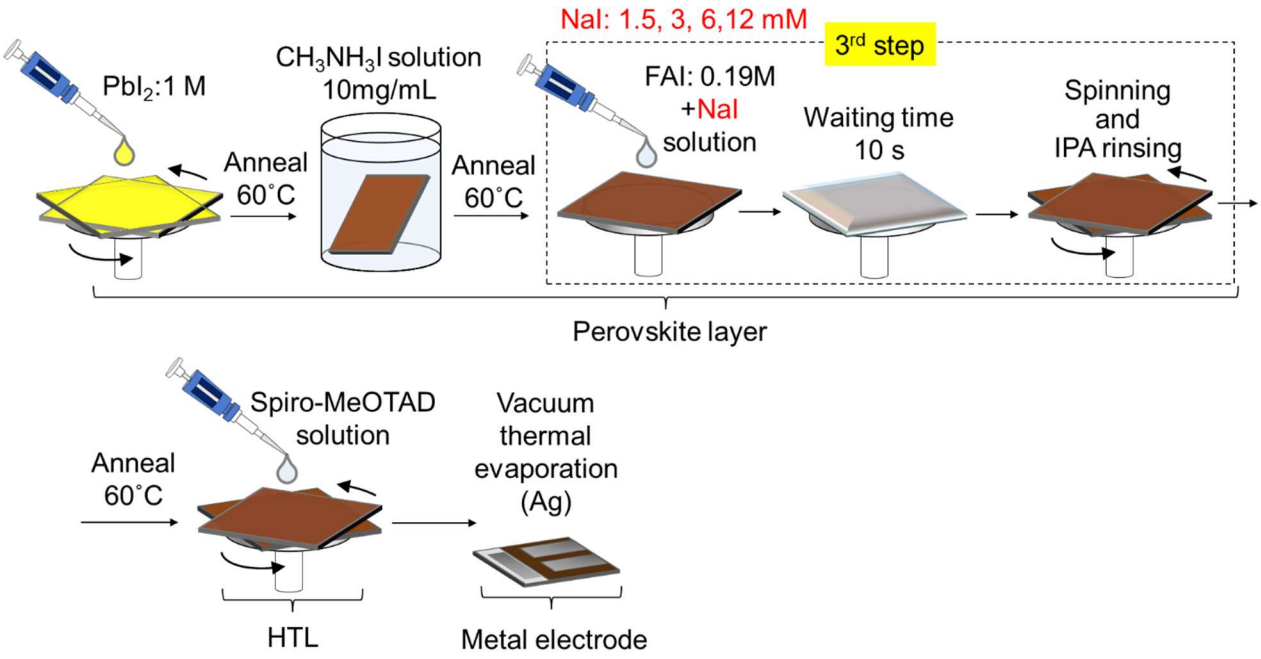

Fig. 4.3 Schematic illustration of preparation processes of perovskite layer, hole transport layer (HTL), and metal electrodes.

Hereinafter, we denote the samples with spin-coating of "FAI solution" as "FAI only" and those with "FAI + NaI (1.5, 3, 6 and 12 mM) solutions" as "+NaI:1.5mM", "+NaI:3mM", "+NaI:6mM", and "+NaI:12mM" as summarized in **Table 4.1**.

Table 4.1 Relationship between sample names and preparation conditions in Chapter 4.

Additional spin-coating	FAI:0.19 M	FAI: 0.19 M + NaI: 1.5 mM	FAI: 0.19 M + NaI: 3 mM	FAI: 0.19 M + NaI: 6 mM	FAI: 0.19 M + NaI: 12 mM
Sample names	FAI only	+NaI:1.5mM	+NaI:3mM	+NaI:6mM	+NaI:12mM

4.2.2 Characterizations

X-ray diffraction (XRD)

Crystal structure and phases analyses of the prepared perovskite layers or completed cell were carried out by using XRD (Multiflex, Cu-K_α, 40 kV and 40 mA, Rigaku). The sample was set so that the height of surface matches that of sample holder (**Fig. 2.7**).

X-ray Photoelectron Spectroscopy

XPS measurements of the surface of prepared perovskite layers were carried out using a JPS 9010 TR (JEOL) and an Al-Kα X-ray source (1486.6 eV).

Scanning electron microscopy (SEM)

The surface morphology and cross-section of the perovskite layers on ETLs were observed using SEM (JSM-6500F, JEOL). For the cross-sectional observation, the samples were broken into two pieces by making a notch with a diamond cutter, and the fracture surface was observed (**Fig. 2.9**).

Atomic force microscopy (AFM)

The surface roughness of the prepared perovskite layers was measured by AFM (E-sweep, High-technologies) in a dynamic force mode.

Ultraviolet-visible absorption spectroscopy (UV-Vis)

Optical absorbance and transmittance of the prepared perovskite layers on ETLs were measured by UV-Vis (UV-1280, Shimadzu). The light was irradiated from back TCO glass side (**Fig. 2.8**).

Steady-state photoluminescence (PL)

PL of the prepared perovskite layers were measured using Ramascope System1000 (Renishaw) with an excitation laser of wavelength 325 nm (IK5651R-G, Kimmon).

Current density-voltage (*J-V*) characterization

J-V characteristics were measured for the evaluation of photovoltaic performance with a DC voltage and current source/monitor (6241A, ADC Co.) and with a solar simulator (XES-40S1, SAN-EI Electric) which was calibrated to AM 1.5, 100 mW/cm^2 with a standard silicon photodiode (BS-520BK, Bunkokeiki). The voltage step and delay time were 20 mV and 50 ms, respectively. The voltage scan range was 0-1.1 V. The active area was limited to 0.084 cm^2 by using black mask. The *J-V* curves were measured by reverse (1.1 V → 0 V) and forward (0 V → 1.1 V) scans.

4.3 Results and Discussion

4.3.1 Phase and crystal structure analysis of perovskite layer

First of all, the estimation of composition x in $FA_xMA_{1-x}PbI_3$ was carried out. **Figure 4.4** shows XRD patterns of the perovskite layers prepared on the ETLs by 2-step method and 3-step method using additional FAI spin-coating. As for the 2-step prepared perovskite layer, strong peaks corresponding to tetragonal $MAPbI_3$ and relatively large peaks of unreacted PbI_2 were confirmed. After the FAI additional spin-coating, the peak intensity of unreacted PbI_2 peak was significantly reduced by the conversion into a perovskite phase. In addition, a peak at ~ 28.4° for perovskite phase did not show a split and the peak position shifted to smaller angle. These results indicate a phase transformation from tetragonal to cubic and lattice expansion due to the substitution of MA^+ in $MAPbI_3$ with FA^+ ($FA_xMA_{1-x}PbI_3$), which is in good agreement with the results of Chapter 3.

It is known that the FA^+ ratio in $FA_xMA_{1-x}PbI_3$ and the amount of peak shift in XRD has a proportional relationship (Vegard's law) [14,15]. Therefore, the composition x in the 3-step prepared $FA_xMA_{1-x}PbI_3$ was estimated by calculating the difference of lattice constant a between the 2-step (tetragonal $MAPbI_3$) and 3-step (cubic $FA_xMA_{1-x}PbI_3$) prepared perovskite layers and by referring to the reported relationship [16]. The value of $\tilde{a} = a/\sqrt{2}$ was used for the 2-step prepared tetragonal $MAPbI_3$ layer to compare with the lattice constant a of the 3-step prepared cubic $FA_xMA_{1-x}PbI_3$ layer. The $\tilde{a}$ for the 2-step tetragonal $MAPbI_3$ layer was calculated from the peak position of 220 reflection, the lattice constant a for the 3-step cubic $FA_xMA_{1-x}PbI_3$ layer was calculated from the peak position of 200 reflection. The 2-step prepared and 3-step prepared perovskite layers had $\tilde{a}$ = 6.277 Å and a = 6.333 Å, respectively, with the difference of 0.056 Å. By using the relationship between the lattice constant a and the composition x in $FA_xMA_{1-x}PbI_3$ reported by Slimi et al. [16], x value of $FA_xMA_{1-x}PbI_3$ layer in this study was estimated to be ~0.4, i.e., $FA_{0.4}MA_{0.6}PbI_3$.

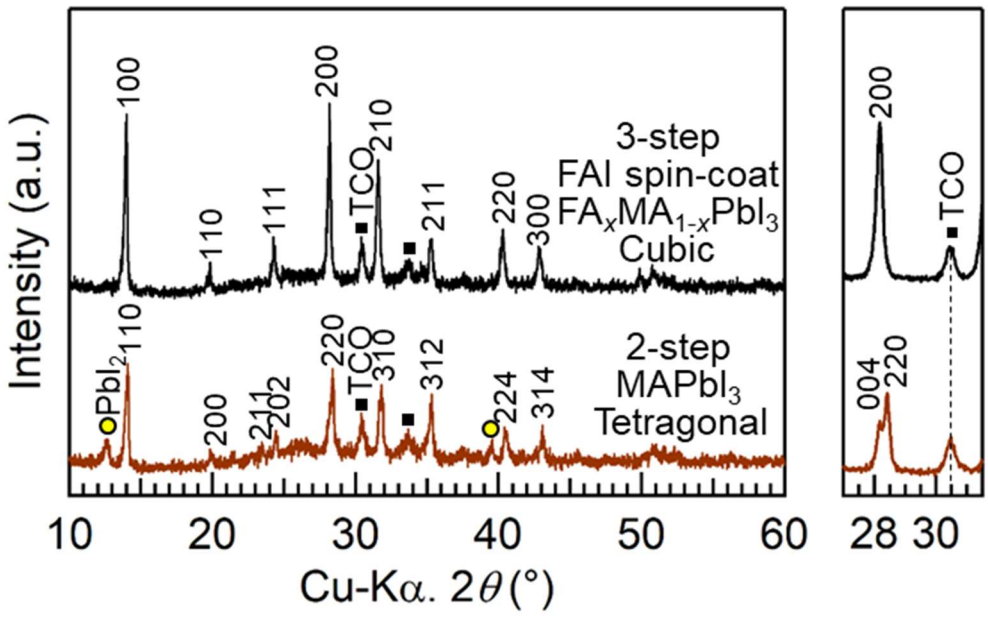

Fig. 4.4 XRD patterns of the perovskite layers prepared by 2-step and 3-step methods.

Then, the effect of NaI addition on the composition and crystal structure of $FA_{0.4}M_{0.6}PbI_3$ was investigated. **Figure 4.5(a)** shows XRD patterns of the 3-step prepared perovskite layers on ETLs with and without NaI addition. Since the unreacted PbI_2 peaks at ~12.6° were hardly observed in all the samples, the NaI addition does not hinder the conversion of unreacted PbI_2 into perovskite phase. As for the perovskite peaks, all the NaI added samples showed the peaks at the almost same positions as those of $FA_{0.4}MA_{0.6}PbI_3$ (FAI only). The obvious peak shift was not confirmed even from the 100 peaks in the zoomed range of 13-15° and 200 peaks in the zoomed range of 27-31.5°, possibly due to the small concentration of NaI. Full width at half maximum (FWHM) was calculated from the 100 peaks as shown in **Fig. 4.5(b)**. The FWHM showed a decreasing tendency with increasing the addition amount of NaI, which implies an increase of grain size.

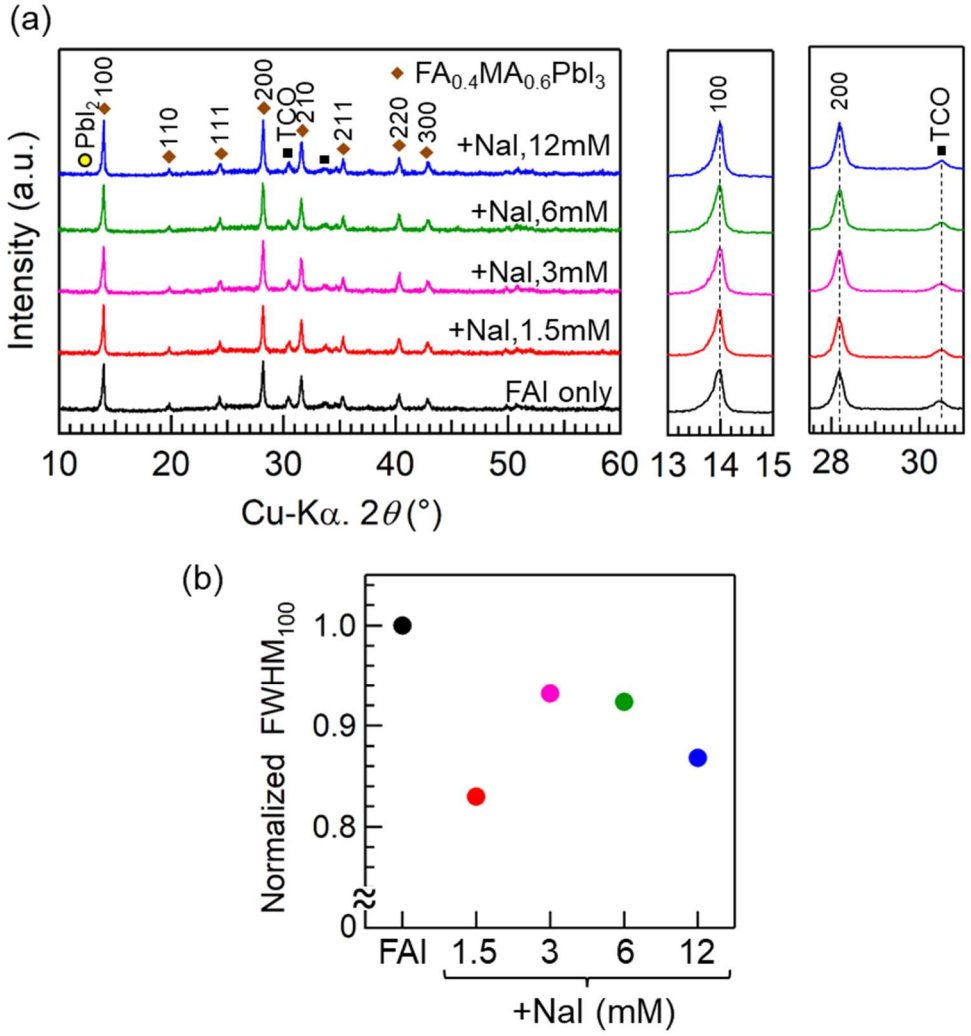

Figs. 4.5 (a) XRD patterns of the perovskite layers prerpared by the 3-step method using additional spin-coating of FAI solutions with and without NaI addition. **(b)** Full width at half maximum (FWHM) calculated from the 100 peaks of the prepared perovskite layers in XRD.

Figure 4.6 shows surface XPS spectra of narrow scan for C 1s, Pb 4f, I 3d, and Na 1s of the perovskite layers prepared by 3-step method using an additional spin-coating of the FAI solution without and with NaI addition of 3 or 12 mM. The C 1s peaks at ~286.5 eV may correspond to a C-C bond from organic contamination and that at ~288.5 eV may correspond to a C-N bond from FA or MA part. The position of C

1s peak slightly shifted to larger energy than some reported positions [17,18] probably due to the surface charging, but the peak positions were comparable among the three samples. There were also no significant difference in the position and intensity of Pb 4f peaks (~138.8 eV and ~143.6 eV) and I 3d peaks (~619.7 eV and ~631.2 eV) [9] among the three samples.

As for the Na 1s peak, the FAI only spin-coated sample did not have a peak in the range of 1068-1078 eV, whereas the +NaI:12mM sample had a peak at ~1072.5 eV, which indicate the existence of Na on the perovskite layer of the +NaI:12mM sample. To confirm the homogeneity of Na^+ distribution on the surface of perovskite layer, XPS spectra were collected at two different points on the surface of +NaI:12mM sample as shown in **Fig. 4.7**. Although the intensity and position of C 1s, Pb 4f, and I 3d peaks were comparable between the two points, the peak intensity of Na 1s peak were different. The difference of peak intensity suggests the heterogeneous Na distribution on the perovskite layer. An apparent Na 1s peak (detectable in +NaI:12mM) were not confirmed for the +NaI:3mM sample due to its small Na amount. However, the graph seems to have a small inflection at ~1072-1074 eV compared to the FAI only spin-coated sample, and it implies the existence of Na even on perovskite layer of the +NaI:3mM sample.

Atomic ratios were estimated from the integrated intensity of the XPS spectra. The atomic ratio of Pb:I was estimated to be ~1:4 in all the sample, which was somewhat different from the theoretical Pb:I ratio of 1:3 in $FA_xMA_{1-x}PbI_3$. The difference is attributable to some excess I coming from the additionally spin-coated FAI solution. The atomic % of Pb:I:Na for the +NaI:12mM sample were 77.5:20.4:2.1 (%). Considering the chemical formula of $FA_xMA_{1-x}PbI_3$, the atomic % of Na in the perovskite layer is less than 1%.

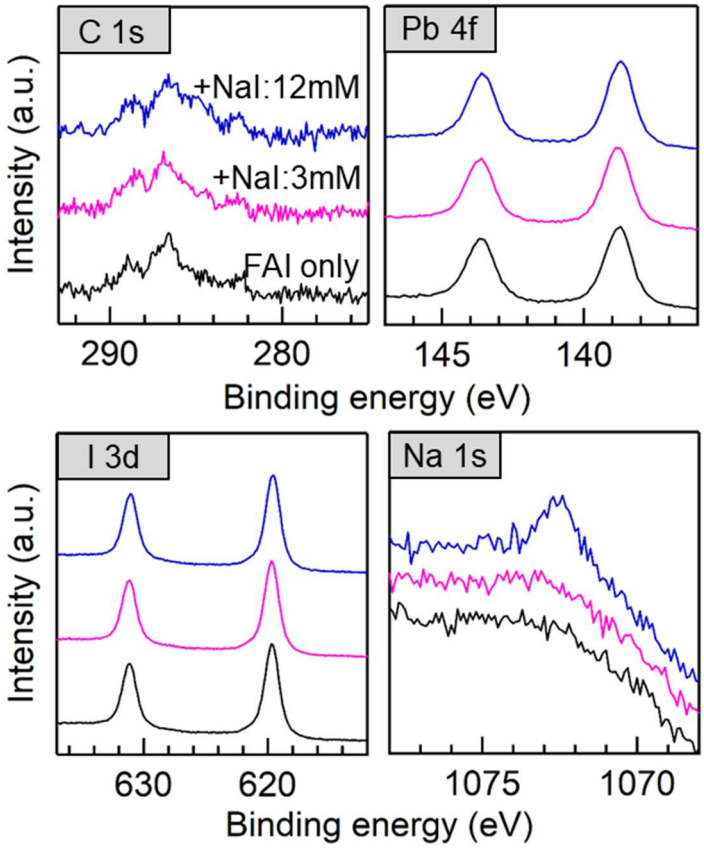

Fig. 4.6 The surface XPS spectra of narrow scan for C 1s, Pb 4f, I 3d, and Na 1s of the additionally FAI spin-coated perovskite layer without and with NaI addition of 3 or 12 mM.

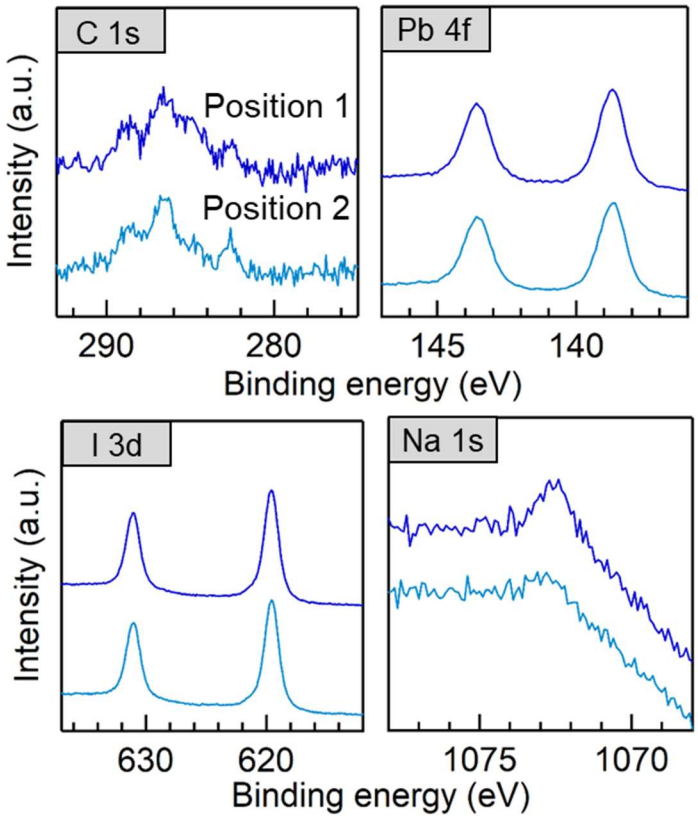

Fig. 4.7 Surface XPS spectra measured at two different points in the +NaI:12mM sample.

4.3.2 Microstructure observation and surface roughness measurement of perovskite layer

Figure 4.8 shows surface SEM images of the prepared perovskite layers on the ETLs. The perovskite-particle size of the FAI only spin-coated sample was distributed in ~0.5-1 μm. The perovskite particles partially fused with the other particles, which is in good agreement with the results in Chapter 3. The surface of 2-step prepared $MAPbI_3$ particles were slightly dissolved in the spin-coated solution, and the particles partially fused with other particles (liquid-phase assisted grain growth). However, there were still spatial gaps among the perovskite particles.

As for the NaI added samples, the surface morphology of the +NaI:1.5 mM sample was similar to that of the FAI-only spin-coated sample. Meanwhile, with increasing the NaI addition amount, the spatial gaps and grain boundaries tended to disappear by accelerating the fusion among the perovskite particles, which resulted in an increase of grain size. Although some pinholes were still confirmed, the spatial gaps almost disappeared for the +NaI:12mM sample and the grain size became larger than that of FAI only spin-coated sample. The decrease of FWHM with increasing the NaI addition amount in the XRD (**Fig. 4.5(b)**) is attributable to this increase of grain size.

For the 1-step method, Bag et al., [5] reported an increase of grain size by adding NaI into a precursor solution for the perovskite layer, where possible mechanisms were proposed as (1) promotion of nucleation of perovskite particles or (2) enhancement of grain boundary mobility by the added small Na^+ ions. For the 3-step method in this study, the first mechanism (promotion of nucleation) is not applicable, since the additional spin-coating is a post-treatment and it does not relate to the nucleation. The second one (enhancement of grain

boundary mobility) may be possible, but another one, i.e., an acceleration of the liquid-phase assisted grain growth by the NaI addition, can be a most probable mechanism through the SEM observation (**Fig. 4.8**).

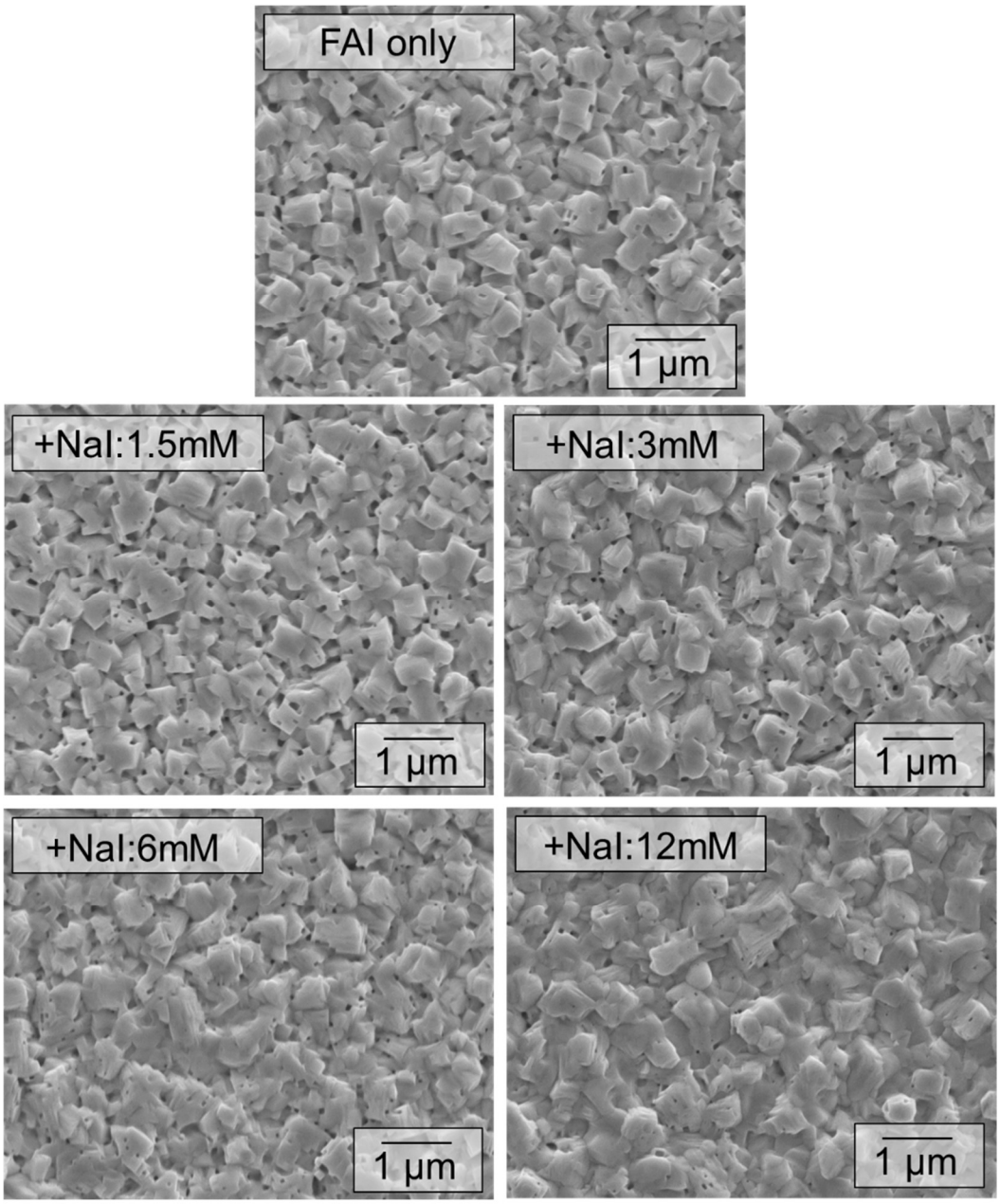

Fig. 4.8 Surface SEM images of the prepared perovskite layers on the ETLs.

Figure 4.9 shows AFM images of the perovskite layers for the +NaI:3mM and +NaI:12mM samples. A roughness of root mean square (R_{MS}) for the +NaI:12mM sample was 74.9 nm, and it was similar to that of +NaI:3mM (73.9 nm). On the other hand, a surface area of the +NaI:12mM sample (116 μm^2) was smaller than that of the +NaI:3mM sample (120 μm^2) in the measured area of 10×10 μm^2. These results suggest that the macroscopic shapes of perovskite capping layers were similar between the two samples, but microscopically, the perovskite particles in the +NaI:12mM sample had the flatter surface than the +NaI:3mM sample due to the accelerated liquid-phase assisted grain growth.

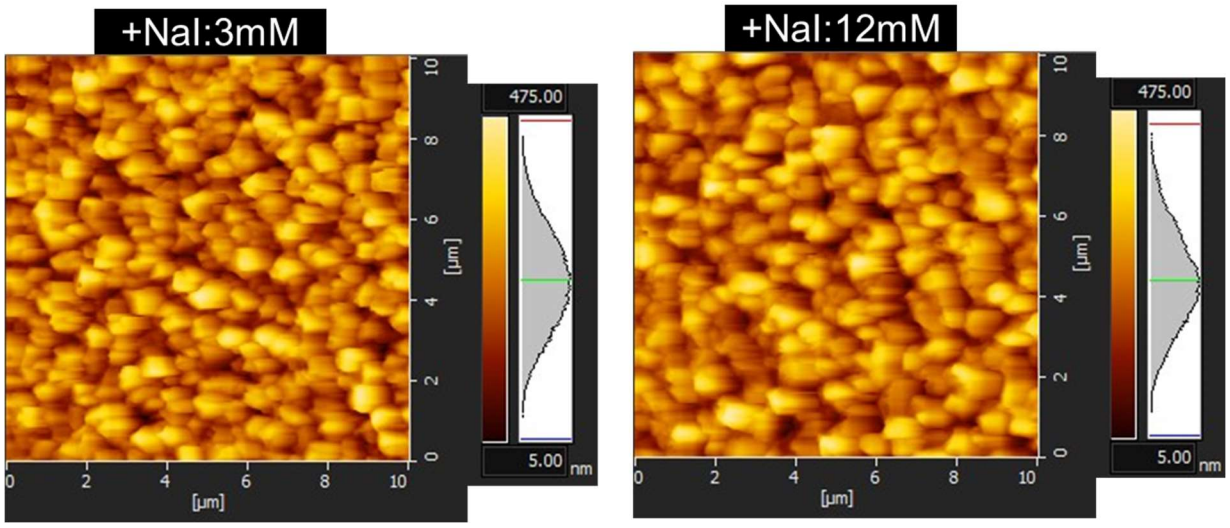

Fig. 4.9 AFM images of the perovskite layers for +NaI:3mM and 12mM.

Figure 4.10 shows cross-sectional SEM images of the prepared perovskite layers on ETLs. For all the samples, the thicknesses of TiO_2 compact layer, TiO_2 mesoporous/perovskite layer, and perovskite capping layer were ~40 nm, ~150 nm and ~400 nm, respectively. As for the perovskite capping layer, the vertical grain boundary was hardly confirmed in the +NaI:12mM sample due to the accelerated liquid-phase assisted grain growth. In addition, all the samples had the macroscopically comparable shape for the perovskite capping layer, but the microscopic surface texture tended to decrease with increasing the amount of NaI addition, which is in good agreement with the AFM results.

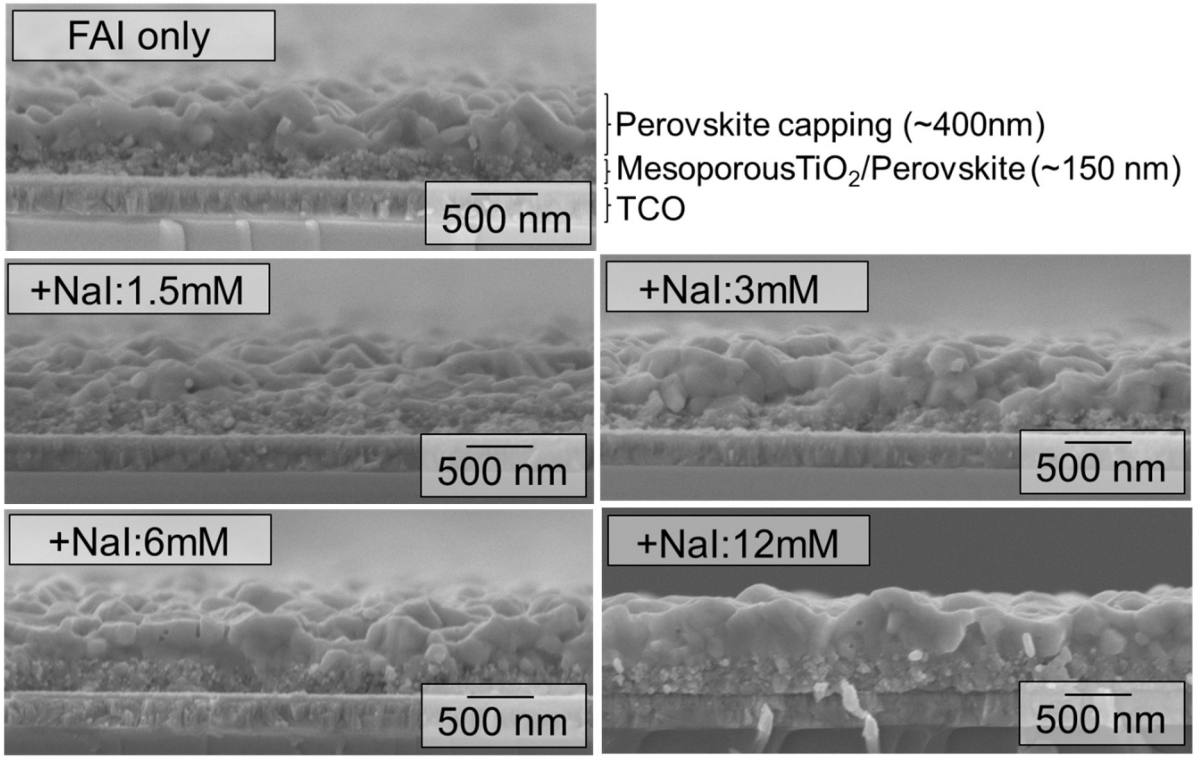

Fig. 4.10 Cross-sectional SEM images of the prepared perovskite layers for FAI only, +NaI:1.5mM, +NaI:3mM, +NaI:6mM, and +NaI:12mM samples on ETLs.

4.3.3 Optical property analysis and bandgap estimation of perovskite layer

Fig. 4.11 shows absorbance spectra of the prepared perovskite layers on ETLs. The bandgaps were estimated by converting the absorbance spectra into Tauc plots **(Fig. 4.12)** and were summarized in **Table 4.2**. All the samples had the comparable bandgap values of ~1.55 eV, but the bandgap of the +NaI:12 mM sample was slightly larger than the others. The slight increase of bandgap implies a partial substitution of FA^+/MA^+ with Na^+, since $NaPbI_3$ was reported to have a larger bandgap than that of $(FA,MA)PbI_3$ [10,11]. The absorbance of the +NaI:1.5-6mM samples were slightly larger than that of FAI only spin-coated sample at $\lambda <$ ~800 nm, which is beneficial to produce larger J_{SC}. The increase of absorbance is possibly ascribed to the increase of grain size by the NaI addition (**Fig. 4.8**). On the other hand, the absorbance decreased by increasing the amount of NaI addition up to 12 mM, probably due to a less light scattering by the microscopically flatter surface texture of the perovskite layer (**Fig. 4.9 and 4.10)**.

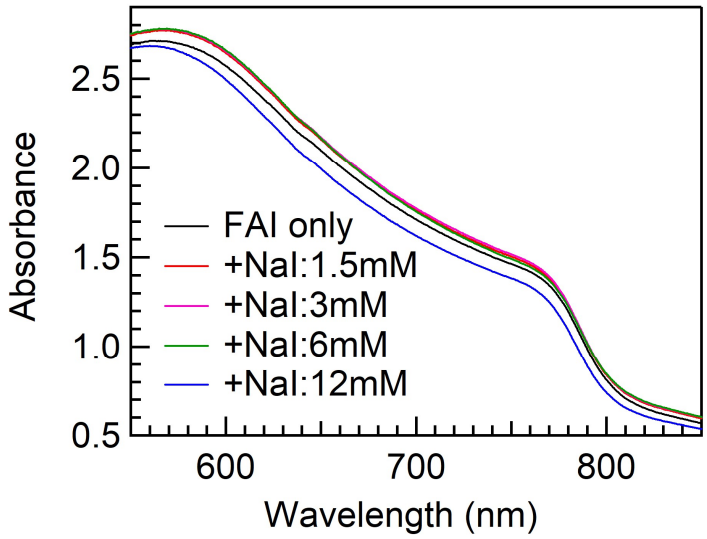

Fig. 4.11 Absorbance spectra of the prepared perovskite layers on ETLs.

Table 4.2 Bandgaps of the prepared perovskite layers on ETLs estimated from the band edge of the absorbance spectra and Tauc plot.

Samples	Bandgap (eV)
FAI only	1.546
+NaI:1.5mM	1.546
+NaI:3mM	1.546
+NaI:6mM	1.546
+NaI:12mM	1.550

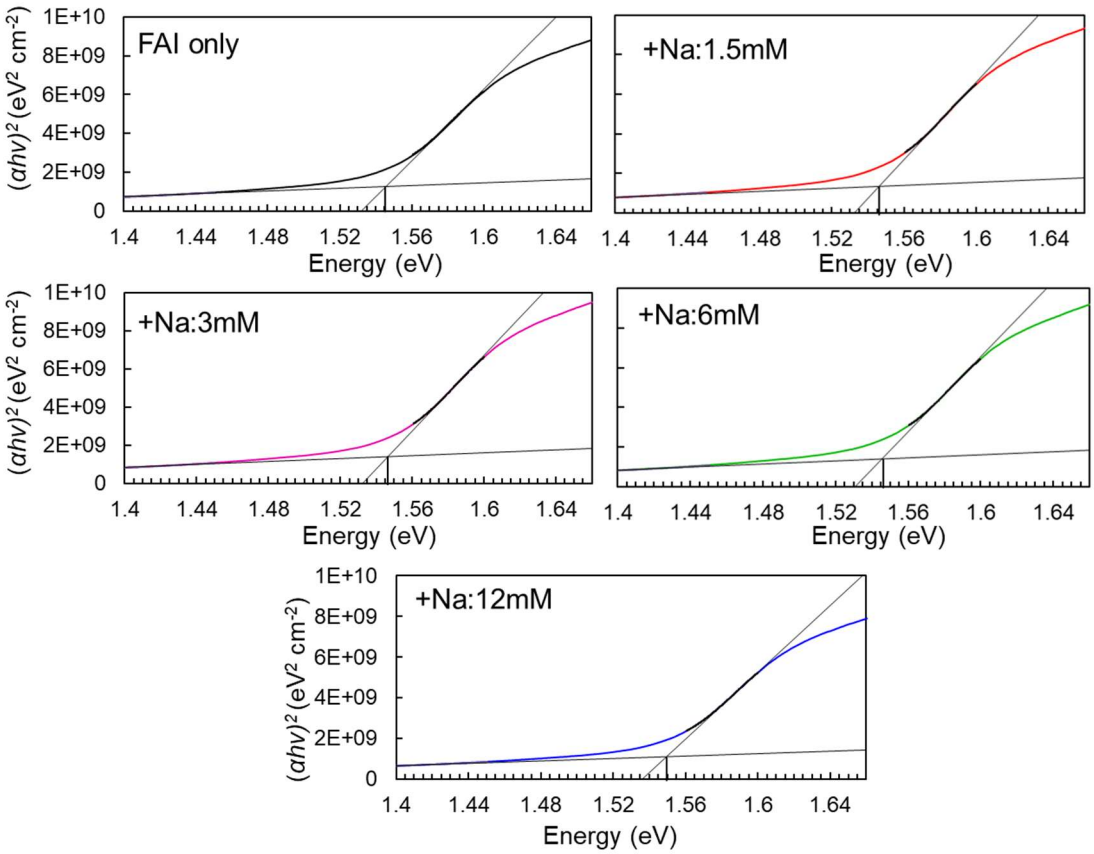

Fig. 4.12 Tauc plots of the prepared perovskite layers converted from their absorbance spectra.

4.3.4 Band structure analysis of perovskite layer

Then, a detection of the multiple bandgap structure by the bandgap gradients was carried out by measuring PL spectra from the top side (perovskite layer side) and back side (substrate side) of the perovskite layer. A commercial slide glass plate (No. 10005000, Marienfeld) was used as the substrate to avoid an absorption of the laser by the TCO layer. He-Cd laser with the wavelength of 325 nm was used to excite the samples. The penetration depth of the laser into the (FA,MA)PbI_3 layer was estimated to be ~25-50 nm as described in Chapter 3. The PL spectra were measured at 5 points for each sample. The PL peak positions did not depend on the measurement points as shown in **Fig. 4.13**.

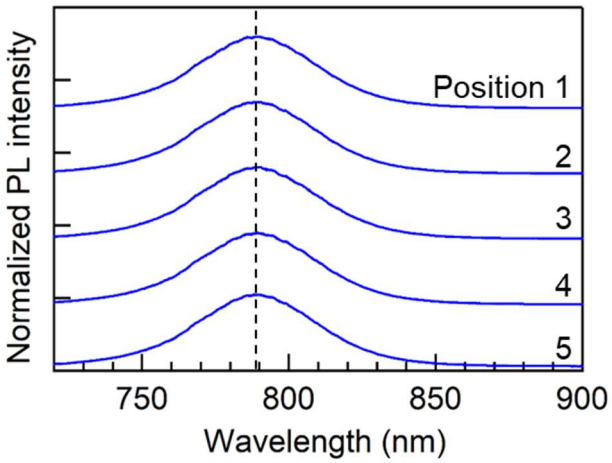

Fig. 4.13 PL spectra measured at 5 points on the top surface of perovskite layer of the +NaI:12mM sample.

Figures 4.14 show normalized PL spectra of the perovskite layers on ETLs measured from (a) the top perovskite layer side and (b) the back substrate side. When measuring from the top side (**Fig. 4.14(a)**), the position of PL peaks, which corresponds to a band to band transition of perovskite, was ~792 nm for the FAI only spin-coated sample. As for the NaI added samples, the +NaI:1.5 and 3mM samples had the peaks at the comparable position to the FAI only spin-coated sample, but the peak positions for the +NaI:6mM and 12mM were shifted to shorter wavelength, which indicate the increase of bandgap by the NaI addition. These results also imply the substitution of MA^+ and FA^+ with Na^+.

When measuring from the back side (**Fig. 4.14(b)**), the normalized PL peak position of the FAI only spin-coated sample shifted to ~798 nm, which indicates the formation of the FA rich layer with smaller bandgap near the ETL by the additionally spin-coated FAI solution as described in Chapter 3. As for the NaI added samples, all the samples had the PL peaks at the comparable position with FAI only spin-coated sample. These results imply that Na^+ did not substantially reach to the FA rich layer near the ETL due to the small NaI concentration. As a result, the bandgap gradients were successfully formed at the top and bottom sides of the perovskite layer simultaneously as shown in **Fig. 4.14(c)**, i.e. FA rich layer with smaller bandgap near the ETL and Na^+ doped layer with the larger bandgap at the top surface.

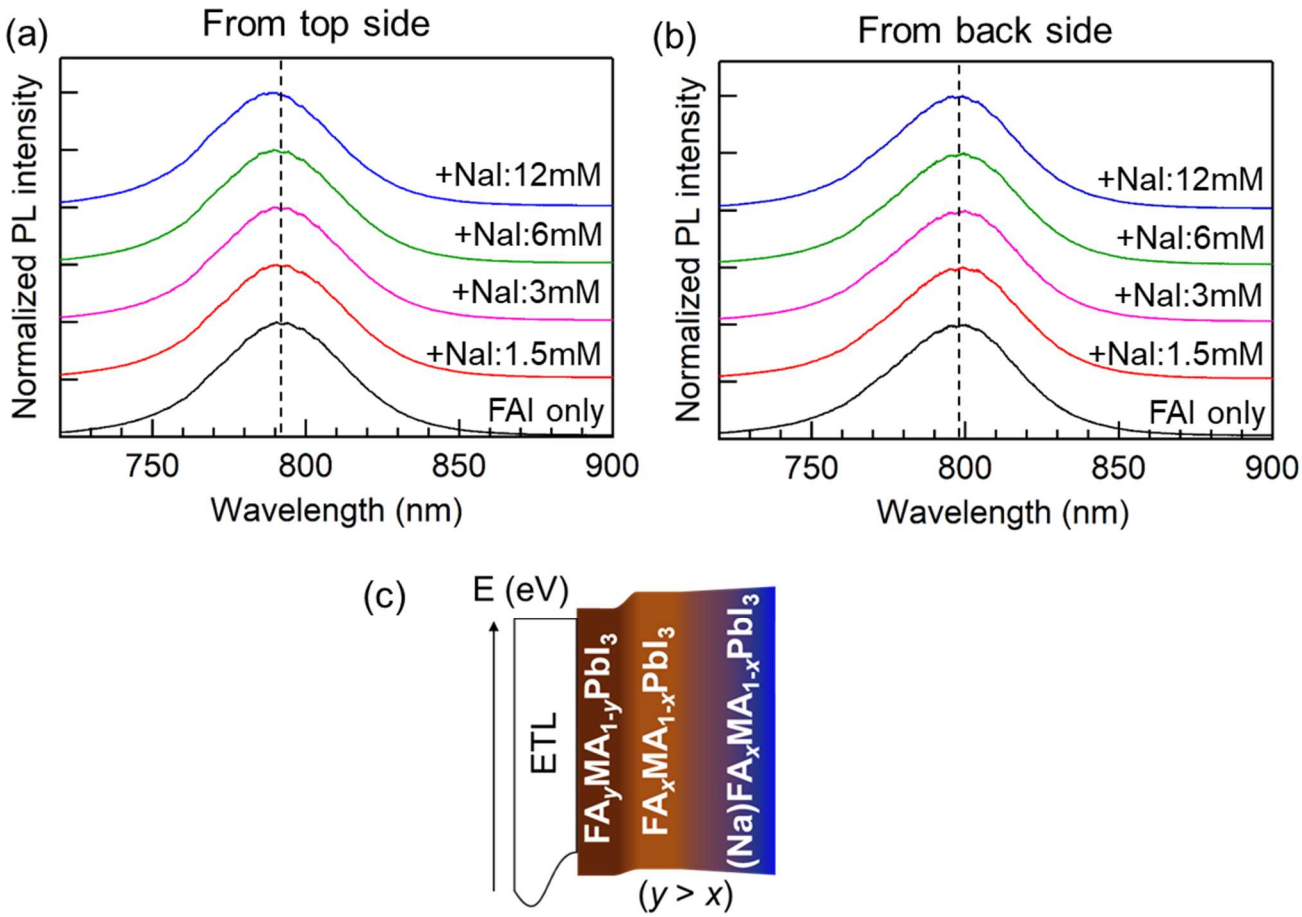

Figs. 4.14 Steady-state photoluminescence (PL) spectra of the prepared perovskite layers on ETLs measured from the (a) top side (from perovskite layer side) and (b) back side (from substrate side). (c) Expected band structure of the additionally FAI spin-coated perovskite layer with NaI addition.

Then, the PL peak intensity was focused. **Figures 4.15** shows (a) the PL spectra of the perovskite layers measured from the top side and (b) their relative peak intensities. For this measurement, the perovskite layer was prepared on a quartz glass (MT-WKS100PP01, MONOTECH Co., Ltd.) without ETL to avoid a quenching of the PL intensity. Although the +NaI:1.5mM samples had the comparable PL peak intensity with the FAI only spin-coated sample, the intensity tended to decrease with further increasing the addition amount of NaI.

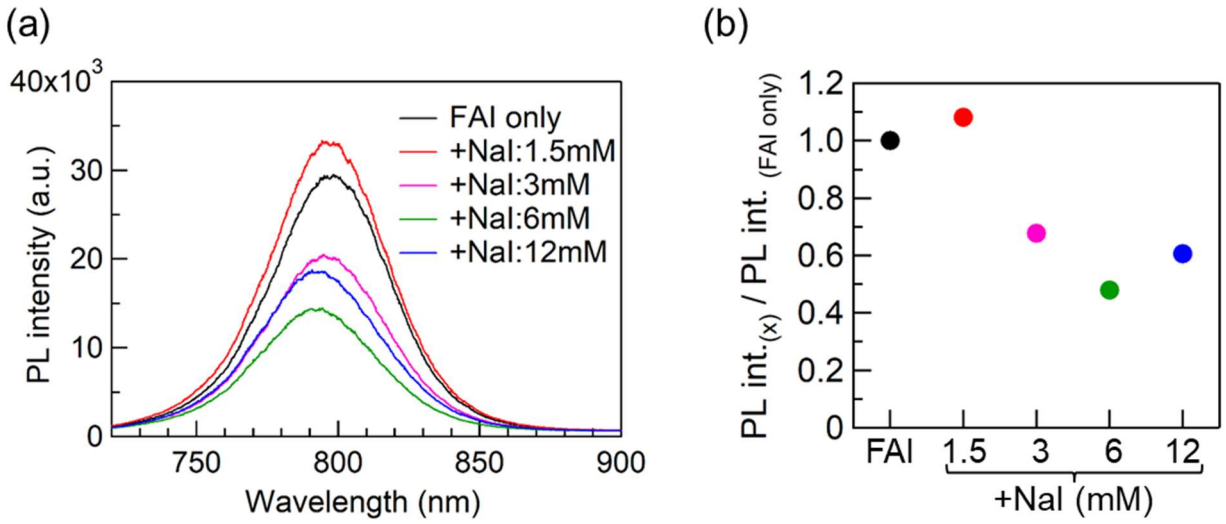

Figs. 4.15 (a) PL spectra of the perovskite layers measured from the top side and (b) their relative peak intensities. The perovskite layer was prepared on a quartz glass without ETL.

The decrease of PL intensity is caused by an increase of non-radiative recombination related to trap states or defects [19], and DeQuilettes et al. [20] reported that the non-radiative recombination frequently occurred at the grain boundary in the perovskite layer. In this study, the grain boundary was decreased by the NaI addition, nevertheless, the PL intensity decreased with increasing the amount of NaI addition (**Figs. 4.15**). It implies that the doped Na^+ ions acted as the trap states or defects, and it caused the increase of non-radiative recombination.

The tendency is different from the reported tendency by Chang et al. [8] and Zhao et al. [9]. In the literatures, the appropriate amount of NaI or KI addition into the perovskite precursor solution was effective to increase the PL intensity and carrier lifetime by reducing the non-radiative recombination. However, it was also reported that the addition of too much NaI or KI decreased the PL intensity and carrier lifetime possibly due to an excess Na^+ or K^+ ions [6,8]. In this study, the peak intensity of Na in XPS was dependent to the measurement points as shown in **Fig. 4.7** (i.e., heterogeneous Na^+ distribution particularly for +NaI:12mM). On the other hand, the PL peak positions were identical at the five different points (**Fig. 4.13**). Hence, it is deduced that further excess Na^+ ions were not incorporated within the (Na)$FA_xMA_{1-x}PbI_3$ top layer (**Fig. 4.14(c)**) but heterogeneously remained on the top layer, and these excess Na^+ possibly caused the non-radiative recombination.

4.3.5 Evaluations of photovoltaic performance and stability in air

Evaluation of photovoltaic performance

The current density-voltage (*J-V*) curves of the prepared perovskite solar cells measured with a reverse scan are shown in **Fig. 4.16**, and *J-V* characteristics are summarized in **Table 4.3**. The values in **Table 4.3** are averages of 15 cells. Box plots of the *J-V* characteristics are shown in **Fig. 4.17**. The FAI only spin-coated cell demonstrated J_{SC}: 23.85 mA/cm^2, V_{OC}: 0.985 V, *FF*: 0.771 and PCE: 18.12%. As for the NaI added samples, +NaI:1.5 and 3 mM showed the slightly increased J_{SC} of 24.09 mA/cm^2 and 24.16 mA/cm^2. By increasing the addition amount of NaI up to 6mM and 12mM, J_{SC} slightly decreased to 23.74 mA/cm^2 and 23.11 mA/cm^2, respectively. The increases of J_{SC} for +NaI:1.5 and 3mM are due to the enhanced light absorption by the increase of perovskite grain size (**Fig. 4.11)**, while the decrease of J_{SC} for +NaI:12mM is attributable to the decrease of light absorption by the decreased microscopic surface texture (**Fig. 4.10**). Since Chang et al. [11] also confirmed the decrease of J_{SC} by adding too much Na^+, the increase of non-radiative recombination (**Figs. 4.15**) could also cause the decrease of J_{SC}.

As for the V_{OC}, all the NaI added samples showed larger V_{OC} than the FAI only spin-coated sample, but V_{OC} of the +NaI:12mM sample (0.996 V) was smaller than those of the other NaI added samples (1.000,1.005, and 1.004 V for the +NaI:1.5,3, and 6mM samples, respectively). Since the reduction of carrier recombination increases the V_{OC}, the increase of V_{OC} for +NaI:1.5-6mM is mainly attributable to the decrease of trap sites or defects (via liquid-phase assisted grain growth), whereas the decrease of V_{OC} for +NaI:12mM is mainly attributable to the increase of trap sites or defects (via excess Na^+ heterogeneous dispersion on the surface). The multiple bandgap structure shown in **Fig. 4.14(c)** may also contribute to the enhancement of V_{OC}. However, this effect should be minor in this chapter, since the +NaI:12mM sample which had the largest bandgap gradient (hence the highest expected V_{OC}) showed the smaller V_{OC} than the other NaI added samples.

The *FF* of the +NaI:1.5, 3 and 6mM samples also increased to 0.781, 0.785, and 0.783, respectively. The improvement of *FF* is due to the decrease of grain boundary by the NAI addition, which can reduce an interface resistance. The smaller *FF* of the +NaI:12mM sample (0.774) than the other NaI added samples are also attributable to the increased trap sites or defects via the excess Na^+ on the surface.

As for the PCE, the +NaI:1.5, 3, 6mM samples demonstrated the higher PCEs (18.82, 19.07, and 18.66%) and the +NaI:12mM sample showed smaller PCE (17.83%) than that of the FAI only spin-coated sample. The larger scattering of *J-V* characteristics for the +NaI:12mM sample (**Fig. 4.17**) is ascribed to the heterogeneous distribution of excess Na^+ on the surface. As a result, it was found that the appropriate amount of NaI addition into the FAI solution is beneficial to boost the photovoltaic performance of the 2-step perovskite solar cells. In this study, the NaI addition amount of 3 mM demonstrated the largest PCE.

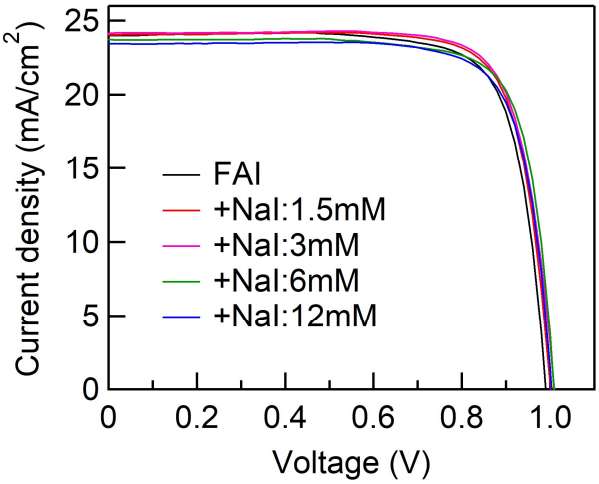

Fig. 4.16 *J-V* curves of the prepared perovskite solar cells.

Table 4.3 *J-V* characteristics of the prepared perovskite solar cells. The values are averages of 15 cells.

Samples	J_{SC} (mA/cm^2)	V_{OC} (V)	*FF*	PCE (%)
FAI only	23.85	0.985	0.771	18.12
+NaI:1.5mM	24.09	1.000	0.781	18.82
+NaI:3mM	24.16	1.005	0.785	19.07
+NaI:6mM	23.74	1.004	0.783	18.66
+NaI:12mM	23.11	0.996	0.774	17.83

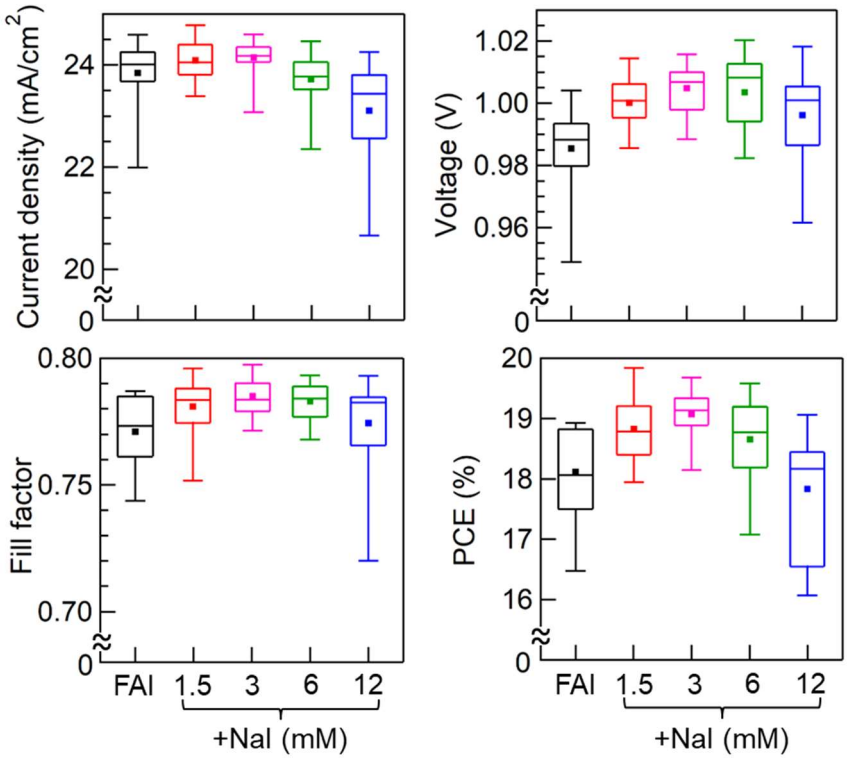

Fig. 4.17 Box plots of the J_{SC}, V_{OC}, *FF* and PCE of the prepared perovskite solar cells. 15 cells were prepared for each condition. In the box plot, center dots and horizontal lines represent average and median values.

Evaluation of stability in air

Then, stability in air of the prepared cells were evaluated. **Figure 4.18(a)** shows normalized PCEs as a function of time. After the *J-V* measurement, the devices were stored in dark and in air with humidity of ~50%, and these processes were repeated. The FAI only spin-coated sample gradually degraded after the fabrication, and its PCE decreased down to ~80% of the original value after ~350 h. Similarly, the +NaI:1.5mM and 3mM samples showed comparable degrading speed as the FAI only spin-coated sample. Their PCEs also decreased to ~80 % of the original value after ~350 h. As for the +NaI:6mM and 12mM samples, the PCE decreased to ~70% after 350 h. These results indicate that only the appropriate amount of NaI addition can enhance the PCE without the decrease of stability in air.

Figure 4.18(b) shows XRD patters at 10-18° for the prepared cells just after the fabrication and after 350 h. Due to a decomposition of perovskite into PbI_2, the peak intensity of PbI_2 slightly increased in all the cells after 350 h. Particularly, the increasing amount of PbI_2 peak intensity for the +NaI:12mM samples was larger than those of the other samples, which is in good agreement with the poor stability (**4.18(a)**). Although the obvious peak shift by the NaI addition was not confirmed in the XRD patterns of **Fig. 4.5(a)** and **Fig. 4.18(b)**, the small Na^+ ions might destabilize the perovskite structure, which possibly causes the poor stability by the large amount of NaI addition.

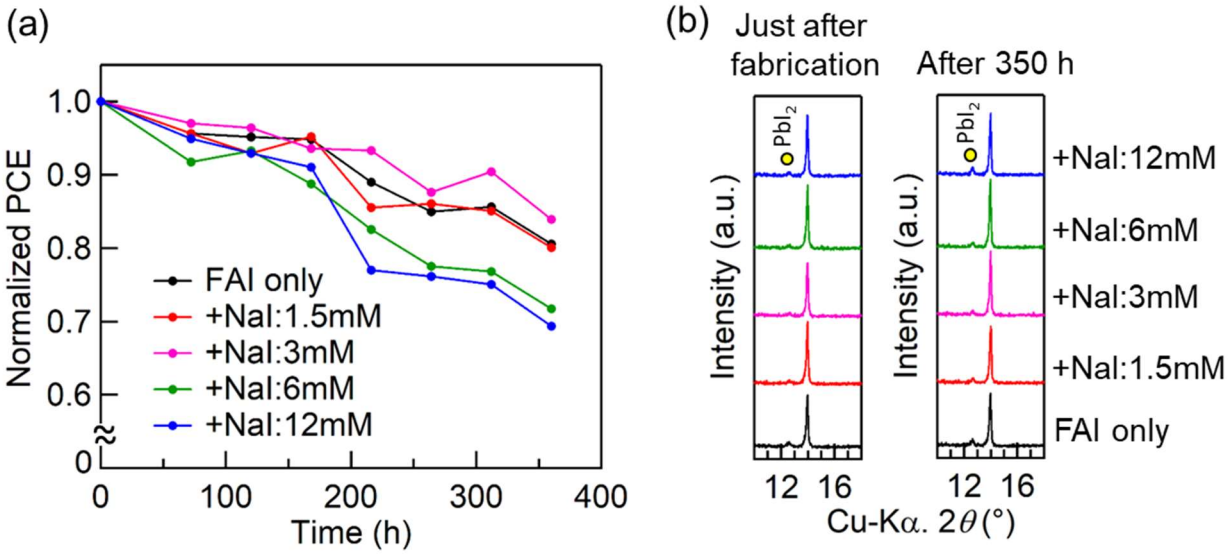

Figs. 4.18 (a) Normalized PCEs as a function of time. The cells were stored in the dark and in air with humidity of ~50% after the measuring, this process was repeated. (b) XRD patters of the prepared devices just after fabrication and after 350 h.

4.4 Conclusions

In conclusion, the bandgap gradients were formed at the top and bottom sides of the perovskite layer simultaneously by adding NaI into the additional FAI spin-coating solution. The NaI addition accelerated the grain growth of the perovskite layer and effectively decreased the grain boundary. The increase of grain size slightly improved the light absorption, while +NaI:12 mM showed decreased absorbance due to the microscopically flatter surface texture. The PL peak positions suggested that the NaI addition could form the

Na^+ doped layer with the larger bandgap at the top side with keeping the FA rich layer with smaller bandgap at the bottom side. On the other hand, the increase of the nonradiative recombination by the NaI addition was also implied from their relative PL intensities. As a result, the PCE was enhanced from 18.12% (FAI only spin-coating) to 19.07% (+NaI:3mM), while too much NaI addition decreased the PCE to 17.83% (+NaI:12mM).

The additional spin-coating of FAI solution with trace NaI addition on the 2-step prepared perovskite layer can produce the bandgap gradients at the both top and bottom sides. In addition, the appropriate amount of NaI addition is beneficial to enhance the photovoltaic performance.

Most part of this chapter will be published in *ACS Appl. Energy Mater*. (accepted).

References

[1] Y. Okamoto, Y. Suzuki, Perovskite solar cells prepared by a new 3-step method including a PbI_2 scavenging step, *Mater. Sci. Semicond. Process*., **71**, 1-6 (2017).

[2] Y. Okamoto, T. Yasuda, M. Sumiya, Y. Suzuki, Perovskite solar cells prepared by advanced three-step method using additional $HC(NH_2)_2I$ spin-coating: efficiency improvement with multiple bandgap structure, *ACS Appl. Energy Mater*., **1**, 1389−1394 (2018).

[3] G. Kieslich, S. Sun, A. K. Cheetham, Solid-state principles applied to organic–inorganic perovskites: new tricks for an old dog, *Chem. Sci*., **5**, 4712-4715 (2014).

[4] M. Saliba, T. Matsui, K. Domanski, J. Y. Seo, A. Ummadisingu, S. M. Zakeeruddin, J. P. Correa-Baena, W. R. Tress, A. Abate, A. Hagfeldt, M. Grätzel, Incorporation of rubidium cations into perovskite solar cells improves photovoltaic performance. *Science,* **354**, 206−209 (2016).

[5] S. Bag, M. F. Durstock, Large perovskite grain growth in low-temperature solution-processed planar p-i-n solar cells by sodium addition, *ACS Appl. Mater. Interfaces*, **8**, 5053−5057 (2016).

[6] J. K. Nam, S. U. Chai, W. Cha, Y. J. Choi, W. Kim, M. S. Jung, J. Kwon, D. Kim, J. H. Park, Potassium incorporation for enhanced performance and stability of fully inorganic cesium lead halide perovskite solar cells, *Nano Lett*., **17**, 2028−2033 (2017).

[7] R. D. Shannon, Revised effective ionic radii and systematic studies of interatomic distances in halides and chalcogenides. *Acta. Cryst*., **A 32**, 751–767 (1976).

[8] J. Chang, Z. Lin, H. Zhu, F. H. Isikgor, Q. H. Xu, C. Zhang, Y. Haoa, J. Ouyang, Enhancing the photovoltaic performance of planar heterojunction perovskite solar cells by doping the perovskite layer with alkali metal ions, *J. Mater. Chem. A*, **4**, 16546–16552 (2016).

[9] W. Zhao, Z. Yao, F. Yu, D. Yang, S. (F). Liu, Alkali metal doping for improved $CH_3NH_3PbI_3$ perovskite solar cells, *Adv. Sci.,* **5**, 1700131 (2018).

[10] M. R. Filip, G. E. Eperon, H. J. Snaith, F. Giustino, Steric engineering of metal-halide perovskites with tunable optical band gaps, Nat. Commun., **5**, 5757 (2014).

[11] L. Dimesso, M. Wussler, T. Mayer, E. Mankel, W. Jaegermann, Inorganic alkali lead iodide semiconducting APbI3 (A = Li, Na, K, Cs) and NH_4PbI_3 films prepared from solution: Structure, morphology, and electronic structure, *AIMS Mater Sci.*, **3**, 737-755 (2016).

[12] M.C. Kim, B. J. Kim, D.Y. Son, N. G. Park, H. S. Jung, M. Choi, Observation of enhanced hole extraction in Br concentration gradient perovskite materials, *Nano Lett*. **16**, 5756-5763 (2016).

[13] K. T. Cho, S. Paek, G. Grancini, C. Rolda´n-Carmona, P. Gao, Y. Lee, M. K. Nazeeruddin, Highly efficient perovskite solar cells with a compositionally engineered perovskite/hole transporting material interface, *Energy Environ. Sci.*, **10**, 621–627 (2017).

[14] H. Zheng, J. Dai, J. Duan, F. Chen, G. Zhu, F. Wanga, C. Xu, Temperature-dependent photoluminescence properties of mixed-cation methylammonium–formamidium lead iodide $[HC(NH_2)_2]_x[CH_3NH_3]_{1-x}PbI_3$ perovskite nanostructures, *J. Mater. Chem. C*, **5**, 12057-12061 (2017).

[15] F. Ji, L. Wang, S. Pang, P. Gao, H. Xu, G. Xie, J. Zhang, G. Cui, A balanced cation exchange reaction toward highly uniform and pure phase $FA_{1-x}MA_xPbI_3$ perovskite films, *J. Mater. Chem. A*, **4**, 14437-14443, (2016).

[16] B. Slimi, M. Mollar, I. B. Assaker, I. Kriaa, R. Chtourou, B. Marí, Perovskite $FA_{1-x}MA_xPbI_3$ for solar cells: films formation and properties, *Energy Procedia*, **102**, 87−95 (2016).

[17] Y. Fan, H. Qin, W. Ye, M. Liu, F. Huang, D. Zhong, Improving the stability of methylammonium lead iodide perovskite solar cells by cesium doping, *Thin Solid Films,* **667**, 40–47 (2018).

[18] T. W. Ng, C. Y. Chan, M. F. Lo, Z. Q. Guan, C. S. Lee, Formation chemistry of perovskites with mixed iodide/chloride content and the implications on charge transport properties, *J. Mater. Chem. A*, **3**, 9081-9085 (2015).

[19] N. G. Park, Methodologies for high efficiency perovskite solar cells. *Nano Convergence*, **3:15**, (2016).

[20] D. W. DeQuilettes, S. M. Vorpahl, S. D. Stranks, H. Nagaoka, G. E. Eperon, M. E. Ziffer, H. J. Snaith, D.

S. Ginger, Impact of microstructure on local carrier lifetime in perovskite solar cells. *Science*, **348**, 683–686 (2015).

Chapter 5

Summary and Conclusions

Chapter 5: Summary and Conclusions

The band alignment of each layer in perovskite solar cells is important to achieve high photovoltaic performance. As for the perovskite light absorbing layer, the formation of the bandgap gradients at the both top and bottom sides is a promising way to enhance the power conversion efficiency (PCE). However, the formation of bandgap gradient at the bottom side is difficult for the wet processes, such as spin-coating and dipping method, since the composition difference is produced by post treatments. In general, the post-treatment can form the bandgap gradient only at the top surface side. Therefore, in this thesis, the author attempted to develop a new 3-step method using additional MAI/FAI solution which forms the bandgap gradients at the both top and bottom sides of the perovskite layer and also enhances the photovoltaic performance.

In Chapter 2, the conversion of unreacted PbI_2 into perovskite phase and the compositional control were demonstrated using an additional spin-coating of MA(I/Br) solutions (3^{rd} step) on the 2-step prepared perovskite layer. The additional spin-coating successfully converted the unreacted PbI_2 into perovskite phase, and it improved the light absorption of the perovskite layer. Furthermore, the additional spin-coating of MA(I/Br) solutions formed $MAPbI_{3-x}Br_x$ by substituting I^- with Br^- in $MAPbI_3$, which changed the bandgap of the perovskite layer. As for the morphological effects, the formation of networks and decrease of grain boundary in the perovskite layer were observed by the liquid-phase assisted grain growth. The additional MAI spin-coating increased both J_{SC} and V_{OC}, which resulted in the large improvement of PCE from 12.9% to 14.4%. Furthermore, the stability in air was also improved by the additional spin-coating.

In Chapter 3, the multiple bandgap structure was formed by producing the bandgap gradients at the bottom side of the perovskite layer using the additional FAI spin-coating on the 2-step prepared perovskite layer. The additional FAI spin-coating transformed $MAPbI_3$ into $FA_xMA_{1-x}PbI_3$ by substituting the MA^+ with FA^+. Also, the unreacted PbI_2 was converted into FA rich $FA_yMA_{1-y}PbI_3$ ($y > x$) with the smaller bandgap. These FA^+ concentration difference produced the multiple bandgap structure at the bottom side of perovskite layer. As for the effects on the photovoltaic performance, J_{SC} was improved by the FAI spin-coating without a decrease of V_{OC} compared with MAI spin-coated cell due to the multiple bandgap structure. These improvements resulted in the enhancement of PCE from 16.3% (MAI spin-coated cell) to 17.2% (FAI spin-coated cell).

In Chapter 4, the simultaneous formation of bandgap gradients at the both top and bottom sides of perovskite layer were carried out by adding NaI into the FAI solution. The PL measurement suggested that Na^+ was doped only at the top side of perovskite layer and enlarged the bandgap with keeping the bandgap gradient at the bottom side. Additionally, the NaI addition accelerated the grain growth of the perovskite layer and effectively decreased the grain boundary. On the other hand, the increase of non-radiative recombination by the added Na^+ was also suggested. Because of these effects, the PCE was enhanced from 18.12% (FAI only spin-coating) to 19.07% (+NaI:3mM), while too much NaI addition decreased the PCE to 17.83% (+NaI:12mM).

As a whole, the new 3-step method using additional spin-coating of FAI-NaI solution on the 2-step prepared perovskite layer was developed here. The formation of bandgap gradient at the bottom side of perovskite layer is difficult by the wet fabrication processes. However, the developed 3-step method realized the simultaneous formation of the bandgap gradients at the both top and bottom sides just by a simple spin-coating process. The 3-step method is thus effective to enhance the photovoltaic performance of perovskite solar cells. Since the further control of the band alignment is possible by changing the spin-coating solution, such as CsI and KI, the 3-step method opens a new way to enhance the conversion efficiency of perovskite solar cells. Finally, the author hopes that this new 3-step method strongly supports the development and productization of perovskite solar cells.

Appendices

Appendices

In the main part of this thesis, the author described about the studies on improvement of the band alignment of a perovskite light absorbing layer. This idea is based on author's previous studies which focused on controlling a band alignment of an electron transport layer of perovskite solar cells. Therefore, those studies will be described as the appendices Appendix 1 and 2.

In addition, the perovskite solar cell has also attracted much attention as a top cell of tandem type solar cell with a silicon (Si) solar cell, since the bandgap of perovskite solar cell is suitable to absorb the light which cannot be absorbed by Si solar cells. Therefore, the author also focused on the silicon solar cells and worked on the improvement of production process of high purity Si at the Sumiya laboratory, National Institute for Materials Science (NIMS). This research will be also described as the Appendix 3.

Appendix 1: Perovskite solar cells using $BaTiO_3/TiO_2$ double mesoporous layer for electron transport

A1.1 Introduction

As the author described in the main part, the electrons and holes generated in a perovskite light absorbing layer ($CH_3NH_3PbI_3$, $MAPbI_3$) are transported to outside through a conduction band of electron transport layer (ETL) and a HOMO level of hole transport layer (HTL). For the electron transport, the conduction band of ETL has to be located at a lower position than that of $MAPbI_3$, since the band offset is a driving force of the electron transport. However, in the electron transporting process, a V_{OC} loss usually occurs due to the band offset between the conduction band of ETL and $MAPbI_3$. Therefore, the V_{OC} and conversion efficiency can be improved by optimizing the oxide material used for the ETL. In this chapter, the author focused on a control of the band alignment in the ETL to improve the photovoltaic performance of perovskite solar cells.

As an ETL material, anatase TiO_2 is the most popular oxide material. Meanwhile, some other oxides, such as $SrTiO_3$ [1,2], Al_2O_3 [3,4], ZnO [5,6], SnO_2 [7], $BaSnO_3$ [8], and ZrO_2 [9], have also been studied as the ETL materials. For example, $SrTiO_3$ has the conduction band at a higher position than that of anatase TiO_2 [10], and hence, the band offset between ETL and perovskite layer becomes smaller, which results in larger V_{OC} [1,2]. In addition, a combination of those other oxide materials and TiO_2 has also attracted much attention to improve the photovoltaic performance. For example, by forming a thin $SrTiO_3$ layer at the surface of TiO_2 layer (core-shell structure), a gradient of conduction band was obtained, and it was effective to improve the electron transport and the photovoltaic performance of dye-sensitized solar cells [11].

$BaTiO_3$ also has a potential to improve the band alignment of perovskite solar cells. $BaTiO_3$ has a tetragonal perovskite structure (ABO_3) and has been widely used as a material for a ferroelectric device [12]. The bandgap of $BaTiO_3$ is similar to that of anatase TiO_2 (~3.2 eV), but the conduction band is located at higher position than that of anatase TiO_2 [10]. Therefore, the multiple bandgap structure can be obtained by combining with TiO_2 mesoporous layer, and it will improve the photovoltaic performance of perovskite solar cells. In this

chapter, the double mesoporous layer composed of TiO_2 mesoporous bottom layer and $BaTiO_3$ mesoporous top layer was prepared to improve the photovoltaic performance of perovskite solar cells (**Fig. A1.1**).

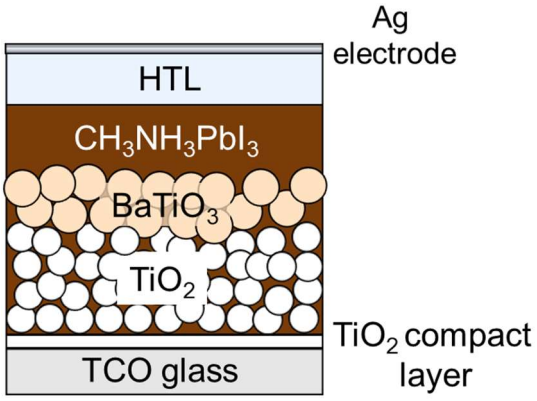

Fig. A1.1 Schematic illustration of the perovskite solar cells using $BaTiO_3/TiO_2$ double mesoporous layer.

A1.2. Experimental

A1.2.1 Preparation of TiO_2 and $BaTiO_3$ pastes

Firstly, TiO_2 and $BaTiO_3$ pastes for the mesoporous layers were prepared. TiO_2 powder with particle size of ~30 nm (P-25, Nippon Aerosil) and $BaTiO_3$ powder with particle size of ~50 nm (KZM-50, Sakai Chemical industry) were used for the preparation of pastes (**Fig. A1.2**). The powder: 0.1 g was mixed with ethyl cellulose: 0.05 g (80~120 cps, Nacalai tesque), α-Terpineol: 0.37 mL (96.0 %, Alfa Aesar), lauric acid: 5 mg (>98.0 %, Tokyo chemical industry) and ethanol: 0.8 mL. The mixture was stirred for 30 min with heating at 120°C and ultrasonicated for 1 h.

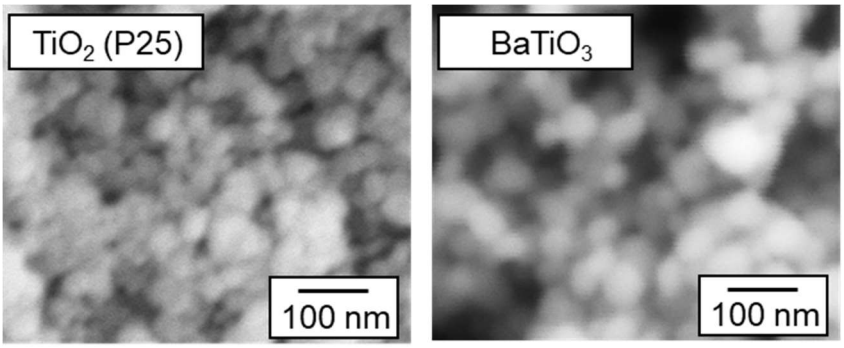

Fig. A1.2 SEM images of TiO_2 (P25) and $BaTiO_3$ powers used in this chapter.

A1.2.2 Preparation method of perovskite solar cell

Preparation of electron transport layer (ETL) on TCO glass

Transparent conductive oxide (TCO, Type-0052, 10 Ω/sq., Geomatec) glasses were used as the substrate. The TCO substrates were patterned by etching with Zn powder (>96.0%, Tokyo Chemical Industry) and 1 M HCl (Wako Pure Chemical Industry). After the patterning, the TCO substrates were washed in distilled water, ethanol and acetone by the ultrasonication and dried in air. For the preparation of TiO_2 compact layer, a 0.15 M titanium diisopropoxide bis (acetylacetonate) (TAA, 75 % in isopropanol, Sigma-Aldrich) solution mixed

with 1-butanol was spin-coated on the TCO substrates for 20 s at 2000 rpm, followed by annealing at 125°C for 5 min. Then, the spin-coating was repeated two times with a 0.3 M TAA solution. The coated substrates were annealed at 500°C for 30 min in air.

Then, the TiO_2 mesoporous bottom layer was prepared by spin-coating the prepared TiO_2 paste for 25 s at 4000 rpm and by annealing at 500°C for 15 min. The substrates were immerged in a 40 mM $TiCl_4$ solution with distilled water at 70°C for 30 min. After that, the substrates were rinsed with ethanol and annealed at 500°C for 15 min. The $BaTiO_3$ mesoporous top layer was prepared by spin-coating the prepared $BaTiO_3$ paste on the TiO_2 mesoporous bottom layer for 25 s at 4000 rpm. The thickness of $BaTiO_3$ layer was controlled by repeating the spin-coating of $BaTiO_3$ paste (1, 2 and 3 times, denoted as S, D and T, respectively). The coated substrate was annealed at 500°C for 45 min.

Preparation of perovskite layer, hole transport layer (HTL) and metal electrodes

The perovskite layers and the HTLs were prepared in air. The ETL coated substrates and a 1 M PbI_2 solution (>98.0%, Tokyo Chemical Industry) in DMF (99.5%, Nacalai tesque) were pre-heated at 60°C. The PbI_2 solution was spin-coated on the substrates at 3000 rpm for 20 s (1^{st} step). After annealing at 60°C for 10 min, the substrates were dipped in a 10 mg/mL solution of MAI (98%, Wako Pure Chemical Industry) dissolved in isopropanol (99.5%, Nacalai tesque) for 20 s, followed by rinsing with isopropanol and by annealing at 60°C for 10 min (2^{nd} step). The HTLs with the thickness of ~200 nm were prepared by spin-coating a spiro-MeOTAD solution at 4000 rpm for 35 s. The spiro-MeOTAD solution in 1 mL chlorobenzene (99%, Nacalai tesque) was composed of 73 mg spiro-MeOTAD (99%, Sigma-Aldrich), 28.8 µL 4-*tert*-butylpyridine (TBP, 96.0%, Sigma-Aldrich) and 17 µL solution of [520 mg/mL lithium bis(trifluoromethylsulphonyl)imide salt (>98.0%, Tokyo Chemical Industry) in acetonitrile (99.5%, Wako Pure Chemical Industry)]. Finally, Ag electrodes with the thickness of ~50 nm were deposited on the HTLs with a thermal evaporator under the pressure of 3×10^{-5} Torr.

A1.2.3 Characterizations

Cross-section and surface morphology of the prepared ETLs and perovskite layers were observed by scanning electron microscopy (SEM, SU-70, Hitachi High-Technologies, JSM-5600LV, JEOL). Elementary analysis of the prepared ETL was carried out by SEM-EDS (Miniscope TM3000Plus, Hitachi High-Technologies). Optical transmittance and absorbance spectra of the prepared perovskite layers on ETLs were measured by UV-Vis (UV3100PC, Shimadzu). Current density-voltage (*J-V*) characteristics were measured with a solar simulator (XES-40S1, SAN-EI Electric) calibrated to AM 1.5, 100 mW/cm^2 with a standard silicon photodiode (BS-520BK, Bunkokeiki). The active area was limited to 8.7 mm^2 by using a black mask. The voltage step and delay time were 20 mV and 50 ms, respectively. Crystal structures of the prepared perovskite layers on ETLs were characterized by X-ray diffraction (XRD, Multiflex, Cu-K_α, 40 kV and 40 mA, Rigaku). The IPCE spectra were recorded with a spectral response & IPCE measurement system (SM-250, Bunkoukeiki). Steady-state photoluminescence were measured by Ramascope System1000 (Renishaw) with an excitation laser of wavelength 325 nm (IK5651R-G, Kimmon).

A1.3 Results and Discussion

A1.3.1 Microstructure observation of electron transport layer (ETL)

Fig. A1.3 shows the cross-sectional SEM images of the prepared ETLs on the TCO glasses. The thickness of mesoporous layer in TiO_2(S) was ~150-200 nm. By spin-coating the $BaTiO_3$ paste, the thickness of ETL slightly increased. Since the $BaTiO_3$(T)/TiO_2(S) had the thickness of ~250 nm, the mesoporous $BaTiO_3$ layers with the thickness of ~50-100 nm were formed on the TiO_2 mesoporous layer. As for the $BaTiO_3$ spin-coated samples, some rough surfaces composed of aggregated $BaTiO_3$ particles were also observed.

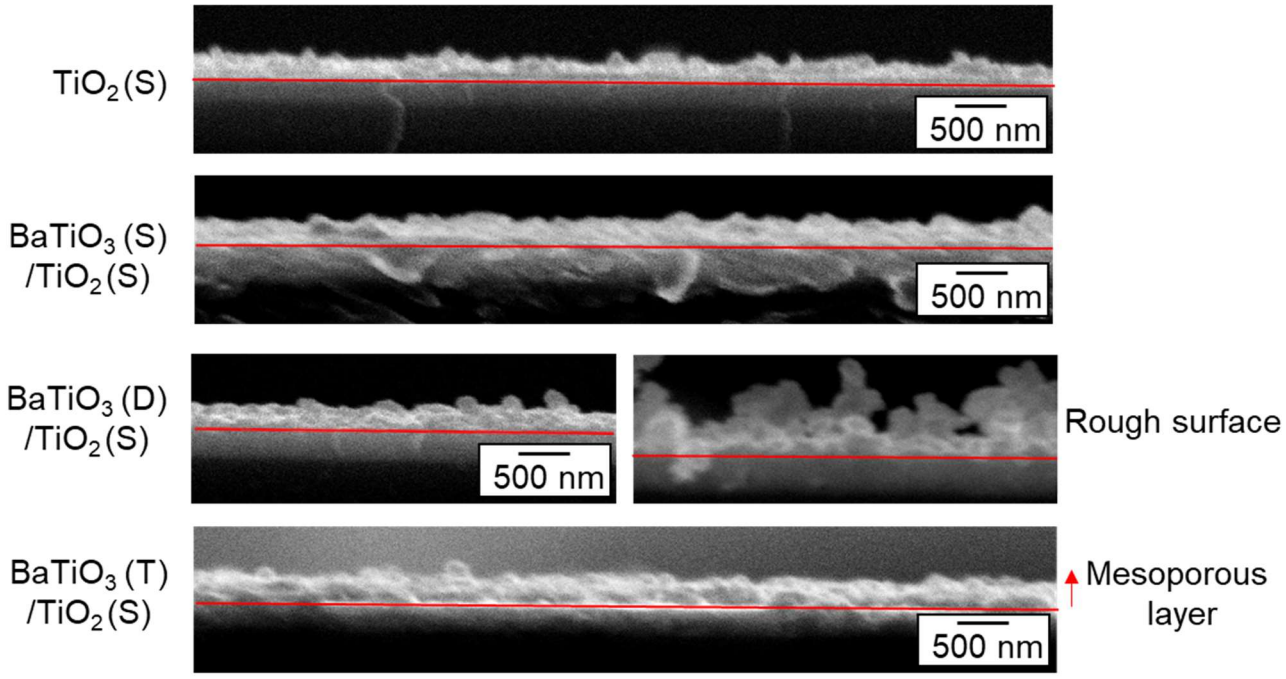

Fig. A1.3 Cross-sectional SEM images of the prepared ETLs on TCO glasses.

The increase of ETL thickness (~50-100 nm) by the $BaTiO_3$ paste was confirmed from **Fig. A1.3**, but the increased amount was smaller than the expectation considering the particle size of $BaTiO_3$ powder (~50 nm). Hence, the elemental analysis of the ETL surface was carried out by SEM-EDX to make sure the existence of $BaTiO_3$. The atomic % of Ba, Ti, and O at 10 points on the prepared ETLs were analyzed by a point analysis mode as shown in **Fig. A1.4(a)** (only 5 points are shown in the **Fig. A1.4(a)**. The other 5 points were also analyzed in the different area). The scattering of the measured Ba ratio is shown in **Fig. A1.4(b)**, and the averaged atomic % of the 10 points are summarized in **Table A1.1**. The barium (Ba) was not detected in the TiO_2(S) sample, while the atomic % of Ba increased with increasing the spin-coating number of $BaTiO_3$ paste, which indicates the existence of $BaTiO_3$ particles and the increase in thickness of $BaTiO_3$ mesoporous layer. In addition, since Ba was detected at all the analyzed 10 points, the $BaTiO_3$ particles may well-cover the TiO_2 mesoporous bottom layer. The different ratio of titanium (Ti) and oxygen (O) from the theoretical ratio of TiO_2 or $BaTiO_3$ is attributable to the detection of oxygen from TCO glass, since indium (In), tin (Sn) and silicon (Si), which were included in the TCO glass, were also detected.

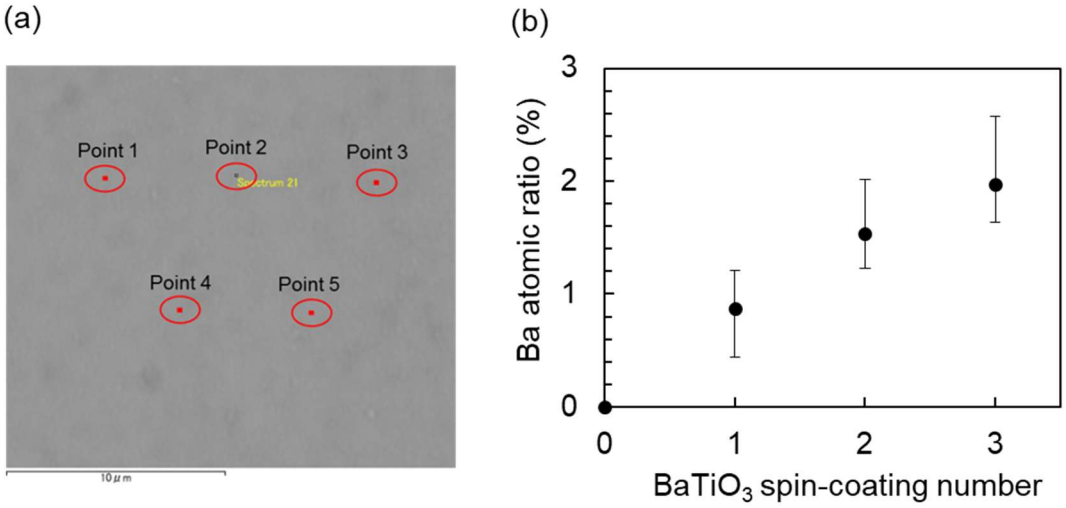

Figs. A1.4 (a) Surface element analysis by EDX using a point analysis mode. (b) Relationship between the atomic % of Ba and $BaTiO_3$ paste spin-coating number.

Table A1.1 Atomic % of Ba, Ti, and O at the surface of ETLs. The values are average of 10 points.

Samples	Ba (%)	Ti (%)	O (%)
TiO_2(S)	0.0	9.0	91.0
$BaTiO_3$(S)/TiO_2(S)	0.9	13.1	86.0
$BaTiO_3$(D)/TiO_2(S)	1.5	13.2	85.3
$BaTiO_3$(T)/TiO_2(S)	1.9	16.0	82.1

A1.3.2 Evaluation of photovoltaic performance

The *J-V* characteristics of the prepared cells are summarized in **Table A1.2**. These values are averages of 4 cells. TiO_2(S) demonstrated J_{SC} of 18.3 mA/cm^2, V_{OC} of 0.88 V, *FF* of 0.61, and PCE of 9.89%. As for the cells with $BaTiO_3$ mesoporous layers, $BaTiO_3$(S)/TiO_2(S) showed the comparable photovoltaic performance to TiO_2(S). By increasing the spin-coating number of $BaTiO_3$ paste from 1 time ($BaTiO_3$(S)/TiO_2(S)) to 2 times ($BaTiO_3$(D)/TiO_2(S)), all the parameters were improved and a highly enhanced PCE of 12.4% was obtained. However, further increase of spin-coating number to 3 times ($BaTiO_3$(T)/TiO_2(S)) decreased the V_{OC} and *FF*, which resulted in the smaller PCE compared to $BaTiO_3$(D)/TiO_2(S). As a result, the largest PCE was obtained from the $BaTiO_3$(D)/TiO_2(S).

The similar *J-V* characteristics of $BaTiO_3$(S)/TiO_2(S) toTiO_2(S) may be due to the too thin thickness of $BaTiO_3$ top mesoporous layer. The decrease of the *J-V* characteristics for $BaTiO_3$(T)/TiO_2(S) is attributable to the too thick $BaTiO_3$ top mesoporous layer which may produce some negative effects. Since the photovoltaic performance largely depended on the spin-coating number of $BaTiO_3$ paste, the $BaTiO_3$ top mesoporous layer must be a key factor for the enhancement of photovoltaic performance in $BaTiO_3$(D)/TiO_2(S).

Table A1.2 *J-V* characteristics of the prepared perovskite solar cells. The values are averages of 4 cells.

Samples	J_{SC} (mA/cm^2)	V_{OC} (V)	*FF*	PCE (%)
TiO_2(S)	18.3	0.88	0.61	9.89
$BaTiO_3$(S)/TiO_2(S)	18.0	0.90	0.60	9.70
$BaTiO_3$(D)/TiO_2(S)	19.3	0.96	0.67	12.4
$BaTiO_3$(T)/TiO_2(S)	19.0	0.91	0.60	10.3

A1.3.3 Phase and crystal structure analysis of perovskite layer

To clarify reasons of the improved photovoltaic performance in $BaTiO_3$(D)/TiO_2(S), XRD analysis was carried out. **Figure A1.5** shows XRD patterns of the perovskite layers on TiO_2(S) and $BaTiO_3$(D)/TiO_2(S). The both samples had peaks corresponding to tetragonal $CH_3NH_3PbI_3$ ($MAPbI_3$) and relatively large peaks corresponding to unreacted PbI_2. The $MAPbI_3$ peaks were slightly larger and the unreacted PbI_2 peaks were smaller in $BaTiO_3$(D)/TiO_2(S) than those in TiO_2(S), which indicates the better conversion of PbI_2 into perovskite. It is still in controversial if the complete conversion of PbI_2 into perovskite is favorable to obtain the better photovoltaic performance in perovskite solar cells. Still, the decrease of unreacted PbI_2 by the conversion into perovskite can improve the photovoltaic performance [13].

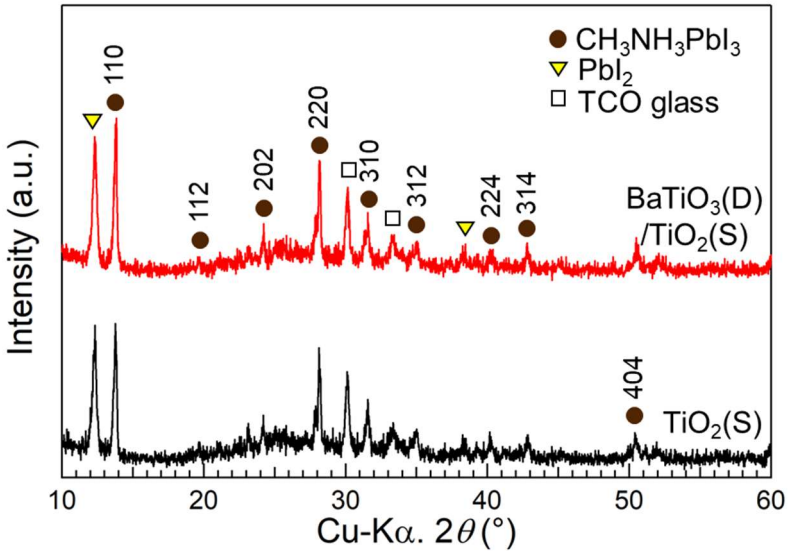

Fig. A1.5 XRD patterns of the prepared perovskite layers on TiO_2(S) and $BaTiO_3$(D)/TiO_2(S).

A1.3.4 Microstructure observation of perovskite layer and estimation of particle size distribution

Figure A1.6 show the surface SEM images of the perovskite layers on TiO_2(S), $BaTiO_3$(S)/TiO_2(S), $BaTiO_3$(D)/TiO_2(S), and $BaTiO_3$(T)/TiO_2(S) mesoporous layers. Distributions of perovskite particle size were estimated by analyzing the surface SEM images with a ImageJ as shown in **Fig. A.1.7**. The perovskite particles on the TiO_2(S) mesoporous layer had cubic shape, and the particle size was mainly distributed in ~0.4–0.8 μm. The perovskite particles on the $BaTiO_3$/TiO_2 mesoporous double layers had comparable particle shape to that of TiO_2(S), but the particle size was mainly distributed ~0.5–1.2 μm, which indicates the increase of particle size by the better crystal growth.

Appendix 1

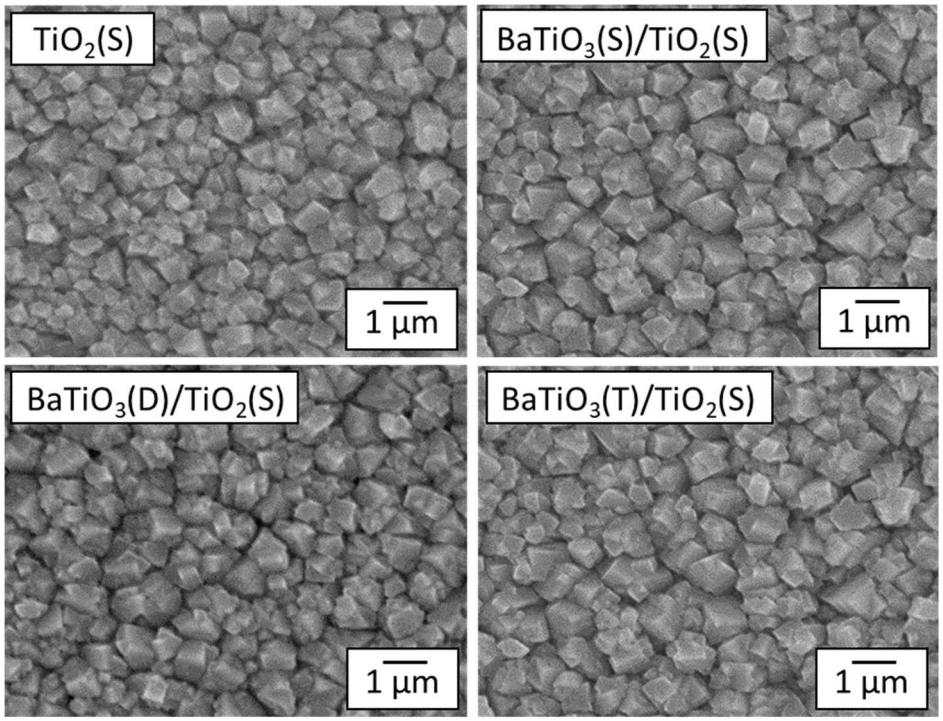

Fig. A1.6 Surface SEM images of the prepared perovskite layers on TiO_2(S), $BaTiO_3$(S)/TiO_2(S), $BaTiO_3$(D)/TiO_2(S), and $BaTiO_3$(T)/TiO_2(S) mesoporous layers.

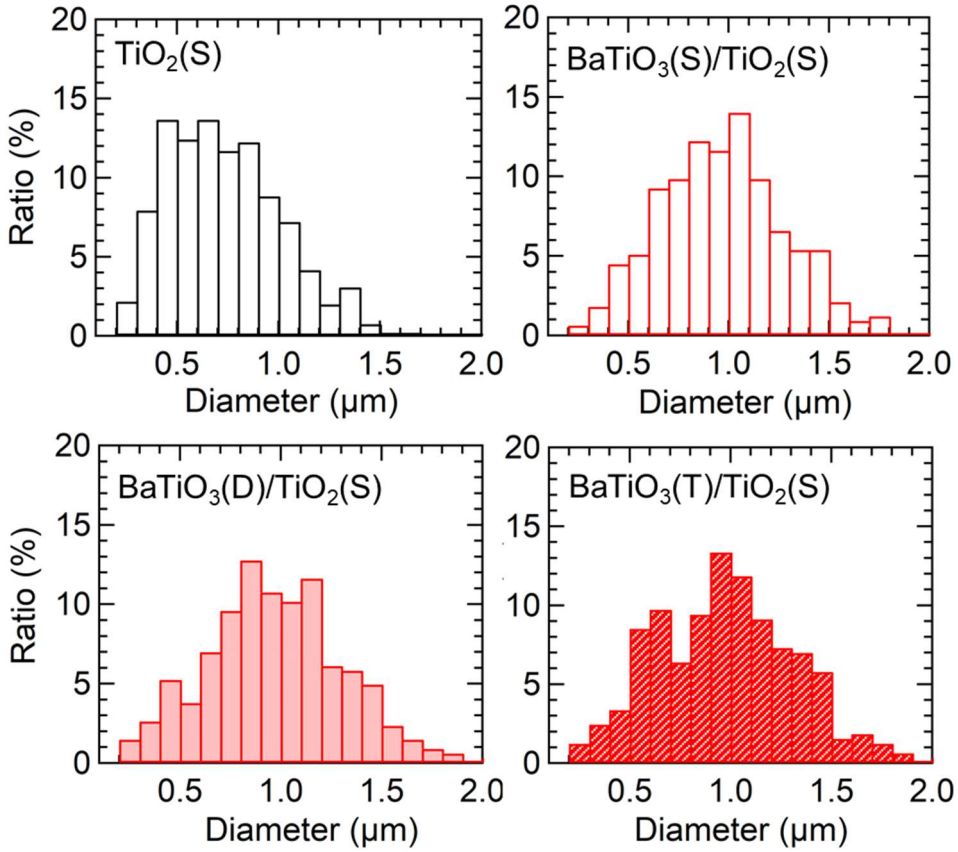

Fig. A1.7 Distribution of perovskite particle size estimated by analyzing the SEM images with a ImageJ.

To clarify the reason of larger particle size in the $BaTiO_3/TiO_2$ samples, surface SEM observation of PbI_2 layer (i.e., before dipping in MAI solution) was carried out. **Figure A1.8** shows the surface SEM images of the PbI_2 layers on TiO_2(S) and $BaTiO_3$(D)/TiO_2(S). The PbI_2 layer on TiO_2(S) had many pores and its surface was rough, while that on $BaTiO_3$(D)/TiO_2(S) was denser and smoother. $BaTiO_3$(S)/TiO_2(S) and $BaTiO_3$(T)/TiO_2(S) also had the similar morphology for PbI_2 layers. In the 2-step method, the $MAPbI_3$ particles are produced by the reaction between PbI_2 layer and MAI. The denser PbI_2 layer can provide more source to grow the perovskite crystals, and hence, the larger perovskite particles were formed on the $BaTiO_3/TiO_2$ mesoporous double layers.

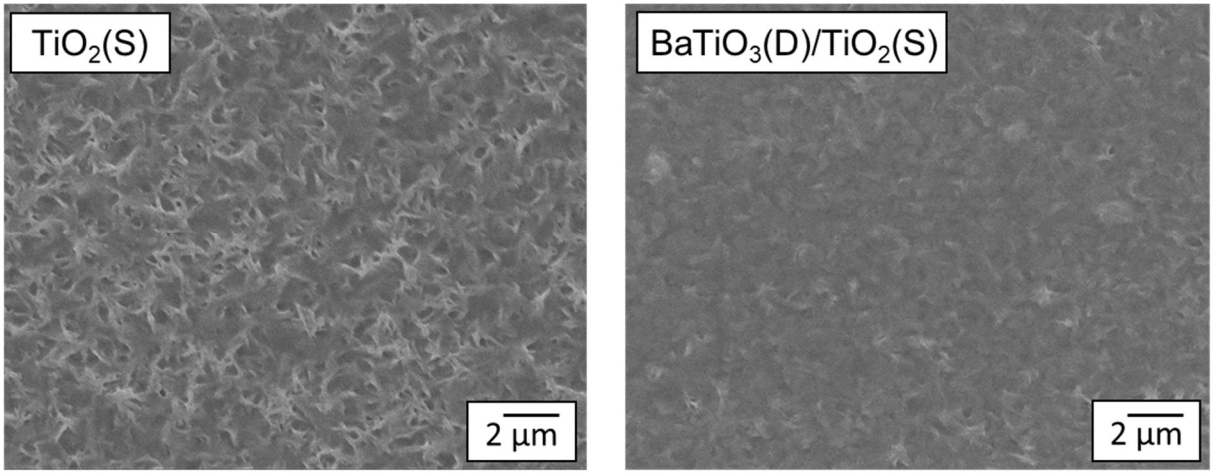

Fig. A1.8 Surface SEM images of the PbI_2 layers (i.e., before dipping in MAI solution) on TiO_2(S) and $BaTiO_3$(D)/TiO_2(S).

Figure A1.9 show the cross-sectional SEM images of the perovskite layers on TiO_2(S) and $BaTiO_3$(D)/TiO_2(S) mesoporous layers. In the both samples, the mesoporous/perovskite layer and perovskite capping layer were observed. The total thickness of these layers for TiO_2(S) was ~400 nm. The thickness of perovskite layer on $BaTiO_3$(D)/TiO_2(S) was comparable to that of TiO_2(S), but the surface seemed smoother than that of TiO_2(S) due to the larger perovskite particle. This smoother surface will increase the volume of perovskite layer and is effective to improve the light absorption.

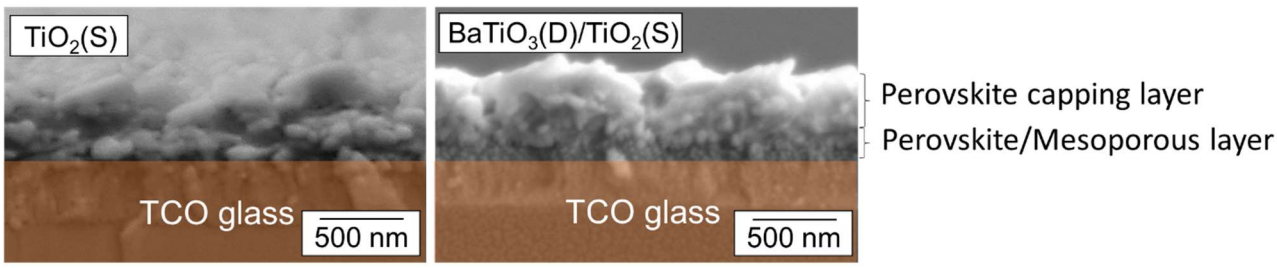

Fig. A1.9 Cross-sectional SEM images of the perovskite layers on TiO_2(S) and $BaTiO_3$(D)/TiO_2(S) mesoporous layers.

A1.3.5 Optical property analysis and estimation of bandgap of perovskite layer

Figures A1.10 show (a) absorbance and (b) transmittance spectra of the perovskite layers on TiO_2(S) and $BaTiO_3$(D)/TiO_2(S). The bandgaps were estimated using Tauc plots converted from the absorbance spectra. The both samples showed absorption edges at the ~780 nm and the comparable bandgaps of ~1.58 eV. This result indicates that the $BaTiO_3$ mesoporous top layer has no significant effect on the bandgap of perovskite layer. On the other hand, the transmittance of perovskite layer on the $BaTiO_3$(D)/TiO_2(S) was slightly lower than that on TiO_2(S), which indicates the better light absorption. This improved light absorption can be attributed to the better conversion of PbI_2 into perovskite, the larger volume of the perovskite layer, and light scattering effect by the larger perovskite crystals in $BaTiO_3$(D)/TiO_2(S) [14].

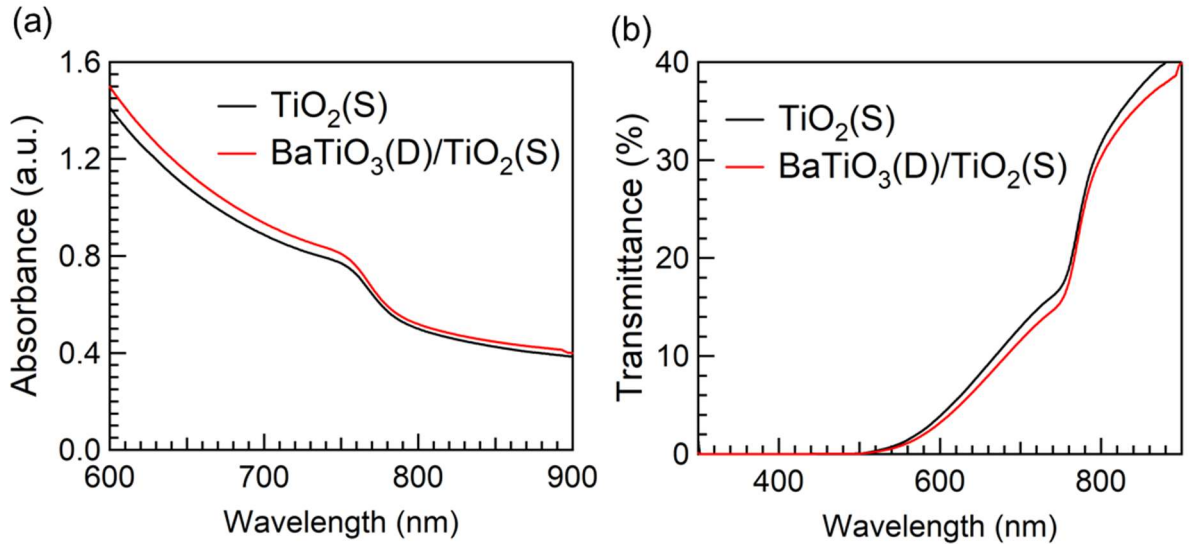

Figs. A1.10 (a) Absorbance and (b) transmittance spectra of the prepared perovskite layers on TiO_2(S) and $BaTiO_3$(D)/TiO_2(S).

Figure A1.11 shows IPCE spectra of the TiO_2(S) and $BaTiO_3$(D)/TiO_2(S) cells. The IPCE spectrum of $BaTiO_3$(D)/TiO_2(S) was larger than that of TiO_2(S), which is in a good agreement with the result of transmittance. Hence, the enhanced J_{SC} of $BaTiO_3$(D)/TiO_2(S) can be ascribed to the better light absorption by the better conversion of PbI_2 into perovskite, larger volume of perovskite layer, and the light scattering effect. Furthermore, the increase of perovskite particle size is effective to improve *FF*, since it decreases a number of the grain boundary and decreases a series resistance (R_S) [15]. The *R*s values were roughly estimated from the slope of *J-V* curve at around V_{OC}. Actually, the R_S of $BaTiO_3$(D)/TiO_2(S) was 11.1 Ω and it was smaller than that of TiO_2(S): 13.4 Ω, which contributed to the improved *FF* for $BaTiO_3$(D)/TiO_2(S).

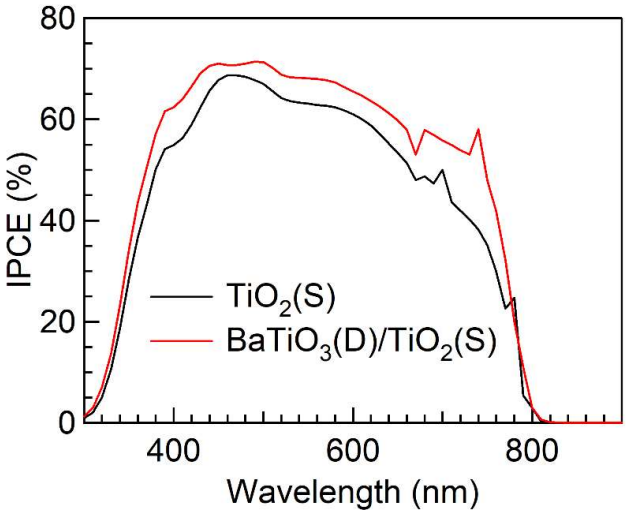

Fig. A1.11 IPCE spectra of the TiO_2(S) and $BaTiO_3$(D)/TiO_2(S) cells.

A1.3.6 Evaluation of electron transport efficiency

Then, in order to investigate the reason of improvement in V_{OC} for the $BaTiO_3$(D)/TiO_2(S), photo luminescence (PL) of the perovskite layers were measured. **Figure A1.12** shows the PL spectra of the perovskite layers on the TiO_2(S) and $BaTiO_3$(D)/TiO_2(S) mesoporous layers. The excitation laser was irradiated from the TCO glass substrate side. The PL peaks at ~775 nm were obtained for the both TiO_2(S) and $BaTiO_3$(D)/TiO_2(S) samples, which corresponded to a band to band shift of $MAPbI_3$. On the other hand, the PL intensity was significantly quenched in $BaTiO_3$(D)/TiO_2(S) compared to that of TiO_2(S) in spite of the comparable thickness of the perovskite layers. This suggests that the electrons were transported from perovskite layer to ETL more efficiently in $BaTiO_3$(D)/TiO_2(S) than TiO_2(S), which is effective to decrease the carrier recombination.

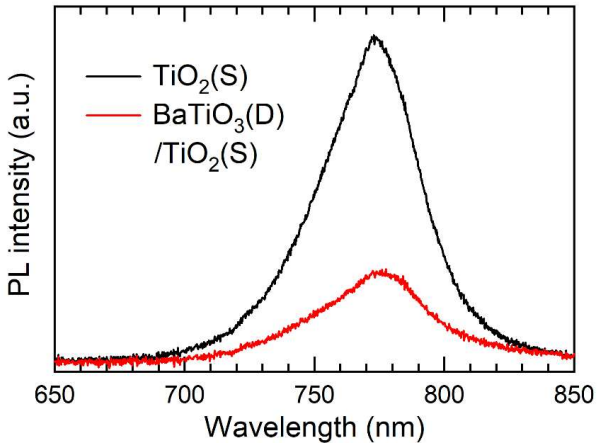

Fig. A1.12 PL spectra of the perovskite layers on the TiO_2(S) and $BaTiO_3$(D)/TiO_2(S) mesoporous layers measured from TCO glass side.

It was reported that the grain boundary produces trap site of the generated carriers and leads to non-radiative recombination [16]. The increase of perovskite particle size is effective to decrease the number of grain boundary, which can reduce the carrier recombination. Therefore, the increase of perovskite particle size

in the $BaTiO_3$(D)/TiO_2(S) is a possible reason for the better electron transport. Furthermore, as described in the introduction part, the multiple bandgap structure can be obtained by covering TiO_2 with $BaTiO_3$. In this study, the top surface of TiO_2 mesoporous bottom layer was covered by the $BaTiO_3$ mesoporous top layer. Therefore, the multiple bandgap structure was formed at the interface of TiO_2 and $BaTiO_3$ mesoporous layers, which is also effective to improve the electron transport and the V_{OC}.

A.1.4 Conclusions

In conclusion, the author demonstrated the enhanced photovoltaic performance of perovskite solar cells from 9.89% to 12.4% by forming the $BaTiO_3$ mesoporous top layer on the standard TiO_2 ETL. The photovoltaic performance largely depended on the spin-coating number of the $BaTiO_3$ paste, which indicates that the thickness of the $BaTiO_3$ mesoporous layer is important factor on the photovoltaic performance. The size of perovskite particles on $BaTiO_3$/TiO_2 mesoporous top layers were larger than that on TiO_2(S) due to the denser PbI_2 layer. The better PbI_2 conversion into perovskite and the larger perovskite particles in $BaTiO_3$(D)/TiO_2(S) increased the light absorption, and it resulted in the increase of J_{SC}. Furthermore, the electron transport was improved in $BaTiO_3$(D)/TiO_2(S) possibly due to the decrease of grain boundary and the multiple bandgap structure, which contributed to the improvement of V_{OC}. These results demonstrate that the use of $BaTiO_3$ as the mesoporous top layer is an effective way to boost the photovoltaic performance of TiO_2-based perovskite solar cells.

Most part of this chapter has been published in *J. Phys. Chem. C*, **120**, 13995−14000 (2016). http://dx.doi.org/10.1021/acs.jpcc.6b04642 [17].

References

[1] A. Bera, K. Wu, A. Sheikh, E. Alarousu, O. F. Mohammed, T. Wu, Perovskite oxide $SrTiO_3$ as an efficient electron transporter for hybrid perovskite solar cells, *J. Phys. Chem. C*, **118**, 28494–28501 (2014).

[2] C. Wang, Y. Tang, Y. Hu, L. Huang, J. Fu, J. Jin, W. Shi, L. Wanga, W. Yang, Graphene/$SrTiO_3$ nanocomposites used as an effective electron-transporting layer for high performance perovskite solar cells, *RSC Adv.*, **5**, 5204-52047 (2015).

[3] M. M. Lee, J. Teuscher, T. Miyasaka, N. T. Murakami, H. J. Snaith, Efficient hybrid solar cells based on meso-superstructured organometal halide perovskites. *Science*, **338**, 643–647 (2012).

[4] B. Suarez, V. Gonzalez-Pedro, T. S. Ripolles, R. S. Sanchez, L. Otero, I. Mora-Sero, Recombination study of combined halides (Cl, Br, I) perovskite solar cells, *J. Phys. Chem. Lett.*, **5**, 1628–1635 (2014).

[5] D.Y. Son, J. H. Im, H. S. Kim, N. G. Park, 11% efficient perovskite solar cell based on ZnO nanorods: an effective charge collection system, *J. Phys. Chem. C*, **118**, 16567–16573 (2014).

[6] M. H. Kumar, N. Tantara, S. Dharani, M. Grätzel, S. Mhaisalkar, P. P. Boix, N. Mathews, Flexible, low-temperature, solution processed ZnO-based perovskite solid state solar cells, *Chem.Commun*., **49**, 11089–11091 (2013).

[7] W. Ke, G. Fang, Q. Liu, L. Xiong, P. Qin, H. Tao, J. Wang, H. Lei, B. Li, J. Wan, Low-temperature solution-processed tin oxide as an alternative electron transporting layer for efficient perovskite solar cells, *J. Am. Chem. Soc*., **137**, 6730–6733 (2015).

[8] L. Zhu, Z. Shao, J. Ye, X. Zhang, X. Pan, S. Dai, Mesoporous $BaSnO_3$ layer based perovskite solar cells, *Chem. Commun*., **52**, 970–973 (2016).

[9] D. Bi, S. J. Moon, L. Häggman, G. Boschloo, L. Yang, E. M. J. Johansson, M. K. Nazeeruddin, M. Grätzel, Using a two-step deposition technique to prepare perovskite ($CH_3NH_3PbI_3$) for thin film solar cells based on ZrO_2 and TiO_2 mesostructures, *RSC Adv*., **3**, 18762–18766 (2013).

[10] J. Fujisawa, T. Eda, M. Hanaya, Comparative study of conduction-band and valence-band edges of TiO_2, $SrTiO_3$, and $BaTiO_3$ by ionization potential measurements, *Chem. Phys. Lett*, **685**, 23–26 (2017).

[11] Y. Diamant, S. G. Chen, O. Melamed, A. Zaban, Core-shell nanoporous electrode for dye sensitized solar cells: the effect of the $SrTiO_3$ shell on the electronic properties of the TiO_2 core, *J. Phys. Chem. B*, **107**, 1977-1981 (2003).

[12] M. Acosta, N. Novak, V. Rojas, S. Patel, R. Vaish, J. Koruza, G. A. Rossetti, J. Rödel, $BaTiO_3$-based piezoelectrics: Fundamentals, current status, and perspectives, *Appl. Phys. Rev*., **4**, 041305 (2017).

[13] Q. Chen, H. Zhou, T. B. Song, S. Luo, Z. Hong, H. S. Duan, L. Dou, Y. Liu and Y. Yang, Controllable self-induced passivation of hybrid lead iodide perovskites toward high performance solar cells, *Nano Lett.*, **14**, 4158-4163 (2014).

[14] J. H. Im, I. H. Jang, N. Pellet, M. Grätzel, N. G. Park, Growth of $CH_3NH_3PbI_3$ cuboids with controlled size for high-efficiency perovskite solar cells, Nat. *Nano-technol*., **9**, 927–932 (2014).

[15] J. H. Lu, Y. L. Yu, S. R. Chuang, C. H. Yeh, C. P. Chen, High-performance, semitransparent, easily tunable vivid colorful perovskite photovoltaics Featuring Ag/ITO/Ag microcavity structures. *J. Phys. Chem. C*, **120**, 4233–4239 (2016).

[16] D. W. deQuilettes, S. M. Vorpahl, S. D. Stranks, H. Nagaoka, G. E. Eperon, M. E. Ziffer, H. J. Snaith, D. S. Ginger, Impact of microstructure on local carrier lifetime in perovskite solar cells, *Science*, **348**, 683-686 (2015).

[17] Y. Okamoto, Y. Suzuki, Mesoporous $BaTiO_3/TiO_2$ double layer for electron transport in perovskite solar cells, *J. Phys. Chem. C*, **120**, 13995−14000 (2016).

Appendix 2: Perovskite solar cells using $SrTiO_3/TiO_2$ composite mesoporous layer for electron transport

A2.1 Introduction

As the author described in section A1.1, $SrTiO_3$ has been studied as the alternative material of TiO_2 for the ETL. In this chapter, the author attempted to improve the photovoltaic performance of perovskite solar cells using $SrTiO_3$ mesoporous layer as the ETL. Before the perovskite solar cells were developed, $SrTiO_3$ had been widely studied as an alternative material of TiO_2-based ETL for the dye-sensitized solar cells (DSCs) [1,2]. Since the $SrTiO_3$ has a conduction band at ~ 0.2 eV higher position than that of anatase TiO_2 [3], a band offset between $SrTiO_3$ and organic dyes is smaller than that with TiO_2, which results in larger V_{OC}. As for the perovskite solar cells, Bera et al. [4] reported perovskite solar cells using $SrTiO_3$ as the mesoporous layer in the ETL. By using $SrTiO_3$ mesoporous layer, V_{OC} was effectively improved compared to the TiO_2-based cells, but J_{SC} was smaller in the $SrTiO_3$-based cells.

The use of $SrTiO_3$ for the ETL usually improves the V_{OC} in the both dye-sensitized solar cells and perovskite solar cells, as expected from its higher conduction band position than TiO_2. However, the $SrTiO_3$-based ETL generally shows a smaller J_{SC} than TiO_2-based cells. As for the DSCs, Wang et al. [5] suggested that the smaller J_{SC} is possibly caused by a decrease of the electron injection rate due to the smaller band offset between ETL and organic dyes. They also implied that the higher resistivity of $SrTiO_3$ than that of TiO_2 may also cause the smaller J_{SC}. As described above, the use of $SrTiO_3$ as the ETL usually has a trade-off correlation between J_{SC} and V_{OC}.

To avoid this trade-off, Wang et al. [6] used a $SrTiO_3$/conductive-graphene composite mesoporous layer. The addition of conductive-graphene improved the electron transfer, and J_{SC} was enhanced with keeping the high V_{OC}. In the author's previous study, an enhancement of J_{SC} with keeping the relatively high V_{OC} was reported by using the composite mesoporous layer of $SrTiO_3/TiO_2$ [7]. Hence, in this chapter, $SrTiO_3/TiO_2$ composite mesoporous layer was prepared for the ETL of the perovskite solar cells to improve the V_{OC} without decrease of J_{SC}.

A2.2. Experimental

A2.2.1 Preparation of $SrTiO_3/TiO_2$ composite paste

The TiO_2-dispersed $SrTiO_3$ sol provided by Denka Company Limited (TDSTS, ST-B, prototype product) was used for the preparation of $SrTiO_3/TiO_2$ composite paste. **Figures A2.1** show (a) SEM image and (b) XRD pattern of the powder obtained by drying the TiO_2-dispersed $SrTiO_3$ sol. The $SrTiO_3/TiO_2$ composite powder (particle size of ~50-100 nm) was mainly composed of cubic $SrTiO_3$ with some anatase TiO_2 (~5 vol.%). The TiO_2-dispersed $SrTiO_3$ sol (TDSTS) was mixed with ethyl cellulose (80-120 cps, Nacalai tesque) and ethanol. The mixture was stirred for 30 min with heating at 120°C and ultrasonicated for 1 h to prepared the paste. The two pates with different concentrations of TiO_2-dispersed $SrTiO_3$ sol were prepared to control the thickness of mesoporous layers.

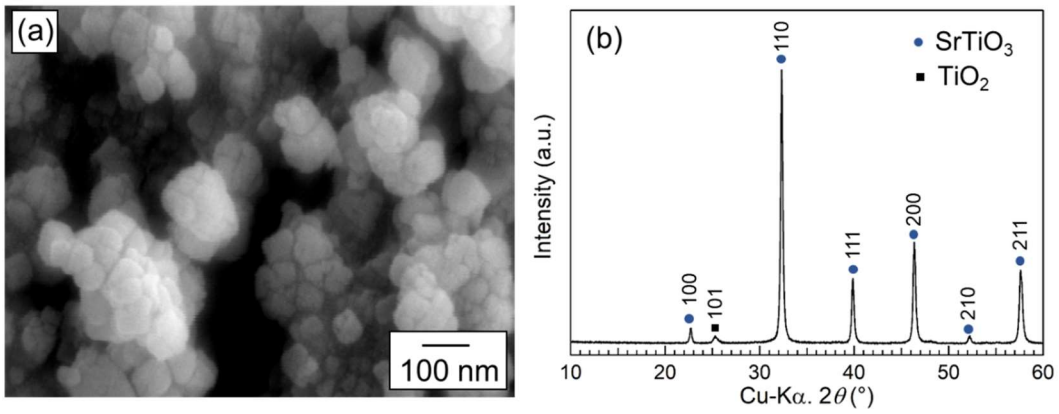

Figs. A2.1 (a) SEM image and (b) XRD pattern of the powder obtained by drying the TiO_2-dispersed $SrTiO_3$ sol.

A2.2.2 Preparation method of perovskite solar cell

Preparation of electron transport layer (ETL) on TCO glass

Transparent conductive oxide (TCO, Type-0052, 10 Ω/sq., Geomatec) glasses were used as the substrates. The TCO substrates were patterned by etching with Zn powder (>96.0%, Tokyo Chemical Industry) and 1 M HCl (Wako Pure Chemical Industry). After the patterning, the TCO substrates were washed in distilled water, ethanol and acetone by an ultrasonication and dried in air. For the preparation of TiO_2 compact layer, a 0.15 M titanium diisopropoxide bis (acetylacetonate) (TAA, 75 % in isopropanol, Sigma-Aldrich) solution mixed with 1-butanol was spin-coated for 20 s at 2000 rpm on the TCO substrates, followed by annealing at 125°C for 5 min. Then, the spin-coating was repeated twice with a 0.3 M TAA solution. The coated substrates were annealed at 500°C for 30 min in air.

The $SrTiO_3/TiO_2$ composite mesoporous layers were prepared by spin-coating the $SrTiO_3/TiO_2$ composite pastes on the TiO_2 compact layers for 25 s at 4000 rpm. The coated substrates were annealed at 500°C for 45 min. The ETL of TiO_2 mesoporous layer was also prepared with the same method as Chapter A1 for comparison.

Preparation of perovskite layer, hole transport layer (HTL) and metal electrodes

The perovskite layers and the HTLs were prepared in air. The ETL coated substrates and a 1 M solution of PbI_2 (>98.0%, Tokyo Chemical Industry) in DMF (99.5%, Nacalai tesque) were pre-heated at 60°C. The PbI_2 solution was spin-coated on the substrates at 3000 rpm for 20 s (1st step). After annealing at 60°C for 10 min, the substrates were dipped in a 10 mg/mL solution of MAI (98%, Wako Pure Chemical Industry) dissolved in isopropanol (99.5%, Nacalai tesque) for 20 s, followed by rinsing with isopropanol and by annealing at 60°C for 10 min (2nd step). The HTLs with the thickness of ~200 nm were prepared by spin-coating a spiro-MeOTAD solution at 4000 rpm for 35 s. The spiro-MeOTAD solution in 1 mL chlorobenzene (99%, Nacalai tesque) was composed of 73 mg spiro-MeOTAD (99%, Sigma-Aldrich), 28.8 μL 4-*tert*-butylpyridine (TBP, 96.0%, Sigma-Aldrich) and 17 μL solution of [520 mg/mL lithium bis(trifluoromethylsulphonyl)imide salt (>98.0%, Tokyo Chemical Industry) in acetonitrile (99.5%, Wako Pure Chemical Industry)]. Finally, Ag electrodes with the thickness of ~50 nm were deposited on the HTLs with a thermal evaporator under the pressure of 3×10^{-5} Torr.

A2.2.3 Characterizations

Cross-section and surface morphologies of the prepared ETLs and perovskite layers were observed by scanning electron microscopy (SEM, SU-70, Hitachi High-Technologies and JSM-5600LV, JEOL). Composition of the power obtained by drying TiO_2-dispersed $SrTiO_3$ sol was characterized by X-ray diffraction (XRD, Multiflex, Cu-K_α, 40 kV and 40 mA, Rigaku). Optical transmittances of the prepared perovskite layers on ETLs were measured by UV-Vis (UV3100PC, Shimadzu). Current density-voltage (*J-V*) characteristics were measured with a solar simulator (XES-40S1, SAN-EI Electric,) calibrated to AM 1.5, 100 mW/cm^2 with a standard silicon photodiode (BS-520BK, Bunkokeiki). The active area was limited to 8.7 mm^2 by suing a black mask. The voltage step and delay time were 20 mV and 50 ms, respectively. Steady-state photoluminescence were measured by Ramascope System1000 (Renishaw) with an excitation laser of wavelength 325 nm (IK5651R-G, Kimmon).

A2.3 Results and Discussion

A2.3.1 Microstructure observation of electron transport layer (ETL) and perovskite layer

Figures A2.2 show cross-sectional SEM images of the prepared mesoporous layers using (a) TiO_2 paste, (b) $SrTiO_3/TiO_2$ paste (low concentration), and (c) $SrTiO_3/TiO_2$ paste (high concentration). The thickness of TiO_2 mesoporous layer was ~250 nm, and the surface was relatively smooth. Meanwhile, the thicknesses of $SrTiO_3/TiO_2$ composite mesoporous layers were ~200 nm for low concentrated paste and ~300 nm for high concentrated paste. The surfaces of $SrTiO_3/TiO_2$ composite mesoporous layers were rougher than that of TiO_2 mesoporous layer due to its larger particle size and some aggregated particles.

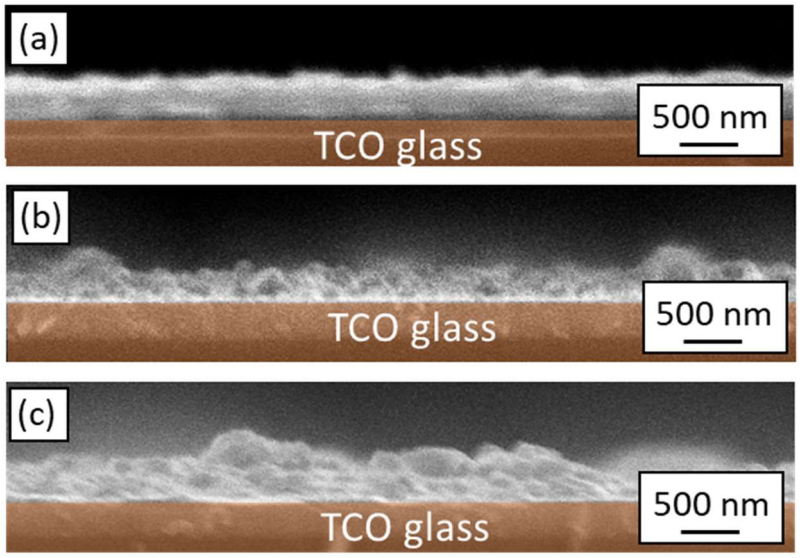

Figs. A2.2 Cross-sectional SEM images of the prepared mesoporous layers using (a) TiO_2 paste, (b) $SrTiO_3/TiO_2$ paste (low concentration), and (c) $SrTiO_3/TiO_2$ paste (high concentration).

Figures A2.3 show cross-sectional SEM images of the prepared perovskite layers on (a) TiO_2 mesoporous layer (~250 nm), (b) $SrTiO_3/TiO_2$ composite mesoporous layer (~200 nm), and (c) $SrTiO_3/TiO_2$ composite mesoporous layer (~300 nm). Herein after, the sample with TiO_2 mesoporous layer will be denoted as TiO_2

(~250 nm), the sample with $SrTiO_3/TiO_2$ composite mesoporous layer (~200 nm) as $SrTiO_3/TiO_2$-cp (~200 nm), and the sample with $SrTiO_3/TiO_2$ composite mesoporous layer (~300 nm) as $SrTiO_3/TiO_2$-cp (~300 nm).

The total thicknesses of the observed layers were similar (~500 nm) in all the samples, but the thickness of $SrTiO_3/TiO_2$-cp (~300 nm) seemed slightly larger than those of the other samples due to its thicker mesoporous layer. **Figure A2.4** shows the transmittance spectra of the prepared perovskite layers on the ETLs. The transmittances of TiO_2 (~250 nm) and $SrTiO_3/TiO_2$-cp (~200 nm) were comparable, while that of $SrTiO_3/TiO_2$-cp (~300 nm) were smaller than the others, which indicates the better light absorption in $SrTiO_3/TiO_2$-cp (~300 nm). This larger absorption is attributable to the slightly increased thickness of perovskite layer.

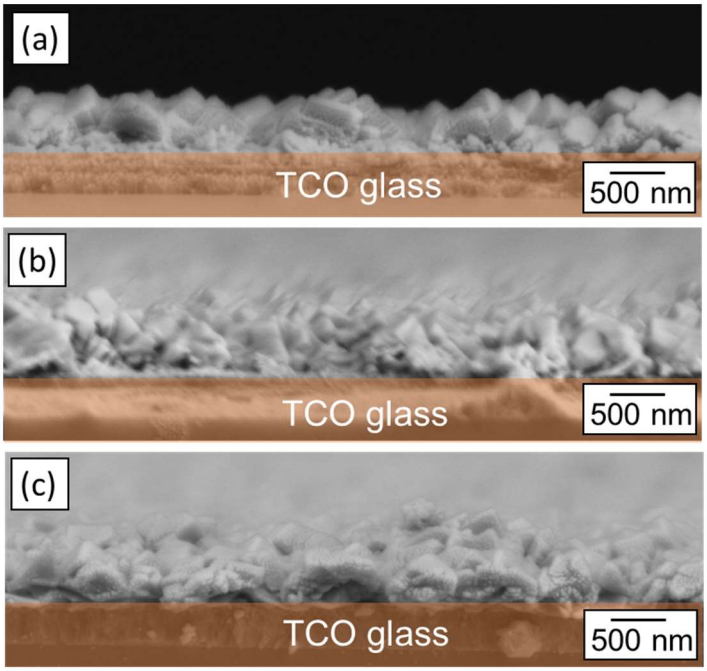

Figs. A2.3 Cross-sectional SEM images of the prepared perovskite layers on (a) TiO_2 (~250 nm), (b) $SrTiO_3/TiO_2$-cp (~200 nm), and (c) $SrTiO_3/TiO_2$-cp (~300 nm).

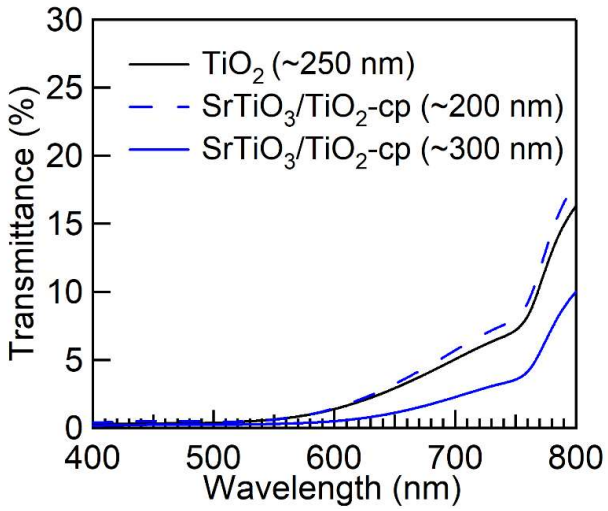

Fig. A2.4 Transmittance spectra of the prepared perovskite layers on ETLs.

A2.3.2 Evaluation of photovoltaic performance

Current density-voltage (*J-V*) curves of the prepared cells in back scan are shown in **Fig. A2.5**, and the *J-V* characteristics are summarized in **Table A2.1**. These data are average of 3 cells. The TiO_2 (~250 nm) and $SrTiO_3/TiO_2$-cp (~200 nm) showed similar J_{SC}, *FF* and PCE, but the V_{OC} of $SrTiO_3/TiO_2$-cp (~200 nm) was higher than that of TiO_2 (~250 nm). When the thickness of the $SrTiO_3/TiO_2$ composite mesoporous layer increased from ~200 nm to ~300 nm, J_{SC} decreased from 19.3 mA/cm^2 to 18.5 mA/cm^2 in spite of the better light absorption in $SrTiO_3/TiO_2$-cp (~300 nm) (**Fig. A2.4**). Other parameters also decreased to V_{OC}: 0.87 V, *FF*: 0.49 and PCE: 7.96 %.

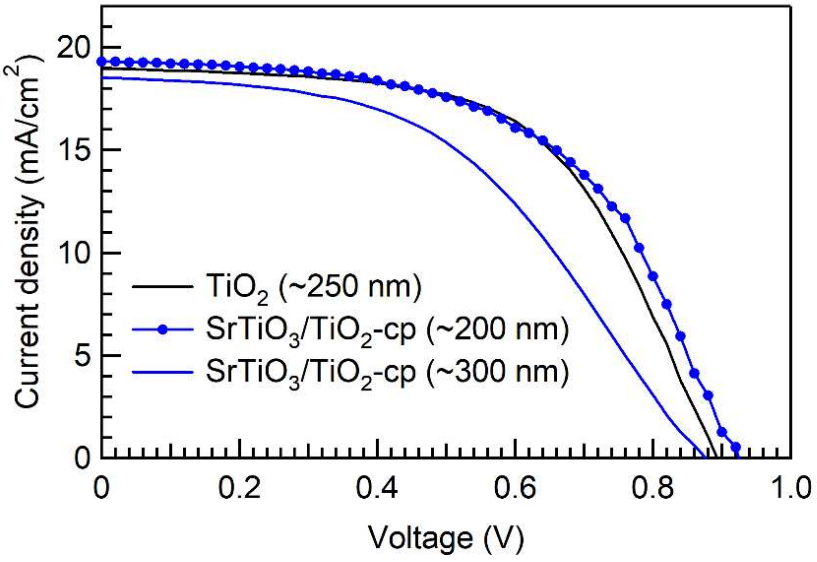

Fig. A2.5 *J*−*V* curves of the prepared perovskite solar cells in back scan.

Table A2.1 *J-V* characteristics of TiO_2 (~250 nm), $SrTiO_3/TiO_2$-cp (~200 nm) and $SrTiO_3/TiO_2$-cp (~300 nm) in back scan. The data are averages of 3 cells.

Samples	J_{SC} (mA/cm^2)	V_{OC} (V)	*FF*	PCE (%)
TiO_2 (~250 nm)	19.0	0.89	0.59	9.98
$SrTiO_3/TiO_2$-cp (~200 nm)	19.3	0.93	0.56	9.98
$SrTiO_3/TiO_2$-cp (~300 nm)	18.5	0.87	0.49	7.96

Although the decrease of J_{SC} was confirmed for $SrTiO_3/TiO_2$-cp (~300 nm) compared to the TiO_2 (~250 nm), the $SrTiO_3/TiO_2$-cp (~200 nm) generated the comparable J_{SC} to that of TiO_2 (~250 nm). As described in the section A2.1, the perovskite solar cells with $SrTiO_3$-pure mesoporous layer generally demonstrates a lower J_{SC} (12-14 mA/cm^2) than that with TiO_2 mesoporous layer due to the inefficient electron transport [4,5]. Furthermore, Bera et al. [4] reported that J_{SC} dramatically decreased from 13.37 mA/cm^2 to 7.95 mA/cm^2 by increasing the thickness of $SrTiO_3$ mesoporous layer from 200 nm to 350 nm. On the other hand, in this study, the decrease of J_{SC} by increasing the thickness of $SrTiO_3/TiO_2$ composite mesoporous layer from ~200 to ~300

nm was just 0.8 mA/cm^2, which was much smaller than that of pure-$SrTiO_3$ mesoporous layer. These results indicate that the decrease of J_{SC} by using $SrTiO_3$ was suppressed in the samples using $SrTiO_3/TiO_2$ composite mesoporous layer.

In the author's previous study, it was reported that a decrease of J_{SC} by using $SrTiO_3$ mesoporous layer was suppressed by using $SrTiO_3/TiO_2$ composite mesoporous layer for DSCs [7]. Considering these results, it seems that anatase TiO_2 included in the $SrTiO_3/TiO_2$ composite mesoporous layer was a key factor to improve the electron transport and generate the high J_{SC} with keeping high V_{OC} for the $SrTiO_3$-based perovskite solar cells. The series resistances (R_S) of the prepared cells were calculated from the slope of *J-V* curves at around V_{OC}. The calculated R_S of $SrTiO_3/TiO_2$-cp (~200 nm) was 15.8 (Ω), and it was larger than that of TiO_2 (~200 nm): 12.7 (Ω). Since this larger R_S resulted in the decrease of *FF* for $SrTiO_3/TiO_2$-cp (~200 nm), the further improvement of photovoltaic performance can be obtained by optimizing the TiO_2 ratio in the composite mesoporous layer and its film thickness.

A2.4 Conclusions

In conclusion, the perovskite solar cells with $SrTiO_3/TiO_2$ composite mesoporous layer including ~5 vol% of anatase TiO_2 was prepared to improve the J_{SC} of $SrTiO_3$-based perovskite solar cells. The $SrTiO_3$-based perovskite solar cells generally show the higher V_{OC} and smaller J_{SC} than that of TiO_2-based cell. However, J_{SC} of $SrTiO_3/TiO_2$-cp (~200 nm) was comparable to that of TiO_2-based cells with keeping the higher V_{OC}, and the J_{SC} value was higher than the reported values for pure $SrTiO_3$-based cells. This improved J_{SC} was attributable to the improvement of electron transport by the anatase TiO_2 included in the $SrTiO_3/TiO_2$ composite mesoporous layer. Further enhancement of photovoltaic performance can be obtained by optimizing the ratio of TiO_2 and the film thickness.

Most part of this chapter has been published in *Mater. Lett.*, **187**, 111-113 (2017).
http://dx.doi.org/10.1016/j.matlet.2016.10.090 [8].

References

[1] P. Jayabal, V. Sasirekha, J. Mayandi, Jeganathan K, V. Ramakrishnan. *J. Alloys Compounds*, **586**, 456–461 (2014).

[2] S. Gholamrezaei, M. S. Niasari, M. Dadkhah, B. Sarkhosh. *J Mater Sci: Mater Electron*, **27**, 118–125 (2016).

[3] J. Fujisawa, T. Eda, M. Hanaya, Comparative study of conduction-band and valence-band edges of TiO_2, $SrTiO_3$, and $BaTiO_3$ by ionization potential measurements, *Chem. Phys. Lett*, **685**, 23–26 (2017).

[4] A. Bera, K. Wu, A. Sheikh, E. Alarousu, O. F. Mohammed, T. Wu, Perovskite oxide $SrTiO_3$ as an efficient electron transporter for hybrid perovskite solar cells, *J. Phys. Chem. C*, **118**, 28494–28501 (2014).

[5] Y. S. Wang, T. T. Chen, Y. J. Huang, T. P. Huang, Y. Y. Lee, H. T. Chiu, C. Y. Lee, $SrTiO_3/TiO_2$ hybridstructure as photoanode in dye-sensitized solar cell, *J. Chin. Chem. Soc*., **60**, 1437-1441 (2013).

[6] C. Wang, Y. Tang, Y. Hu, L. Huang, J. Fu, J. Jin, W. Shi, L. Wanga, W. Yang, Graphene/$SrTiO_3$ nanocomposites used as an effective electron-transporting layer for high performance perovskite solar cells, *RSC Adv.*, **5**, 5204-52047 (2015).

[7] Y. Okamoto, Y. Suzuki, Perovskite-type $SrTiO_3$, $CaTiO_3$ and $BaTiO_3$ porous film electrodes for dye-sensitized solar cells, *J. Ceram. Soc. Jpn*., **122**, 728–731 (2014).

[8] Y. Okamoto, R. Fukui, M. Fukuzawa, Y. Suzuki, $SrTiO_3/TiO_2$ composite electron transport layer for perovskite solar cells, *Mater. Lett.*, **187**, 111-113 (2017).

Appendix 3: Remote supply of hydrogen radical and production of Si from reduction of $SiCl_4$

A3.1 Introduction

Perovskite solar cell has suitable characteristics as a top cell of perovskite/silicon tandem solar cells [1,2]. The tandem solar cell has been widely studied, since it is expected to generate higher conversion efficiency than that of single perovskite solar cell or silicon (Si) solar cell. However, the production cost also increases due to its complex structure. Therefore, a reduction of production cost of each solar cell is important for the future application. In this chapter, the author focused on the Si solar cell and attempted to improve a production process of high purity Si.

A3.1.1 Conventional production method of high purity Si: Siemens method

High purity Si is used as the row material of Si solar cells. For the solar cell application, the purity of Si has to be more than 6 nine grade (99.9999%, solar grade (SOG)-Si) [3,4]. The most popular conventional production process of the high purity Si is the Siemens method [5]. In the Siemens method, relatively low purity Si (metal grade (MG)-Si, purity ~98%) is firstly produced by a carbothermal reduction of SiO_2. Then, the metal grade Si is transformed into trichlorosilane ($SiHCl_3$) by reacting with HCl. After the purification of $SiHCl_3$, it is introduced into a bell jar (Siemens chamber) with H_2 gas. There are Si rods in the bell jar, and they are electrically heated up to ~1000-1200°C. $SiHCl_3$ is reduced by H_2 on the heated Si rods at atmospheric pressure (**eq. A3.1**), and the high purity Si is produced.

$$SiHCl_3 + H_2 \rightarrow Si + 3HCl \qquad \textbf{(eq. A3.1)}$$

However, a pyrolysis of $SiHCl_3$ dominantly proceeds instead of the reduction in the actual process. **Figure A3.1** shows Gibbs free energies (ΔG) of various reactions related to chlorosilane series materials as a function of temperature. At the process temperature of Siemens method: ~1000-1200°C, ΔG of $SiHCl_3$ pyrolysis is lower than that of H_2 reduction, and hence, the pyrolysis of $SiHCl_3$ dominantly proceeds. Since the pyrolysis of $SiHCl_3$ produces 1 mol of Si and 3 mol of tetrachlorosilane ($SiCl_4$) as a byproduct from 4 mol of $SiHCl_3$ as shown in **eq. A3.2**, its Si yield is very low (~25%).

$$4SiHCl_3 \rightarrow 3SiCl_4 + Si + 2H_2 \qquad \textbf{(eq. A3.2)}$$

Additionally, a production of Si from the H_2 reduction of $SiCl_4$ is difficult, since $SiCl_4$ is more stable than $SiHCl_3$. Theuerer [6] reported the H_2 reduction of $SiCl_4$, and the deposition rate of Si in the literature was ~0.3 mm/h. This deposition rate is slower than that of H_2 reduction of $SiHCl_3$ considering that the deposition rate of Si in the Siemens method is ~1 mm/h [7]. As a result, the Si yield of Siemens method becomes ~30%, and the low Si yield is a problem of the Siemens method.

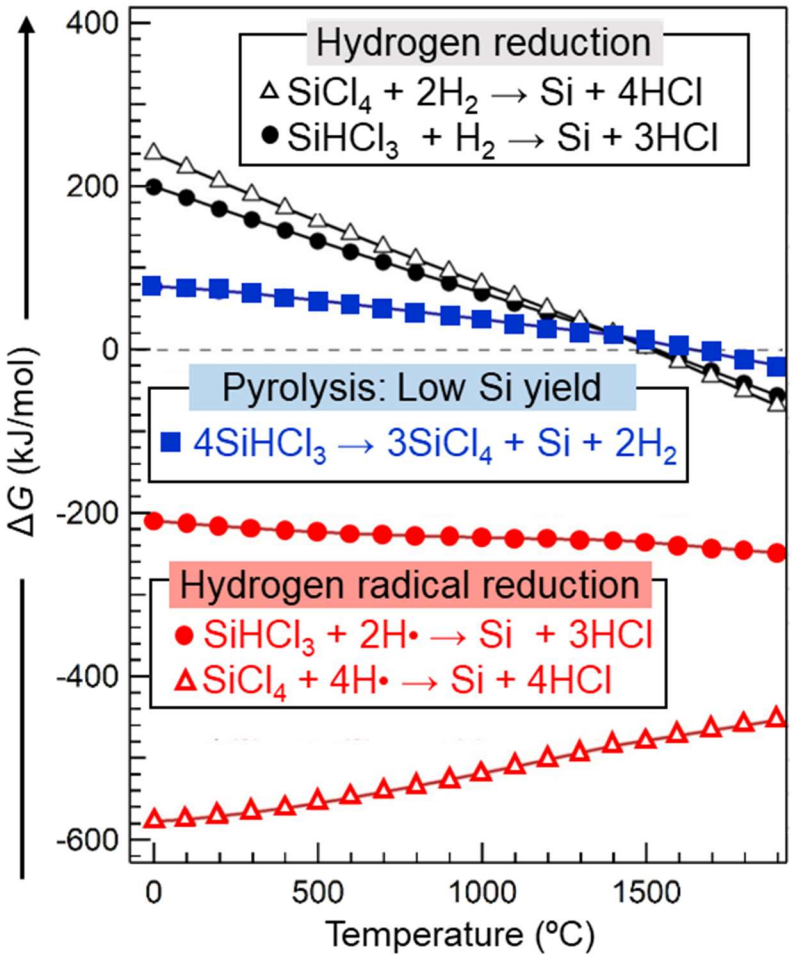

Fig. A3.1 Gibbs free energies (ΔG) of the various reactions related to chlorosilane series materials as a function of temperature.

A3.1.2 Potential of hydrogen radical (H-radical) for enhancement of Si yield in Siemens method

To increase the Si yield in the Siemens method, the author focused on a usage of hydrogen radical (H-radical) instead of H_2. The H-radical is a hydrogen atom generated from a homolytic cleavage of H_2 molecule (**Fig. A3.2**). Since the H-radical is unstable and more active than H_2 molecule, it is expected that the Gibbs free energy of the H-radical reduction of $SiHCl_3$ is lower than that of the $SiHCl_3$ pyrolysis as shown in **Fig. A3.1**. Hence, the usage of H-radical instead of H_2 will suppress the pyrolysis of $SiHCl_3$, and the reduction of $SiHCl_3$ will dominantly proceed. Furthermore, since the H-radical is also expected to decrease the ΔG of the reduction of $SiCl_4$ as shown in **Fig. A3.1**, the amount of Si produced from the reduction of $SiCl_4$ will be also increased. Because of these reasons, H-radical is promising to improve the Si yield of Siemens method.

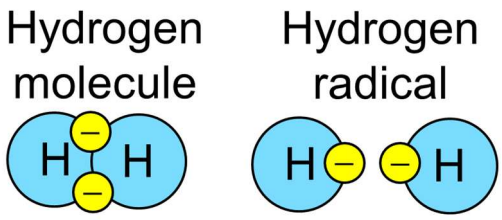

Fig. A3.2 Schematic illustration of hydrogen molecule and hydrogen radical.

A3.1.3 Requirements to apply H-radical into Siemens method

H-radical is commonly generated by producing hydrogen plasma [8,9] or by a hot-wire method [10,11]. In this study, the hot-wire method was used to generate H-radical. For the hot-wire method, heated metal filaments, such as tungsten (W) and platinum (Pt) filaments, are used as a catalyst to generate the H-radical. H_2 molecules are dissociated on the heated W filaments (~2000°C) by the catalytic effect, and H atoms are thermally desorbed as the H-radicals (**Fig. A3.3**). The H-radical generated by the hot-wire method has been used for productions of amorphous or polycrystalline Si [10] and diamond thin films [11,12]. Besides, a passivation of dangling bonds for the amorphous Si solar cells [13], surface and chamber cleaning [14,15], dry etching of crystalline Si [16], and photoresist removal [17] are also well known.

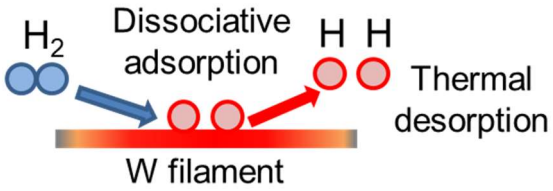

Fig. A3.3 Mechanism of the H-radical generation by a hot wire method.

To apply the H-radical into the Siemens method, the H-radical has to be remotely supplied into the Siemens chamber. If the generation of H-radical and production of Si are carried out in the same chamber, the surface of W filaments will be contaminated by the source gas or produced Si, and the generation rate of H-radical will decrease. In addition, the H-radical have to be generated at pressure > 1 atm, (~101 kPa), since the H-radical needs to be transported into the 1 atm reaction chamber as shown in **Fig. A3.4** considering the operational pressure of conventional Siemens method (1 atm). In the previous studies, H-radical has been generated with the hot wire method at the pressure < ~10 kPa [10,11]. Hence, the generation of H-radical at the pressure > 1 atm (~101 kPa) and its transportation will give us new insights about the H-radical.

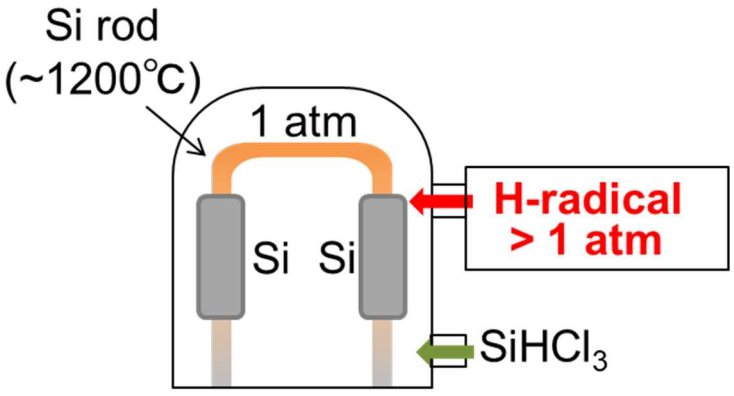

Fig. A3.4 Requirements for the application of H-radical into the Siemens method.

A3.1.4 Objective

The objectives of this chapter are (1) to generate the H-radical at the pressure > 1 atm (~101 kPa) and to transportation them into the 1 atm reaction chamber, and (2) to promote the production of Si from the reduction of $SiCl_4$ at the pressure of 1 atm by using the remotely supplied H-radical.

Part 1: Generation of H-radical at pressure > 1 atm and transportation

A3.2 Experimental

A3.2.1 Apparatus

First of all, an apparatus for the generation and transportation of H-radical was assembled. The schematic illustration of apparatus is shown in **Fig. A3.5**. The apparatus is composed of two chambers, a H-radical generation chamber and a detection chamber. An internal diameter of the H-radical generation chamber was ~30 cm, and its inside was covered with Al_2O_3 plates to avoid a deactivation of the H-radical by contacting with the metal wall. 4 tungsten (W) filaments (length: 30 cm, φ: 0.5 mm) were connected to the electrodes in series which attached on the chamber walls. The total length of W filament was ~120 cm. As for the detection chamber, it consisted of several connected NW50 stainless tubes, and it was connected to the H-radical generation chamber. There was an aperture (φ = 3 mm) on the wall of the H-radical generation chamber at the joint point with the detection chamber. A ceramic heater (2.5×2.5 cm^2) was fixed at the center of stainless tube and a tungsten oxide (WO_3) doped phosphate glass plate was placed on the ceramic heater to evaluate a H-radical density (details will be described in section A3.2.3).

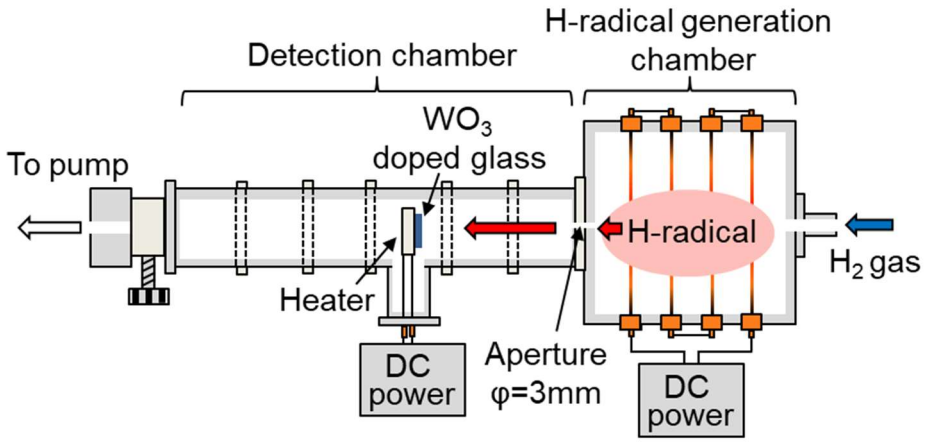

Fig. 3.5 Schematic illustration of an apparatus for H-atom generation and transportation.

A3.2.2 H-radical generation and transportation

H_2 gas with a flow rate of 4.2 SLM (4.2 standard L/min) was firstly introduced into the apparatus from the H-radical chamber, and then, the W filaments were electrically heated with a DC power supply (S-130-40HMD, Yamabishi Denki). The pressure in the apparatus was controlled by adjusting a pumping conductance. H_2 was decomposed into H-radical on the surface of the heated W filaments. The temperature of W filament was estimate by the calculation using the following reported equation (**eq. A3.3**) [18],

$$I^2 \times \rho / (\pi d^2 / 4) = \varepsilon \sigma T^4 \times \pi d \qquad \textbf{(eq. A3.3)}$$

where I is an applied current, ρ is a resistivity, d is a diameter of the filament, ε is an emissivity, σ is Stefan Boltzmann constant, and T is the filament temperature. The resistivity of tungsten was calculated using the

following reported equation (**eq. A3.4**) [19].

$$\rho = -1.72573 + 2.14350 \times 10^{-2}T + 5.74811 \times 10^{-6}T^2 - 1.13698 \times 10^{-9}T^3 + 1.1167 \times 10^{-13}T^4 \qquad \textbf{(eq. A3.4)}$$

The ε of tungsten was calculated using the following equation (**eq. A3.5**) [18].

$$\varepsilon = -3.7 \times 10^{-8}T^2 + 0.00026T - 0.112 \qquad \textbf{(eq. 3.5)}$$

Since the H_2 gas significantly decreases the filament temperature, a larger current than that under the vacuum condition was applied to the W filaments. The generated H-radical was transported into the detection chamber thorough the aperture.

A3.2.3 Detection of H-radical and evaluation of the density

The H-radical density was estimated using the tungsten oxide (WO_3) doped phosphate glass (Sankei, HAS-A20). The WO_3 doped glass changes its color from transparent to dark blue by reacting with the H-radical, which has an absorption peak at ~600 nm. Morimoto et al. [20] investigated a relationship between $-\ln(T/T_0)$ and H-radical density under the conditions of the exposure time: 1 h and the annealing temperature of WO_3 doped glass: 600 K (327°C) as shown in **Fig. A3.6(a)**, where the T and T_0 are transmittances of the WO_3 doped glass at 600 nm before and after the exposure to the H-radical, respectively. In this study, the H-radical density was estimated using the reported relationship.

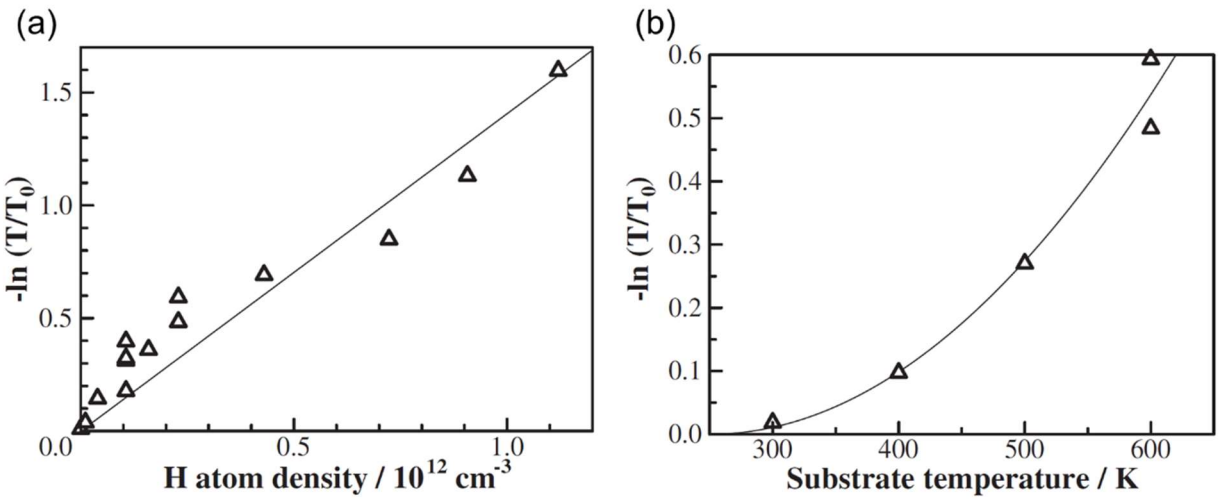

Figs. A3.6 Relationship between (a) hydrogen radical density and $-\ln(T/T_0)$ and (b) $-\ln(T/T_0)$ and annealing temperature for WO_3 doped glass during the exposure to H-radical, reported by Morimoto et al. [20].

The WO_3 doped glass was fixed on the ceramic heater in the detection chamber, and it was exposed to the generated H-radical for 1 h. After the exposure, the transmittance of the WO_3 doped glass at 600 nm was measured by UV-Vis (UV-3150, Shimadzu). Since the transmittances at 600 nm after the H-radical exposure were too low (less than 0.1 %) with some experimental conditions, the heating temperature of WO_3 doped

glass was changed from 600 K (327°C) to 550 K (277°C) or 500 K (227°C). Morimoto et al. [20] also showed a relationship between $-\ln(T/T_0)$ and annealing temperature of WO_3 doped glass during the exposure to H-radical as shown in **Fig. A3.6 (b)**. Since the $\ln(T/T_0)$ at 600 K is roughly 1.36 and 1.96 times larger than those at 550 K and 500 K, 1.36 or 1.96 was multiplied to the calculated $-\ln(T/T_0)$ when the annealing temperature of the WO_3 doped glass was 550 K or 500 K, and then, the H-radical density was estimated using **Fig. A3.6(a)**.

The variation of WO_3 glass transmittances were measured under various gas pressure (10-105 kPa) and with various distances (30-70 cm) from the H-radical generation chamber. The temperature of the W filament was also varied from room temperature to ~2000°C by changing the applied current (0-30 A).

A3.3 Results and Discussion

A3.3.1 Effect of generation pressure on H-radical density

First of all, to confirm that the WO_3 doped glass is not affected by H_2, the WO_3 doped glass was exposed to H-radical or H_2 gas (i.e. with or without heating the W filaments). The H_2 gas flow rate was 4.2 SLM, and the pressures of H-radical generation chamber and detection chamber were kept at 20 kPa and 19 kPa, respectively. The distance from the H-radical generation chamber to the WO_3 doped glass was 30 cm. The W filaments were electrically heated up to ~2000°C by applying the current of 30 A. **Figure A3.7** shows transmittance spectra of the WO_3 doped glass before and after the exposure to H-radical or H_2 gas. The transmittance of the original WO_3 doped glass was 82.1% at 600 nm. After the exposure to H-radical (filament temperature: ~2000°C, applied current: 30 A), the transmittance at 600 nm decreased to ~12.1%. On the other hand, there was no apparent change on the transmittance (~79.4%) by the exposure to H_2 gas (filament temperature: room temperature, applied current: 0 A) compared to the original value. These results indicate that the WO_3 doped glass reacts with only H-radical, and the effect of H_2 gas on the transmittance can be ignored.

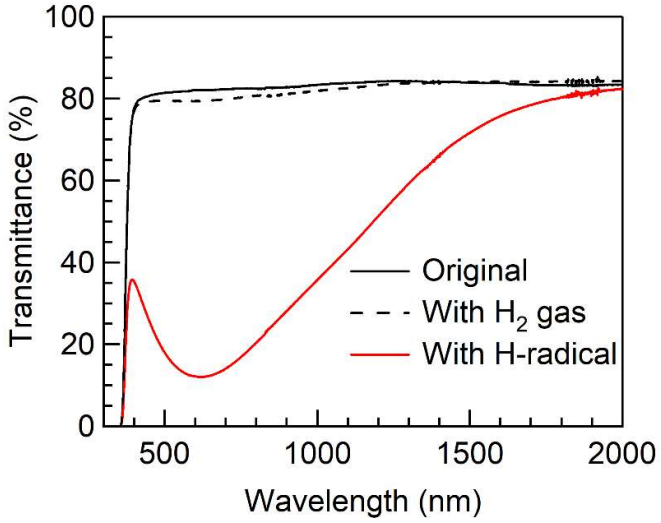

Fig. A3.7 Transmittance spectra of WO_3 doped glass before and after the exposure to H-radical or H_2 gas, i.e. with or without heating the W filaments.

Then, the generation of H-radical at pressure > 1 atm was carried out. The H_2 gas flow rate was 4.2 SLM, the distance from the H-radical generation chamber to WO_3 doped glass was 30 cm, and W filament temperature was ~2000°C (applied current: 30 A). The pressures of H-radical generation chamber and detection chamber were controlled by changing a pumping conductance. **Figure A3.8(a)** shows the transmittance spectra of the original WO_3 doped glass and those after the H-radical exposure with the generation pressure of 10, 20, 40, 60, 80, and 101 kPa. The Pressures in the detection chamber were 9, 19, 38, 58, 78, and 98 kPa, respectively. The transmittance at 600 nm of the WO_3 doped glass exposed to H-radical with the generation pressure of 10 kPa was ~10%, which is a significantly lower than that before the H-radical exposure. With increasing the generation pressure, the transmittance became larger, and it became ~20% with the generation pressure of 101 kPa.

Figure A3.8(b) shows the H-radical density generated at 10, 20, 40, 60, 80, 101, and 105 kPa. The pressures written in the graph are the detection chamber pressure. The estimated H-radical density at generation pressure of 10 kPa was ~2.9×10^{12} cm^{-3}, and the density decreased with increasing the H-radical generation pressure. Although the decrease of H-radical density was confirmed with increasing the generation pressure, the H-radical density of 1.1×10^{12} cm^{-3} was successfully obtained under the conditions of H-radical generation pressure of 105 kPa (> 1 atm) and detection chamber pressure of 101 kPa (= 1 atm). Schwarz et al. [11] and Meier et al. [21] reported the larger H-radical density of ~10^{14}-10^{15} cm^{-3} at the generation pressure of ~1-10 kPa. However, considering the experimental conditions of this study, i.e. higher pressure (> 1 atm) and transportation of H-radical, the H-radical density of 10^{12} order seems reasonable value.

The decreasing tendency of the H-radical density with increasing the generation pressure is in good agreements with some reported results [22,23]. The decreasing tendency is attributable to an increase of three-body recombination: $H + H + M\ (H_2) \rightarrow H_2 + M\ (H_2)$ due to an increase of the M (H_2) density at higher pressure [22,23]. Moreover, according to Le Chatelier's principle, when the pressure increased in equilibrium state, the equilibrium moves to counteract the change. In the case of $2H \leftrightharpoons H_2$, the equilibrium moves to right direction by increasing the pressure, which also results in the smaller H-radical density at higher pressure [24].

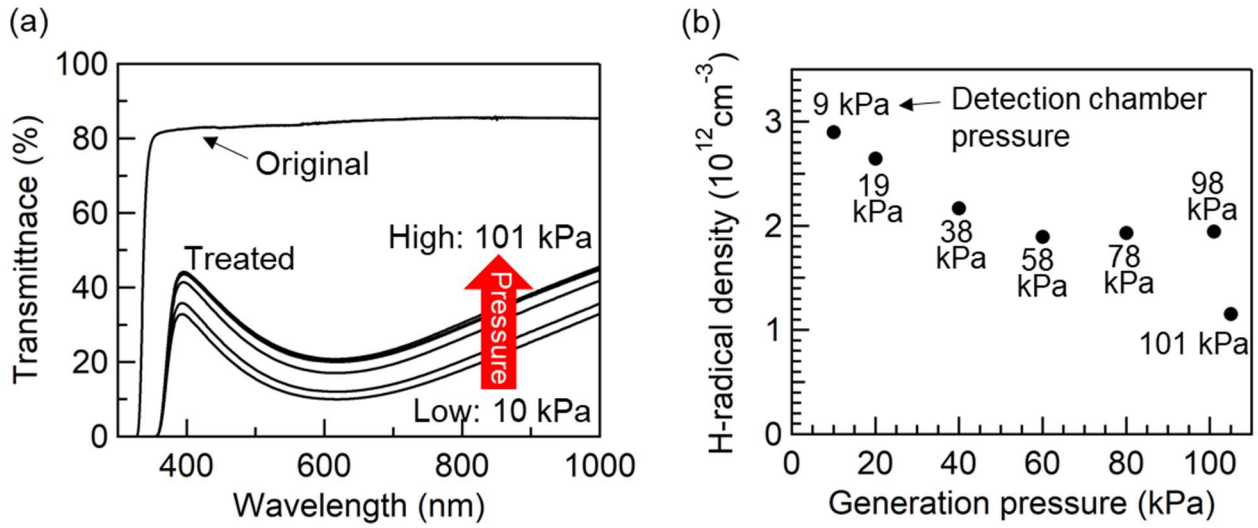

Figs. A3.8 (a) Transmittance spectra of the original WO_3 doped glass and those after H-radical exposure at the generation pressure of 10-101 kPa, and (b) estimated H-radical density.

A3.3.2 Effect of applied current to W filaments (filament temperature) on H-radical density

Figure A3.9 shows the H-radical density generated with various applied currents (18, 22, 24, 26, and 30 A) to W filaments. The temperatures written in the graph are the estimated W filament temperatures. H_2 gas flow rate was 4.2 SLM, and the pressures in the H-radical generation chamber and detection chamber were 105 kPa and 101 kPa, respectively. The distance from the H-radical generation chamber to the WO_3 doped glass was 30 cm.

The apparent color change of WO_3 doped glass after the H-radical exposure was not confirmed with the applied current of 18 A (filament temperature: ~550°C). With the applied current of 22 A (filament temperature: ~1300°C), the color of WO_3 doped glass visibly changed, and the H-radical density was estimated to be 1.4×10^{11} cm^{-3}. By increasing the applied current to 24, 26 and 30 A (filament temperature: ~1500, 1700, 2000°C), the H-radical density rapidly increased. These results suggest that the H-radical was effectively generated from the W filament temperature: ~1500°C by the catalytic effect, and the generation rate was enhanced by increasing the temperature.

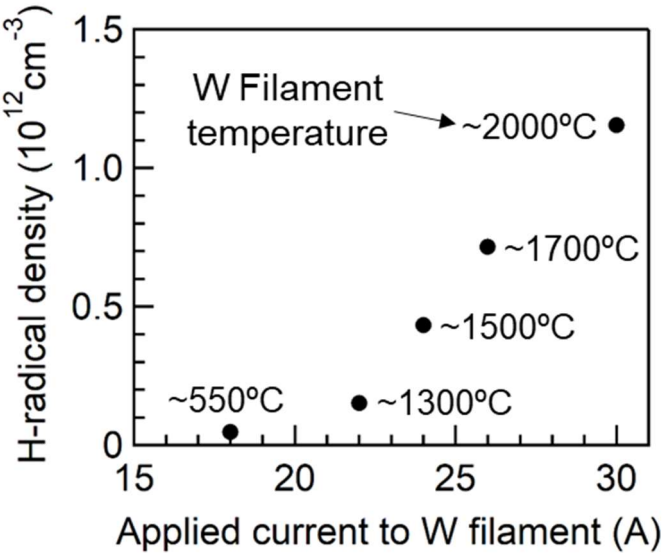

Fig. A3.9 Estimated H-radical density generated with various applied currents to W filaments (18-30 A).

A3.3.3 Effect of distance from H-radical generation chamber to detection point on H-radical density

Figure A3.10 shows the estimated H-radical density detected at the positions of 30, 40, 50, 60 and 70 cm from the H-radical generation chamber. H_2 gas flow rate was 4.2 SLM, and the pressures in the H-radical generation chamber and detection chamber were 101 kPa and 98 kPa, respectively. The W filament temperature was ~2000°C (applied current: 30 A). The highest H-radical density was obtained at the detection point of 30 cm from the H-radical generation chamber. With increasing the distance between the generation and detection points, the H-radical density exponentially decreased. Still, H-radicals were successfully detected up to ~50-60 cm from the generation chamber.

The decrease of H-radical density at the farther position is due to the three-body recombination: $H + H + M(H_2) \rightarrow H_2 + M(H_2)$ during the transportation [22,23]. In addition, the deactivation of generated H-radical by contacting with the stain-less steel wall of the detection chamber is also a reason for the decreasing tendency [25]. Since Al_2O_3 or SiO_2 has smaller H-radical recombination probability (Al_2O_3: 0.0018±0.0003, SiO_2:

0.00004±0.00003) than that of stainless steel (0.032±0.015) [26], the H-radical loss must be minimized by coating the metal wall of the detection chamber with Al_2O_3 or SiO_2.

The flow velocity of H-radical or H_2 gas in the apparatus was not well understood, and hence, the lifetime of the H-radical cannot be estimated. However, the H-radical was detected even at ~50-60 cm from the generation chamber, which suggests that the life time of H-radical may be sufficiently long to be used for the remote supply application.

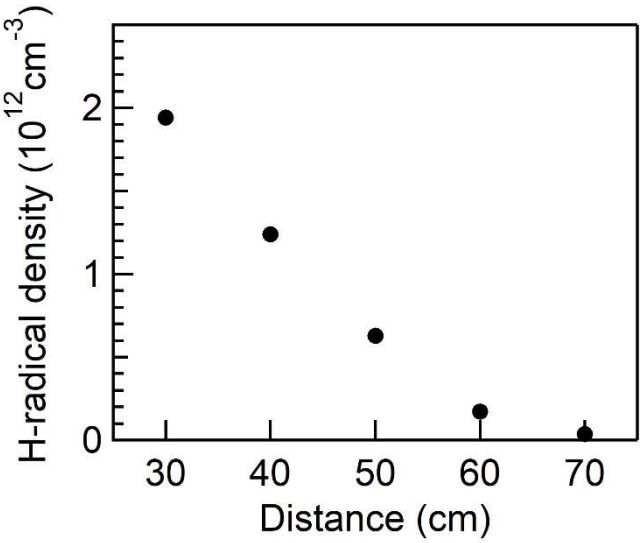

Fig. A3.10 Estimated H-radical density detected at the positions of 30-70 cm from the H-radical generation chamber.

A3.4 Conclusions

In Part 1, the generation of H-radical using the hot wire method at the pressure >1 atm and its transportation were carried out. Although the density of H-radical decreased with increasing the H-radical generation pressure, the estimated H-radical density of ~1.1×10^{12} cm^{-3} was successfully obtained under the generation pressure of 105 kPa (> 1 atm) and detection chamber pressure of 101 kPa (1 atm). In addition, H-radicals were detected even at the positions of ~50-60 cm from the generation chamber, which indicated that H-radical has a sufficiently long lifetime to realize the remote supply application.

Appendix 3

Part 2: Production of Si from reduction of $SiCl_4$ by H-radical at 1 atm

In the Part 1, hydrogen radical (H-radical) was successfully generated at pressure > 1 atm (101 kPa) and transport into the 1 atm detection chamber. In this part, tetrachlorosilane ($SiCl_4$) was reduced by the generated H-radical, and Si was produced.

A3.5 Experimental

A3.5.1 Apparatus

The schematic illustration of an apparatus used for the reduction of $SiCl_4$ is shown in **Fig. A3.11(a)**. The same H-radical generation chamber as the Part 1 was used to generate H-radical, but an introduction part of $SiCl_4$ and a reaction chamber were installed instead of the detection chamber. A quartz tube ($\varphi = 42$ mm, length: 50 cm) was used as the reaction chamber. To deposit the produced Si, 4 quartz glasses (size: 1×1 cm^2) were placed in the quartz tube. The position of quartz glasses is shown in **Fig. A3.11(b)**. The reaction chamber was heated with a tubular furnace (ARF-50K, ASH) and a temperature controller (YKC-92, YAMADA DENKI). A thermocouple for the temperature controller was inserted through a hole at the center of tubular furnace, and it was touched on the outside of quartz tube.

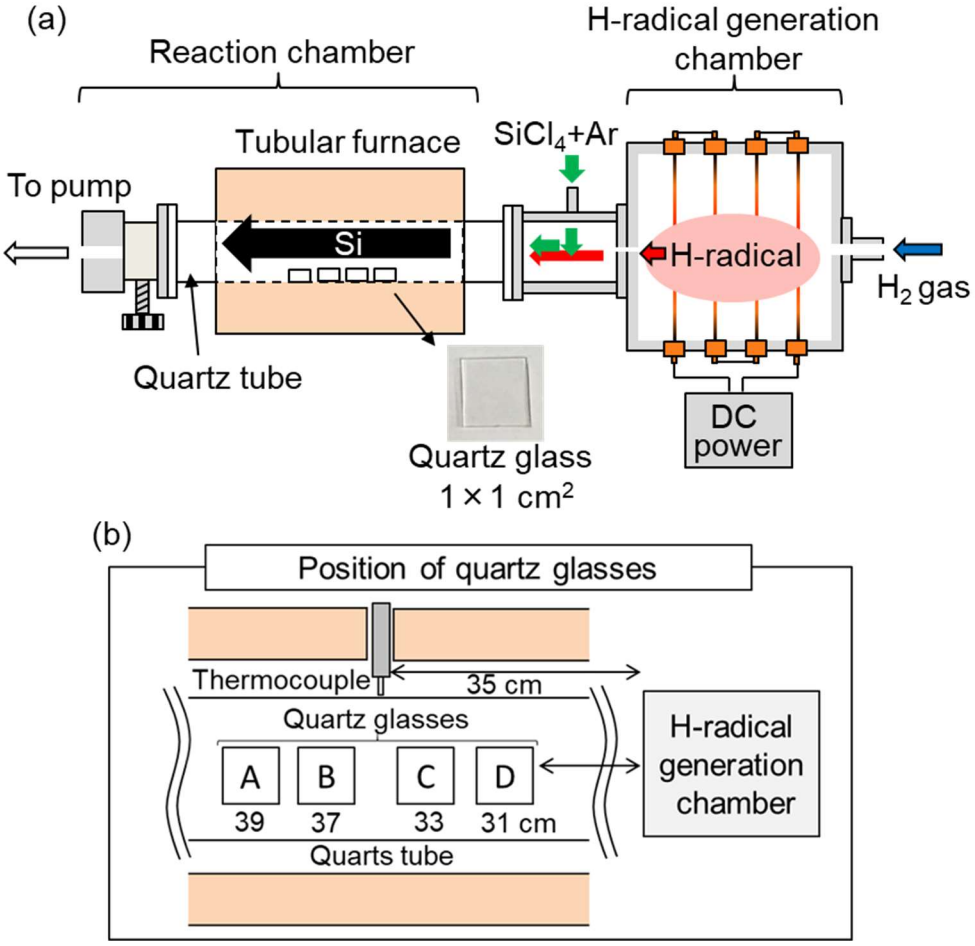

Figs. A3.11 Schematic illustration of (a) apparatus used for reduction of $SiCl_4$ and (b) position of quartz glasses.

A3.5.2 Reduction of $SiCl_4$ by H-radical

H_2 gas with flow rate of 4.2 SLM was introduced into the H-radical generation chamber. Then, the H-radical was generated by electrically heating the W filaments, and the generated H-radicals were transported into the reaction chamber. $SiCl_4$ was also introduced into the reaction chamber as the source gas by bubbling a liquid $SiCl_4$ (99.9999%, Tri Chemical Laboratories) with Ar gas and by transporting the vapor of $SiCl_4$. The introduction amount of $SiCl_4$ was controlled by the flow rate of Ar gas (15 or 30 sccm), temperature of liquid $SiCl_4$ (10 or 20°C), and pressure in the container of the liquid $SiCl_4$. The mixed gas of the H-radical and $SiCl_4$ with Ar carrier gas were heated at ~850-900°C in the reaction chamber for 30 min to reduce $SiCl_4$. The produced Si was deposited on the quarts tube and quartz glasses.

A3.5.3 Characterizations

Transmittance of the WO_3 doped glass was measured by UV-Vis (UV-3150, Shimadzu). The composition of the obtained substance was analyzed by X-ray diffraction (XRD, Multiflex, Cu-K_α, 40 kV and 40 mA, Rigaku) and Raman spectroscopy (Photon design). The cross-section of the deposited Si was observed by scanning electron microscopy (SEM, JSM-5600LV, JEOL).

A3.6 Results and Discussion

A3.6.1 Reduction of $SiCl_4$ by H-radical at the reaction pressure of ~1.8 kPa

In Part 1, the H-radical density showed the decreasing tendency with increasing the generation pressure, which suggests that a low-pressure condition is more suitable to investigate the effect of H-radical. Therefore, the experiments were firstly carried out under relatively low H-radical generation pressure of ~3 kPa and reaction pressure of ~1.8 kPa. The H_2 gas flow rate was 4.2 SLM, and the W filaments were electrically heated from room temperature to ~2000°C.

Before the experiment of $SiCl_4$ reduction, the H-radical density under those experimental conditions was estimated. The temperature of W filament was ~2000°C. The WO_3 doped glass was placed at the position B in the quartz tube (~40 cm from the H-radical generation chamber, **Fig. A3.11(b)**), and it was exposed to the H-radical for 1 h with heating at 327°C (600 K). **Figure A3.12** shows transmittance spectra of the WO_3 doped glass before and after the exposure to H-radical. The transmittance of the original WO_3 glass was ~83.5% at 600 nm, and it decreased to 14.1% after the H-radical exposure. From these transmittance data, the H-radical density was estimated to be 1.3×10^{12} cm^{-3}.

Appendix 3

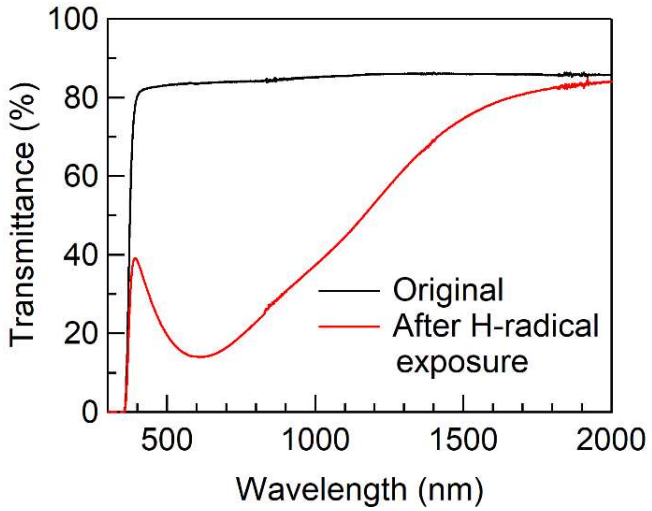

Fig. A3.12 Transmittance spectra of WO_3 doped glass before and after the exposure to H-radical.

Then, the reduction of $SiCl_4$ by the H-radical was carried out. **Figure A3.13** shows the appearance of quartz tubes and quartz glasses after the experiments. The reaction chamber was heated up to 900°C, the introduction amount of $SiCl_4$ was ~330 μmol/min, and the reaction time was 30 min. With H_2 gas, i.e., applied current to W filaments: 0 A and filament temperature: R.T., dark-gray substance was confirmed only on the inside of the quartz tube. By increasing the applied current to up to 22 A (filament temperature: ~1300°C), the amount of dark-gray substance increased, and the deposition of the dark-gray substance was also confirmed on the quartz glasses. By further increasing the applied current up to 26 A and 30 A (filament temperature: ~1700°C and ~2000°C), the amount of dark-gray substance significantly increased.

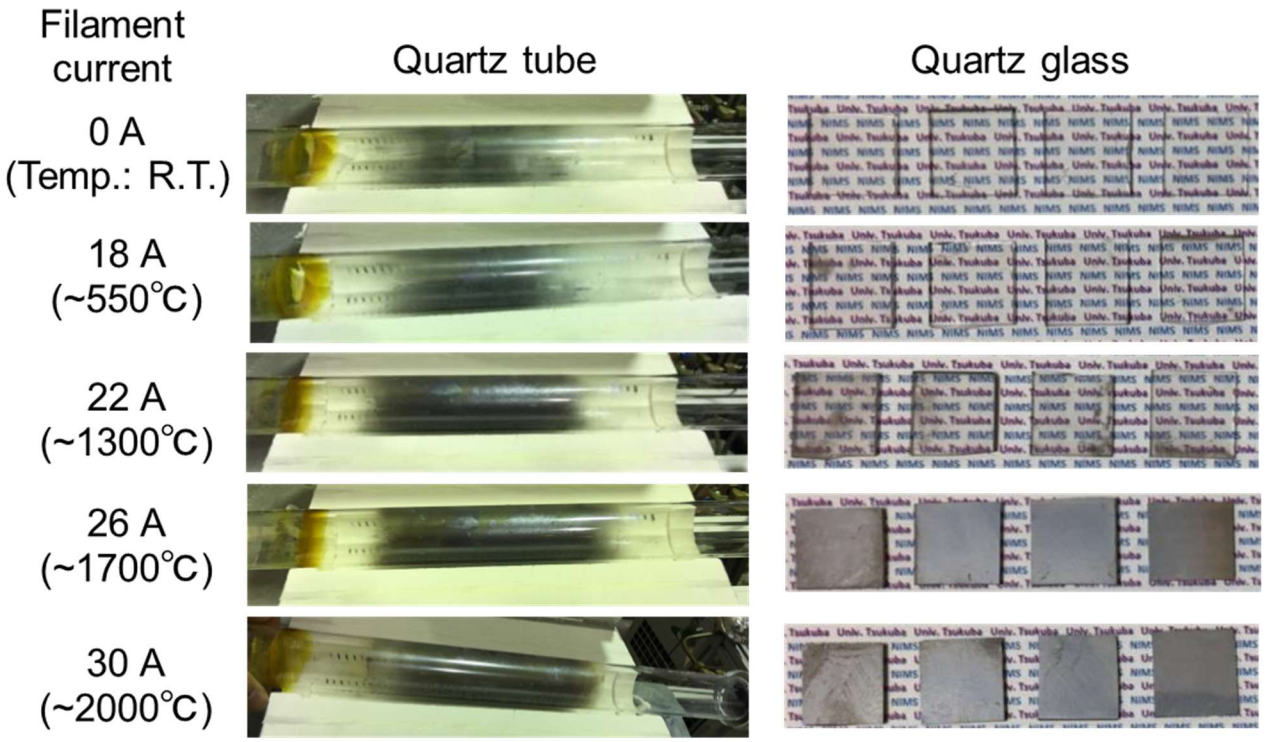

Fig. A3.13 Appearance of quartz tubes and quartz glasses after the experiments for reduction of $SiCl_4$.

To identify the gray substance on the quartz glasses, XRD analysis was carried out. **Figure A3.14** shows a XRD pattern of the quartz glass (position B) after the experiment with applied current of 30 A. The sample had three peaks at 2θ = ~28.4°, 47.3°, and 56.2° corresponding to Si, which suggests that the deposited substance on the quartz tube and quartz glasses were Si.

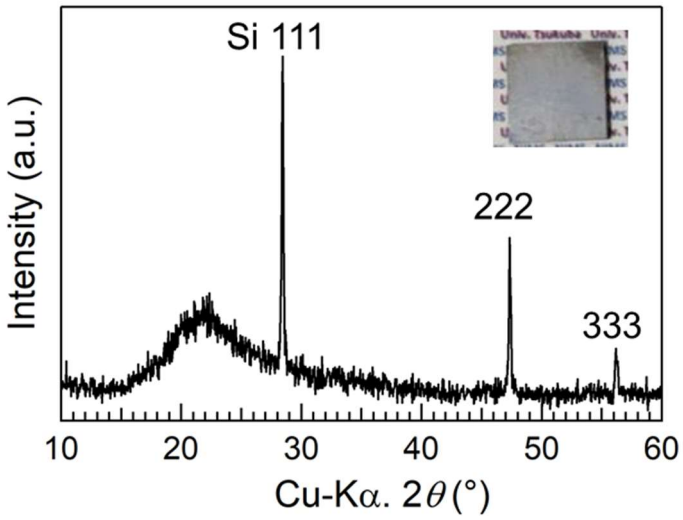

Fig. A3.14 XRD pattern of the quartz glass (position B) after the experiment with applied current of 30 A.

In Part 1, the relationship between H-radical density and applied current to W filament under the generation pressure of ~105 kPa and the detection chamber pressure of ~101 kPa was shown in **Fig. A3.9**. It demonstrated the significant increase of H-radical density from the applied current of ~22 A (filament temperature: ~1300°C). Although the experiments were operated under the relatively low reaction pressure of ~1.8 kPa in this part, the relationship between H-radical density and applied current may be similar to that under ~101 kPa (**Fig. A3.9**). Since the amount of deposited Si increased from 22 A as seen in **Fig. A3.13**, these results indicate that the reduction of $SiCl_4$ was promoted and the amount of produced Si was increased by the generated H-radical. Therefore, the effect of H-radical on the reduction of $SiCl_4$ was successfully demonstrated.

Then, the thickness of the deposited Si was observed by SEM. **Figure A3.15** shows the cross-sectional SEM image of the quartz glass after the experiment with the applied current: 30 A (position B). The thickness of deposited Si was ~1 μm. Since the experiment time was 30 min, the deposition rate of Si was estimated to be ~2 μm/h. The production of Si from the H_2 reduction of $SiCl_4$ was reported by Theuerer [6], and the deposition rate was ~300 μm/h in the literature. Compared with the reported deposition rate, the deposition rate of ~2 μm/h in this study is relatively small. Theuerer also showed a decreasing tendency of the deposition rate with decreasing a mol fraction of $SiCl_4$ in H_2 gas, and the $SiCl_4$ mol fraction was 0.1 to obtain the deposition rate of ~300 μm/h. In this study, $SiCl_4$ mol fraction was calculated to be $\sim 1.9\times10^{-3}$ from the flow rates of $SiCl_4$ (~330 μmol/min) and H_2 gas (~0.188 mol/min, 4 SLM), which is significantly smaller than that in the literature [6]. Therefore, the relatively small Si deposition rate is attributable to the small flow rate of $SiCl_4$. The deposition rate will increase by increasing the flow rate of $SiCl_4$.

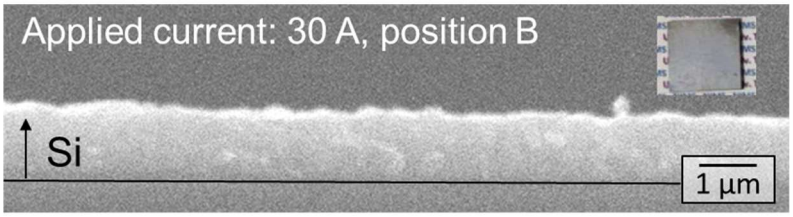

Fig. A3.15 Cross-sectional SEM image of the quartz glass (position B) after the experiment with applied current of 30 A.

A3.6.2 Reduction of $SiCl_4$ by H-radical at the reaction pressure of 1 atm

Then, the reduction of $SiCl_4$ by H-radical was carried out at 1 atm (~101 kPa). In the same way as the low-pressure condition, the H-radical density was firstly estimated before the reduction of $SiCl_4$. The WO_3 doped glass was placed at the position B in the quartz tube (**Fig. A3.11(b)**), and it was exposed to the H-radical for 1 h with heating at 327°C (600 K). The H_2 gas flow rate was 4.2 SLM, and the pressures in the H-radical generation chamber and the reaction chamber were ~105 kPa and~101 kPa, respectively. The W filaments were electrically heated to ~2000°C (applied current: 30 A).

Figure A3.16 shows transmittance spectra of the WO_3 doped glasses before and after the exposure to H_2 gas or H-radical. After the exposure to H_2 gas (without heating the W filaments), the transmittance was slightly smaller than that of the original WO_3 doped glass, but a drop of transmittance at 600 nm was not confirmed. On the other hand, after the exposure to H-radical (with heating the W filaments to ~2000°C, applied current: 30 A), a drop of transmittance from 83.5% (for the original) to 76.6% at ~600 nm was confirmed, which indicates the generation and detection of the H-radical. From the transmittance change, the H-radical density was estimated to be 6.1×10^{10} cm^{-3}. The H-radical density under these conditions was smaller than those obtained in Part1 possibly due to the differences of apparatus.

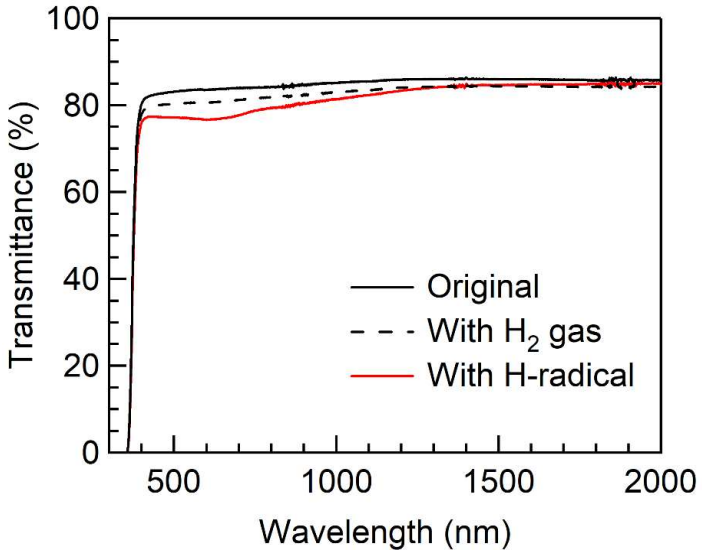

Fig. A3.16 Transmittance spectra of the WO_3 doped glass before and after the exposure to H_2 gas or H-radical.

Then, the H-radical reduction of $SiCl_4$ was carried out at the reaction pressure of ~101 kPa. **Figure A3.17** shows appearances of quartz tubes and quartz glasses after the reduction of $SiCl_4$ by H_2 and H-radical, and

cross-sectional SEM images of the quartz glasses placed at the position B. The H_2 gas flow rate was 4.2 SLM, and the pressures in the H-radical generation chamber and the reaction chamber were ~105 kPa and ~101 kPa, respectively. The reaction chamber was heated up to 900°C, and the introduction amount of $SiCl_4$ was ~100 μmol/min.

A relatively large amount of deposited Si was confirmed on the quartz tube and quartz glasses even only with H_2 gas (applied current: 0 A, filament temperature: R.T.) under the reaction pressure of 101 kPa, since the density of $SiCl_4$ and H_2 in the reaction chamber were larger than those under ~1.8 kPa. However, the quartz tube still kept a transparency after the experiment with H_2 gas. On the other hand, after the experiment with H-radical, the transparency of the quartz tube was lost due to the deposited Si, which indicates the increase of deposited Si by the H-radical. As for the quartz glasses, the apparent difference was not confirmed between with H_2 gas and with H-radical from the appearance of quartz glasses placed at position A, B, and C. The thicknesses of the deposited Si on the glasses at position B were observed from their cross-sectional SEM images. The thickness of the deposited Si for the sample with H_2 gas was ~1.3 μm, and it slightly increased to ~1.5 μm with H-radical. Although a difference was small possibly due to the small H-radical density, the increase of deposited Si was confirmed by using H-radical.

As for the quartz glass placed at the position D, the deposition of Si was hardly confirmed with H_2 gas. This phenomenon is attributable to the lower temperature of the position D than those of the positions B and C. The quartz tube was set so that the thermocouple measured the temperature of the middle of position B and C. Since the temperature may be the highest near the thermocouple (i.e. middle of the tubular furnace), the temperature of position D must be lower than those of positions B and C, and hence, the reduction of $SiCl_4$ did not proceed effectively. This situation can be also applied to the position A. However, the mixed gas of H_2 and $SiCl_4$ was transported through the positions B and C, i.e., higher temperature area, before reaching to the position A, which enabled the deposition of Si at the position A. On the other hand, with H-radical, the quartz glass at the position D was totally covered by Si, which implies that the H-radical reduction of $SiCl_4$ proceeded at lower temperature than that by H_2 gas.

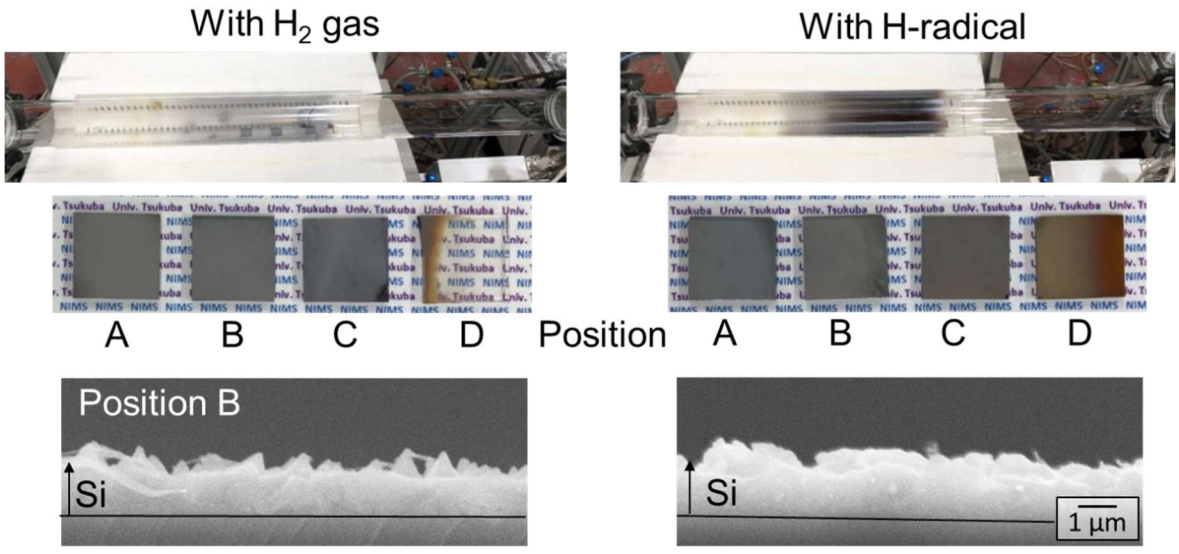

Fig. A3.17 Appearance of quartz tubes and quartz glasses, and cross-sectional SEM images of the quartz glasses placed at position B after the reduction of $SiCl_4$ with H_2 and H-radical at 900°C.

Appendix 3

To confirm the effect of H-radical on the reduction of $SiCl_4$ more clearly, the experiment was carried out at the lower reaction temperature of 850°C. **Figure A3.18** shows the appearance of quartz tubes and quartz glasses after the reduction of $SiCl_4$ with H_2 and H-radical at 850°C, and cross-sectional SEM images of the quartz glasses. With H_2 gas, the amount of deposited Si on the quartz glasses was significantly decreased compared to that with the reaction temperature of 900°C. Although the deposition of Si can be confirmed for the positions A and B, some parts of the quartz glasses were not covered by Si as observed from the cross-sectional SEM image, due to its small amount of deposited Si. In addition, the quartz glasses at the positions C and D kept transparency even after the experiment.

On the other hand, with H-radical, the quartz glasses at the positions A, B, and C were completely covered by Si. The cross-sectional SEM images of the quartz glasses at the positions B and C also showed the complete coverage of the quartz glasses by the deposited Si with the thickness of > ~1 μm. Although needle-shaped Si was confirmed on the surface, the formation mechanism is not clear yet. The substance deposited on the position D with H-radical had brown color which is different from the other positions. To identify the brown substance, XRD and Raman spectroscopy were carried out. **Figures A3.19** show (a) XRD pattern and (b) Raman spectrum of the brown substance (position D, with H-radical). There seems to be a small inflection at ~28.4° in the XRD pattern, but an apparent peak of Si was not confirmed. On the other hand, the Raman spectrum showed a strong peak at ~520 cm^{-1} corresponding to crystal Si, but the bottom of the peak was broadened from ~510 to 450 cm^{-1}. Since an amorphous Si has a broad peak at ~480 cm^{-1} in the Raman spectrum [27], the blown substance may correspond to an amorphous Si.

These results indicate that the H-radical is effective to promote the reduction of $SiCl_4$ even at 1 atm and to produce larger amount of Si than the conventional hydrogen reduction method (Siemens method).

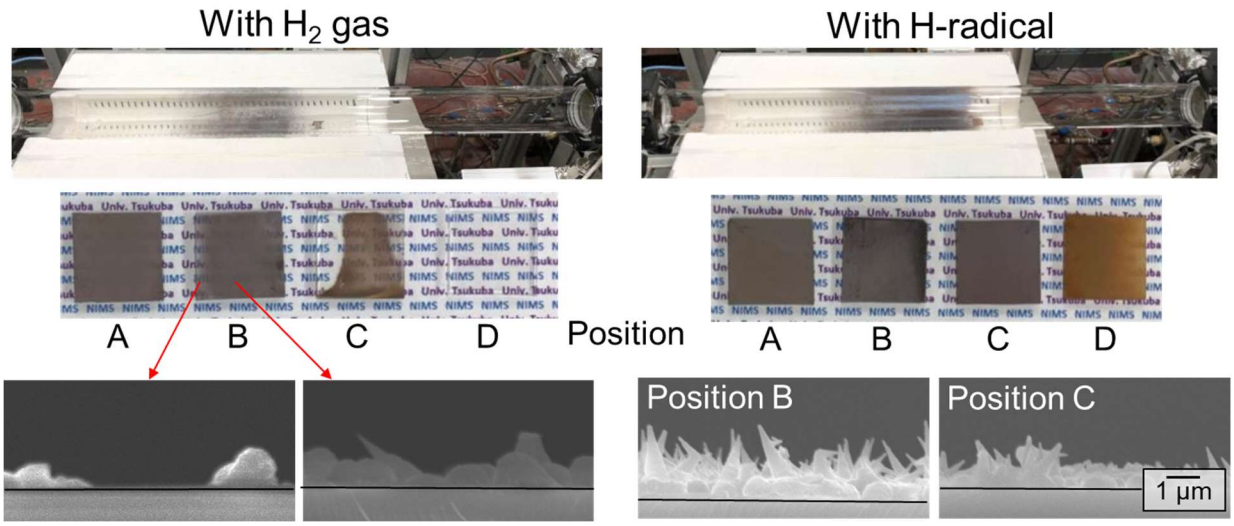

Fig. A3.18 Appearance of quartz tubes and quartz glasses, and cross-sectional SEM images of the quartz glasses after the reduction of $SiCl_4$ with H_2 and H-radical at 850°C.

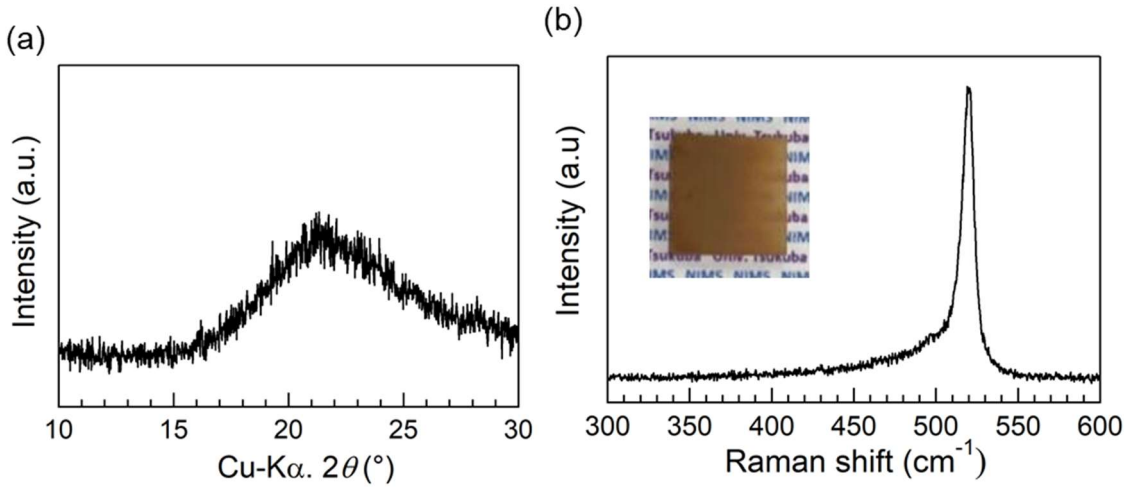

Figs. A3.19 (a) XRD pattern and (b) Raman spectrum of the brown substance (position D, with H-radical).

A3.7 Conclusions

In Part 2, the reduction of $SiCl_4$ using remotely supplied H-radical was carried out to produce Si at the reaction pressure of 1 atm (~101 kPa). At the relatively low reaction pressure of ~1.8 kPa, the amount of produced Si increased with increasing the applied current to the W filaments, which indicates that the reduction of $SiCl_4$ was promoted by the H-radical. Even at the reaction pressure of ~101 kPa, the amount of produced Si increased by using the H-radical instead of H_2 gas, although the difference was smaller than that confirmed at ~1.8 kPa due to the smaller H-radical density. As a result, it was successfully demonstrated that the H-radical can reduce $SiCl_4$ and produce Si more effectively than conventional H_2 reduction (Siemens method).

As the summary through the Part 1 and Part 2, H-radical was successfully generated at the pressure > 1 atm and transported to the 1 atm reaction chamber. Besides, H-radical produced Si more efficiently than H_2 gas by promoting the reduction of $SiCl_4$. These results strongly suggest the possibility of the application of H-radical into the Siemens method and the enhancement of Si yield.

Most part of this chapter is under preparation for publication.

References

[1] C. D. Bailie, M. G. Christoforo, J. P. Mailoa, A. R. Bowring, E. L. Unger, W. H. Nguyen, J. Burschka, N. Pellet, J. Z. Lee, M. Grätzel, R. Noufi, T. Buonassisi, A. Salleo, M. D. McGehee, Semi-transparent perovskite solar cells for tandems with silicon and CIGS, *Energy Environ. Sci.*, **8**, 956-963 (2015).

[2] J. P. Mailoa, C. D. Bailie, E. C. Johlin, E. T. Hoke, A. J. Akey, W. H. Nguyen, M. D. McGehee, T. Buonassisi, A 2-terminal perovskite/silicon multijunction solar cell enabled by a silicon tunnel junction, *Appl. Phys. Lett*., **106**, 121105 (2015).

[3] M. Zhong, K. Yasuda, T. Homma, T. Nohira, Purity and minority carrier lifetime in silicon produced by direct electrolytic reduction of SiO_2 in molten $CaCl_2$, *Electrochemistry*, **86**, 77–81 (2018).

[4] L. Zong, B. Zhu, Z. Lu, Y. Tan, Y. Jin, N. Liu, Y. Hu, S. Gu, J. Zhu, Y. Cui, Nanopurification of silicon from 84% to 99.999% purity with a simple and scalable process, *PNAS*, **112**, 13473-13477 (2015).

[5] J. Sakai, Process of manufacture of polysilicon using hydrogen, *Hydrogen energy system*, **33**, 15-21, in Jpn. (2008).

[6] H. C. Theuerer, Epitaxial silicon films by the hydrogen reduction of $SiCl_4$, J. Electrochem. Soc., **108**, 649-653 (1961).

[7] K. Yasuda, K. Morita, T. Okabe, Production process of solar grade silicon by hydrogen reduction and/or thermal decomposition, *Journal of MMIJ*, **126**, 115-123, in Jpn. (2010).

[8] M. Abdel-Rahman, V. Schulz-von der Gathen, T. Gans, K. Niemi, H. F. Döbele, Determination of the degree of dissociation in an inductively coupled hydrogen plasma using optical emission spectroscopy and laser diagnostics, *Plasma Sources Sci. Technol*., **15**, 620–626 (2006).

[9] S. Takahashi, S. Takashima, K. Yamakawa, S. Den, H. Kano, K. Takeda, M. Hori, Development of atomic radical monitoring probe and its application to spatial distribution measurements of H and O atomic radical densities in radical-based plasma processing, *J. Appl. Phys*. **106**, 053306 (2009).

[10] H. Umemoto, K. Ohara, D. Morita, Y. Nozaki, A. Masuda, H. Matsumura, Direct detection of H atoms in the catalytic chemical vapor deposition of the SiH_4/H_2 system, *J. Appl. Phys*., **91**, 1650 (2002).

[11] S. Schwarz, S.M. Rosiwal, M. Frank, D. Breidt, R.F. Singer, Dependence of the growth rate, quality, and morphology of diamond coatings on the pressure during the CVD-process in an industrial hotfilament plant, *Diamond and Related Materials*, **11**, 589–595 (2002).

[12] T. Otsuka, M. Ihara, H. Komiyama, Hydrogen dissociation on hot tantalum and tungsten filaments under diamond deposition conditions, *J. Appl. Phys*., **77**, 893-898 (1995).

[13] S. Agarwal, A. Takano, M. C. M. van de Sanden, D. Maroudas, E. S. Aydil, Abstraction of atomic hydrogen by atomic deuterium from an amorphous hydrogenated silicon surface, *J. Chem. Phys*., **117**, 10805-10816, (2002).

[14] Y. J. Chun, T. Sugaya, Y. Okada, M. Kawabe, Low temperature surface cleaning of InP by irradiation of atomic hydrogen, *Jpn. J. Appl. Phys.*, **32**, 287-289 (1993).

[15] Y. Okada, H. Shimomura, T. Sugaya, M. Kawabe, Low-temperature substrate annealing of vicinal Si(100) for epitaxial growth of GaAs on Si, *Jpn. J. Appl. Phys.*, **30**, 3774-3776 (1991).

[16] A. Izumi, H. Matsumura, Photoresist removal using atomic hydrogen generated by heated catalyzer, *Jpn. J. Appl. Phys*., **41**, 4639–4641 (2002).

[17] A. Izumi, H. Sato, S. Hashioka, M. Kudo, H. Matsumura, Plasma and fluorocarbon-gas free Si dry etching process using a Cat-CVD system, *Microelectronic Engineering*, **51 –52**, 495–503 (2000).

[18] K. Tanuma, H. Ohba, T. Shibata, Temperature distributions of conductivity heated filament, *JAERI-Tech*, **99-050**, in Jpn. (1999).

[19] P. D. Desal, T. K. Chu, H. M. James, C. Y. Ho, Electrical resistivity of selected elements, *J. Phys. Chem. Ref. Data,* **13**, 1069-1096 (1984).

[20] T. Morimoto, H. Umemoto, K. Yoneyama, A. Masuda, H. Matumura, K. Ishibashi, H. Tawarayama, H. Kawazoe, Quantification of gas-phase H-atom number density by tungsten phosphate glass, *Jpn. J. Appl. Phys*., **44**, 732–735 (2005).

[21] U. Meier, K. Kohse-Hoinghaus, L. Schafer, C. P. Klages, Two-photon excited LIF determination of H-atom concentrations near a heated filament in a low pressure H_2 environment, *Applied Optics*, **29**, 4993-4999 (1990).

[22] S.A. Redman, C. Chung, M.N.R. Ashfold, H atom production in a hot filament chemical vapour deposition reactor, *Diamond and Related Materials*, **8**, 1383–1387 (1999).

[23] D. W. Comerford, U. F. S. D'Haenens-Johansson, J. A. Smith, M. N. R. Ashfold, Y. A. Mankelevich, Filament seasoning and its effect on the chemistry prevailing in hot filament activated gas mixtures used in diamond chemical vapour deposition, *Thin Solid Films,* **516**, 521–525 (2008).

[24] H. Umemoto, H. Matsumura, Future prospect of remote Cat-CVD on the basis of the production, transportation and detection of H atoms, *Thin Solid Films*, **516**, 500–502 (2008).

[25] H. Umemoto, Production and detection of H atoms and vibrationally excited H_2 molecules in CVD processes, *Chem. Vap. Deposition*, **16**, 275–290 (2010).

[26] H. B. Profijt, S. E. Potts, M. C. M. van de Sanden, W. M. M. Kessels, Plasma-assisted atomic layer deposition: basics, opportunities, and challenges, *J. Vac. Sci. Technol. A*, **29**, 050801 (2011).

[27] Q. Shabir, A. Pokale, A. Loni, D. R. Johnson, L. T. Canham, R. Fenollosa, M. Tymczenko, I. Rodríguez, F. Meseguer, A. Cros, A. Cantarero, Medically biodegradable hydrogenated amorphous silicon microspheres, *Silicon*, **3**, 173–176 (2011).

Achievements

List of publications

[1] **Y. Okamoto**, and Y. Suzuki, "Mesoporous $BaTiO_3/TiO_2$ double layer for electron transport in perovskite solar cells", *J. Phys. Chem. C*., **120**, [26], 13995-14000 (2016).

[2] **Y. Okamoto**, R. Fukui, M. Fukazawa, and Y. Suzuki, "$SrTiO_3/TiO_2$ composite electron transport layer for perovskite solar cells", *Mater. Lett*., **187**, 111-113 (2017).

[3] **Y. Okamoto**, and Y. Suzuki, "Perovskite solar cells prepared by a new 3-step method including a PbI_2 scavenging step", *Mater. Sci. Semicond. Process*., **71**, 1-6 (2017).

[4] **Y. Okamoto**, T. Yasuda, M. Sumiya, and Y. Suzuki, "Perovskite solar cells prepared by advanced 3-step method using additional $HC(NH_2)_2I$ spin-coating: efficiency improvement with multiple bandgap structure", *ACS Appl. Energy Mater*., **1**, [3], 1389-1394 (2018).

[5] **Y. Okamoto**, M. Sumiya, and Y. Suzuki, "Perovskite solar cells with >19% efficiency achieved by advanced three-step method using additional $HC(NH_2)_2I$-NaI spin-coating, *ACS Appl. Energy Mater.,* (accepted).

List of related publications

[1] **Y. Okamoto**, and Y. Suzuki, "Perovskite-type $SrTiO_3$, $CaTiO_3$ and $BaTiO_3$ porous film electrodes for dye-sensitized solar cells", *J. Ceram. Soc. Jpn.*, **122**, [8], 728-731 (2014).

[2] **Y. Okamoto**, and Y. Suzuki, "Double-layer dye-sensitized solar cells using $SrTiO_3$ and $BaTiO_3$ second layer with enhanced photovoltaic performance", *J. Ceram. Soc. Jpn.*, **123**, [10], 967-971 (2015).

[3] M. Nukunudompanich, S. Chuangchote, **Y. Okamoto**, Y. Shinoda, and Y. Suzuki, "TiO_2 nanorods and semi-nanotubes prepared from anodic aluminum oxide template and their applications as photoelectrodes in dye-sensitized solar cells", *J. Ceram. Soc. Jpn*., **123**, [5], 428-432 (2015).

[4] **Y. Okamoto**, Y. Harada, N. Ohta, K. Takada, and M. Sumiya, "Preparation of Si nano-crystals with controlled oxidation state from SiO disproportionated by ZrO_2 ball-milling", *Jpn. J. Appl. Phys*., **55**, 090304, (2016).

[5] K. Kawashima, **Y. Okamoto**, O. Annayev, N. Toyokura, R. Takahashi, M. Lippmaa, K. Itaka, N. Matsuki, Y. Suzuki, and H. Koinuma, "Combinatorial screening of halide perovskite thin films and solar cells by mask-defined IR laser MBE", *Sci. Tech. Adv. Mater*., **18**, [1], 307-315 (2017).

[6] F. Z. Dahmani, **Y. Okamoto**, D. Tsutsumi, T. Ishigaki, H. Koinuma, S. Hamzaoui, S. Flazi, and M. Sumiya, "Density evaluation of remotely-supplied hydrogen radicals produced via tungsten filament method for $SiCl_4$ reduction", *Jpn. J. Appl. Phy*., **57**, 051301, (2018).

Proceedings

[1] Y. Suzuki, **Y. Okamoto**, and N. Ishii, "Dye-sensitized solar cells using double-oxide electrodes: a brief review", *J. Phys. Conf. Ser.*, **596**, 012001 (2015). (Tunisia-Japan Symposium: R&D of Energy and Material Sciences for Sustainable Society, Gammarth, Tunisia, (Nov. 2014))

[2] N. Ishii, **Y. Okamoto**, and Y. Suzuki, "Semiconductor $MgTiO_3$, $MgTi_2O_5$ and Mg_2TiO_4 double-oxide electrodes for dye-sensitized solar cells", *Int. Lett. Chem. Phys. Astro.*, **46**, 9-15 (2015).

Prizes

[1] **Y. Okamoto**, and Y. Suzuki, IWP2014 PRIZE, "Perovskite cells using $SrTiO_3$ for the electron transport layer", Interdisciplinary Workshop on Science and Patents (IWP) 2015, Tsukuba, Japan, (Sep., 2015)

[2] **Y. Okamoto**, and Y. Suzuki, Award of the Outstanding Papers Published in the JCerSJ in 2015, "Double-layer dye-sensitized solar cells using $SrTiO_3$ and $BaTiO_3$ second layer with enhanced photovoltaic performance", The Ceramics Society of Japan, Tokyo, Japan, (Jun., 2016).
(岡本裕二, 鈴木義和, 2015 JCS-JAPAN 優秀論文賞, "Double-layer dye-sensitized solar cells using $SrTiO_3$ and $BaTiO_3$ second layer with enhanced photovoltaic performance", 公益社団法人　日本セラミックス協会, 東京, 日本, (2016 年 6 月)).

Research funds

[1] **Y. Okamoto**, and Y. Suzuki, 2015 Kato Foundation for Promotion of Science research grant, Kato Foundation for Promotion of Science, No. 2726, (Jun. 2015-Apr. 2016).
(岡本裕二, 鈴木義和, 平成 27 年度加藤科学振興会研究奨励金, "無機・有機エピタキシャルペロブスカイト型太陽電池の創製", 番号 2726, 加藤科学振興会, 2015 年 6 月~2016 年 3 月.)

[2] **Y. Okamoto**, and Y. Suzuki, 2016 Kato Foundation for Promotion of Science research grant, Kato Foundation for Promotion of Science, No. KS-2816, (Jun., 2016-Apr., 2017).
(岡本裕二, 鈴木義和, 平成 28 年度加藤科学振興会研究奨励金, "強誘電性を有する電子輸送層を用いたペロブスカイト太陽電池の高効率化", 登録番号 KS-2816, 加藤科学振興会, 2016 年 6 月 ~2017 年 3 月.)

[3] **Y. Okamoto**, Grants-in-Aid for Scientific Research, No. 17J01387, Ministry of Education, Culture, Sports, Science and Technology, Japan, (2017-2019).
(岡本裕二, 特別研究員奨励費、水素ラジカル還元法による高純度シリコンの高効率作製プロセスの開発), 課題番号 17J01387, 文部科学省, 2017 年-2019 年.)

Support programs

[1] **Y. Okamoto**, "Nano Technology Platform Japan" program, Ministry of Education, Culture, Sports, Science and Technology (MAXT), National Institute of Advanced Industrial Science and Technology (AIST), Tsukuba, Japan, (29-31, Aug., 2016).
(岡本裕二, 文部科学省テクノロジープラットフォーム平成 28 年度学生研修プログラム, "極端紫外光光電子分光（EUPS）により最表面原子層の電子状態を見る - 原理と測定実習", 文部科学省, 国立研究開発法人産業技術総合研究所 (AIST), 筑波, 日本, (2016 年 8 月 29-31 日).

Achievements

[2] **Y. Okamoto**, National Nanotechnology Coordinated Infrastructure (NNCI) International Research Experience for Graduates, "Enhancing the current density of record-efficiency perovskite/silicon solar cells via engineered, nano-scale light scattering structures", Ministry of Education, Culture, Sports, Science and Technology (MAXT), Japan as part of the cooperation with National Science Foundation (NSF), Arizona State University, Tempe/Phoenix, Arizona, USA, (19 May-9 Aug., 2017).
(岡本裕二, 文部科学省ナノテクノロジープラットフォーム平成２９年度米国 NNCI 施設利用研修プログラム, "Enhancing the current density of record-efficiency perovskite/silicon solar cells via engineered, nano-scale light scattering structures", 文部科学省, Arizona State University, Tempe/Phoenix, Arizona, USA, (2017 年 5 月 29 日-8 月 9 日)).

Conference/Symposium/Workshop

International

[1] **Y. Okamoto**, and Y. Suzuki, "Dye-sensitized solar cells with semiconductor electrodes made of perovskite-type double oxide", Junior Euromat 2014 - The Major Event for Young Materials Scientists, B/No. 79, Lausanne, Switzerland (July, 2014) (Poster)

[2] **Y. Okamoto**, and Y. Suzuki, "Perovskite cells using $SrTiO_3$ for the electron transport layer", Interdisciplinary Workshop on Science and Patents (IWP) 2015, Tsukuba, Japan (Sep., 2015) (Poster).

[3] **Y. Okamoto**, and Y. Suzuki, "Double-layer dye-sensitized solar cells using $SrTiO_3$ and $BaTiO_3$ second layer with improved photovoltaic performance", 4th International Workshop on Nano and Microstructure Design (IWNMD2015), Busan, Korea, (Dec., 2015) (Oral)

[4] **Y. Okamoto**, and Y. Suzuki, "Mesoporous $BaTiO_3/TiO_2$ double layer for electron transport in perovskite solar cells", Interdisciplinary Workshop on Science and Patents (IWP) 2016, Tsukuba, Japan (Sep., 2016) (Poster)

[5] **Y. Okamoto**, and Y. Suzuki, "Effects of mesoporous $BaTiO_3/TiO_2$ double layer for electron transport and enhanced photovoltaic performance in perovskite solar cells, International Photovoltaic Science and Engineering Conference (PVSEC-26), Singapore, Singapore, (Oct., 2016) (Oral)

[6] **Y. Okamoto**, and Y. Suzuki, "Mesoporous $BaTiO_3/TiO_2$ double layer for enhancement of photovoltaic performance in perovskite solar cells", The 3rd Best-Efficiency Engineering Research Workshop for Perovskite Photovoltaics and Beyond (BWP-3): Student –Oriented Junior Scientist's Union for PV in 2017", Seoul, Korea, (Jan., 2017) (Oral).

[7] **Y. Okamoto**, and Y. Suzuki, $BaTiO_3/TiO_2$ mesoporous double layer for the electron transport layer of organic/inorganic hybrid solar cells, The 2017 E-MRS Spring Meeting and Exhibit, Strasbourg, France (Feb., 2017) (Poster).

[8] **Y. Okamoto**, and Y. Suzuki, "Perovskite solar cells prepared by 3-step method including PbI_2 scavenging step, 11th Aseanian Conference on Nano-Hybrid Solar Cells (NHSC11), Himeji, Japan, (Oct., 2017) (Poster)

[9] **Y. Okamoto**, T. Yasuda, M. Sumiya, and Y. Suzuki, "Perovskite solar cells with multiple bandgap structure prepared by advanced 3-step method using $HC(NH_2)_2I$ spin-coating", Grand Renewable Energy 2018 International Conference and Exhibition (GRE2018), Yokohama, Japan, (Jun., 2018) (Oral)

[10] **Y. Okamoto**, T. Yasuda, M. Sumiya, and Y. Suzuki, "Perovskite solar cells prepared by 3-step method using additional CH_3NH_3I or $HC(NH_2)_2I$ spin-coating: multiple bandgap structure for efficiency improvement", Brussels, Belgium, (Sep., 2018) (Poster).

Domestic

[1] **Y. Okamoto**, K. Aisu, M. Sumiya, H. Koinuma, and Y. Suzuki, "Preparation and Evaluation of DSC Using Double Oxide", 第 33 回エレクトロセラミックス研究討論会, Ibaraki, Japan, (Oct., 2013) (Poster).

[2] **Y. Okamoto**, K. Aisu, Y. Suzuki, M. Sumiya, and H. Koinuma, "複酸化物電極を用いた色素増感太陽電池の作製と評価", The Ceramic Society of Japan Annual Meeting 2014, Tokyo, Japan, (Mar. 2014) (Poster).

[3] **Y. Okamoto**, and Y. Suzuki, "ペロブスカイト構造を有する複酸化物粉末の色素増感太陽電池電極への適用", Japan Society of Powder Metallurgy Spring Meeting 2014, Tokyo, Japan, (Jun., 2014) (Oral).

[4] **Y. Okamoto**, and Y. Suzuki, "ペロブスカイト型構造を有する複酸化物を用いた色素増感太陽電池の作製と評価", SAT Technology Showcase 2015, Ibaraki, Japan, (Jan., 2015) (Poster).

[5] **Y. Okamoto**, and Y. Suzuki, "Preparation of double-layer dye-sensitized solar cells using perovskite-type double oxides", The 62nd The Japan Society of Applied Physics (JSAP) spring meeting, Kanagawa, Japan, (Mar., 2015) (Oral).

[6] **Y. Okamoto**, and Y. Suzuki, "Perovskite solar cells using $BaTiO_3/TiO_2$ mesoporous layer for the electron transport layer", The Ceramic Society of Japan Annual Meeting 2017, Tokyo, Japan, (Mar. 2017) (Oral).

[7] **Y. Okamoto**, and Y. Suzuki, "Perovskite solar cells prepared by a new 3-step method including a PbI_2 scavenging step", The 78th The Japan Society of Applied Physics (JSAP) Autumn meeting, Fukuoka, Japan, (Sep., 2017) (Poster).

Acknowledgements

The author would like to show my greatest appriciation to my super visor Associate Professor Yoshikazu Suzuki in the Development of Materials Science at the Graducate School of Pure and Applied Sciences, University of Tsukuba for his generous help and excellent guidance in coordinating this investigateion. The author would like to thank Professor Kiyoto Matsuishi and Professor Hiroko Tokoro in the Development of Materials Science at the Graducate School of Pure and Applied Sciences, University of Tsukuba for reviewing this thesis and their helpful suggestion. The author woluld like to express the gratitude to Principal Researcher Dr. Takeshi Yasuda at Molecular Design and Function Group, National Institute for Materials Science (NIMS) for reviewing this thesis, his helpful suggestion and use of IPCE measuement system.

The author is deeply grateful to Chief Researcher Dr. Masatomo Sumiya at Wide Bandgap Semiconductors Group, National Institute for Materials Science (NIMS) for his kind guidance on the research about the production of Si from $SiCl_4$ reduction using hydrogen radical and for the use of spin-coater, SEM, AFM and PL measurement. The author woluld like to express the gratitude to Professor Hideomi Koinuma for his continuous encouragement. The author geatly thanks to Group Leader Dr. Tohru Suzuki at Ceramics Processing Group and Engineer Dr. Yoshitomo Harada at Surface Chemical Analysis Group, National Institute for Materials Science (NIMS) for the use of SEM-EDS and their help. The author would like to thank Faculty of Pure and Applied Sciences and the Open Facility Network Office, Research Facility Center for Science and Technology, University of Tsukuba, for allowing me to use FE-SEM (SU-8020) and XPS/UPS (JPS-9010TR).

The author appreciates to the financial supports by the Research Grant of Kato Foundation for Promotion of Science, the Research Fellowships for Young Scientists of the Japan Society for Promotion of Science, and the Grant-in-Aid for Scientific Research from the Ministry of Education, Culture, Sports, Science and Technology, Japan. The author greatfully acknowledges to author's colleagues of Yoshikazu Suzuki Laboratory for their kind frendships and help.

The author appriciates Hawa Alima Binti Abdul Lattif for her kind supports and help. Finally, the author would like to express the deep appreciation to my parents, Hideki Okamoto and Sumiko Okmamoto, my older sister, Sayuri Kato for their hearty supports and understandings.

Yuji Okamoto

February, 2019
Tsukuba, Japan